Dynamics and Numerical Modeling of River Plumes in Lakes

A Dissertation
Presented to
The Academic Faculty

by

Navid Nekouee

In Partial Fulfillment of the degree of
Doctor of Philosophy
In the School of Civil and Environmental Engineering

Georgia Institute of Technology
August 2010

Approved by:

Dr. Philip J. W. Roberts, Advisor
School of Civil and Environmental Engineering
Georgia Institute of Technology

Dr. David J. Schwab
Great Lakes Environmental Research Laboratory
National Oceanic Atmospheric Administration

Dr. Donald Webster
School of Civil and Environmental Engineering
Georgia Institute of Technology

Dr. Thorsten Stoesser
School of Civil and Environmental Engineering
Georgia Institute of Technology

Dr. Emanuele Di Lorenzo
School of Earth and Atmospheric Sciences
Georgia Institute of Technology

Date Approved: May 18, 2010

ACKNOWLEDGEMENTS

I express my sincere heartfelt gratitude to my major professor, Dr. Philip Roberts, the most knowledgeable, humble and noble human I have ever met, for giving me an opportunity to work with him. There aren't enough words to express my appreciation for his continuous encouragement and guidance over the period of this dissertation.

The dissertation would not have been completed without the support of my dissertation committee member, Dr. David Schwab. I am especially thankful for the countless hours he spent discussing the Grand River field data and explaining various issues regarding numerical modeling.

I am also grateful of others at NOAA Great Lakes Environmental Research Laboratory, especially Dr. Dima Beletski, for providing POMGL whole lake simulations, and Dr. Mike McCormick and his team during the CTD experiments, and Dr. Sandra McLellan and her crew from Great Lakes Water Institute for bacterial sampling.

I extend my deepest appreciation to the other committee members, Dr. Donald Webster, Dr. Thorsten Stoesser and Dr. Emanuele Di Lorenzo for their constructive advice and help in fulfilling the dissertation requirements.

To my parents, Alireza Nekouee and Ashraf Pakravan, and brothers, Farhad and Farzad Nekouee, who have blessed me with an endless supply of patience, encouragement and support throughout my life and education, I am incredibly grateful and love you all very much.

Finally, I would like to acknowledge NOAA and the Oceans and Human Health Initiative for funding this research.

TABLE OF CONTENTS

LIST OF TABLES

LIST OF FIGURES

NOMENCLATURE

a	Aspect ratio of discharge channel; $a = b / d$
A	Discharge channel cross-sectional area; $A = bd$
b	Discharge channel width;
c	Internal gravity wave speed;
c_e	Local shallow water wave speed; $\sqrt{gH}$
c_i	Baroclinic phase speed proportional to $\sqrt{H}$;
c_s	Speed of sound;
C	Local tracer concentration
C_1	Empirical coefficients for Eqns. 2-11 and 4-5;
C_2, C_3	Empirical coefficients for Eqns. 2-12 and 2-13;
$n_1, ..., n_9$	Empirical powers for Eqn. 2-12, 2-13 and 4-5;
C_0	Source (river) tracer concentration;
C_b	Background ambient concentration;
d	Discharge channel depth;
f	Corilois parameter;
f_p	Fraction of bacteria attached to the particles;
Fr'	Local densimetric Froude number;
Fr'_0	Source densimetric Froude number for a buoyant discharge; $Fr'_0 = U_0 \Big/ \left(g'_0 L_Q\right)^{1/2}$ or for a line diffuser; $Fr'_0 = u^3 / j_0$
Fr'_{h0}	River densimetric Froude number adjusted for plume thickness; $Fr'_{h0} = U_{0h_0} / \sqrt{g'_0 h_0}$
Fr'_d	River densimetric Froude number based on full channel velocity; $Fr'_d = U_0 / \sqrt{g'_0 d}$
g	Acceleration due to gravity;
g'	Local modified acceleration due to gravity; $g' = g\,\Delta\rho / \rho_a$

g_0' Modified acceleration due to gravity at source; $g_0' = g\,\Delta\rho_0/\rho_a$

h Plume thickness in the lake;

h_0 Plume thickness at the river mouth;

h_c Critical depth a buoyant discharge in rectangular channel; $h_c = (q_0^2/g')^{1/3}$

H Water depth;

$I_0(t)$ Solar radiation as a function of time;

j_0 Buoyancy flux per unit length (e.g. for a line diffuser); $j_0 = g_0' q_0$

J_0 Buoyancy flux (e.g. in the river); $J_0 = g_0' Q_0$

k Bacterial decay rate;

k_d Base mortality;

k_e Sunlight attenuation coefficient;

k_I Insolation inactivation rate;

K_h Horizontal turbulent (eddy) diffusion coefficients;

K_v Vertical turbulent (eddy) diffusion coefficient;

L_b Plume-crossflow length scale; $l_b = J_0/U_a^3$

L_m Jet-crossflow length scale; $l_m = M_0^{1/2}/U_0$

L_M Jet-plume length scale; $l_M = M_0^{3/4}/J_0^{1/2}$

L_Q Discharge length scale; $l_Q = Q_0/M_0^{1/2}$

L_T Jet-plume-crossflow length scale; $l_T = M_0^{2/3}/(J_0 U_a)^{1/3}$

M_0 Discharge momentum flux; $M_0 = U_0 Q_0$

n_s Total number of time steps;

N Buoyancy frequency; $N = \sqrt{\frac{-g}{\rho_a}\cdot\frac{d\rho}{dz}}$

q_0 Volume flux per unit length;

Q_0 Discharge volume flux; $Q_0 = U_0 A$

r	Radial distance from the river mouth;
r_0	Initial radial distance from the river mouth;
Ri	Richardson number;
S_{mean}	Mean dilution;
$S_{\min}$	Minimum dilution; $S_{\min} = (C_0 - C_b)/(C_0 - C)$;
T	Water temperature;
T_{90}	Time for bacteria to reduce by 90%;
u	Currents speed in x direction;
U_a	Ambient longshore current velocity; U_x
U_0	Full-depth discharge velocity;
$V_{i,j,k}$	Current vector;
v	Currents speed in y direction;
v_s	Stoke's velocity of particles;
w	Currents speed in z direction;
W	Arc length of the plume;
W_0	Initial arc length of the plume;
W_y	Offshore wind component;
x	Horizontal downstream coordinate (in x direction);
y	Horizontal coordinate (in y direction) perpendicular to ambient cross flow;
z	Vertical coordinate;
z_0	Bottom roughness height;
α	Ratio of full-discharge velocity to longshore ambient current speed; U_0/U_a
β	Power in radial spreading formula;
Δt	Time step;
$\Delta x, \Delta y, \Delta z$	Grid size or displacement in x, y or z direction;
$\Delta x_{i,j,k}$	Displacement in x, y or z direction;
$\Delta\rho$	Local density difference; $\Delta\rho = \rho_a - \rho$

$\Delta\rho_0$	Initial density difference at source; $\Delta\rho_0 = \rho_a - \rho_0$
γ	Constant multiplier in radial spreading formula;
η	Water surface elavation;
$\eta_{i,j}^k$	Random particle displacement;
ρ_a	Ambient water density
ρ_0	Initial discharge density
σ	Sigma coordinate;
ξ	Distance along the plume trajectory;
ξ_0	Plume potential core length;

SUMMARY

Models of the fate and transport of river plumes and the bacteria they carry into lakes are developed. They are needed to enable informed decisions about beach closures to avoid economic losses, and to help design water intakes and operate combined sewer overflow schemes to obviate exposure of the public to potential pathogens. This study advances our understanding of river plumes dynamics in coastal waters by means of field studies and numerical techniques.

Extensive field measurements were carried out in the swimming seasons of 2006 and 2007 on the Grand River plume as it enters Lake Michigan. They included simultaneous aerial photography, measurements of lake physical properties, the addition of artificial tracers to track the plume, and bacterial sampling. Our observed results show more flow classes than included in previous studies (e.g. CORMIX). Onshore wind can have a significant effect on the plume and whether it impacts the shoreline. A new classification scheme based on the relative magnitude of plume-crossflow length scale and Richardson number based on the wind speed is devised.

Previous studies on lateral spreading are complemented with a new relationship in the near field. The plume thickness decreased rapidly with distance from the river mouth and a new non-dimensional relationship to predict thickness is developed. Empirical near field models for surface buoyant plumes are reviewed and a near field trajectory and dilution model for large aspect ratio surface discharge channels is devised.

Bacterial reductions due to dilution were generally small (less than 10:1) up to 4.5 km from the river mouth. E. coli decay rates were significantly affected by solar radiation and ranged from 0.2 to 2.2 day^{-1} which were within the range of previous studies in Lake Michigan. Total coliform survived longer than E. coli suggesting different die-off mechanisms.

Mathematical models of the bacterial transport are developed that employ a nested modeling scheme to represent the 3D hydrodynamic processes of surface river discharges in the Great Lakes. A particle tracking model is used that provides the capability to track

a decaying tracer and better quantify mixing due to turbulent diffusion. Particle tracking models have considerable advantages over gradient diffusion models in simulating bacterial behavior nearshore that results in an improved representation of bacteria diffusion, decay and transport.

Due to the complexity and wide variation of the time and length scale of the hydrodynamic and turbulent processes in the near field (where plume mixing is dominated by initial momentum and buoyancy) and far field (where plume mixing is dominated by ambient turbulence), a coupling technique is adapted. The far field random walk particle tracking model incorporates the empirical near field model. It simulates the transport, diffusion and decay of bacteria as discrete particles and employs the near field output as the source and transports the particles based on ambient currents predicted by the 3D hydrodynamic model. The coupled model improves dilution predictions in the near field. The new techniques advance our knowledge of the nearshore fate and transport of bacteria in the Great Lakes and can be ultimately applied to the NOAA Great Lakes Coastal Forecasting System to provide a reliable prediction tool for bacterial transport in recreational waters.

CHAPTER 1

INTRODUCTION

1.1 Beach Closure Problem and Significance

Bacterial contamination at beaches is a major cause of beach closings and a potential human health hazard. One prospective source is nearby rivers that carry pollutants from agricultural and urban runoff, domestic sewage, combined sewer overflow and animal droppings. An example is the Grand Haven River plume in Lake Michigan shown in Figure 1.1. Swimming ban signs and bacteria warnings are the preemptive tactics implemented by environmental authorities around beaches that are prone to closure.

Figure 1.1 Beach closure warning sign as a consequence of high level of bacteria and the effect of the Grand River plume on adjacent beaches.

Despite significant efforts to mitigate levels of bacteria and pathogens in the river, water samples regularly show pathogen indicators like E. coli or fecal coliforms. The results of tests carried out by beach monitoring authorities take about two days to complete. During this time, the transport and decay of pathogens may change the water quality indicator concentration. Therefore a rapid tool for prediction of nearshore pollutants is needed.

The goal of this study is to devise models by means of field studies and advanced numerical techniques that improve nearshore dilution predictions. Based on extensive and unique field studies near Grand Haven, a new classification for surface buoyant plumes is presented that advances our understanding of plume behavior. An empirical near field model is developed that expands previous studies in large aspect ratio (width to length) channels. In addition, a hybrid particle tracking model is developed to assist in forecasting and near real-time assessment of pathogen indicators in nearshore receiving waters. This far field model incorporates the currents from a 3D hydrodynamic model and the initial dilution and trajectory of the plume from the near field model. This modeling scheme is shown to improve the predictions and understanding of the Grand River plume behavior in Lake Michigan.

1.2 Lake Michigan Recreational Water Regulations

Human health can be seriously influenced by poor water quality in nearshore areas. Waterborne microbial pathogens may pose a significant health threat, and an integrated approach for predicting and preventing these potential hazards is needed. Lake Michigan beaches are closed by local officials whenever bacteria levels exceed health standards. Beach closings due to bacterial pollution rose sharply in 2001 with a record-breaking 599 beach closings according to the Alliance for the Great Lakes. The environmental authorities have begun beach monitoring programs to monitor and mitigate this problem. But there is still an urgent need for prediction tools and prevention of beach closures.

Beach advisories are issued when pathogen indicators exceed some specified limit. These microorganisms are categorized to three different types of bacteria, protozoa, and viruses. Waterborne pathogens can be found in the feces of human and other warm-

blooded animals. They can cause vomiting, diarrhea, nausea, headaches, giardiasis, rashes, and pink eye. Gastroenteritis is the most common result of swimming in contaminated water. The severity of the disease or illness depends on the degree of exposure and the type of pathogen (USEPA, 2001), and MDEQ (2006). The USEPA (1986, 2002) uses E. coli to indicate the presence of waterborne pathogens in fresh water.

The Michigan Department of Environmental Quality requires beaches to be monitored according to a provision for microorganisms of the Natural Resources and Environmental Protection Act, 1994 PA 451, as follows:

"All waters of the state protected for total body contact recreation shall not contain more than 130 E. coli per 100 milliliters (ml), as a 30-day geometric mean. Compliance shall be based on the geometric mean of all individual samples taken during five or more sampling events representatively spread over a 30-day period. Each sampling event shall consist of three or more samples taken at representative locations within a defined sampling area. At no time shall the waters of the state protected for total body contact recreation contain more than a maximum of 300 E. coli per 100 ml. Compliance shall be based on the geometric mean of three or more samples taken during the same sampling event at representative locations within a defined sampling area."

All surface waters of the state are protected for total body contact according to the designated uses rules, as follows:

"All surface waters of the state are designated for, and shall be protected for, total body contact recreation from May 1 to October 31 in accordance with the provisions of microorganisms. Total body contact recreation immediately downstream of wastewater discharges, areas of significant urban runoff, combined sewer overflows, and areas influenced by certain agricultural practices is contrary to prudent public health and safety practices, even though water quality standards may be met."

Beach closures in Michigan are most commonly issued because of elevated counts of E. coli in water samples collected from the shoreline. Health departments use the daily and the 30-day geometric mean to determine if a beach closure or an advisory should be issued. The health department notifies the beach owner when a beach should be closed. If necessary, the health department can petition the court for an injunction to force the

owner to close the beach. The beach closure or advisory remains in effect until additional tests meet the water quality standard.

Anyone who heavily uses near shore areas for recreation - including kayakers and swimmers - can come into contact with bacteria and viruses. These arise from various sources, specially the sewage discharged into the lake that contains animal and human waste. Untreated wastewater can enter the lake when heavy rains cause sewage and runoff to bypass treatment plants. Among all the pollutant sources, rivers carry the most pollutants to the lake.

1.3 Grand Haven Water Quality

The Grand Haven beaches and recreational sites are open to thousands of tourists and visitors every year. Due to their importance, this study focuses on the effect of the Grand River plume on nearby beaches (Figure 1.2).

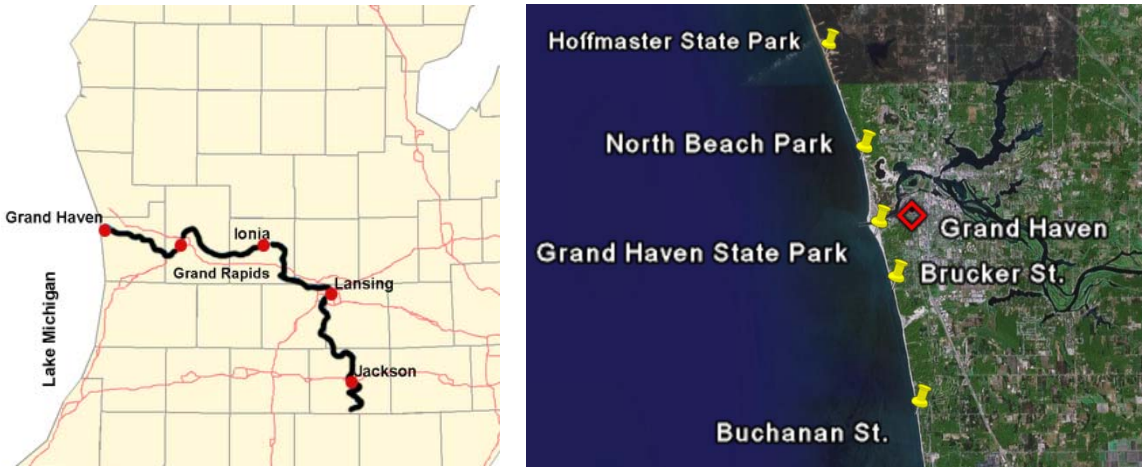

Figure 1.2 Grand Haven and the Grand River map (left); the most popular Grand Haven recreational beach sites (right).

According to recent studies of the 12 major tributaries of Lake Michigan, the Grand River is a major contributor of contaminants entering Lake Michigan (Shafer, et al., 1995; Hall and Behrendt, 1995; and Cowell, et al., 1995, and Robertson 1997). Large-scale metal finishing and plating industries in Grand Rapids and Lansing have contributed heavy metals in the past due to ineffective wastewater treatment (USEPA,

1999). Studies indicated that the lower Grand River exceeded sediment quality guidelines for heavy metals and selected organic chemicals (USEPA, 1999). Other impacts have included discharges from a large tannery in the Grand Haven area and wood processing facilities throughout the lower region of the Grand River. The Lake Michigan "Mass Balance Study" showed that the Grand River is the largest source of lead, DDT and atrazine and the second largest source of mercury to the lake (Great Lakes Commission, 2009).

The Grand River is Michigan's longest river, winding 256 miles from Jackson to Grand Haven encompassing 19 counties and having 12 major tributaries. The Grand River watershed constitutes about 13% of the total Lake Michigan watershed. Although several cities impact the river, most of the Grand River watershed is agricultural (53 percent), so non-point sources are a major concern. Non-point source pollution cannot be readily traced and includes sediments, nutrients, pesticides, bacteria, bird droppings, and road salt. Nutrients and bacteria can also be caused by failing septic systems, pet wastes, manure run-off, over-fertilized lawns, and sewage overflow from nearby cities. The Grand River contaminants can reach Grand Haven nearby beaches (Chambers and Eadie, 1980).

On July 27, 2007, a Grand Haven local report in the Muskegon Chronicle stated: "the no-swim advisory was issued for Grand Haven beaches. Ottawa County health officials urged people to stay out of the water at Grand Haven's two beaches -- on the first day of the popular Coast Guard Festival -- after tests taken the day before showed elevated bacteria concentrations in Lake Michigan. Levels of E. coli in the water at City Beach were 624 MPN per 100 ml, more than twice the 300 MPN per 100 ml considered safe for human exposure. Health officials only found unsafe bacteria readings at City Beach but extended the no-swimming advisory to the adjacent Grand Haven State Park beach as a precaution."

The elevated bacteria readings and consequent closure are believed to be caused by a combination of heavy rainfall and onshore winds that trap sediment and bacteria on the south side of the Grand Haven pier. The daily average rainfall data over the last three days from the local meteorological stations (Grand Rapids and Muskegon) NOAA

(National Oceanic and Atmospheric Association) correspond to the existing rainfall peak before the beach advisory was issued in Grand Haven (Figure 1.3).

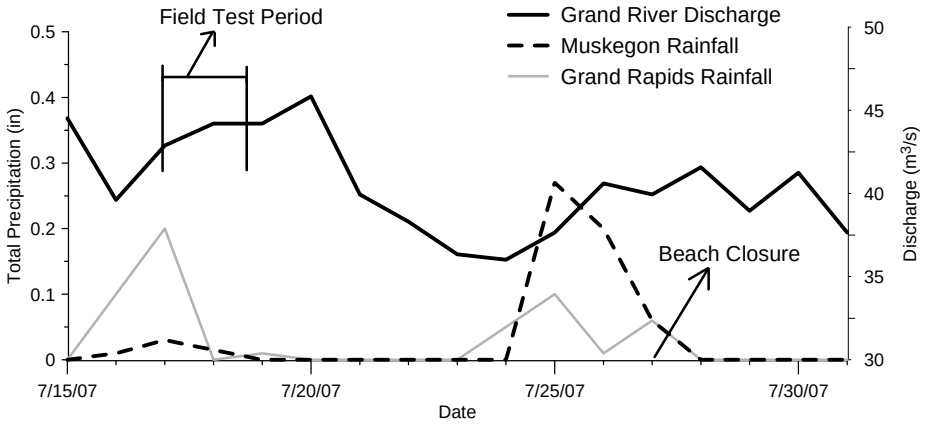

Figure 1.3 Daily average rainfall records at NOAA meteorological stations at Muskegon and Grand Rapids, July 15-30, 2007.

There is one large caveat in beach monitoring programs: The no-swim advisories are based on data collected the previous day. Would the lake be cleaner, or more polluted, the next day? This is the question that needs answering by improving the available models to make them capable of forecasting beach bacteria levels.

1.4 Classification of Hydrodynamic Processes

Plume transport processes in nearshore areas are complex and occur over a broad range of temporal and spatial scales (Figure 1.4). This makes it almost impossible to develop a comprehensive model to cover all effluent behavior. When the contaminated river water enters the lake, its dynamics are initially affected by its momentum and buoyancy. This region is called the “near field”. The time scale of near field mixing process is of the order of minutes to hours and the spatial scale is a few hundred meters. Beyond the near field the plume enters a region that is dominated by buoyant spreading and is called the “mid field”. The time scale of mid field mixing is less than a day and the spatial scale a few thousand meters. Farther from the source, mixing becomes dominated by ambient turbulence. This region is called the “far field”. Far field mixing process

occurs over hours to days and longer and extend for thousands of meters (Bleninger, 2004).

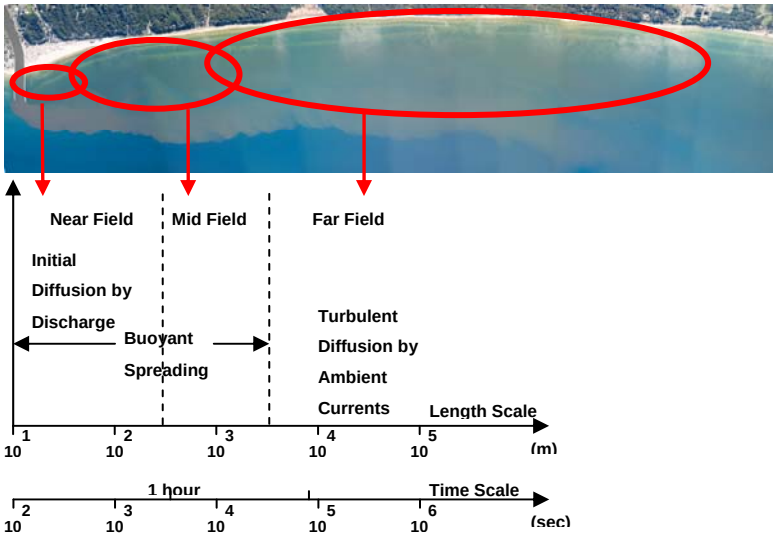

Figure 1.4 Classification of River Plume Hydrodynamic Processes.

The variety of hydrodynamic processes necessitates prediction techniques that represent both near field and far field processes. Models that predict ocean circulation are usually used to predict the far field hydrodynamics in coastal areas. These models are based on primitive equations (Navier-Stokes, thermodynamics and pressure equations) representing the hydrodynamic processes in large scales, but the entrainment processes occur at smaller scales in the near field are neglected. Therefore hydrodynamic models cannot adequately resolve the near field processes, and the mass transport models that use these models output are limited in predicting the fate and transport of constituents in small scales.

Near field models predict initial mixing and dilution at small scales but ignore ambient turbulent diffusion at larger scales and break down farther from the source. In this study a mass transport model (random walk model) is used that employs the output of an empirical near field model and a hydrodynamic model in the far field. This

approach overcomes previous model deficiencies by incorporating the near field process predictions, and includes the ambient diffusion at larger scales in the far field. In the following we review the objectives and approach of this study in detail and present the coupling technique.

1.5 Objectives

The objective of this study is to improve understanding and devise new and reliable prediction techniques for nearshore bacterial transport. Field studies were conducted at Grand Haven that provided much valuable information on river plumes. Based on this data, a new surface buoyant plume categorization scheme is developed. Also, trajectory and dilution formulae for large aspect ratio rivers are devised that expands the few previous studies and is used as the near field model.

Hydrodynamic models are typically hydrostatic and ignore vertical accelerations that are important in plume entrainment, and near field models are incapable of representing ambient turbulent diffusion. A combination of the two will overcome these deficiencies. Therefore a coupling technique is developed to predict surface discharges and the transport of the Grand River plume bacterial contaminants to nearshore Lake Michigan. Although hybrid or coupled models have been applied to submerged sources, there are few applications to surface buoyant jets, especially for wide aspect ratio channels typical of natural rivers.

The coupling method applies a random walk particle tracking (RWPT) model that is tested by comparing to the observed behavior and dynamics of the Grand River plume. It can be extended to other coastal areas in the Great Lakes, and is intended to ultimately provide real-time, nowcast and forecast predictions of bacterial impacts on recreational beaches and be incorporated into the Great Lakes Coastal Forecasting System (GLCFS). This will provide early warning of potential water bacterial contamination for beach managers, aid in planning and interpretation of field measurements of bacterial impacts, assess the efficacy of measures to reduce impacts, for example, the operation of Combined Sewer Overflow (CSO) schemes, and planning for the engineering design of water infrastructure such as siting of water intakes, and outfall designs.

The new model is a considerable advance as it simulates the dynamics associated with bacterial dispersion more realistically and improves numerical modeling of nearshore water quality. It is more flexible than conventional gradient diffusion models in being able to better incorporate multiple and diverse sources with differing properties and also other processes as knowledge of them improves. The particle tracking model can also be extended to include bacterial sources resulting from wave-induced sediment resuspension.

1.6 Approach

Extensive field measurements were carried out in 2006 and 2007 that included simultaneous aerial photography, measurements of lake physical properties, and the addition of artificial tracers, to track the plume. Acoustic Doppler current profilers (ADCPs) were deployed alongside buoys that measured wind speed and direction and air temperature. GPS-tracked surface drifters measured surface water motions. Water quality sampling was also carried out in the river and the lake. Based on the field data, dilution and trajectory formulae are presented that improve previous studies on large aspect ratio rivers and will be used as the empirical near field model. The bacterial data are analyzed to investigate the relationship between dilution and decay.

Numerical modeling is conducted using a 3D hydrodynamic model POMGL, a version of the Princeton Ocean Model modified by the Great Lakes Environmental Research Laboratory (GLERL) that provides the ambient currents. The whole Lake Michigan was simulated by GLERL for 2006 and 2007 with a 2 km grid. The same model is applied to a high resolution nested domain for June and August 2006 and June and July 2007 where it obtains its open boundary condition from the whole lake hydrodynamic simulations. The nested model simulates the hydrodynamics of the Grand River plume and the coastal circulation near the local beaches on a 24 × 6 km domain with a finer grid size of 100 m.

Despite the small size of the nested model grid, a near field model is still needed to represent the plume entrainment accurately within a few hundred meters from the river mouth. Therefore a particle tracking model is used that integrates other model predictions

in the far field and near field simultaneously, in order to overcome the complexity and differing time and length scales of the governing hydrodynamic processes. The conceptual diagram of the hybrid model is shown in Figure 1.5.

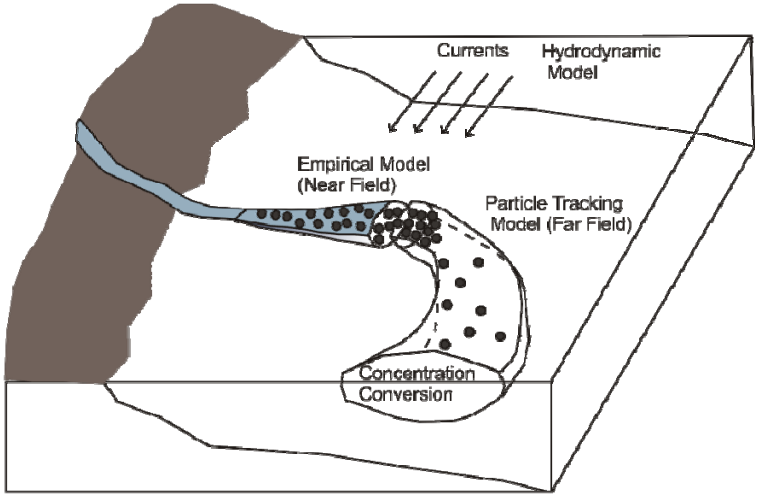

Figure 1.5 Conceptual diagram for the coupling approach.

The random walk particle tracking model simulates the transport and decay of bacteria as discrete particles that advect, diffuse and decay. The particles are introduced based on the near field model predictions of dilution and trajectory, and plume cross-section dimensions which determines the number and location of the particles to be released. The particles are advected and diffused over the nested domain based on the ambient currents and diffusivities predicted by the far field model. Every particle is assigned a mass and decay rate that leads to the concentration at each cell. A flowchart of the coupled near and far field model scheme is shown in Figure 1.6.

Bacterial and tracer data (conductivity or fluoresence) were used to calibrate and validate the model, and determine its accuracy with the decay rate estimated from the literature and field observations. Predictions of bacteria with variable and constant decay rates are compared with the measurements during the simulation periods of summer 2006 and 2007. The variable decay rate includes the effects of solar radiation, depth, temperature and turbidity of the plume.

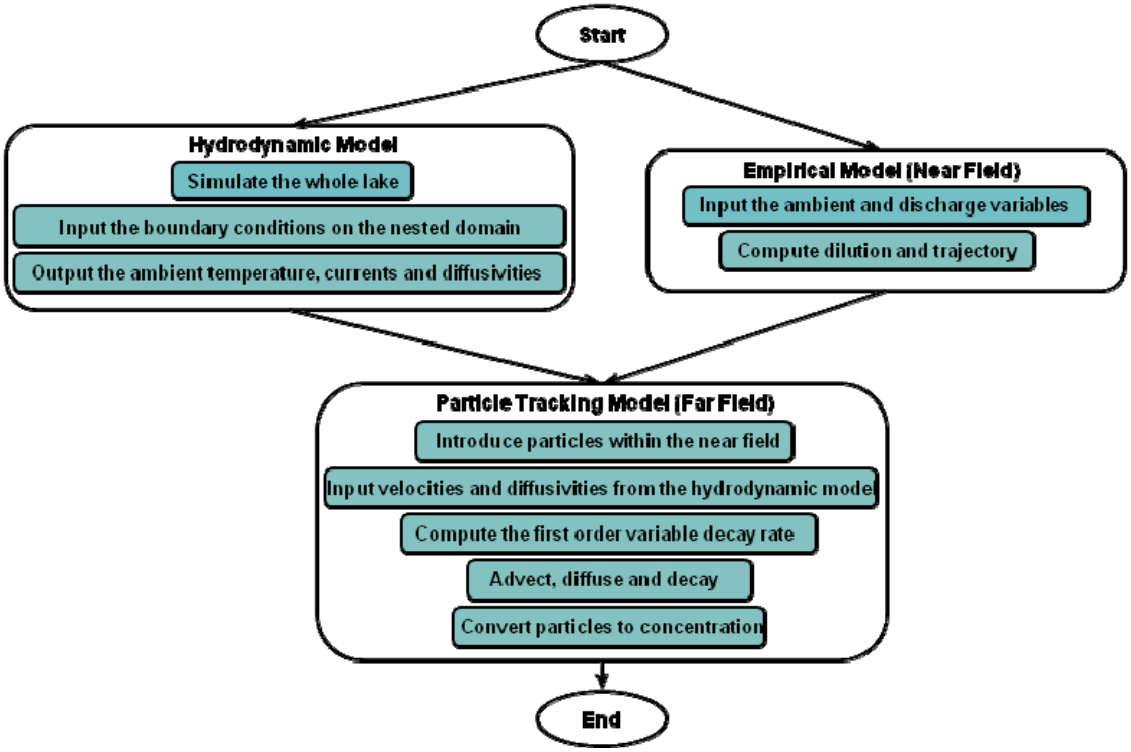

Figure 1.6 Flowchart of the proposed coupling method.

1.7 Dissertation Outline

The literature on surface buoyant plume models, hydrodynamic models, particle tracking techniques and coupling methods in nearshore transport is reviewed in Chapter 2. The field studies conducted around Grand Haven in summer of 2006 and 2007are summarized in Chapter 3. The results are further analyzed and a new classification for surface buoyant plumes, a near field trajectory and dilution model, and bacterial decay rates are presented in Chapter 4. Hydrodynamic simulations for the four study periods are presented in Chapter 5. The particle tracking model results and the coupling technique are described in Chapter 6. Conclusions are presented in Chapter 7.

CHAPTER 2

LITERATURE REVIEW

2.1 Introduction

Predicting the fate and transport of river plumes in nearshore waters is a challenge due to the wide range of length and time scales of the hydrodynamic processes. Near field models predict initial mixing and dilution due to entrainment at small scales near the source. Far field models predict transport and diffusion at larger scales farther from the mouth. Combining both types of models can capture the wide range of spatial and temporal scales. In this chapter, previous modeling approaches and the dynamics of the surface buoyant plumes are discussed.

2.2 Surface Buoyant Plumes

Streams discharging to lakes usually form a buoyant plume on the surface in the summer, e.g. the Grand River entering Lake Michigan as shown in Figure 1.1, because they are warmer than the lake water. They are categorized as buoyant surface jets and are of great oceanographic and limnological interest (Figure 2.1).

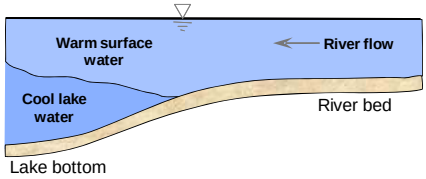

a) Cross section

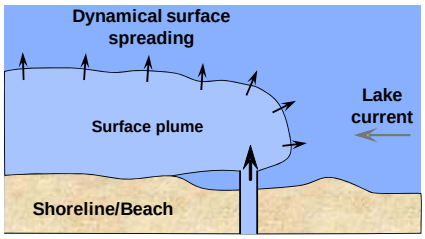

b) Plan view

Figure 2.1 Sketches of a buoyant surface discharge.

They have unique biogeochemical characteristics and often exhibit extremely complex flow. In the near and mid fields, the plume dynamics depend primarily on the bathymetry, discharge momentum and buoyancy fluxes, geometry, and crossflow. An idealized sketch of the flow configuration is shown in Figure 2.2. In the near field their mixing is modified by buoyant damping and collapse and by interaction with adjacent boundaries and ambient crossflows. In the mid field the plume is advected by the ambient current, but will undergo further mixing and lateral spreading through buoyant frontal motions and passive diffusion.

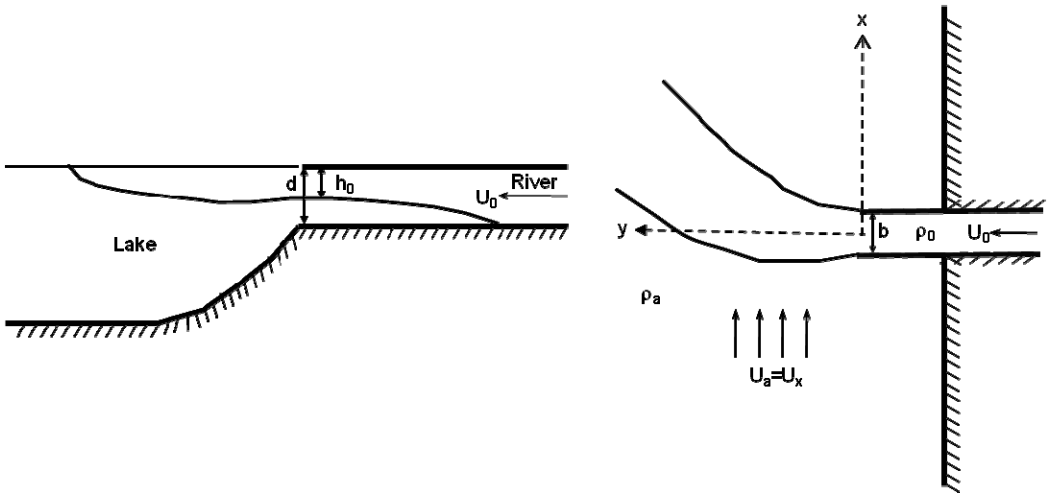

Figure 2.2 Schematic geometry of the channel and the flow parameters; side view (left), and plan view (right).

The river discharge is characterized by U_0 (full-depth river velocity), b channel width, d channel depth, and ρ_0 the discharge density. The ambient water body is represented by a velocity U_a (= U_x), and density ρ_a. The discharge can be better characterized by its fluxes of volume, momentum and buoyancy defined as:

$$Q_0 = U_0 A, \qquad M_0 = Q_0 U_0, \qquad J_0 = Q_0 g_0' \tag{2-1}$$

where $A = bd$, $g_0' = (\Delta\rho_0/\rho_a)g$ is the modified acceleration due to gravity, $\Delta\rho_0 = \rho_a - \rho_0$, g is the acceleration due to gravity, and h_0 is the plume thickness at the mouth.

In order to parameterize the flow behavior the following length scales (L_Q the discharge length scale; L_M the jet-plume length scale; L_m the jet-crossflow length scale; L_b the plume-crossflow length scale; and L_T the jet-plume-crossflow length scale) are defined from the flux quantities (Jirka et al., 2007, McCorquodale, 2007):

$$L_Q = Q_0 / M_0^{1/2} = A^{1/2} \tag{2-2}$$

$$L_M = M_0^{3/4} / J_0^{1/2} \tag{2-3}$$

$$L_m = M_0^{1/2} / U_a \tag{2-4}$$

$$L_b = J_0 / U_a^3 \tag{2-5}$$

$$L_T = M_0^{2/3} / (J_0 U_a)^{1/3} \tag{2-6}$$

These length scales have physical significances. L_Q designates the zone of flow establishment that is influenced by the channel dimensions. L_M defines the distance where the flow shifts from momentum-dominated to buoyancy dominated; L_m denotes the length where the ambient crossflow dominates the inflow; L_b is a measure of the region where the plume intrudes upstream against the ambient flow; and L_T is the length scale where the momentum effect overcomes the buoyancy and inflow. Jones et al. (1996) used ratios of some of these length scales to classify buoyant jets in CORMIX3 model (and CorSurf, a later version in Jirka et al, 2007 for surface buoyant plumes in the near field) as explained below.

2.2.1 Plume Classification

Buoyant surface discharges have been classified into four categories by Jones et al. (1996, 2007) based on their hydrodynamic characteristics and length scales as shown in Figure 2.3: free jets, shoreline-attached jets, wall jets, and plumes. Free jets are strong jets with a slight and gradual deflection as they encounter the ambient flow. Shoreline-attached jets have a recirculating zone inshore, created by either a strong ambient cross current that causes the plume to hug the shore or a full depth inflow that blocks off the

ambient current and makes a wake region downstream. Wall jets are discharged parallel to the shore and deflect in a longshore coflow current and spread along the shore.

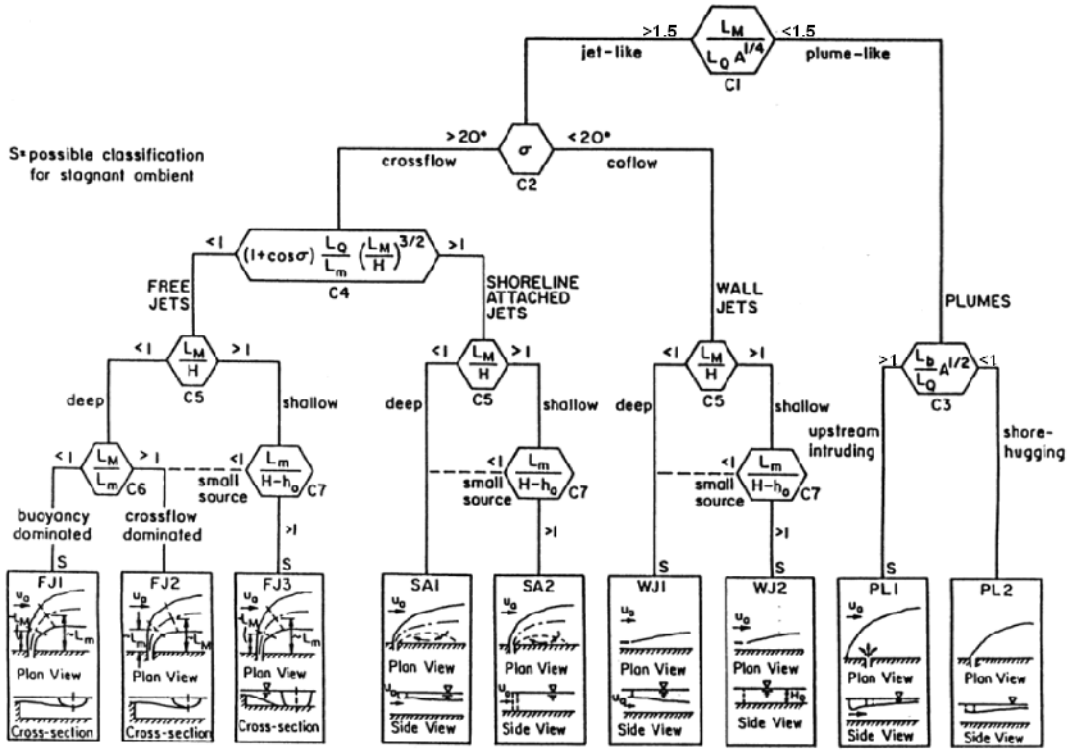

Figure 2.3 Schematic characterizations of buoyant surface jets (Jones et al., 2007).

A flow is classified as plume-like when the buoyancy-induced lateral spreading overcomes momentum-driven mixing (or $L_M / L_Q a^{1/4} < C1$), where $a = b/d$ is the channel aspect ratio. The constant *C1*, demarking the plume-jet criteria is corrected from 1.0 to 1.5, based on Chu and Jirka (1986). Depending on the longshore currents speed and buoyancy, the plume can be either upstream intruding or shore-hugging (PL1 or PL2). Upstream intrusion occurs when the buoyancy dominates the ambient current and a front is formed that intrudes upstream. Shore-hugging occurs when the buoyancy is weaker and the plume is deflected downstream after it exits the outlet.

The CORMIX3 model uses a modular methodology based on this classification, which only allows for an aspect ratio of 0.05 to 5 and excludes the wide and shallow

mouths typical of natural rivers, which is the case for many channels in the Great Lakes. The Grand River channel aspect ratio is large (a=16) with an offshore extended outlet. In addition, this classification does not encompass all the shapes and dynamic of the plumes that are reported in Chapter 3. Wind forcing can also strongly affect the plume through the surface shear stress. This is not well covered in previous studies. Therefore a new classification is suggested for the plume-like flows based on the ratio of plume-crossflow length scale, L_b, over the channel depth, and the Richardson number based on wind stress that will be explained further in Chapter 4.

2.2.2 Plume Dynamics

In order to understand the dynamics of mixing in the near and mid-fields (as defined in Chapter 1), it is crucial to recognize the spreading mechanism. Spreading of buoyant ocean outfall plumes in a current has been studied by Koh and Brooks (1975), who applied a Galilean transformation to the two-dimensional buoyant surface spreading problem. They predicted the field to grow linearly with distance. The growth rate was independent of the water depth, but dependent on $Fr_0'^{-1/3}$, where Fr_0' is the Froude number that equals u^3/j_0, where u is the ambient current speed and j_0 is the buoyancy flux per unit length for a line diffuser. The relationship was extended assuming the frontal velocity to be perpendicular to the plume front (Roberts, 1979) to yield a better approximation for the spreading rate.

Dynamic lateral spreading is also a major characteristic of surface buoyant plumes from rivers and estuaries, which begins when the plume exits the river mouth. It is driven by the density difference between the plume and the ambient. In addition, a strong density gradient can reduce vertical mixing. Lateral gravitational spreading in density currents is similar to the lock exchange flow where a lighter density fluid propagates over a more dense fluid (Chen et al, 2008). They suggest that in the near-field, within the first 2 km from the river mouth, spreading is ruled by buoyancy.

Buoyancy is related to the barotropic forcing term $(-g'\partial h_0/\partial n)$ in the lateral momentum equation that explains the pressure gradient due to the interfacial slope. This

gradient is also proportional to the local internal gravity wave speed, $c = \sqrt{g'h}$, where h is the local plume thickness (Hetland and MacDonald, 2008). Therefore the rate of plume spreading, δ is proportional to the local internal gravity wave speed (with a factor of 2 or $\delta \propto 2c$ because lateral spreading is from both sides). Hetland (2009) formulated the local spreading rate of a small parcel of the fluid in a layer model:

$$\delta = \frac{dW}{dx} = 2Fr^{r-1} \tag{2-7}$$

Hetland and MacDonald (2008) assumed that the relative arc length of the plume, $\frac{W}{W_0}$ is related to the radial distance from the river mouth by a power-law expression based on river estuary observations:

$$\frac{W}{W_0} = \left(\frac{r}{r_0}\right)^{1/\beta} \tag{2-8}$$

where W is the plume arc length at a given radial distance of r from the mouth, W_0 is the initial plume width at a distance of $r_0 = 1$ km from the river mouth. Whether β is greater or smaller than 1 determines the convergence or divergence of the plume. If β <1, the plume is categorized as "divergent", when side expansion happens faster than its offshore transport and the plume boundaries take a convex shape. If $\beta > 1$, it is called "divergent", when the side expansion is more rapid and a concave shape at the boundaries is observed. Pure radial spreading happens when $\beta = 1$.

They found that the Merimack river (with an aspect ratio or *b/d* = 44) formed a divergent spreading plume. Their theory does not readily determine the width of the plume at any distance of r, since the initial width at a distance of r_0 must be first determined based on the local internal velocity, *c*. In the present study, a simple relationship similar to the Hetland et al. model is fitted to the field data and is dependent on the channel width, *b* instead of the initial width, W_0. The new relationship is presented for the near field (within a few kilometers from the mouth), since most of our experiments were carried out in that region.

2.2.3 Mathematical Models

In the engineering literature, the main mathematical model types developed for submerged and surface buoyant jets are entrainment models. They have often been called reduced gravity "layer models" in the oceanographic literature (Fong and Geyer, 2001; Yankovsky and Chapman, 1997; Hetland, 2005), where plumes from large engineering aspect ratio outfalls (>>1 or in the order of 1000 to 10000) have been discussed. These models concentrate on the mixing at the frontal boundary. Other researchers have also developed numerical solutions to represent entrainment within the plume interior (O'Donnell, 1990; Jay et al, 2010).

Lateral entrainment is also a considerable feature in buoyant plumes but is usually neglected in layer models formulations for plumes from larger aspect ratio channels (Hetland, 2009); because vertical entrainment and lateral spreading dominates in the near field (Garvine, 1999; Hetland, 2005; Hetland, 2009). The effect of earth's rotation also becomes important for plumes from very wide channels.

Some entrainment models use a jet integral technique that consists of ordinary differential equations derived from the cross-sectional integration of jet properties such as volume, momentum, buoyancy and mass fluxes. The rate of change in these fluxes in a jet element are generally related to the entrainment, turbulent mixing, net buoyancy, drag, and interfacial forces, and decay of mass. The geometry of the trajectory and spreading relations are separately defined. Two common jet integral models are described below.

2.2.3.1 CORMIX3

CORMIX3 is the surface buoyant jet module of the CORMIX system developed by Jones et al (1996). It is an Eulerian jet integral model that includes surface discharge behaviors such as buoyant damping of turbulence and cross-sectional distortion (lateral spreading). The system of equation is parabolic that is solved by simple forward marching numerical schemes along the jet trajectory. The conservation of volume, momentum, buoyancy, and mass are formulated for a jet element. Due to boundary layer nature of the flow, it is assumed to be hydrostatic, acceleration due to jet curvature is negligible, and turbulent momentum and scalar fluxes are considered to be proportional

to the mean fluxes. A turbulent entrainment mechanism is also considered that includes the effects of horizontal entrainment (at the jet lateral periphery), vertical entrainment (at the jet bottom), advected puff entrainment (at the strongly bent stage), frontal entrainment (at the plume boundaries), and interfacial entrainment (at the plume interface with wind, and ambient). As mentioned earlier, CORMIX3 is limited to aspect ratios <5 and is not recommended for our study.

2.2.3.2 PDS

Shirazi and Davis (1974) developed an Eulerian jet integral three-dimensional plume model (PDS) for surface discharges to water bodies from channels such as cooling water discharges. It is capable of simulating temperature, plume trajectory, average and centerline dilution, plume width and depth, and centerline excess temperature over a wide range of discharge conditions (details are in Davis, 1999). It also includes the effects of surface heat transfer.

In PDS the plume is assumed to remain at the surface with buoyancy causing it to rise and spread laterally in all directions. The initial discharge momentum causes the plume to penetrate the ambient and the current bends the plume in the flow direction. A Gaussian profile in the horizontal and a half-Gaussian profile in the vertical direction for the excess temperature and velocity are assumed and used to determine the energy, volume, and momentum fluxes from the conservation equations. In the mass conservation equation the jet and ambient entrainment turbulent mixing is included; in the energy conservation, surface heat exchange is incorporated, and the momentum equation considers the internal pressure forces due to buoyancy, form drag to the ambient current, and interfacial shear forces. In an evaluation of several fate and transport models for offshore drilling effluent disposal activities in outer continental shelf marine environment, the performance of PDS was shown to be the best for high Froude numbers (> 10) and deep waters (Runchel, 1983). Its accuracy degraded for low Froude numbers. For the Grand River plume, observed Froude number during the swim season was always near 1. Therefore PDS is not recommended.

2.2.4 Empirical Models

Many field and laboratory studies have been carried out on surface buoyant plumes (Motz and Benedict, 1970; Carter et al. 1973; Koester 1974; Kuhlman and Prahl 1974; Abdelwahed and Chu 1981; Dinelli and Parrini, 1975). A few recent ones (Carnelos, 2003; McCorquodale et al., 2000 and 2004; McCorquodale, 2007) have focused more on wider channels (aspect ratio > 3) which have not been previously reported in engineering literature.

Rajaratnam (1988) reviewed the experimental and analytical research on buoyant surface jets and suggested a horizontal trajectory formula for a surface buoyant jet in a crossflow:

$$y/\alpha d = 3.8\left(x/\alpha d\right)^{0.38} \tag{2-9}$$

for α<15, where α is the ratio of inflow velocity, U_0 to the longshore ambient velocity, U_a. McCorquodale (2000, 2004), and Carnelos (2003) developed a simple regression model for wide weak plumes in crossflows based on Lake Ponchartrain shoreline data and laboratory experiments. They were categorized as weak plumes, because they were normally shore attached and were deflected by wind-generated currents of approximately 10 cm/s ($\alpha = U_0/U_a \approx 3.5$), with a weak tide. They obtained an equation for centerline dilution for $3 < b/d < 20$:

$$S_{\min} = \max\left\{1.0, \left[0.6 + 0.12\left(\xi/b\right)\right]\right\} \tag{2-10}$$

where $S_{\min}$ is the minimum (centerline) dilution, ξ is the distance along the plume trajectory, and b is the channel width. They subsequently improved the model and estimated dilution based on more laboratory experiments for $3 < b/d < 20$ and $3 < \xi/b < 20$ (McCorquodale, 2007):

$$S_{\min} = C_1\left(\xi/d\right)^{1/2}\alpha^{0.06}\left[1+\left(1+Fr_0'\right)^{-1}\right]^{1.5}\left(d/b\right)^{0.2} \geq 1.0 \tag{2-11}$$

where $Fr_0' = U_0 \Big/ \left(g_0' L_Q \right)^{1/2}$ is the densimetric Froude number based on outlet length scale, L_Q as in Eqn. 2-2. C_1 is an empirical coefficient (equal to 0.9 for attached plumes and 1.3 for unattached plumes), and α is the ratio U_0 / U_a.

Abdel-Gawad et al. (1996) investigated the near field mixing of effluents from buoyant and non-buoyant pipe outfalls discharging into the cross flowing ambient currents in a trapezoidal channel to determine the jet trajectory, velocity field, and dilution. Abdel-Gawad and McCorquodale (1985) and Abdel-Gawad et al. (1996) developed empirical equations (AGM model) for the minimum dilution and centreline trajectory of surface or slightly submerged buoyant and sinking jets from shore-based and extended outfalls discharging horizontally into cross flowing streams for $\xi > \xi_0$:

$$S_{\min} = C_3 \left(\xi / d \right)^{n_5} \alpha^{n_6} \left[1 + \left(1 + Fr_0' \right)^{-1} \right]^{n_7} \left[\exp\left(-H/d \right) + 1 \right]^{n_8} \left(1 + Z_p / H \right)^{n_9} \quad (2\text{-}12)$$

$$y/d = C_2 \left(x / d \right)^{n_1} \alpha^{n_2} \left[1 + \left(1 + Fr_0' \right)^{-1} \right]^{n_3} \left[\exp\left(-H/d \right) + 1 \right]^{n_4} \exp\left[0.092 \alpha \left(Z_p / H \right)^2 \right] \quad (2\text{-}13)$$

where ξ is the distance along the plume trajectory, ξ_0 is the potential core length (or zone of flow establishment), $n_1, ..., n_9$ are empirical powers, and C_2 and C_3 are empirical coefficients. McCorquodale (2007) has presented the following for ξ_0 by fitting an empirical relationship to the previous studies:

$$\xi_0 / d = 1.12 + 4.98 \tanh(\alpha^{0.9} \pi / 41) + 0.00075 \alpha^{0.5} \quad (2\text{-}14)$$

Shirazi and Davis (1972) also considered the effect of outlet aspect ratio b/d, on ξ_0 and proposed the following for surface buoyant jets with no crossflow:

$$\xi_0 / b = 5.4 \Big/ \left[(b/d) Fr_0' \right]^{1/3} \quad (2\text{-}15)$$

There have been a few studies that focused on large aspect ratio channels. In addition, systematic field studies are scarce due to high costs, but they are essential to develop simple and practical formulae for surface discharges and to valuate numerical models. Therefore in Chapter 4, an empirical model for the dilution and trajectory of

surface buoyant plumes is developed based on the new field studies. This model will complement previous studies and expand them to greater aspect ratios (16 for the Grand River plume). Empirical formulae for lateral spreading and thickness of the plume are also developed and compared with the literature.

Surface buoyant plume models have been mainly developed to predict near field dilutions, however, beach bacteria can travel many kilometers beyond the near field. Therefore, a far field model is also needed to predict beach bacteria. Models that have been used to predict far field transport are discussed below.

2.3 Transport Models

Fate and transport models are by definition far field models because they represent the diffusion that is effected by the natural turbulence of the water body. They are categorized into two types: Eulerian and Lagrangian. These models are explained below.

2.3.1 Eulerian Models (EM)

Eulerian models (EM) are mostly associated with the "concentration or gradient-diffusion models" and directly solve the mass transport equation:

$$\frac{\partial c}{\partial t}+u\frac{\partial c}{\partial x}+v\frac{\partial c}{\partial y}+w\frac{\partial c}{\partial z}=\frac{\partial}{\partial x}\left(K_h\frac{\partial c}{\partial x}\right)+\frac{\partial}{\partial y}\left(K_h\frac{\partial c}{\partial y}\right)+\frac{\partial}{\partial z}\left(K_v\frac{\partial c}{\partial z}\right)-kc \qquad (2\text{-}16)$$

where c is the concentration of some tracer, u, v, and w are the mean velocities in the u, v, and w directions, K_h and K_v are horizontal and vertical turbulent (eddy) diffusion coefficients, and kc represents loss of tracer (e.g. loss of bacteria due to mortality, settling, etc). Eulerian models have a fixed coordinate system, and the solution is obtained relative to a fixed grid where the pollutant concentrations are computed. The boundary conditions and source terms are readily defined in the fixed grid system, but this approach can be computationally demanding when using small grid cells and time steps to satisfy stability and accuracy constraints.

Although gradient-diffusion models are still widely used in coastal areas and estuaries where the flow is mostly dominated by advection, they have several deficiencies. They create numerical diffusion near the plume boundaries and the source,

so they cannot represent the sharp gradients and they give erroneous results there. In addition, they predict smooth spatial concentration gradients and cannot reproduce the patchy fields observed in natural bacteria behavior. They also resolve diffusion on a grid structure rather than at a physical point, so they cannot resolve concentration on sub-grid scales, smaller than discretization.

Liu et al. (2006) developed a two-dimensional (2D) gradient-diffusion model to investigate the diffusion of bacteria on several beaches on the southeastern coast of Lake Michigan. The Great Lakes Coastal Forecasting System (GLCFS) beach forecasting tool is also presently a 2D gradient-diffusion model. Its predictions for Grand Haven can be seen at www.glerl.noaa.gov/res/glcfs/ghf (May 2010). Many common models, including GLCFS, are 2D and use depth-averaged currents. Although these models are less complex than three-dimensional (3D) models, they are a poor approximation to the thin surface spreading layer that actually occurs in the Great Lakes where the processes are clearly 3D (see Chapter 3).

2.3.2 Lagrangian Models (LM)

In Lagrangian Models (LM), the advection-diffusion equation is written in terms of a total derivative, so that the change of concentration is computed following a moving fluid parcel. A Lagrangian model computes concentrations using either puff or particle approaches. In a puff model, the source is simulated by releasing pollutant puffs at regular intervals over the duration of the release. Each puff contains the appropriate fraction of the pollutant mass and diffuses as it travels. In a particle model, the source is simulated by releasing many particles over the duration of the release. In addition to the mean advective motion of each particle (i.e. its trajectory), a random diffusion component is added at each time step according to the turbulence at that time. In this way a cluster of particles released at the same point will expand in space and time, simulating diffusion. Concentrations are calculated by summing the mass of all the particles in a grid cell. Lagrangian models reduce numerical errors and can better mimic the actual physical processes that occur.

Random Walk Particle Tracking models (RWPT) represent mass with a certain number of particles. At each time step the displacement is computed from an advective, deterministic component and an independent, random Markovian component given by:

$$\Delta x_{i,j,k} = \underbrace{V_{i,j,k}\Delta t}_{\text{deterministic displacement}} + \underbrace{\eta_{i,j,k}}_{\text{random displacement}} \tag{2-17}$$

RWPT models have been applied in diverse areas such as groundwater transport, coastal biophysical problems, sediment plume behavior, coastal oceanic fronts of river discharges, coral reef modeling, and chemical exposure assessment. RWPT models do not have the problems of numerical diffusion near high concentration gradients, and can better resolve concentrations on scales smaller than the grid size than gradient-diffusion models.

Another advantage of RWPT models that make them very suitable for bacterial predictions is that there is more control over the properties of particles that are represented as real entities spread across the computational domain rather than as only concentration. Each particle is associated with a certain mass and age. Other properties can also be readily incorporated such as a settling velocity for heavy particles or an upward velocity for bacteria attached to, for example, buoyant particles such as grease and oil. Variable decay rates such as experienced by a particle exposed to differing levels of solar radiation as it moves up and down through the water column can also be incorporated. In addition, turbulent diffusion can be represented in the random walk formulation for each particle. The shortcomings of this method, however, are that the numbers of particles are restricted by memory and computation time (that we try to overcome by using high speed computers), and errors that arise when converting particle numbers to concentration.

RWPT models have been used extensively in ocean outfall pollutant transport predictions (Zhang, 1995; Dimou and Adams, 1992; Kim and Seo, 2001). Chin and Roberts (1985) proposed a RWPT model in which a finite number of particles was released at every time step from an ocean outfall source (at the end of the near field) and horizontally advected by deterministic and stochastic components of the velocity field

and vertically by a stochastic diffusion velocity. They assigned a mass distribution at any point $\vec{x} = (x, y, z)$ and time t after the source release on a Lagrangian framework:

$$M(\vec{x}, t) = \int_0^t \int_{V_S} M_0(\vec{x}_S, t_0)\ P\left(\vec{x}, t \mid \vec{x}_S, t_0\right)\ dx_S dy_S dz_S dt_0 \tag{2-18}$$

where M_0 is the mass flux from the source at $\vec{x}_S$ and at time t_0 and $P\left(\vec{x}, t \mid \vec{x}_S, t_0\right)$ is the probability distribution over the $\vec{x}$ and t of finding a particle that was released at the source with the coordinates $\vec{x}_S = (x_s, y_s, z_s)$ at time t_0. Their model converted the particle numbers to mass based on a probability distribution.

$$c(l, m, n, I) = \frac{\Delta y_s \Delta z_s \Delta t}{\Delta x \Delta y \Delta z} \sum_{i=1}^{I} M_0\left((i - \frac{1}{2})\Delta t\right) \sum_{j=1}^{J} \sum_{k=1}^{K} p_m\left(l, m, n, I \mid (j - \frac{1}{2})\Delta y_s, (k - \frac{1}{2})\Delta z_s, i\Delta t\right) \tag{2-19}$$

where Δx, Δy, Δz are the dimensions of the concentration grid elements, and p_m is the probability that a particle released at the time $i\Delta t$ from the location $((j - \frac{1}{2})\Delta y_s, (k - \frac{1}{2})\Delta z_s)$ is found at time $I\Delta t$ in the concentration grid element corresponding to (l, m, n). The probability distribution was determined by the total mass associated with each of the concentration grid element over the number of simulation and time steps:

$$p_m\left(l, m, n, I \mid (j - \frac{1}{2})\Delta y_s, (k - \frac{1}{2})\Delta z_s, i\Delta t\right) = \frac{m_e\left(l, m, n, I \mid (j - \frac{1}{2})\Delta y_s, (k - \frac{1}{2})\Delta z_s, i\Delta t\right)}{n_s(I - i)} \tag{2-20}$$

The total mass is the summation of individual particle mass in each cell element $(m_e = \sum m_p)$. The mass associated with each particle released at the previous time $(r - i)\Delta t$, is computed by an exponential decay:

$$m_p(r-i) = \exp\left[-k(r-i)\Delta t\right] \tag{2-21}$$

They carried out the above release-advection procedure until *r* equals *i* and repeated the simulation several times in order to obtain an ensemble particle and mass distribution with n_s number of simulations. The horizontal and vertical coordinates of the particles included both deterministic and stochastic component of the velocity as follows:

$$x(r+1) = x(r) + u(r)\Delta t \tag{2-22}$$

$$y(r+1) = y(r) + v(r)\Delta t \tag{2-23}$$

$$z(r+1) = z(r) + \varepsilon l_v(z(r)) \tag{2-24}$$

where ε is a random number in the range $[-\sqrt{3}, \sqrt{3}]$, u and v are the velocities in the *x* and *y* directions, $l_v(z)$ is the vertical length scale of advection that is $\sqrt{2K_v(z)\Delta t}$, where $K_v(z)$ is the vertical diffusion coefficient.

Particle tracking models have also been implemented by many researchers in oil spill studies to assess the risk of shoreline contamination. Examples are Korotenko et al. (2004) who developed a 3D flow and transport model to predict the dispersal of oil pollution resulting from river discharges. They used the model to simulate a continuous oil release from the Volga River into the coastal waters of the north part of the Caspian Sea. Their transport model, a particle tracking method, used predetermined currents and turbulent diffusivities to predict the motion of individual particles (droplets), the sum of which constituted hypothetical oil spills. The currents and turbulent diffusivities were generated by a numerical ocean circulation model (POM). The basic processes affecting the fate of the oil spill, e.g. evaporation, were taken into account and parameterized with a new technique based on a pseudo-component approach. Varlamov et al. (1999) also simulated spilled oil in the Sea of Japan using a particle tracking model incorporating advection by currents, and random diffusion from the GFDL-MOM ocean model.

The particle tracking model that is used in the present study is called PARTIC3D. It was originally written by Jarle Berntsen (1991, Institute of Marine Research, Bergen-Nordnes, Norway) and adapted by the Great Lakes Environmental Research Laboratory

(Schwab, 1994). The model will be further explained and the literature supporting its modification to include diffusion and near field process will be presented in Chapter 6.

The velocity field for transport models (EM or LM) must be determined by hydrodynamic models which are described in the next section.

2.4 Hydrodynamic Models

Hydrodynamic models have been increasingly used in the past decades to predict pollutant dispersion in coastal waters. Free surface, terrain-following (sigma or s-coordinates) ocean models emerged about 20 years ago from the need to model turbulent processes in surface and bottom boundary layers and to simulate flows in estuaries and coastal regions. A hydrodynamic model solves the equations of continuity, momentum, and mass conservation for salinity and temperature. Some commonly used ocean circulation models are listed in Table 2.1. Some are proprietary and some are open source (free).

Models such as POM, ECOM, and ROMS use curvilinear orthogonal horizontal coordinates, a horizontal numerical staggered ‘‘Arkawa-C’’ grid, and a vertical staggered grid with either a sigma or a more general s-coordinate system. Most models assume the vertical pressure distribution to be hydrostatic, and this is adequate for most coastal processes of interest. The models are either finite element, finite difference, or finite volume, of which finite difference is the most common. Although the basics of the models are similar, there are considerable differences in numerics and parameterizations.

The early history of the 2D and 3D hydrodynamic models used in the Great Lakes was reviewed by Wu (1993), who developed an integrated hydrodynamic/pollutant transport model for the near shore area of the Great Lakes. The model was applied to the St. Clair River for bacteriological pollution prediction in the bay. A nested grid model was later applied to study current patterns in Hamilton Harbor, Canada (Tsanis, 2000), with a random-walk model was used to predict concentration peaks.

Table 2.1 Examples of hydrodynamic ocean circulation models

Name	Assum-ptions	TCM	Main applications	Extensions/ Application	Comments
Delft3D	FVM,SW, HY	k-ε, k-L, algebraic, constant	Coastal, rivers and estuaries	GG, WQ, SD, W, PT, MD, EC	Delft Hydraulics. Commercial; pre- and post-processing packages are available
POM (Princeton Ocean Model)	FDM, BO, HY	Mellor-Yamada	Estuaries, coastal regions, basin and global oceans	None	Blumberg and Mellor (1987). Open source, no pre or post-processing packages
ECOM	Outgrowth of POM	Mellor-Yamada	Rivers, lakes, estuaries and coastal waters	WQ, SD, W	HydroQual. Blumberg and Mellor (1987). Open source, updated version of POM, post processing packages are available
ROMS	FDM, BO, HY	Mellor-Yamada, k-ε, k-w	Ocean, coastal waters and estuaries	TR, WQ, PT, ST, W	Rutgers University (1994). Open source, well documented. Updated POM, pre and post processing packages available
Mike	FVM, BO, HY	Constant eddy viscosity, Smagorinsky subgrid scale, k-ε, mixed Smagorinsky/k-ε	Lakes, estuaries and coastal waters	TR, EC, ST, MT, WQ, PT	DHI Group. Commercial, pre- and post-processing graphical user interface packages are available
Telemac 3D	FEM, BO, HY and non-HY	Mixing length	Lakes, estuaries and coastal waters	SD, WQ, W, GF, HA	Sogreah Consult. Commercial, pre- and post-processing packages are available
ELCOM	FDM, BO, HY	Eddy-viscosity or mixed layer	Lakes, coastal waters and estuaries	CAEDYM (WQ)	CWR, University of Western Australia, open source, well documented

BO = Boussinessq Approximation
EC = Ecology and Water Quality Model
EFT = Ekman Flow Theory
FEM = Finite Element Method
FDM = Finite Difference Method
FVM = Finite Volume Method
GG = Grid Generator
HA = Harbor Agitation
HY = Hydrostatic Assumption
WQ = Water Quality
LWT = Long Wave Theory
MT = Mud Transport
PT = Particle Tracking
RANS = Reynolds-Averaged Navier-Stokes
RLT = Rigid Lid Theory
SD = Sediment Transport Module
SW = Shallow Water Approximation
TCM = Turbulence Closure Model
TR = Transport Module
UF = Groundwater Flow
W = Wave

Recent studies have also been conducted on surface discharges in other lakes. Carnelos (2003) developed a 3D hydrodynamic and mass transport model based on a modification of the Princeton Ocean Model (Blumberg and Mellor, 1987) for assessing the risk associated with recreational activities in the south shore waters of Lake Pontchartrain, New Orleans after a storm water event. It is a high-resolution nearshore

model that includes density currents due to temperature and salinity as well as an integrated bacteria fate and transport sub-model. The model agreed fairly well with a 2- to 3-day impact period associated with storm water discharges as well as highly variable wind-driven plume migration patterns that are often characterized by shore reattachment, as was observed in the field.

McCorquodale et al. (2004) applied ECOMSED (HydroQual, Inc. 2005) and the Princeton Ocean Model (Blumberg and Mellor, 1987) to predict discharges from drainage channels into a crossflow created by tides and wind stresses. Ye and McCorquodale (1997) also studied the importance of secondary currents on lateral mixing in a meandering river using a 3D boundary fitted hydrodynamic model. In Chapter 5, a version of Princeton Ocean Model (Blumberg and Mellor, 1987) developed by the Great Lakes Environmental Research Laboratory (GLERL) is used to provide hydrodynamic predictions for the Grand River plume.

As stated earlier, hydrodynamic models have significant predictive capabilities in the large scale 3D field, but they do not represent all the small scale processes that occur in the near field. McCorquodale (2007) in a detailed review of storm water jet and plume models discusses existing Computational Fluid Dynamics (CFD) models and concludes that they are not accurate in the near field and emphasizes the need for unified near field-far field or hybrid models that can utilize the best features from empirical models, integral models for the near field, and 3D numerical models to simulate far-field flows. Some of the important previous literature on coupled models are reviewed below.

2.5 Coupled Models

The wide range of time and spatial scales of mixing in the near and far fields and limitations of single models to comprehensively represent all hydrodynamic processes have caused researchers to apply coupled approaches (two interfaced models in the near and far fields) for coastal waters. Zhang (1995) coupled a near field model with a far field particle tracking model and applied a 3D hydrodynamic model (ECOMsi) to predict the trap height of an ocean outfall. Dimou and Adams (1992) developed a 3D finite element Eulerian-Lagrangian far field model and coupled it with a particle tracking model near

the source using an initial dilution model for simulating passive pollutant transport and applied it to the Boston outfall.

Kim and Seo (2001) developed a coupled model that uses line plume equations to determine initial mixing in the near field and a particle tracking model to simulate the far field transport in order to predict the mixing characteristics of wastewater plumes discharged from ocean outfalls. The particles introduced at the end of the near field were advected by the ambient current, which was calculated by a σ-layer 3D hydrodynamic model. The particle locations were described by a non-linear Langevin equation with two deterministic and random terms. The deterministic term included a scaled velocity and a pseudo velocity that made a symmetrical distribution in the physical domain by moving particles in the transformed grid.

Kim et al. (2002) also used a coupling technique that incorporates a jet integral method for the initial mixing and a particle tracking model for the far field advection-diffusion processes of a single submerged jet. They showed that a combination of a Gaussian and vortex-pair distribution of particles in the vicinity of the port and farther away in the advected thermal region gives better results for plume trajectories. The conventional spreading equations were modified with a constant spreading coefficient to consider variations in spreading rate relative to the direction of ambient flow and the velocity ratio.

Roberts (1999) applied statistical short- and long-term models to predict the far field behavior of an outfall in Mamala Bay, Hawaii. The short term model was coupled with a near field model, a modified version of the EPA RSB model, that used measurements obtained from Acoustic Doppler Current Profilers.

Zhang and Adams (1999) suggested four possible coupling techniques to introduce loadings to a far field model using the trap height predicted by a near field model: (a) introduce both flow and loading at the source; (b) introduce flow at the source, loading at the trap height; (c) introduce both diluted flow and loading at the trap height; (d) introduce only loading at the trap height. They concluded that methods (a) and (d) are generally preferable: Method (a) with dynamic controlling of the diffusion coefficients is most accurate, but has high computation costs for long-term simulations; Method (d) is

appropriate for many practical problems while giving sufficient accuracy in the near field.

Bleninger (2007) coupled a near field model (CORMIX, Jones et al. 1996) for a submerged outfall with a mass transport model (the water quality module of Delft3D) in which Delft3D provided the hydrodynamic predictions. He applied it for a planned outfall for the city of Cartagena, Colombia.

Suh (2006) presented a coupling approach to predict the diffusion of contaminants such as suspended solids or heated water dispersion in coastal waters. A random walk particle tracking method was applied near the source, where steep concentration gradients occurred, and a gradient-diffusion model was used in the far field. The model was tested for two cases: with and without buoyancy, which in the former a buoyancy term was added to the horizontal diffusivity. In order to link the near and far field models they used a puff concept assuming a Gaussian concentration profile for each parcel or patch of mass. They tested it for a thermal power plant surface heat discharge. Their results strongly advocated the use of an Eulerian–Lagrangian approach (a random walk model in the near field and a gradient-diffusion model in the far field).

In Chapter 6, a particle tracking model is developed and coupled to an empirical dilution and trajectory model in the near field. The empirical model based on field data overcomes the deficiencies of hydrodynamic models in the near field. Based on the empirical formulae for the geometry (width and thickness) of the plume, and near field concentrations along the plume centerline, certain numbers of particles are released to the far field. The procedure is further explained in Chapter 6.

2.6 Bacterial Models

Attempts to model and predict bacterial impacts at beaches have been both statistical and deterministic. Statistical models predict beach bacteria by purely regression methods with explanatory variables. An example is the model Virtual Beach (Frick, et al. 2008) which is a multiple linear regression model. The most common variables that show some correlations with bacteria are turbidity, wave height, cloud cover, onshore wind component. Other studies include Whitman and Nevers (2008) who evaluated observed

bacterial levels at 23 Chicago beaches and extracted best fit relationships (with $r^2<0.5$) for E. coli, wave height, and an interactive term comprised of wind direction and creek turbidity. They found considerable variability, with wave height being a significant factor. These models usually only explain a fairly small fraction of the observed variations, however.

McLellan et al. (2007) also investigated the fate of E. coli from urban storm water and combined sewer overflows in Lake Michigan. Their results suggested that a combination of dilution and decay is responsible for the rapid disappearance of E. coli. They also suggested that fecal coliform survived longer than E. coli in the lake. E. coli is generally believed to be a better indicator of human pathogens than fecal coliforms, since this organism does not survive as long in the environment as other members of the fecal coliform group.

Numerous chemical and biological factors also affect bacteria. They are summarized in a recent extensive review by Hipsey et al. (2008). Removal mechanisms include biotic stresses from grazing and predation, inactivation by sunlight, exposures to temperature, salinity, and pH, and even, should conditions be favorable, growth. Mortality and growth depend on nutrient availability. This is further complicated where organisms originate from enriched sources such as Combined Sewer Overflows (CSO) or wastewater discharges, where a lag can occur between introduction and decay, whereas organisms washed in from a catchment may begin to decay immediately on entering the coastal environment. This is a further reason that particle tracking models are attractive in that they can readily trace different types of bacteria and particles with different decay (or growth) characteristics.

Bacterial decay rates are normally assumed to follow a first order decay model according to Chick's Law (Chick, 1910):

$$dC/dt = -kC \tag{2-25}$$

where C is the bacteria concentration (CFU/100ml), t is the time (minute), and k the die off rate (min^{-1}). Assuming k is a constant, this yields an exponential decay:

$$C/C_0 = e^{(-kt)} \tag{2-26}$$

The decay rate can also be expressed as T_{90}, where

$$T_{90} = \ln 10 / k \tag{2-27}$$

T_{90} is the time for bacteria to reduce by 90% of the original amount.

A few studies have focused on modeling bacterial transport in the Great Lakes. Liu et al. (2006) investigated the existence and decay rates of E. coli and Enterococci in the nearshore waters of Lake Michigan. Their study indicated the transport of human fecal pollution from tributaries to the beach. They showed that Entrococci had a longer survival rate than E. coli that had a decay rate in the range of 0.5-2.0 day^{-1}, if described with a first order decay. They suggested the use of a more sophisticated formula for decay including inactivation due to sunlight, temperature and sedimentation which is as follows:

$$k = \left(f_p \frac{v_s}{H} + k_I I_0(t) \right) \theta^{(T-20)} \tag{2-28}$$

where v_s is the settling velocity of particles (assumed to be 5 m/day based on Stokes' formula), H is the water depth, f_p denotes the fraction of bacteria attached to the particles (assumed as 0.1), k_I is the insolation inactivation rate that was assumed 0.0026 $W^{-1}m^2d^{-1}$ (3×10^{-8} $W^{-1}m^2s^{-1}$) for the total range of sunlight bandwidth (300-3000 nm), $I_0(t)$ is the sunlight intensity in Wm^{-2} at the surface as a function of time, θ is the temperature correction factor (set as 1.07), and T is the water temperature.

In a recent study, Thupaki et al. (2010) analyzed E. coli concentrations on two southern Lake Michigan beaches that were impacted by river plumes. They used 3D hydrodynamic and gradient-diffusion transport models to evaluate fluxes of E. coli due to advection, diffusion, and inactivation. They adjusted Eqn. 2-28 to their 3D model and evaluated the inactivation due to settling in every model layer. They also added a coefficient to account for light extinction in deep and turbid waters. Their decay model is as below:

$$k = \left(\frac{f_p v_s}{\Delta z_i} - \frac{f_p v_s}{\Delta z_{i-1}} + k_I I_0(t) e^{-k_e z} + k_d \right) \theta^{(T-20)} \tag{2-29}$$

where k_e is the light extinction coefficient (assumed 0.55 m^{-1}), Δz_i denotes the thickness of the layer *i*, *z* is the depth in m, and k_d is the base mortality (dark death) rate that was assumed 8.6×10^{-5} d^{-1}. They showed that solar inactivation had the greatest impact on E. coli decay, however, the exact decay rate was difficult to determine due to uncertainty of the inactivation from settling, and the effect of water clarity on inactivation rates, and due to lack of quantitative information on the attenuation of different energy bands within the water column, and the importance of biological processes associated with different time scales. In Chapter 6, we use a similar approach to Thupaki et al. (2010) and more simplified for bacterial decay and incorporate it in the particle tracking model.

2.7 Summary

Few experimental and field studies have focused on surface buoyant river plumes with aspect ratios greater than 3. Natural rivers, such as in Lake Michigan, have large aspect ratio outfalls however. This study, with its focus on the Grand River and extensive field studies will advance our knowledge of these types of plumes. A new scheme for categorizing surface buoyant river plumes is presented that will expand previous models by including more flow classes and wind effects. The new model is better suited to conditions typical of the Great Lakes than previous models.

Most previous fate and transport models do not capture all the scales of river plume nearshore transport phenomena. Because most of these models are implicitly far field models, none of the near field processes such as gravitational spreading are incorporated, nor is the reduction in vertical mixing due to the density stratification.

Many coupled models have been developed for submerged plumes but only a few for surface plumes. This is the first study to use a coupled particle tracking technique for surface buoyant plumes from a natural river. It incorporates 3D hydrodynamic modeling and an empirical near field model to improve predictive accuracy. The Lagrangian approach is also expected to better represent bacterial diffusion and patchiness behavior and avoid many of the deficiencies of gradient diffusion models.

Finally, many models, including those in the Great Lakes Coastal Forecasting System, are 2D (depth-averaged). A 3D model is used here that provides a better

approximation to the thin surface spreading layer plumes that actually occur in the Great Lakes, where the processes are clearly 3D.

CHAPTER 3

FIELD STUDIES

3.1 Introduction

The Grand River contributes a large portion of the nutrient, chemical, sediment, and pollutant loads to Lake Michigan (Chambers and Eadie, 1980). These loadings are expected to significantly affect nearshore water quality. The river is the largest tributary flowing directly into Lake Michigan and is the longest river (420 km) in Michigan. Its watershed drains an area of 14431 km^2 and empties into the lake at Grand Haven. Extensive field activities on the river plume were carried out during the swimming seasons (August and June 2006, and June and July 2007). The studies on mixing and transport of the Grand River plume as it enters Lake Michigan were conducted in the vicinity of the Grand Haven coast on the east side of the lake as shown in Figure 3.1. The studies are described in this Chapter.

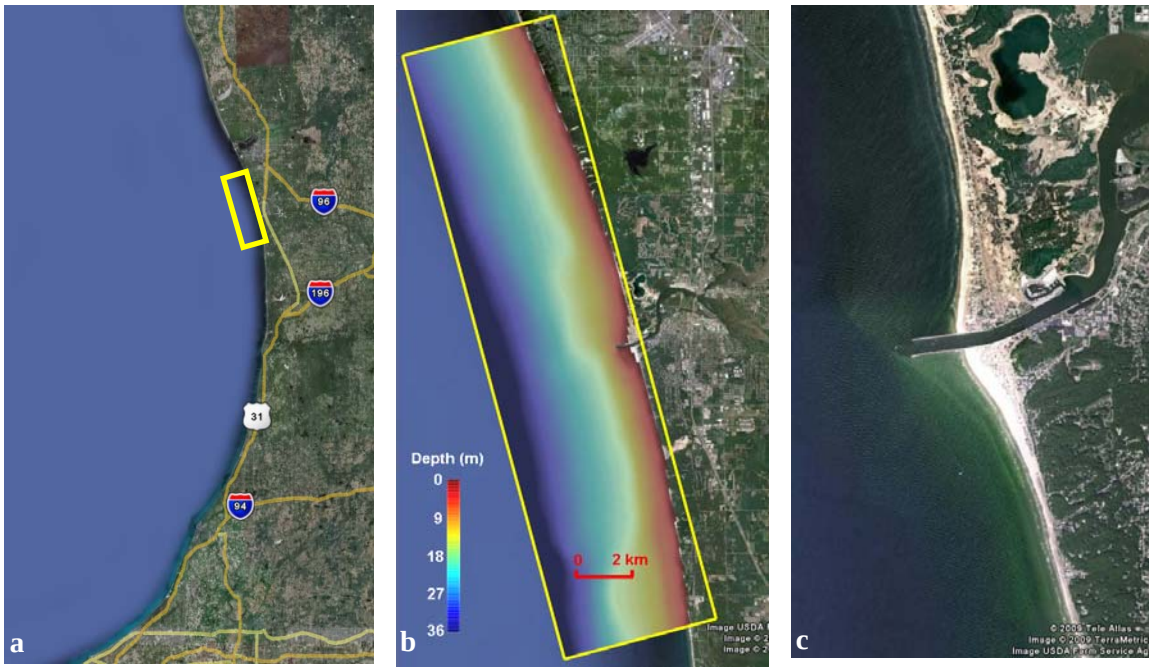

Figure 3.1 a) Location of the Grand Haven on the East side of Lake Michigan, b) the study area and bathymetry near Grand Haven, c) close-up of the Grand Haven pier.

Large volumes of storm water flow during rainfall events can exceed the sewage system capacities in older cities around the Great Lakes and cause combined sewer overflows (CSO) into rivers. Separated sewers can also fail during large rain water infiltrations resulting in sanitary sewer overflows (SSO). Both can be major sources of water body impairments in the US and are primary sources of human fecal pollution in surface water systems (USEPA, 2004). During heavy rainfall events there is a possibility of a CSO or SSO event where the bacteria level can be very high (McLellan, 2007).

The water quality of the Grand River, a major contributor of pollutants to Lake Michigan, and the region's public health are threatened by these overflows, especially from some of the major urban areas in the Grand River watershed such as the city of Grand Rapids. Surface runoff is also a major contributor to impairment of river water quality. Urban developments in recent years have created larger impervious areas, and lacks of environmental management practices increase the nutrients and turbidity of the river water.

There have been few studies to evaluate the fate and transport of waterborne pathogens carried from the river to beach sites near Grand Haven. Most have focused on the Grand River itself or its watershed (Shen et al., 2008, Rose and Phanikumar, 2007). The present study was conducted to understand the influence of wind, surface temperature, water currents and river characteristics on pathogen transport within the plume by performing field observations of the Grand River and tracking contaminant flow in Lake Michigan, particularly to local beaches.

The study site (Figure 3.1), located on the east coast of Lake Michigan between 86.20° W to 86.35° W and 42.95° N to 43.20° N covers the Grand River plume. The Grand River outlet has two piers that extend about 250 meters into the lake in order to accommodate vessels. The study site extends almost 5 km offshore and 15 km alongshore.

3.2 Experimental Methods

The field studies were conducted in four periods in August and June 2006 and June and July 2007 with the support of NOAA-GLERL staff and utilizing their research equipment. It included aerial photography of the plume, ADCP moorings, meteorological buoys, drifters, SF6 and Rhodamine WT tracer studies, and 3D CTD profiling over the plume (Figure 3.2).

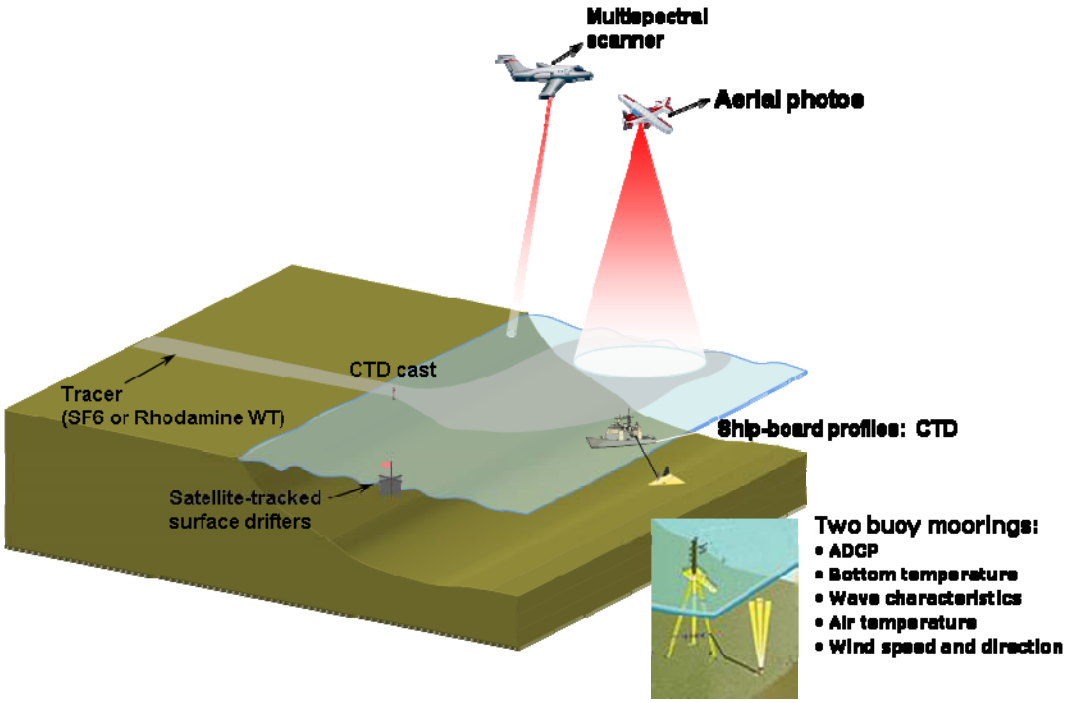

Figure 3.2 Schematic depiction of the Grand Haven field experiments

Two types of CTD profiling were done: First using a V-Fin package towed from the ship that recorded spatially variable plume data and the second making CTD casts from a smaller boat at different points in the river and in the lake. Four intensive surveys were conducted for periods up to four days: August 8-11, 2006, June 20 and 22, 2006, June 5 and 6, 2007, and July 17 and 18, 2007. The experiments are summarized in Table 3.1.

Table 3.1 Summary of the Grand River Plume Field Experiment in 2006 and 2007

Series	1	2	3	4
Dates	Jun 20-23, 2006	Aug 8-11, 2006	Jun 5-6, 2007	Jul 17-18, 2007
Aerial Photography in both morning and afternoon	Jun 19, 20, 22, 23, 24	Aug 8, 9, 10, 11	May 29,30,31 Jun 1,2,5,6,8,9,10,30	Jul 2,6,9,11,13,17, 18,19,20
ADCP 43° 4′ 59.94″ N, 86° 15′ 31.20″ W	N5-06 4/20/06 – 7/20/06			
43º 2′ 1.20″ N, 86º 14′ 33.54″ W (Buried in sand)	S5-06 4/20/06 - 6/14/06	S5-06 4/20/06 - 6/14/06		
43º 4′ 25.68″ N, 86º 15′ 49.74″ W (Not reliable)	N10-06 4/20/06 - 10/14/06	N10-06 4/20/06 - 10/14/06		
43° 2′ 0″ N, 86° 14′ 33.54″ W	S10-06 4/18/06-10/21/06	S10-06 4/18/06-10/21/06		
43°3′ 9.00″ N, 86° 17′ 12.12″ W			M20-07 5/15/07-7/19/07	M20-07 5/15/07-7/19/07
43° 3′ 46.99″ N, 86° 15′ 42.42″ W			N10-07 5/15/07-7/19/07	N10-07 5/15/07-7/19/07
43° 2′ 55.01″ N, 86° 15′ 24.07″ W			S10-07 5/15/07-7/19/07	S10-07 5/15/07-7/19/07
Surface Drifters	4 drifters Jun 20, 21	3 drifters Aug 8		10 drifters Jul 17,18
Tracer Studies	SF6 Jun 21, 22, 23	SF6 Aug 8, 9, 10, 11	Rhodamine WT Jun 5, 6	Rhodamine WT Jul 17,18
CTD (V-Fin) 3D lake profiling	Jun 20, 22	Aug 8, 9, 10, 11	Jun 5, 6	Jul 17,18
CTD (Cast) Lake and river profiles			Jun 6	Jul 17,18
Bacterial Sampling			Jun 5, 6 River, lake and beach	

The aerial photography usually started a few days before and ended a few days after each test period. The current moorings were deployed for longer periods and the meters were usually retrieved at least one month after the last experiments were completed in that year. GPS-tracked surface drifters were released on June 20 and 21, and August 8,

2006, and also on July 17 and 18, 2007. SF6 tracer was released in the river on August 8 to 11, 2006 and Rhodamine WT on June 5 and 6, and July 17 and 18, 2007. Additional CTD casts were performed in the river on June 6 and in the river and on the lake in July 17 and 18, 2007. Bacterial sampling was carried out along with the CTD surveys on June 5 and 6, 2007. These data provided a valuable resource to study the hydrodynamics of a surface buoyant plume and its effects on bacterial transport.

3.2.1 Aerial Photography

The airborne digital imagery provided much useful information on the plume behavior and shape that makes this study unique. Similar imagery has assisted scientists in water quality measurements by providing wide spatial coverage of river plumes (White et al, 2005). The technique was used here to capture comprehensive visual information of the Grand Haven plume dynamics. This information, along with CTD data, will be used to predict the plume trajectories and dilutions in Chapter 4.

The photographs were taken by Marge Beaver (Photography Plus) from an aircraft at low altitude at different times throughout the day. They were transmitted to the vessel within a few hours via email and used to guide the boat sampling protocol. Moreover, the photos provided information about the shape and direction of the plume relative to the wind and currents. The boat tracks were overlaid on the aerial images to indicate the CTD surveying and bacterial sampling points relative to the plume. The photography was performed by Marge Beaver of Photography Plus. Several hundred photographs were taken; they are summarized in Appendix A in thumbnail format.

3.2.2 Current Moorings

Acoustic Doppler current profilers (ADCPs) were deployed by NOAA Great Lakes Environmental Research Laboratory at several locations around the river mouth, nearshore and offshore, for several months before and after each field experiment. The naming scheme for the ADCPs consists of the location (S for South, N for North, and M for Middle), water depth, and year. For example, mooring S10-06 is South of the pier at 10 m depth in 2006. Four ADCPs were deployed in 2006, two south and two north of the pier at 5 and 10 m depths (Figure 3.3). They are S10-06 (GHS10-SN5315), N10-06

(GHN10-SN3748), S5-06 (GHS5-SN6231) and N5-06 (GHN5-SN6232). The names in parentheses are the NOAA original names and the instrument serial numbers. S5-06 was buried in the sand and could not be retrieved, and N10-06 did not record reliable current direction, therefore these two are not considered further. Two other ADCPs (ADP-SN0305 at 43º 5.33′N, 86º 15.89′W and ADP-SN0321 at 43º 4.60′N, 86º 15.58′W) were deployed by NOAA from Sep 28 to Nov 13, 2006. Their time frame was out of the period of present interest, however, so they are not included in Table 3.1.

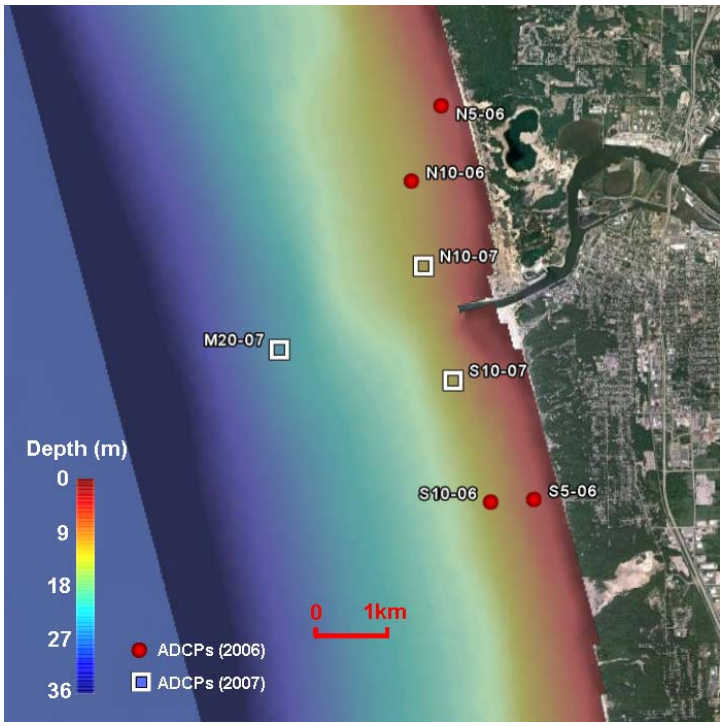

Figure 3.3 ADCP locations; Meteorological stations GHS and GHN are moored to S10-06 and N10-06.

Therefore, among all the ADCPs deployed in 2006, only S10-06 and N5-06 provided useful data that was appropriate for the periods of study. These moorings provided currents at different depths, wave, and water level data measurements. Their record periods were summarized in Table 3.1. N5-06 became trapped in sediment on May 11, 2006 and could not initially be recovered in June 2006. Almost one year later, divers from Michigan Shipwreck Associates located the remainder of the mooring line and a

commercial dredging company recovered the ADCP, which was buried under several feet of sand. But after it was retrieved, in September 2007, the recorded data was valuable (Table 3.1). Both instruments were configured to record data every 30 minutes with broadband frequency of 614 kHz and ensemble average 900 pings. S10-06 recorded data at 15 bins spaced 0.5 m apart. The first bin was at 8.5 m depth and the last bin at 1.5 m from the surface. N5-06 recorded data at 12 bins 0.25 m apart. The first bin reading was at 3.4 m depth and last bin was at 0.9 m from the surface.

The array of instruments in 2007 consisted of two ADCP's at 10 m depth and one at 20 m depth. They recorded data for two months as well as hourly wave height, period, direction, and water level every 5 minutes. These ADCPs are designated as S10-07 (GHS10-SN1057), N10-07 (GHN10-SN0717), and M20-07 (GH20-SN0155). S10-07 and N10-07 are the south and north nearshore, and M20-07 is the middle. They were all configured on 307 kHz broadband frequency and ensemble average of 200 pings. S10-07 and N10-07 recorded data at seven bins spaced 1.0 m apart. The first bin was at 6.8 m depth and the last one 0.8 m from the surface. M20-07 recorded data at 17 bins spaced 1.0 m apart. The first bin was at 16.8 m depth, and the last one 0.8 m from the surface.

3.2.3 Meteorology Stations

Wind speed and direction data was measured by the NOAA Realtime Coastal Observation Network (RECON) Stations, Grand Haven South (GHS) and North (GHN) buoys. The GHS and GHN buoys were moored very close to S10-06 and N10-06 ADCPs (Figure 3.3). They record meteorological data, and the ADCPs record current data. The meteorological records included air temperature and wind speed and direction. GHN was deployed for the spring, summer, and fall seasons of 2006; GHS was deployed for the same period in both 2006 and 2007. Due to proximity of GHN to N5-10, and GHS to S10-06 in 2006, the GHN wind records were used as the local wind at N5-06, and GHS for the S10-06 ADCP. In 2007, the GHS record was the only available local wind. Wind speed and direction were measured by an R.M Young anemometer located 2.3 m above the lake surface at 5-minute averaged intervals. Wind speed resolution was 0.1 m/s with an accuracy of ±1.0 m/s, and wind direction resolution was 1.0 degrees with an accuracy of ±10 degrees (Ruberg et al, 2008).

3.2.4 Tracer Releases

Tracer studies of the river were carried out by Dr. Mike McCormick and his crew from NOAA Great Lakes Environmental Research Laboratory. They released the inert gas Sulfur Hexafluoride (SF6) in August 2006 and Rhodamine WT in June and July 2006 at the sites shown in Figure 3.4. SF6 was released about 10 km upstream of the river mouth at a site off highway 104 and Milpoint Drive at the dock. The gas was introduced into the river and the plume was tracked in the lake for several days by means of surface grab-samples that were subsequently analyzed in the lab by chromatography. Rhodamine WT (McCormick et al, 2007) was released under the US-31 bridge in Grand Haven. Dye concentrations were detected in-situ in the lake and in real-time using a fluorometer attached to the V-Fin towed from the ship.

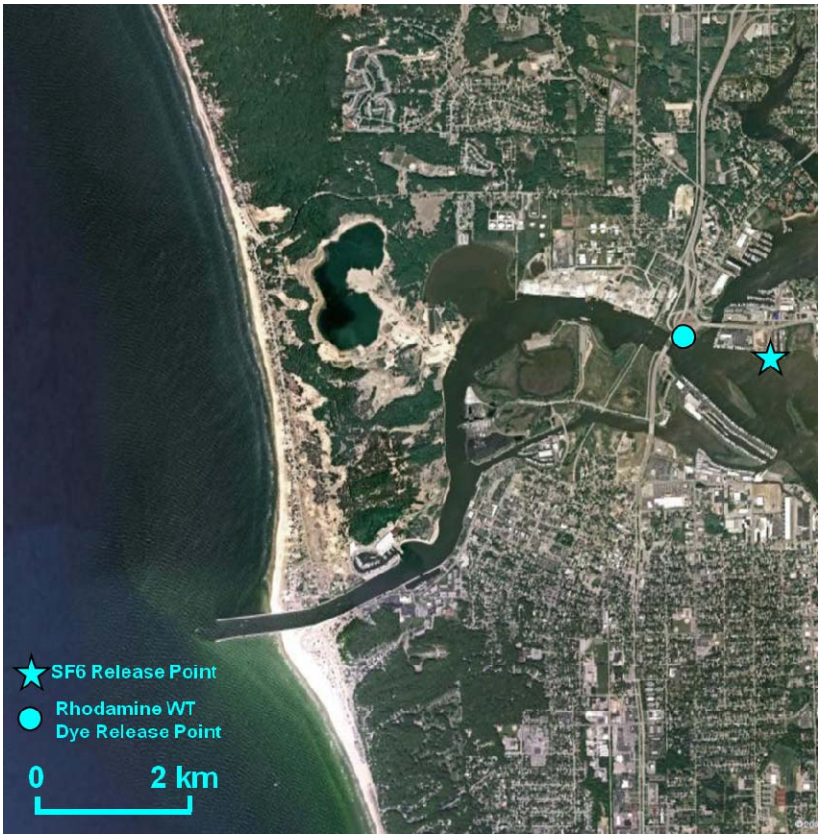

Figure 3.4 Tracer release points.

3.2.5 CTD Survey and Profiling

A V-Fin sensor package was towed by a NOAA research vessel in a towyo pattern. It was winched to within 0.5 m of the surface and lowered to about 1 m above the bottom while the boat travelled at speeds of 2.5 to 5 knots (~1.3-2.5 m/s). The data were used to measure the spatial variability of plume conductivity, temperature, and Rhodamine WT (dye) at various depths. The V-Fin was equipped with CTD (conductivity, temperature and depth) sensors that also sampled dissolved oxygen at approximately 1 Hz. In 2007 a SCUFA™ fluorometer sampling at 2 Hz was added to measure fluorescence due to the Rhodamine dye. In addition, the SCUFA measured turbidity (in NTU units). The vertical temperature profiles determined the density structure in the river plume in the lake. The tracer concentration measurements were designed to capture the spatial and temporal variability of the plume. In addition, profiles at fixed locations consisting of CTD casts at the river mouth were conducted in 2007.

The river salinity was always slightly higher than the lake, so conductivity proved to be a more useful tracer of the river than fluorescence, since it occurs naturally and was a continuous tracer source. Conductivity is reported as microSiemens/cm (μS/cm); it is the ability of a solution to conduct an electric current and is a function of salinity. It can be used as an index of the total solids (TDS) in a water sample where 2 μS/cm ≈ 1 ppm or 1 mg/l. The conductivity of different sources of water have a broad range (e.g. 0.055 μS/cm for absolute pure water, 0.5 μS/cm for distilled water, 1.0 μS/cm for mountain water, 500 to 800 μS/cm for most drinking water sources, and 56 mS/cm for sea water). Typical conductivities observed in the river ranged from 600 to 660 μS/cm and in the lake from 270 to 300 μS/cm.

3.2.6 Drifter Releases

Satellite-tracked drifters, similar to the neutrally buoyant free ocean drifters Argos model 115 made by Brightwaters Instrumentation Corporation, were used to measure Lagrangian surface currents (Figure 3.5). Onboard electronics transmit a radio signal that is detected by a satellite network. Drifters were used on June 20, 21 and August 8, in 2006, and July 17, 18 in 2007 to monitor and measure near-surface currents. In 2007, a

new Garmin Rino 110 tracking GPS system was used. The Rino transmits location signals every 5 seconds which made it possible to track 10 drifters simultaneously up to several miles away. Drifters are very useful for surface current measurements and dispersion calculations because of their precise Lagrangian current data recording capability. Drifters versus tracers have both advantages and disadvantages. Drifters are superior in terms of providing higher sampling frequency data; tracers are better in representing diffusion due to vertical shear dispersion. (Peeters 1994, Stoket and Imberger, 2003). The drifter release experiment was performed by Dr. McCormick and his team.

Figure 3.5 Satellite tracked drifters used in Grand Haven experiments.

3.2.7 Bacterial Sampling

In order to determine the fate of bacteria in the plume, fecal indicator bacteria (E. coli and total coliform) samples were collected along with the CTD profiling in the June 2007 tests. Surface water samples were taken on June 5 and 6, 2007 by dipping a 1-L bucket just below the surface (0 to 0.5 m depth). The samples were transferred into sterile 500-mL polypropylene bottles, stored in a cooler on ice in dark and transferred to the lab within 6 hours of collection. The sample locations were chosen to cover the plume extent

and GPS locations and times were recorded. E. coli and total coliform levels were determined using the enumeration techniques developed by EPA 2004 (USEPA, 2004). This work was carried out by the Great Lakes WATER institute staff led by Sandra McLellan.

3.3 Hydrodynamic Observations

Details of each series of field experiment are presented in this section. In particular, the wind and current records for the four periods shown in Table 3.1 (June 19-24, 2006, August 7-11, 2006, June 4-8, 2007, and July 14-18, 2007) are studied in more detail to form a basis for the hydrodynamic simulation verifications that will be presented in the next chapter. All times are in Greenwich Mean Time; Eastern Daylight Time (EDT) in Michigan is 4 hours behind GMT (EDT=GMT-4). Each period is discussed separately below.

3.3.1 Series 1: June 2006

The Series 1 experiments were conducted from June 20 to 23, 2006. The wind and current observations, their effect on the plume, CTD, and tracer experiments result are discussed below.

3.3.1.1 Current and Wind Observations

The wind and currents for the six day period (June 19 to 24) at mooring N5-06, are shown in Figure 3.6. These are feather plots of wind, depth-averaged currents, and currents in selected bins at depths of 1.1, 1.9, 2.9, and 3.6 m. Similar plots for mooring S10-06 are shown in Figure 3.7; its bins are at depths of 2.0, 3.3, 5.8, and 8.5 m. Polar wind histogram and scatter diagrams of the surface and depth-averaged currents are shown in Figure 3.8. The principal axes of the currents are indicated on the scatter plots.

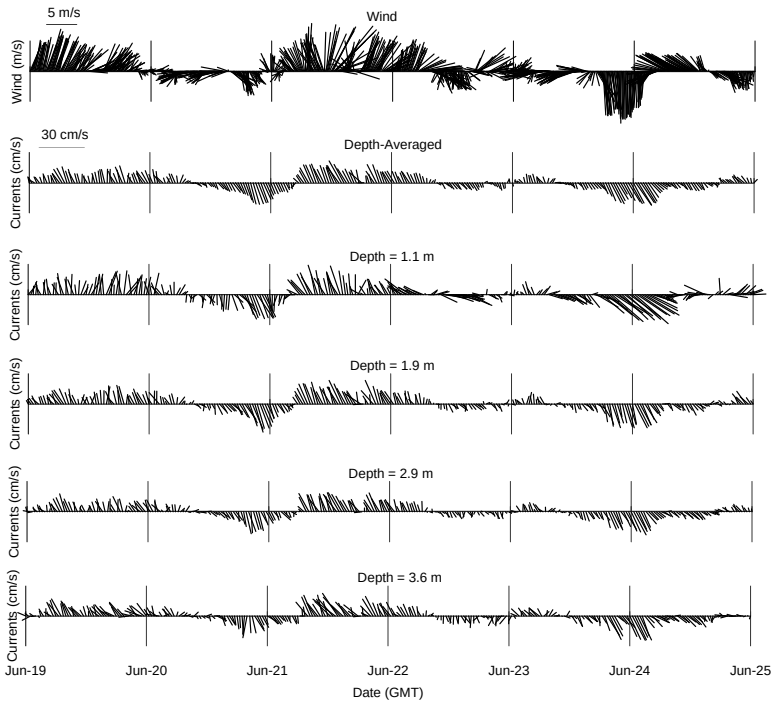

Figure 3.6 Feather plots of the local wind and currents at N5-06 mooring.

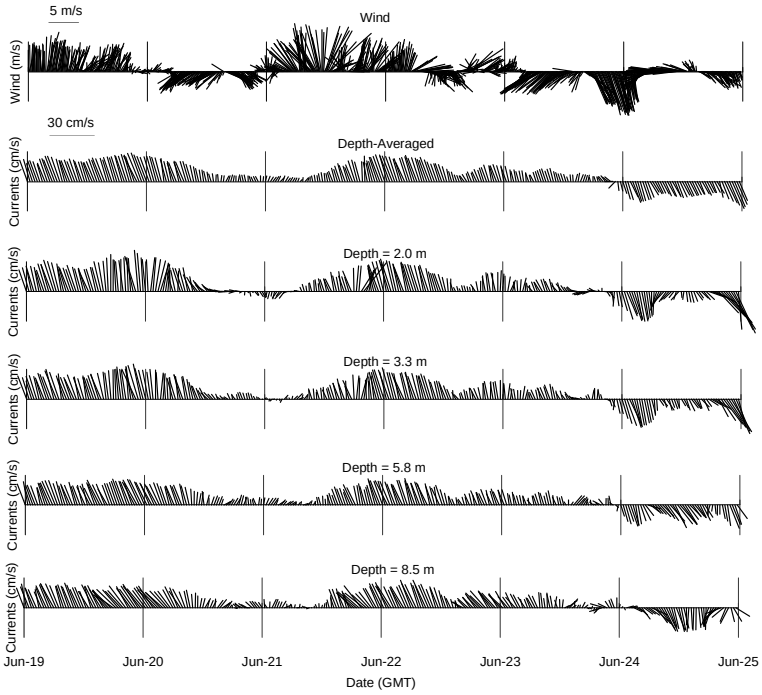

Figure 3.7 Feather plots of the local wind and currents at mooring S10-06.

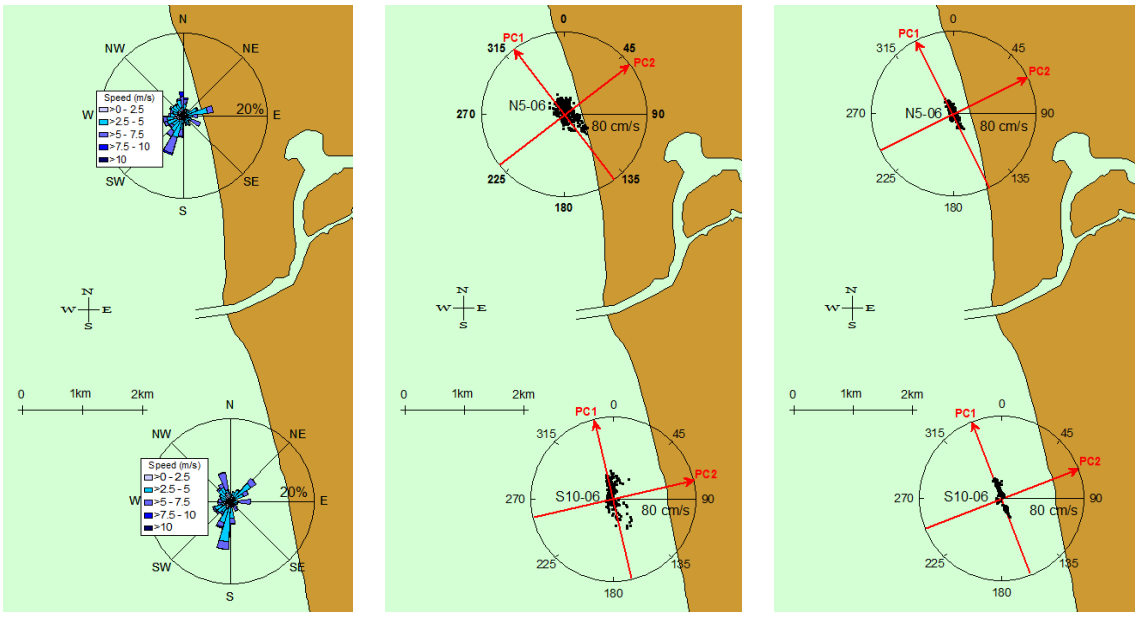

a) Wind histograms **b) Surface currents scatter diagrams** **c) Depth-averaged currents scatter diagrams**

Figure 3.8 Polar wind and currents diagrams at N5-06 and S10-06 from June 19 to 24, 2006.

The feather plots of mooring N5-06 (Figure 3.6) show the wind was mostly to NNE and NE on June 19, and the surface currents were also predominantly to the N until the end of the day. On June 20, the wind reversed and was blowing SW to SE. The currents reversed and followed the wind a few hours later around 12:00. On June 21, the wind was to the NNW to NE with a maximum speed of 9 m/s. The currents were initially to SSE but reversed direction to NNW after 6:00. On June 22, the wind was initially to NNE, reversed to SSE around 7:00, then changed direction to ENE around 15:00. The currents were to NNW before around 10:00 and to SSE after. On June 23, the wind was initially to WSW, then changed direction to the S with speeds greater than 8.5 m/s toward the end of the day. The currents were slow (<10 cm/s) until 16:30, then increased to ~30 cm/s to SE toward the end of the day. The wind reversed from S to NW early June 24 and then reversed again. The currents flowed to SE initially but slowed towards the end of the day.

The wind patterns at mooring S10-06 seen in Figure 3.7 were quite similar to N5-10. The currents were faster, probably because the currents were greater farther offshore at 10 m depth. On June 19, the wind was initially to the North then slowed and changed to NE after 15:00. The currents were Northerly and speed reached a maximum of 27.5

cm/s at the end of the day. On June 20, the wind was mostly to SW until 16:00 and changed to SE afterwards. Currents were to the North. Strong currents continued from the previous day but their speed decreased later. On June 21, the wind varied between NW to NE. Speed reached a maximum of 9.5 m/s around 12:40, resulting in strong currents (~25 cm/s) to the North at the end of the day. On June 22 and 23, the wind reversed several times and the currents were mostly to the North. On June 24, the wind blew strongly (~ 6 m/s) to SSE at the beginning of the day, and then slowed and blew to SE. Current directions followed the wind. Currents were strong (>25 cm/s) initially and at the end of the day.

A principal component analysis (PCA) was performed on current data to determine the variability of the current components. It is a usual technique in oceanography that transforms a number of correlated variables (current speeds and directions) into a number of uncorrelated variables (principal axes). The principal axes of the currents (the axes that maximize and minimize the kinetic energy, or variance of the currents when projected onto them) were determined by computing the Eigenvectors of the current data covariance matrix. The axis that maximizes the energy is the first principal axis, and the component of the currents along this axis is the first principal component; the axis that minimizes the energy is the second principal axis, and the component of the currents along this axis is the second principal component. The first and second principal axes are orthogonal and are indicated on Figure 3.8 as PC1 and PC2.

Characteristics of the winds and currents at N5-06 and S10-06 are summarized in Table 3.2. Current speeds ranged from about 0.6 to 30.7 cm/s with average speeds from 7 to 12 cm/s. Speeds were slightly higher at the deeper (offshore) station. The depth-averaged and near-surface currents had strongly preferred directions along the first principal axes, which were alongshore. The second principal components were much weaker, and the surface currents were more onshore.

The S10-06 and N5-06 wind speeds were quite similar. The maximum speed at N5-06 (~9 m/s) was recorded on June 21, at 12:30, and 10 minutes earlier at S10-06. The most frequent wind direction (>10% of the time) was from SSW at N5-06 and from the South at S10-06. The next two most frequent winds at S10-06 blew from NE (<8% of the time) and NW (<7% of the time). The wind vectors were consistent with the interpolated

wind from the NOAA meteorological grid over the whole study region (Figure 3.1). The spatial variation of the wind over the study area was not substantial.

Table 3.2 Summary of ADCP and meteorology data for June 19 to 24, 2006.

	N5-06			S10-06		
	Surface Currents (1.1 m depth)	**Depth-Averaged Currents**	**Wind**	**Surface Currents (2.0 m depth)**	**Depth-Averaged Currents**	**Wind**
PC1 Direction	322°N (~NW)	333°N (~NNW)		347°N (~NNW)	339°N (~NNW)	
PC2 Direction	52°N (~NE)	63°N (~ENE)		77°N (~ENE)	69°N (~ENE)	
Current Speed (cm/s)	0.9 – 29.3	1.7 – 18.2		0.6 – 30.7	1.9 – 20.3	
Current Speed Average (cm/s)	9.9	6.6		12.0	10.2	
Maximum Surface Current Speed (cm/s)	29.3 (at 1.1 m)			30.7 (at 2.0 m)		
Maximum Bottom Current Speed (cm/s)	15.4 (at 3.6 m)			17.0 (at 8.5 m)		
Wind Speed (m/s)			0 – 9.6			0 – 9.6
Wind Speed Average (m/s)			3.6			3.6
Predominant Wind Direction (>10%)			~SSW			~S
Next Most Frequent Wind Direction (<8%)			~E			~NE & ~NW

Four drifters were released simultaneously in two phases. The first, on June 20, 2006 at 1355 GMT, were retrieved on June 21, 2006 at 1255 GMT. The second drifters were released on June 21, 2006 at 1359 GMT and retrieved on June 21, 2006 at 20:59 GMT. The drifters recorded coordinates and speed at 30 minutes intervals, as shown in Figure 3.9. In the first phase, the trajectories showed the prevailing currents to the NW, and in the second phase, to the N. The maximum speed was 39 cm/s. In the second phase, some drifters reached the shore in about 7 hours. The ADCP showed smaller currents at this time (about 25 cm/s) that can be because the drifters recorded currents 3km farther offshore from N5-06 location and the currents in deeper areas were greater.

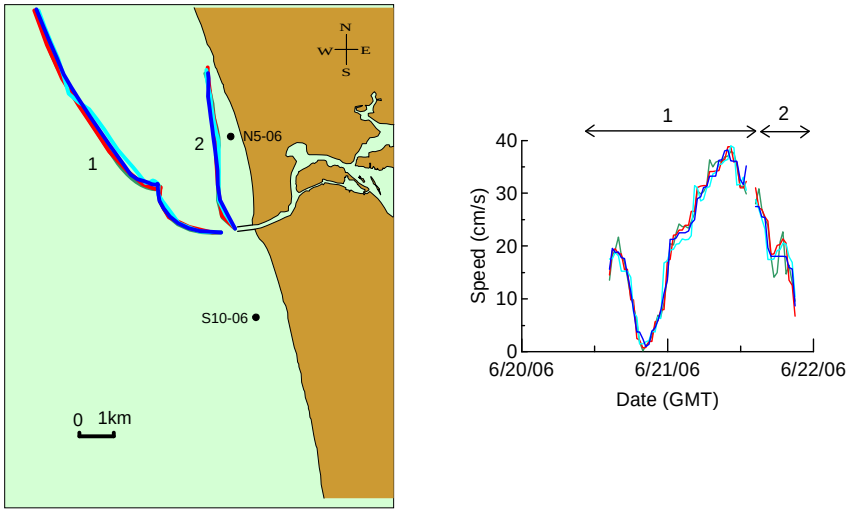

a) Track **b) Speeds**

Figure 3.9 Drifters on June 20 and 21, 2006.

To investigate possible relationships between wind and currents, the 3-hour averaged longshore and onshore surface current and wind components at S10-06 and N5-06 are plotted in Figure 3.10. The onshore currents are generally less than 10 cm/s and are not strongly correlated with the onshore wind. A three-hour lag was observed between the three-hour averaged currents and wind. After the currents were shifted three hours back in time to compensate for this lag, the shifted longshore currents at S10-06 were somewhat correlated with the local wind (r^2=0.50). The shifted nearshore longshore currents (N5-06) showed higher correlation with the wind (r^2=0.62). Longshore currents are less variable than the wind and the high frequency fluctuations in longshore wind are not reflected in the longshore currents.

Figure 3.10 suggests that longshore winds that are greater than about 3 m/s and blow for more than three hours result in currents greater than about 10 cm/s. So the longshore wind speed and duration are both important factors in inducing longshore currents, but, when the local winds are slow and brief, the currents are driven by the large-scale lake circulation. This is consistent with the hydrodynamic simulations that will be discussed in Chapter 5, which shows that when local winds are slow (< 3 m/s), lake circulation drives the local currents through the boundary conditions.

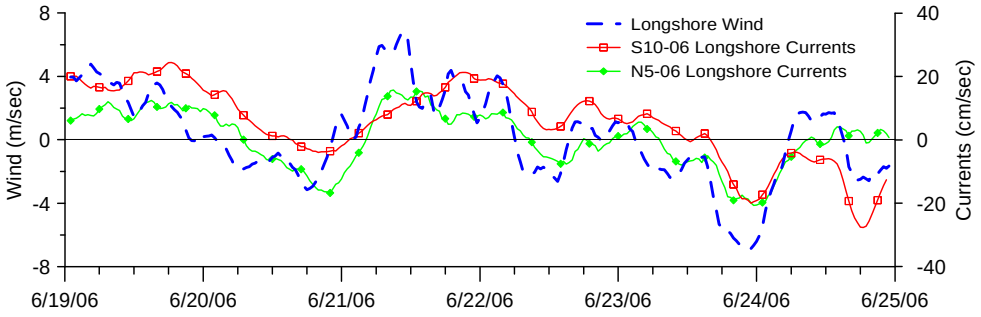

a) Longshore surface current and wind speed

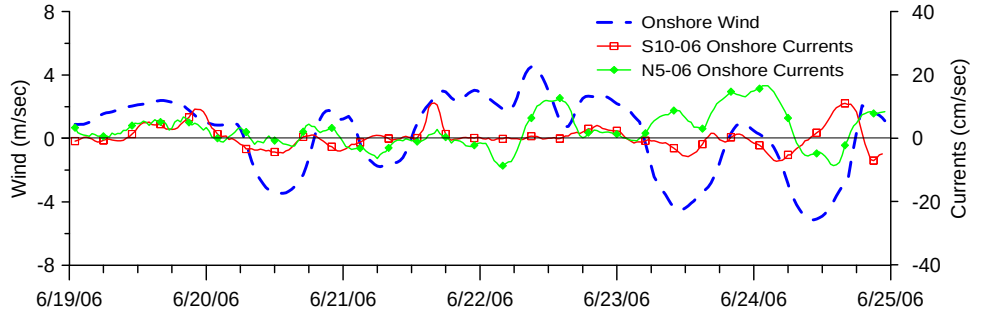

b) Onshore surface current and wind speed

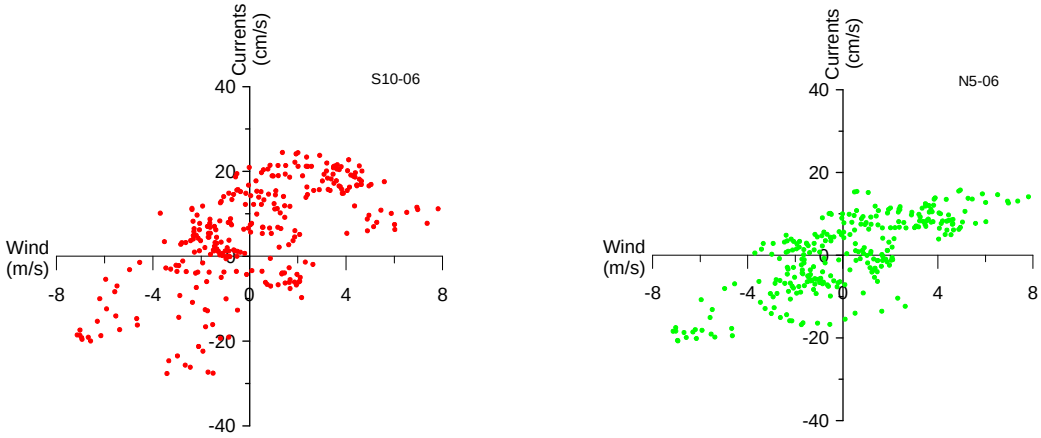

c) Longshore current-wind scatter

Figure 3.10 Three-hour averaged longshore and onshore surface current and wind speed, June 19 to 24, 2006.

3.3.1.2 Plume Observations

Plume observations for Series 1 included wind and current measurement, CTD surveys, and SF6 tracer experiments that are described in the following.

a) Wind and Currents

The wind, current, and river speeds are summarized in Table 3.3 for each period when aerial photographs of the plume were available on June 19, 20, 22, and 23, 2006. Current and wind vectors (red and yellow respectively) are overlaid on the images.

Table 3.3 Summary of wind, river, currents and plume condition for the aerial photographs, June 2006.

Date	6/19/06	6/20/06	6/20/06	6/22/06	6/22/06	6/23/06
Time (GMT)	21:32	15:17	21:03	14:02	21:10	21:42
Wind *						
Speed (m/s)	2.8	3.4	3.2	2.8	2.8	5.7
Direction (deg)	199	54	309	322	235	334
Surface Currents *						
Speed (cm/s)	23.2	4.4	3.1	5.4	10.9	9.4
Direction (deg)	356	276	172	348	357	162
Surface Longshore Currents Speed (cm/s) *	22.8	1.6	-3.1	5.4	10.7	-9.3
River Velocity (cm/s) **	7.9	7.9	7.9	9.5	9.5	10.0
Lake Temp. (°C)	18.0 (Satellite)	18.0 (CTD)	18.0 (CTD)	18.6 (CTD)	18.6 (CTD)	18.2 (Satellite)
River Temp. (°C)	22.2 (Satellite)	23.6 (CTD)	23.6 (CTD)	23.3 (CTD)	23.3 (CTD)	22.2 (Satellite)
Photo Current: 5 cm/s Wind: 5 m/s	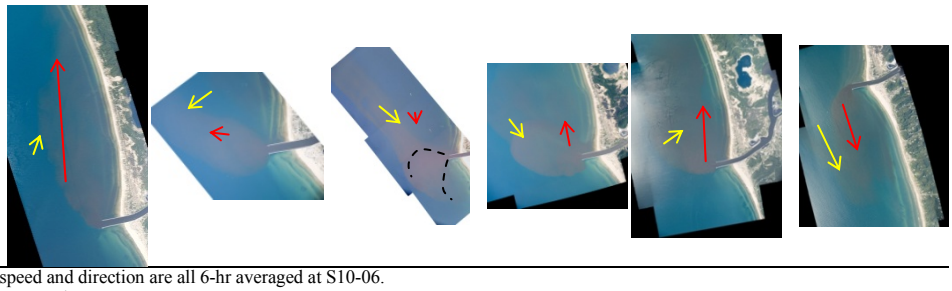					

* wind and lake currents speed and direction are all 6-hr averaged at S10-06.
** river velocity is daily-averaged.

The plume shape is dependent on the surface currents, which are influenced by the local wind and the lake circulation as previously discussed. Since wind and currents change significantly over time, they were averaged over 6 hours. River speeds were computed from USGS daily discharge records at Grand Rapids (http://waterdata.usgs.gov/nwis). The daily averaged discharge was corrected for the effect of the downstream watershed

up to the river outlet by multiplying it by a catchment area correction factor of 1.156 (determined by GLERL).

The surface lake temperature ranged from 18.0 to 18.6°C, and river temperature ranged from 22.2 to 23.6°C, i.e. the river was about 4 to 5°C warmer than the lake. The minimum and maximum temperature differences were 4.0 and 5.6°C on June 23 and 20, 2006 respectively. Further analyses of the plume dynamics will be presented in Chapter 4.

b) CTD Survey

Four CTD survey tracks on June 20 and 22, 2006 are shown in Figures 3.11 and 3.12.

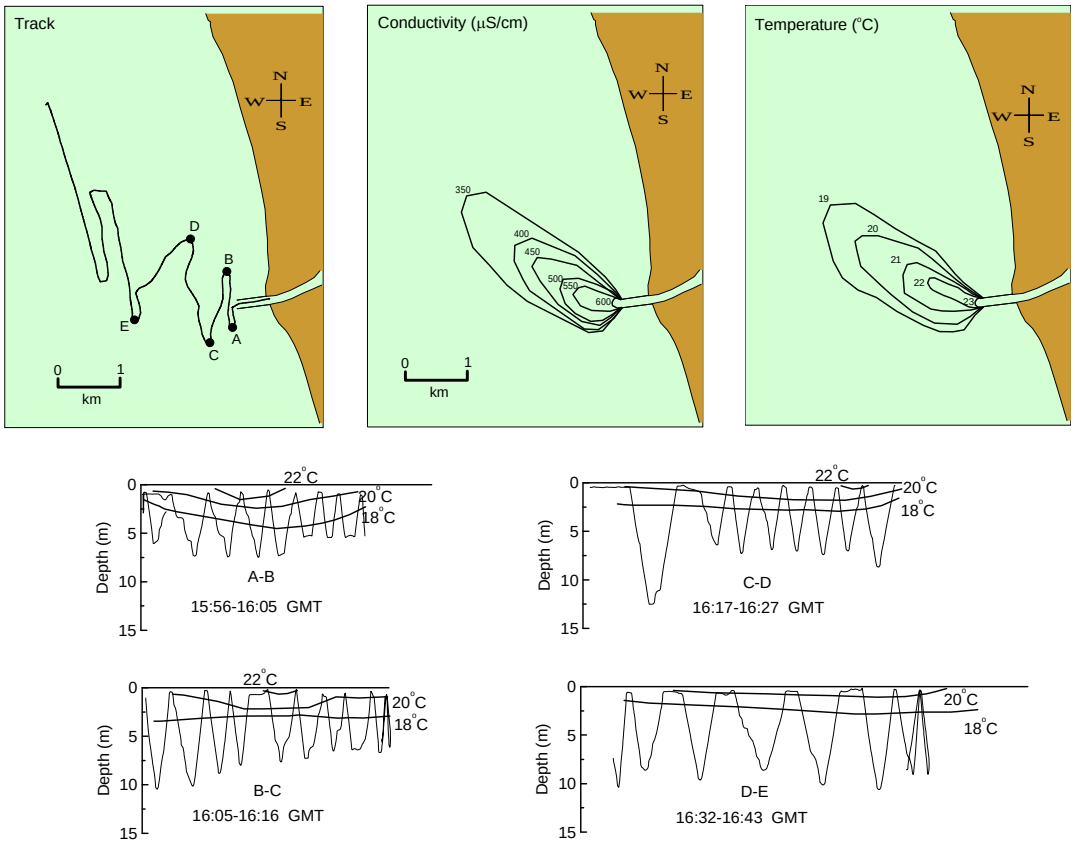

Figure 3.11 CTD survey map and selected temperature transects on June 20, 2006.

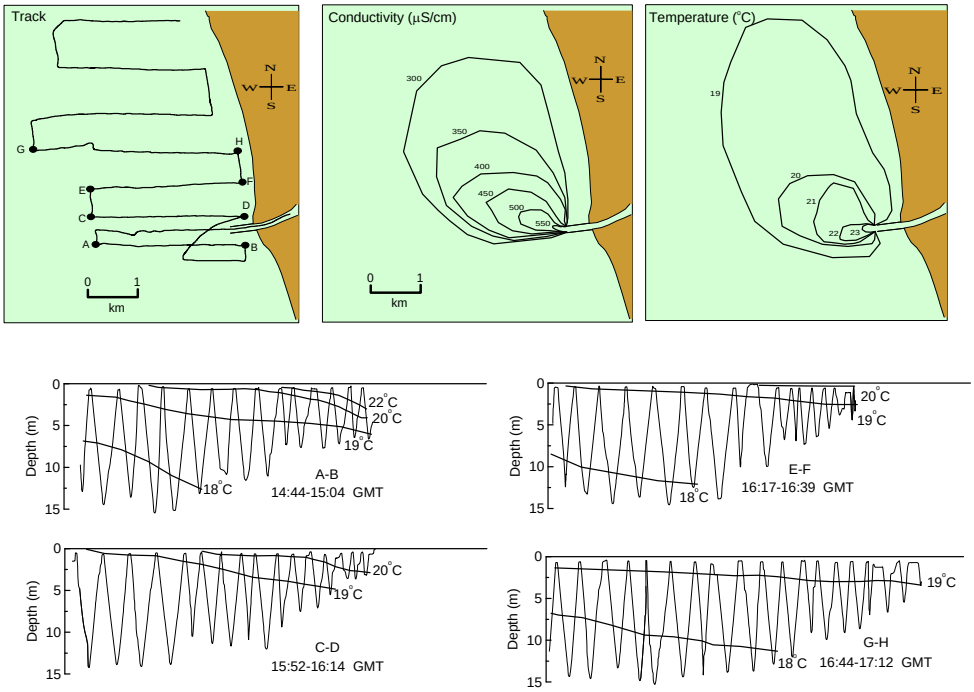

Figure 3.12 CTD survey map and selected temperature transects on June 22, 2006.

The towyoed transects show vertical temperature profiles; only temperature is shown as the conductivity profiles have a similar pattern. The beginning and end points for each transect are noted by letters on the CTD tracks. Profiles closer to the mouth and at the surface always show higher conductivity and temperature due to the higher salinity and temperature of the river. The surface conductivity and temperature contours are shown to indicate the surface extent (width and length) of the plume.

c) Tracer

The SF6 tracer observations conducted on June 21, 22, and 23, 2006, are shown in Figure 3.13. The SF6 release began on June 21, 2006 around 0900 GMT (0500 EDT) and continued for about 5 hours. The measured source concentration near the release point was 13,019 ppt at 1430 GMT. Sampling in the lake started on the next day, June 22 and continued until June 23. With the river average speed of 8.5 cm/s, the tracer would take about one day to reach the mouth from the release point.

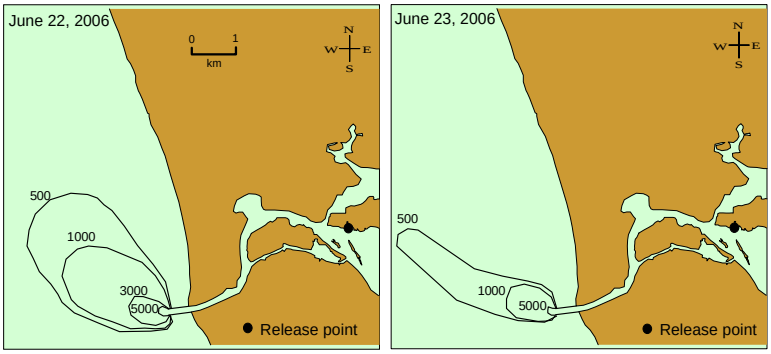

Figure 3.13 SF6 concentrations in ppt on June 21, 22, and 23, 2006.

3.3.1.3 Discussion

The plumes shown in Table 3.3 are quite variable. In the following, dilutions were calculated from the river and lake conductivities. These values were assumed to be the source and background conductivity (or tracer concentration) values to compute the minimum physical dilution from:

$$S = (C_0 - C_b)/(C - C_b) \tag{3-1}$$

where C_0 is the source conductivity (~625 µS/cm), C_b is the background lake conductivity (~285 µS/cm) and C is the conductivity at the point of interest. The surface currents and wind at S10-06 showed more relevance to the plume movement compared to N5-06 so only wind and currents from S10-06 are referred to each day. The results are discussed below.

On **June 19**, the wind was mostly from the S and SW with an average speed of about 7.5 m/s before 21:00, then slowed (<3 m/s). The currents were mostly to the N to NE. The currents were strong with an average of about 25 cm/s to the N. This caused the plume to attach to the northern coast at 21:32.

On **June 20**, the wind was slow (<2.5 m/s) until 4:00, then mostly blew from the E and NE with an average speed of about 7 m/s until about 15:00, then from NW with an average of about 6 m/s until 21:00, and finally from the S. The currents were to the N initially and fairly strong (about 25 cm/s), then calmed down until around 12:00, and

stayed slow (< 5 cm/s) until 24:00. The plume at 15:17 was narrow and extended directly into the lake in a slightly Northerly direction due to the preceding offshore wind. At 21:03, the plume was wider indicating an overlap of the new plume (south of the pier with a sharp edge) on the old one (north of the pier) due to the reversal in wind direction (offshore to onshore). The spreading was accompanied by a rapid vertical thinning of the plume from 3.5 m at the mouth to less than 1.5 m at a distance of 100 m (profile AB, Figure 3.11), and rapid increase of the plume width (see also Chapter 4). The average width was almost 1.2 km (10 times the channel width) at a distance of 1 km from the mouth. The minimum dilutions occurred on the plume centerline and were 2, 5 and 10 at distances of 1.5 km, 3.0 km, and 3.8 km from the mouth.

On **June 21**, the wind started from the E with a speed of around 4 m/s, slowly changed direction and increased speed until around 12:00 that was from the S with a speed of around 12 m/s, then slowly changed direction and decreased speed until 24:00 that was from the SW with a speed of about 10 m/s. The currents were slow (<5 cm/s) until about 6:00, then flowed to the N and their speed increased to about 25 cm/s around 24:00. CTD surveys were not carried out on this day, and the tracer had not reached the river mouth. SF6 release began on June 21, 2006 around 9:00 (5:00 EDT) and continued for about 5 hours.

On **June 22**, the wind was mostly from the S until around 5:00 with an average speed of about 6 m/s, blew from SE and ESE until around 7:00 with an average speed of 8 m/s, then was from the WNW and NW until 14:00 with an average speed of 7 m/s, thereafter was mostly from the SW with an average speed of 8 m/s. The currents were mostly to NNW and the N. They were fairly strong initially (~25 cm/s), then gradually calmed and remained slow between 14:00 to 18:00, thereafter increased to about 15 cm/s around 24:00. The plume at 14:02 spread radially and was slightly to the north; the new plume with a sharp edge around the mouth is seen superimposed on the diffuse older plume to the north. The plume at 21:10 is deflected more strongly to the N impacting the northern shoreline due to the onshore wind. The plume thickness was about 2.5 m at the mouth, and decreased rapidly to about 0.8 m in 1 km from the mouth, where the plume width was almost 2 km. The minimum dilutions of 2, 5 and 10 occurred at distances of 1.1 km, 2.5 km and 4.2 km from the mouth. These are closer to the mouth than on June

20. This is probably due to the fact that the current was more than three times faster than on June 20, resulting in enhanced near-field mixing. SF6 tracer sampling was conducted from 14:43 to 20:58. The minimum dilutions occurred at distances that were in agreement with the CTD results.

On **June 23**, the last day of the Series 1 experiments, the wind was variable from ENE and the S until about 5:00, then was mostly blowing from NE with an average speed of 8 cm/s until about 14:00, thereafter blew from the N and NNW with a higher average speed of 10 cm/s. The currents were to the N with an average speed was about 10 cm/s until 16:30, then slowed until about 20:00, then flowed to the S and SE and the speed increased to about 15 cm/s until 24:00. The fairly strong northerly wind and southerly currents resulted in a narrow southward plume parallel to the shore around 21:42. Tracer sampling started at 16:40 and ended at 21:40. The minimum dilutions of 2, 5 and 10 were at distances of 700 m, 1.5 and 4.1 km from the mouth, in agreement with the CTD results. The near-field dilutions (2 and 5) again occurred closer to the mouth than June 20 and 22, probably due to the strong currents and higher river velocity.

3.3.1.4 Summary

For the Series 1 tests, the wind was mostly from NW and NE with an average speed ranging approximately from 6 to 10 m/s on June 20, 22 (7:00-14:00) and 23. It was from the S and SW on June 19 and 22 (0:00-7:00 and 14:00-24:00) with an average speed of about 8 m/s. The currents were mostly to the N and NNW. On June 19 and 20 (0:00-12:00), the average speeds were 22 cm/s, then currents calmed until June 21, 5:00, speeds increased again and reached 28 cm/s on June 22, 0:00, then decreased until the end of June 24. The currents speed ranged from about 0.6 to 30.7 cm/s, with average speeds from 7 to 12 cm/s.

The first principal components of the surface currents were approximately to the N and NNW (alongshore) for all days of Series 1 experiments (June 19, 20, 22 and 23). The 3-hour averaged current component alongshore was less than 25 cm/s. The onshore component of the currents was weaker and more variable, and was generally less than 10 cm/s. When the longshore local wind was slow (<3 m/s) and brief (less than three hours), lake large-scale circulation dominated the local currents. Longshore surface currents

followed the local wind direction mostly when the local wind was strong (>3 m/s) and blew for at least three hours. In those cases, the plume elongated following the current direction alongshore.

The plumes were attached to (extended along) the coasts on June 19 and 23, because of the strong longshore currents (> 10 cm/s). On June 20 (at 15:17), the offshore wind and currents spread the plume offshore. The plume on June 22 (at 21:10), indicates that the onshore wind can cause the plume to impact the shore (deflect back to the shoreline) instead of attaching or moving parallel to the shore, which implies that onshore wind is an important factor in plume behavior and beach water quality. On June 20 (at 21:03) and 22 (at 14:02), the currents were slower, and the onshore wind forms a plume with a sharp edge at the mouth overlapping with the old diffuse plume.

The surface lake temperatures near the river mouth ranged from 18.0 to 18.6°C, and the river temperature from 22.2 to 23.6°C. The temperature differences ranged from 4.0 to 5.6°C. The plume thickness at the mouth was about 3.3 m (see further discussion in Chapter 4) and this decreased rapidly to less than half (1.5 m), within 100 m from the mouth due to rapid lateral spreading.

Minimum dilutions increased with distance from the mouth to about 10 within 4.2 km. The distance to reach a dilution of 2 ranged from 700 m to 1.5 km from the mouth. Dilutions close to the mouth were higher in June 20 than 22, probably due to greater near field mixing because of stronger lake currents.

3.3.2 Series 2: August 2006

The Series 2 experiments were conducted from August 8 to 11, 2006. The wind and currents observations, their effect on the plume, CTD, and tracer experiment results are discussed below.

3.3.2.1 Current and Wind Observations

The wind and currents for the five day period from August 7 to 11, 2006 at mooring S10-06 are shown in Figure 3.14. These are feather plots of wind, depth-averaged currents and currents in selected bins at depths of 2.0, 3.3, 5.8, and 8.5 m. Polar wind histogram and scatter diagrams of the surface and depth-averaged currents for this period

are also shown in Figure 3.15. The principal axes of the currents are indicated on the scatter plots.

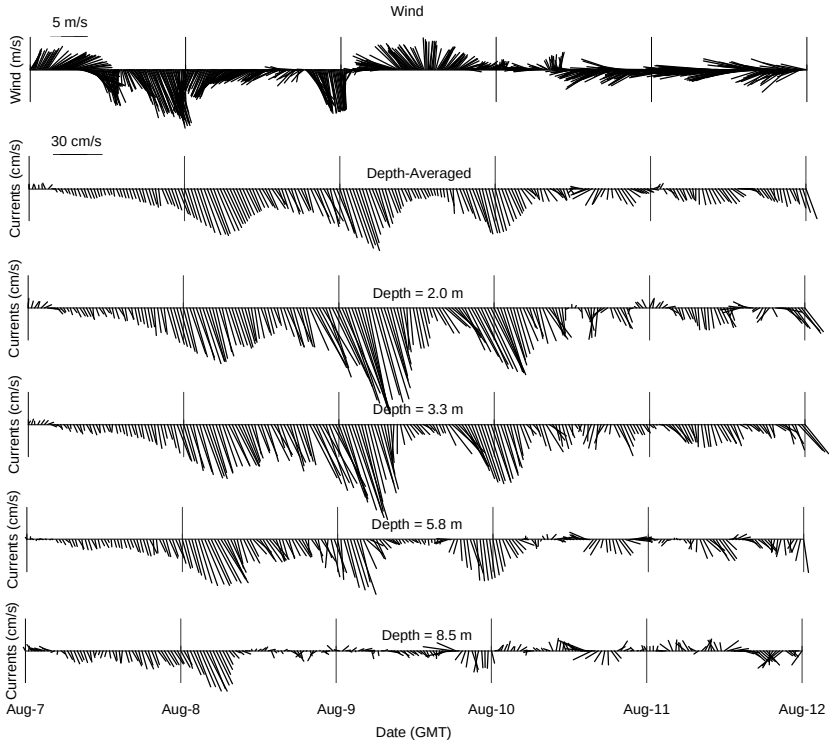

Figure 3.14 Feather plots of the wind and currents at mooring S10-06, from August 7 to 11, 2006.

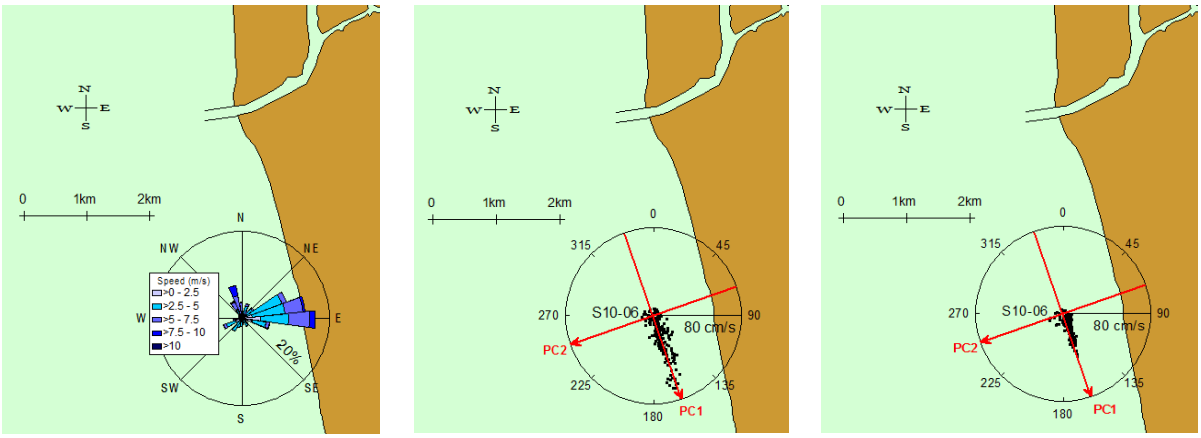

a) Wind histograms **b) Surface currents scatter diagrams** **c) Depth-averaged currents scatter diagrams**

Figure 3.15 Polar wind and currents diagrams at S10-06 from August 7 to 11, 2006.

For this period, the currents flowed predominantly to the south, and the speeds were high, up to 68 cm/s. The predominant winds were offshore with speeds reaching to 9.0 m/s. The wind and current data at S10-06 are summarized in Table 3.4.

Table 3.4 Summary of ADCP and meteorology data at S10-06 for August 7 to 11, 2006.

	Surface Currents (2.0 m depth)	Depth-Averaged Currents	Wind
PC1 Direction	161°N (~SSE)	162°N (~SSE)	
PC2 Direction	251°N (~WSW)	252°N (~WSW)	
Current Speed (cm/s)	1.6 – 68.1	2.4 – 40.4	
Current Speed Average (cm/s)	21.0	13.6	
Maximum Surface Current Speed (cm/s)	68.1 (at 2.0 m)		
Maximum Bottom Current Speed (cm/s)	25.2 (at 8.5 m)		
Wind Speed (m/s)			0.3 – 9.3
Wind Speed Average (m/s)			4.3
Predominant Wind Direction (>18%)			~E
Next Most Frequent Wind Direction (<8%)			~NNW

Surface current speeds ranged from 1.6 to 68.1 cm/s with an average of 21 cm/s. The depth-averaged and near-surface currents had strongly preferred directions along the first principal axes. The first principal axis direction was alongshore, and the second principal components were much weaker. The depth-averaged currents also had a strongly preferred direction along their PC1 and were normally less than 50 cm/s. They showed only a 1° clockwise shift from the surface currents. The second principal current component was very small (generally less than 10 cm/s). Wind speeds varied from 0.3 to 9.3 m/s with an average around 4.3 m/s. The predominant winds blew from the E to NE more than 18% of the time. The next most frequent wind was from the NNW that occurred less than 8% of the time.

Three surface drifters were released on August 8, 2006 at 14:52 and retrieved on August 9, 2006 at 01:52. The drifter tracks and their speeds are shown in Figure 3.16. They traveled south in accordance with the strong southerly currents (Figure 3.14), and passed by the S10-06 ADCP at 16:30 on August 8. At that time, all of the drifters showed SSE (154°) surface currents at an average speed of 29 cm/s and the wind was from the N.

However, the ADCP current speed at 2.0 m depth was 41.4 cm/s, almost 40% higher. This may be because the drifters measured currents closer to the surface that are generally faster and also because the ADCP record from bins less than 2.0 m deep are not reliable due to surface effects. The maximum drifter speed was 37 cm/s. The drifters grounded nearshore in less than 5 hours.

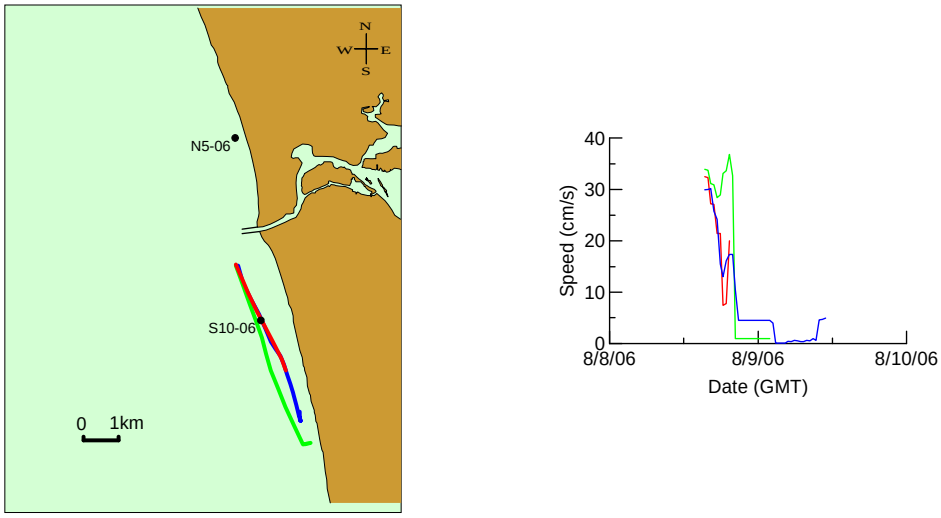

a) Track **b) Speeds**

Figure 3.16 Drifters on August 8 and 9, 2006.

To investigate the relationship between wind and currents, the 3-hour averaged longshore and onshore surface current and wind components at S10-06 are plotted in Figure 3.17. N5-06 was trapped in sediment and not recording.

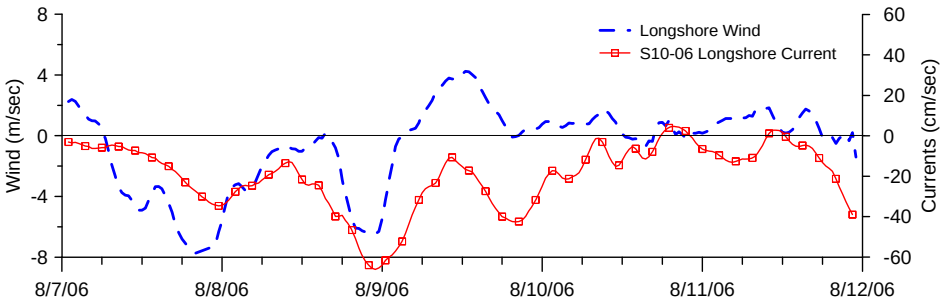

a) Longshore surface current and wind speed

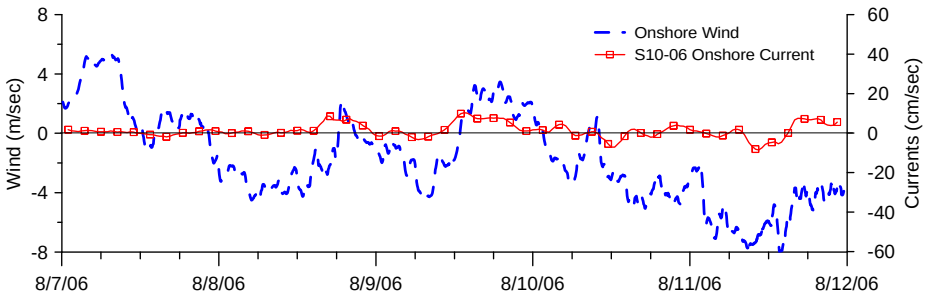

b) Onshore surface current and wind speed

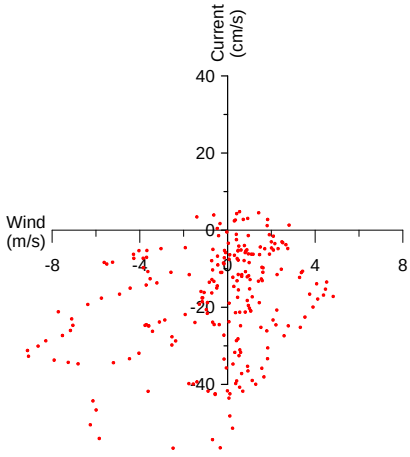

c) Longshore surface current-wind scatter

Figure 3.17 Three-hour average longshore and onshore surface current and wind speed from August 7 to 11, 2006.

The longshore current speed was less than 65 cm/s. The onshore currents were much weaker, smaller than 15 cm/s. Generally the change in longshore current direction is preceded by a shift in the wind with a three-hour lag similar to that observed in Series

1. The shifted longshore currents are only weakly correlated with the wind (r^2 =0.20). The longshore local wind speed and duration are both important in inducing longshore currents, but when the local winds are slow and transient, lake large-scale circulations drive the currents through boundary conditions.

3.3.2.2 Plume Observations

Plume observations for Series 2 included wind and currents measurement, CTD survey, and SF6 tracer experiments as described below.

a) Wind and Currents

Current, wind, and plume conditions on August 8, 9, 10, and 11, 2006 corresponding to the available aerial photographs are summarized in Tables 3.5 and 3.6. The currents and wind vectors (red and yellow) are overlain on the images. The surface lake temperature varied from 20.3 to 23.9°C, and river temperature from 24.2 to 26.5°C, i.e. the average river temperature was 3~4°C warmer than the lake. The minimum and maximum temperature differences were 2.6 and 7°C on August 8 and 11.

Table 3.5 Summary of wind, river, currents and plume condition for August 8, 9 and 10, 2006.

Date	8/8/06	8/8/06	8/9/06	8/9/06	8/10/06
Time (GMT)	13:50	22:30	13:22	21:06	13:16
Wind *					
Speed (m/s)	3.6	4.8	4.5	2.9	2.4
Direction (deg)	62	347	134	234	108
Surface Currents*					
Speed (cm/s)	18.4	50.1	17.3	38.1	9.1
Direction (deg)	162	158	154	154	187
Surface Longshore Currents Speed (cm/s) *	-18.4	-49.8	-17.0	-37.4	-8.4
River Velocity (cm/s) **	9.3	9.3	8.5	8.5	7.8
Lake Temp. (°C)	23.9 (CTD)	23.9 (CTD)	22.7 (CTD)	22.7 (CTD)	23.2 (CTD)
River Temp. (°C)	26.5 (CTD)	26.5 (CTD)	26.1 (CTD)	26.1 (CTD)	26.2 (CTD)
Photo Current: 5 cm/s Wind: 5 m/s					

* wind and lake currents speed and direction are all 6-hr averaged.
** river velocity is daily-averaged.

Table 3.6 Summary of wind, river, currents and plume condition for August 10 and 11, 2006.

Date	8/10/06	8/10/06	8/11/06	8/11/06
Time (GMT)	17:16	23:14	12:42	15:40
Wind *				
Speed (m/s)	3.8	4.1	6.9	6.6
Direction (deg)	72	77	85	84
Surface Currents *				
Speed (cm/s)	10.2	4.6	8.9	7.7
Direction (deg)	180	17	211	244
Surface Longshore Currents Speed (cm/s) *	-9.9	3.9	-6.2	-1.5
River Velocity (cm/s) **	7.8	7.8	7.6	7.6
Lake Temp. (°C)	23.3 (CTD)	23.3 (CTD)	18.0 (CTD)	18.0 (CTD)
River Temp. (°C)	26.2 (CTD)	26.2 (CTD)	25.0 (CTD)	25.0 (CTD)
Photo Current: 5 cm/s Wind: 5 m/s				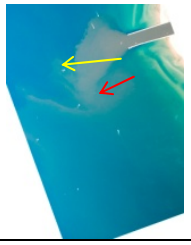

* wind and lake currents speed and direction are all 6-hr averaged.
** river velocity is daily-averaged.

b) CTD Survey

The CTD survey tracks on August 8 to 11, 2006 are shown in Figures 3.18 to 3.21. The beginning and end points for each transect are noted by letters on the CTD track. The towyoed transects show vertical temperature profiles. Profiles closer to the mouth and at the surface show higher conductivity and temperature due to the higher salinity and temperature of the river water. The conductivity vertical profiles were similar to the temperature so only temperature contours are shown. Surface conductivity and temperature contours are shown to indicate the width and length of the plume.

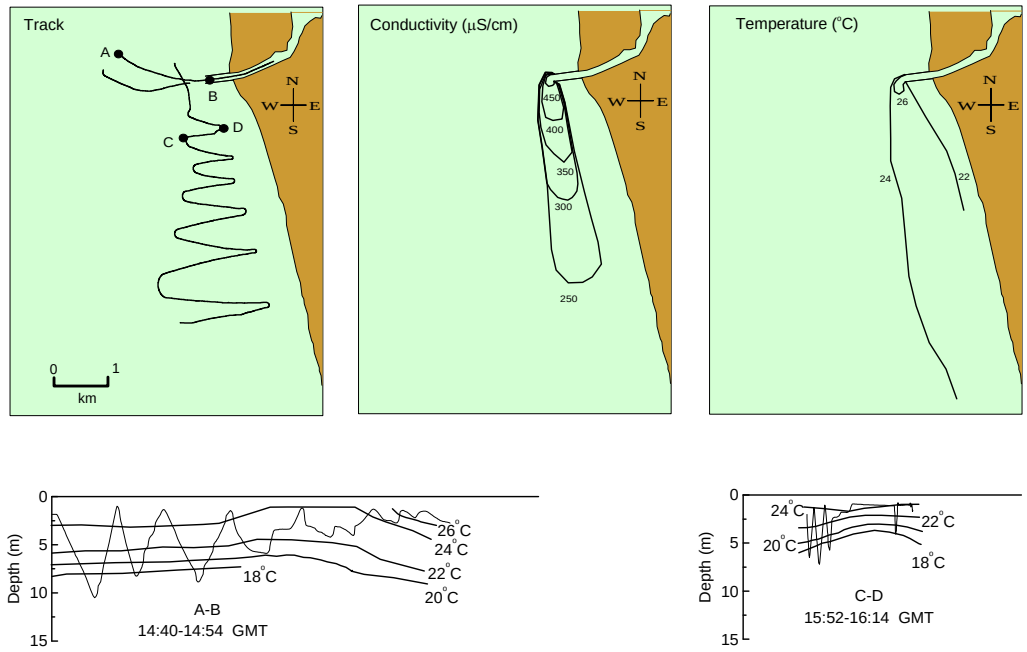

Figure 3.18 CTD survey map and the selected temperature transects on August 8, 2006.

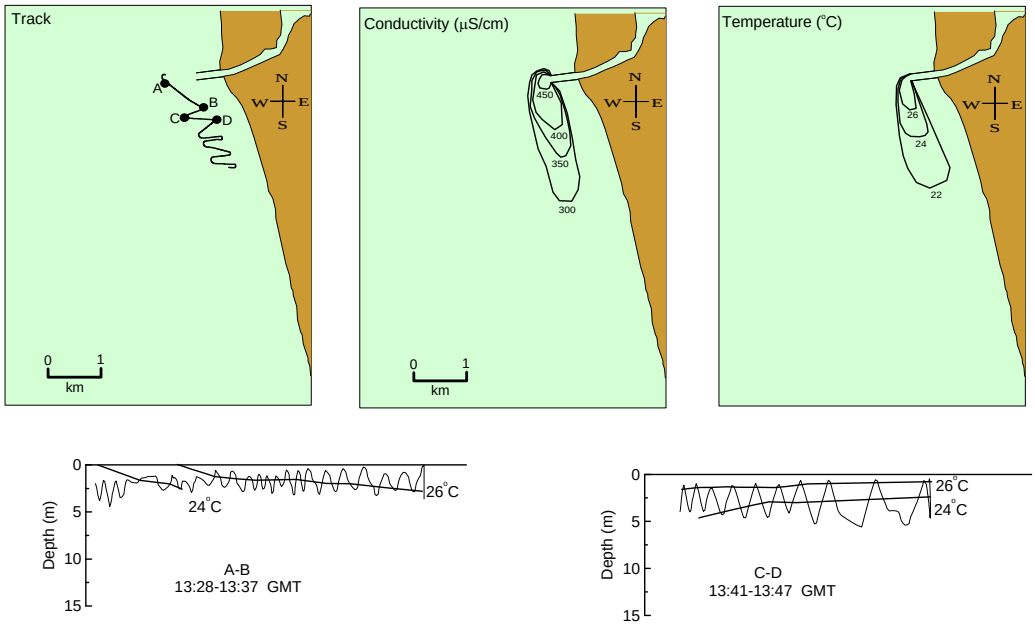

Figure 3.19 CTD survey map and the selected temperature transects on August 9, 2006.

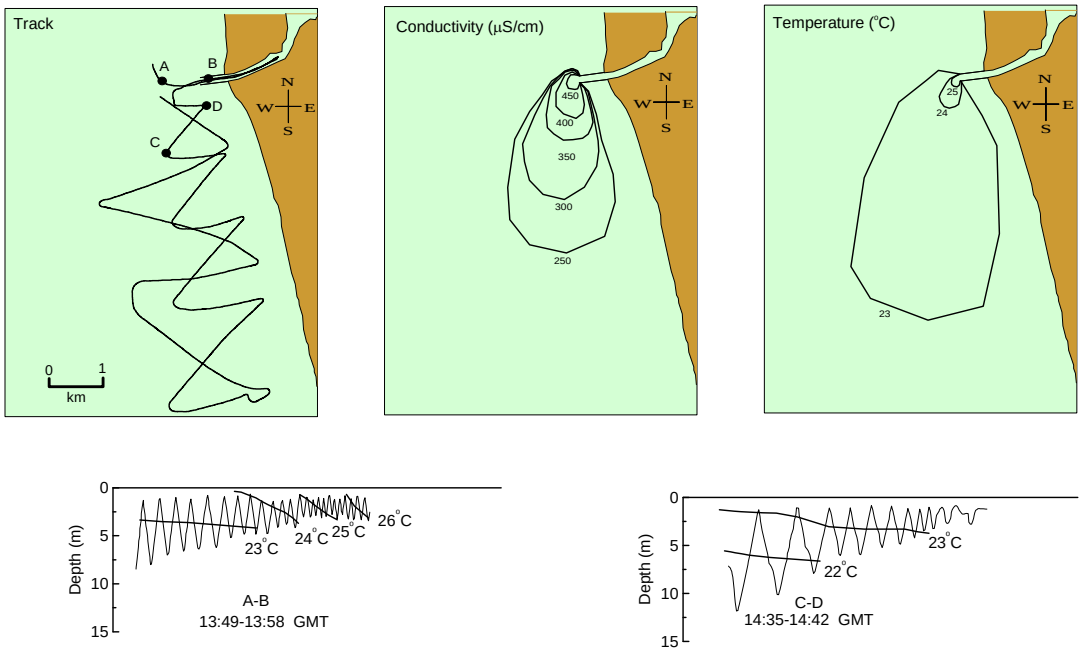

Figure 3.20 CTD survey map and the selected temperature transects on August 10, 2006.

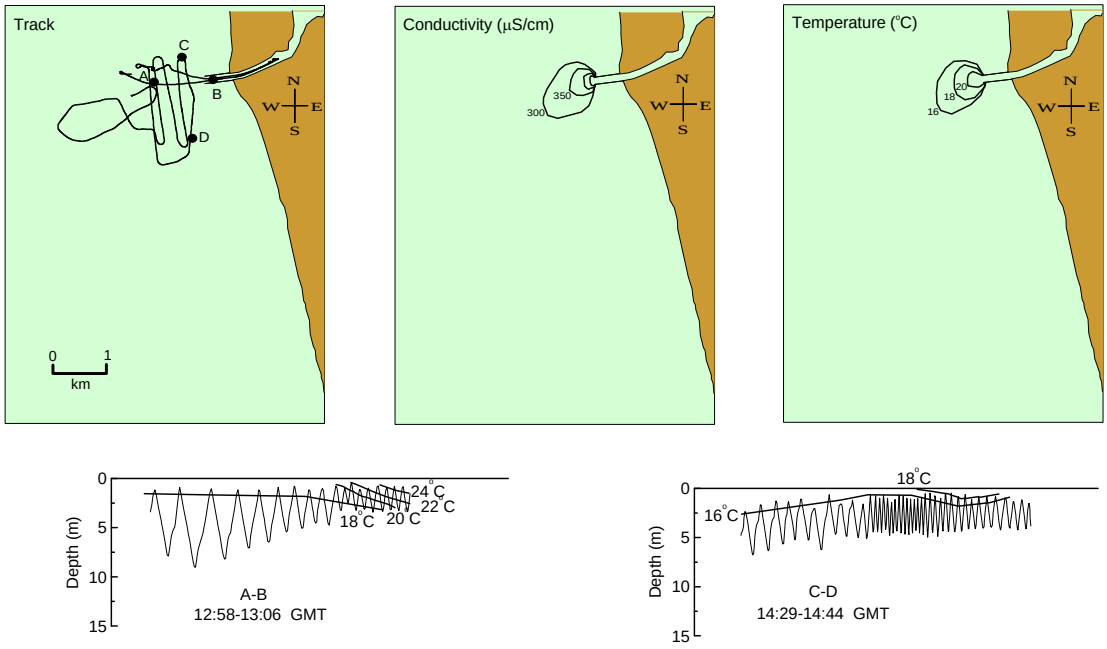

Figure 3.21 CTD survey map and the selected temperature transects on August 11, 2006.

c) Tracer

The SF6 tracer observations conducted on August 8, 9, and 10 are shown in Figure 3.22. The release began on August 8, 2006, around 9:00 (5:00 EDT) and continued for about 5 hours. The source concentration was 2905 ppt, 3 km downstream from the release point at 16:05. Sampling was conducted from 16:06 to 18:42 on August 8, from 18:21 to 20:08 on August 9, and from 17:35 to 20:41 on the last day, August 10.

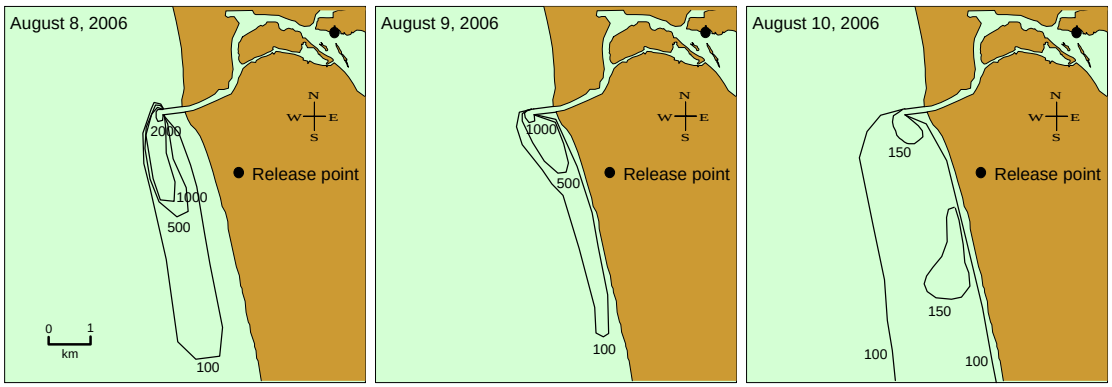

Figure 3.22 SF6 concentrations in ppt on August 8, 9, and 10, 2006.

3.3.2.3 Discussion

The results of the Series 2 experiment from August 8 to 11, 2006 are discussed below.

On **August 8**, the wind was initially from the N with a speed of about 6 m/s. The speed decreased and direction changed gradually until about 18:30 (from NE), then changed direction again blowing from the N and the speed increased to about 6.5 m/s. The currents were consistently to SE. They were strong initially (28 cm/s), increased to 36 cm/s around 3:00, then slowed to 10 cm/s around 12:00, then increased significantly to 53 cm/s around 24:00. The plume at 13:50 and 22:30 moved to the south rapidly after it exited the mouth and was attached to the shore. The plume at 22:30 is narrower attached to the shore because of much stronger currents (about three times). It extended along the south shore for more than 6 km due to the strong currents. The plume thickness decreased rapidly from about 4.0 m to less than 2.5 m after entering the lake. The width was almost

600 m, 1 km from the mouth. This yields minimum dilutions of 2, 5 and 10 at distances of 1.3, 2.2 and 4 km from the mouth. Sampling continued until 18:45. Minimum dilution of 2, 5 and 10 occurred at distances of 1.3, 2.4 and 4.2 km from the mouth, in agreement with to the CTD results.

On **August 9**, the wind was strong (~6.2 m/s) and from the N from 0:00 to 0:30, was calm (< 1 m/s) from 0:30 to 3:00, gradually variable between the E and S (90-180°N) and the speed increased to approximately 5 m/s from 3:00 to 13:00, thereafter until 24:00, the speed decreased to about 1 m/s and the direction slowly changed between the S and W (180-270°N). The currents remained to SSW, and were strong at the begining (53 cm/s), increased to 68 cm/s until 3:00, then decreased significantly to 6 cm/s around 12:00 due to the wind reversal, then again increased and peaked (45 cm/s) at 24:00. The plume at 13:22 and 21:06 was attached to the south shore. The thickness was about 3.5 m at the mouth. The plume width was almost 800 m at one km from the mouth. The minimum dilutions of 2, 5 and 10 computed from the CTD data occurred at 1.1, 2.2 and 2.5 km from the mouth, which were not significantly different from August 8. SF6 tracer sampling started at 18:21 and ended at 20:08. Minimum dilution of 2, 5 and 10 were at distances of 2.5, 3.5 and 4.5 km from the mouth. These dilutions were higher than the CTD results because the SF6 samples were taken at the end of the day when the currents were stronger. The current speeds ranged from 23 to 34 cm/s during SF6 sampling, faster than the speed range for the CTD sampling (6 to 23 cm/s).

On **August 10**, the wind was slow (<3 m/s) and mostly from the E until around 7:00; remained slow but from the SE and S during 7:00-9:00, thereafter it blew offshore (from ENE, E and ESE) with speeds reaching to 5.5 m/s. The currents were initially strong (44 cm/s) to SSE, then slowed to about 20 cm/s around 12:00 to the same direction, thereafter remained mostly to the S and SSE but current speeds were variable (between 0-20 cm/s). As a result, at 13:16, the Easterly or offshore wind (2.4 m/s) and Southerly currents (9.1 cm/s) moved the plume southwest. At 17:16, the stronger offshore wind (3.8 m/s) and Southerly currents (10.2 cm/s) moved the plume southwest but further offshore with diffuse boundaries. At 23:14, the offshore wind (4.1 m/s) and the slow currents (4.6 cm/s) created a plume with diffuse boundaries around the mouth. The

thickness of the plume was less than 3.5 m at the mouth. The plume width increased to 1.5 km at 1 km from the mouth. Minimum dilutions of 2, 5 and 10 were observed at distances of 0.9, 2.1 and 3.0 km from the mouth, similar to the previous days observations. SF6 samples were taken from 17:35 to 20:41. The maximum concentration (150 ppt) was observed at the mouth and about 3 km south of the pier. The SF6 dilutions were variable and were not useful on this day.

On **August 11**, the wind continued offshore (mostly from ESE, E and ENE) reaching high speeds (~9.0 m/s) around 13:45. The currents were mostly to the S and SSW. The current speeds were <9 cm/s until 7:00, then remained consistent (~12 m/s) until 12:00, then were small again (<9 cm/s) until 20:00, thereafter increased to about 20 m/s at 24:00. The slow current didn't affect the plume significantly between 12:40 and 15:40, however the offshore wind diffused the plume directly to the lake, not very far offshore (just about 1 km from the mouth). The thickness was about 2.5 m at the mouth. The maximum plume width occured 500 m from the mouth between these hours. The river temperature decreased more than 2.5 degrees to 25°C from the previous day, but the lake temperature dropped to 18°C (Figure 3.21). The sharp drop in lake temperature could be due to wind-induced upwelling (Beletsky and Schwab, 2001), because the offshore wind was fairly strong (~9 m/s) around 13:45 GMT. The minimum dilutions of 2, 5 and 10 occurred at 0.4, 1 and 2.5 km from the mouth. The dilutions of 2 and 5 occurred the closest to the mouth among all days in Series 2 due to the slow currents.

3.3.2.4 Summary

During Series 1 experiments (August 8, 9, 10 and 11), the strongest winds from the N and NNW occurred around the beginning of August 8 and the end of August 9. The other strong and prevailing wind was from the East (offshore) that occurred most of the August 8, 10 and all August 11. The average wind speed was around 4.3 m/s and the maximum was 9.3 m/s. The currents were mainly to the S and SSE (first principal component).

Two strong Southerly currents (36 and 68 cm/s) occurred at the beginning of August 8 and 9 (around 3:00) which were associated with the preceding strong Northerly winds. These include the highest record of the longshore current component (68 cm/s). A

strong current (44 cm/s) to SSE also occurred at the beginning of August 10 which was not preceded by any strong wind. The longshore currents overall were weakly correlated with the wind. The lake large scale circulation probably dominated the local currents over the wind in this period. The onshore-offshore component of the currents was generally less than 20 cm/s.

The plume was attached to the south shore due to the strong longshore currents. Southerly currents (> 15 cm/s) on August 8 (13:50 and 22:30) and 9 (13:22 and 21:06). On August 10 (13:16), the plume moved more offshore, the currents were slow and wind was offshore. On August 10 (17:16 and 23:14) and August 11 (12:42 and 15:40) the plume was moving offshore because of the weak currents and offshore wind. The plume became more diffuse in stronger offshore winds.

The surface lake temperature near the mouth ranged from 18.0 to 23.9°C, and river temperature from 25 to 26.5°C. The lake temperature drop from August 8 to 11 was probably due to upwelling. The minimum and maximum temperature differences were 2.6 and 7°C respectively on August 8 and 11. The plume thickness ranged between about 3.0 to 4.3 m at the mouth and decreased rapidly as it spread. The rate of lateral spreading was the highest on August 10 when the plume width increased to 1.5 km within 1 km from the mouth. The plume dynamics will be discussed further in the next chapter.

Minimum dilutions generally increased with distances from the mouth to about 10 within 4.5 km. Minimum dilutions of 2 occurred within 400 m to 2.5 km from the mouth depending on the current speed. The distance where that dilution occurred on August 9 ranged from 1.1 to 2.5 km. Stronger currents considerably enhanced near field mixing and caused higher dilutions.

3.3.3 Series 3: June 2007

The Series 3 experiments were conducted from June 5 to 6, 2007. The wind and current observations, their effect on the plume, CTD, and tracer experiment results are discussed below. Aerial photographs were taken between May 29 and June 10, 2007.

3.3.3.1 Current and Wind Observations

The wind and currents from June 4 to 8, 2007 at moorings S10-07, N10-07 and M20-07 are shown in Figures 3.23 to 3.25. These are feather plots of wind, depth-averaged currents, and currents in selected bins. These bins for S10-07 and N10-07 are at depths of 1.8, 3.8, 4.8, and 6.8 m, and for M20-07 are at 1.8, 2.8, 6.8, 11.8, and 16.8 m. The observed wind is at the S10-06 buoy (see Figure 3.3). The wind and currents for this period are characterized by distinctive and well-defined patterns.

Polar wind histogram and scatter diagrams of the surface and depth-averaged currents are shown in Figure 3.26. The principal axes of the currents (PC1 and PC2) are indicated on the current scatter plots.

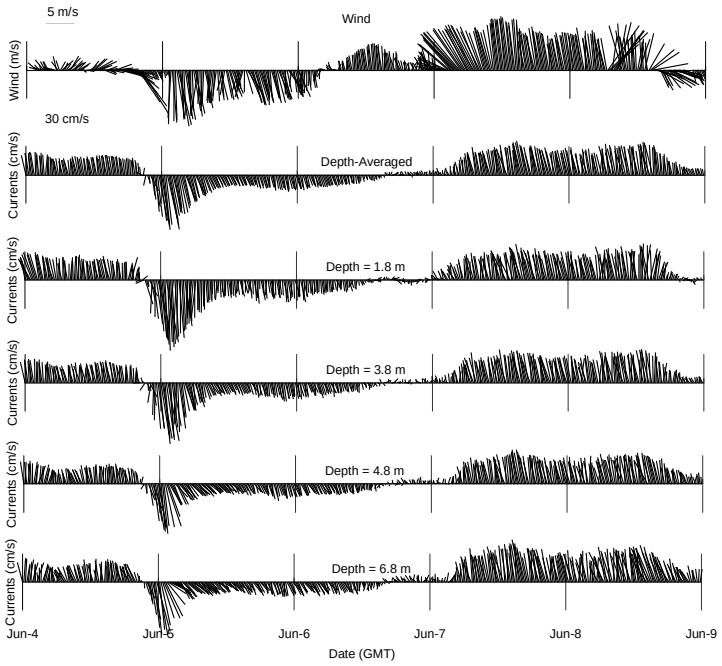

Figure 3.23 Feather plots of the wind and currents at S10-07.

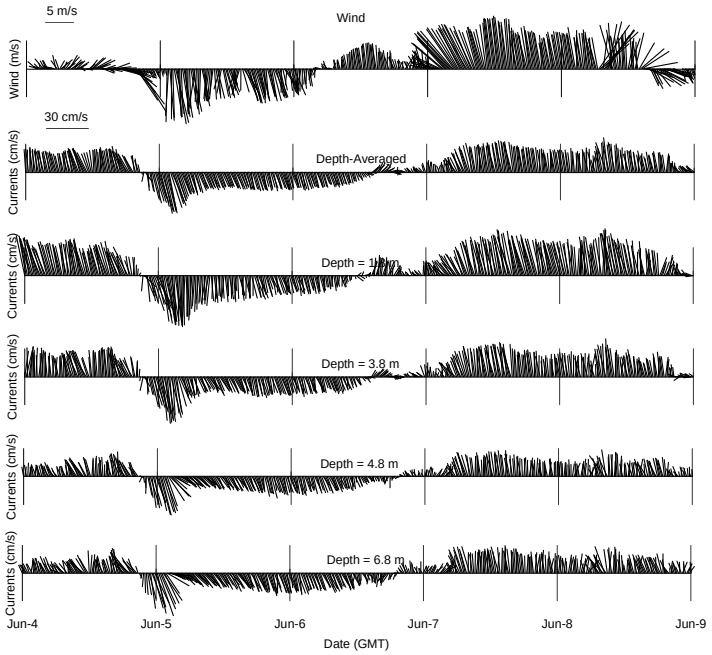

Figure 3.24 Feather plots of the wind and currents at N10-07.

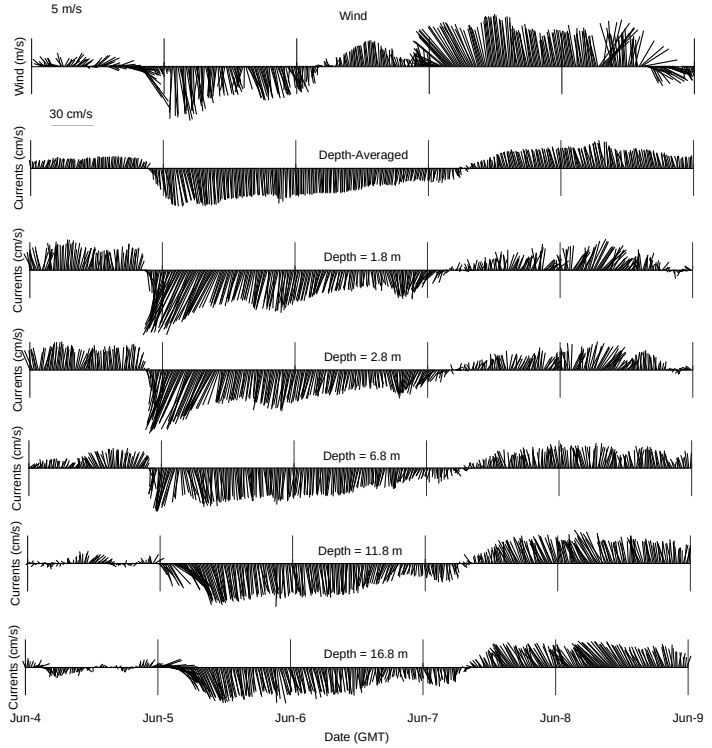

Figure 3.25 Feather plots of the wind and currents at M20-07.

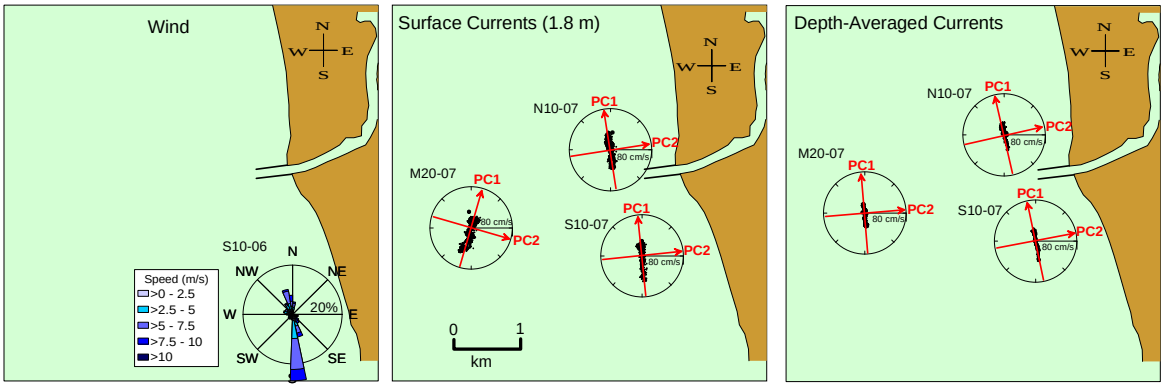

a) Wind histograms **b) Surface currents scatter diagrams** **c) Depth-averaged currents scatter diagrams**

Figure 3.26 Polar wind and currents diagram at S10-07, N10-07 and M20-07, June 4 to 9, 2007.

The currents have a strongly preferred direction along the first principal axes that are alongshore (to the N at S10-07 and N10-07, and NNW at M20-07). The second principal current components (to the E at S10-07 and N10-07, and ESE at M20-07) are much weaker than the first, particularly at M20-07. The wind and current data at S10-06 are summarized in Table 3.7.

Table 3.7 Summary of ADCP and meteorology data for June 4 to 8, 2007.

	S10-07			N10-07		M20-07	
	Surface Currents (1.1 m depth)	**Depth-Averaged Currents**	**Wind**	**Surface Currents (2.0 m depth)**	**Depth-Averaged Currents**	**Surface Currents (2.0 m depth)**	**Depth-Averaged Currents**
PC1 Direction	354°N (~N)	348°N (~N)		351°N (~N)	348°N (~N)	16°N (~N)	355°N (~N)
PC2 Direction	84°N (~E)	78°N (~E)		81°N (~E)	78°N (~E)	106°N (~E)	85°N (~E)
Current Speed (cm/s)	0.2 –49.5	1.1 – 39.5		0.4 – 38.2	1.6 – 31.0	0.2 – 52.5	1.3 – 27.9
Current Speed Average (cm/s)	13.7	12.1		17.9	13.1	16.9	13.3
Maximum Surface Current Speed (cm/s)	49.5 (at 1.8 m)			38.2 (at 1.8 m)		52.5 (at 1.8 m)	
Maximum Bottom Current Speed (cm/s)	32.8 (at 6.8 m)			26.8 (at 6.8 m)		23.9 (at 16.8 m)	
Wind Speed (m/s)			0 – 10				
Wind Speed Average (m/s)			4.6				
Predominant Wind Direction (>25%)			~S				
Next Most Frequent Wind Direction (<10%)			~NNE				

The nearshore surface currents (S10-07 and N10-07) ranged from 0.2 to about 50 cm/s with an average of 15.8 cm/s. The maximum at S10-07 was 10 cm/s higher than N10-07 but the average was about 4 cm/s lower. The offshore surface current speeds (M20-07) were slightly higher than nearshore but their average was within the same range (~ 16 cm/s). The currents at S10-07 and N10-07 were fairly uniform in speed and direction over depth, so the depth-averaged currents were quite similar to the surface currents.

Depth-averaged currents ranged from 1.1 to about 40 cm/s. The depth-averaged currents at S10-07 had an average slightly smaller than the depth-averaged nearshore currents at N10-07 and offshore currents at M20-07. At M20-07, on June 5, depth-averaged currents were rotated 15° counterclockwise from the surface currents. At M20-07, the depth-averaged principal components shift slightly clockwise (about 7°) from S10-07 and N10-07. The depth-averaged currents' first principal components were all to the N with speeds less than 40 cm/s. The second component was to the E with speeds less than 10 cm/s. The predominant wind blew from the S more than 25% of the time. The next most frequent wind blew from NNE less than 10% of the time.

To investigate relationships between wind and currents, the 3-hour averaged longshore and onshore surface current and wind components at S10-07, N10-07 and M20-07 are plotted in Figure 3.27.

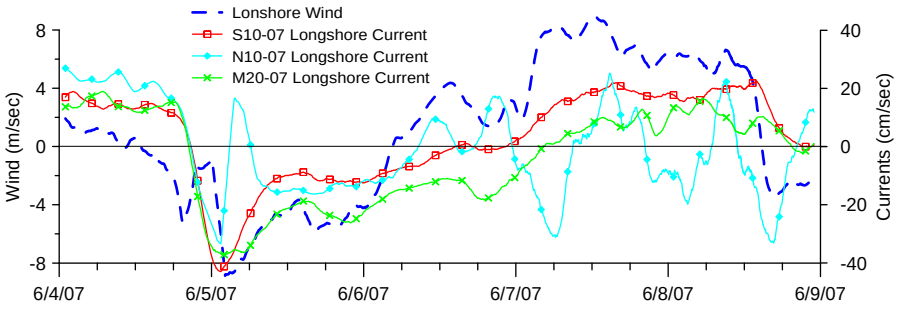

a) Longshore surface current and wind speed

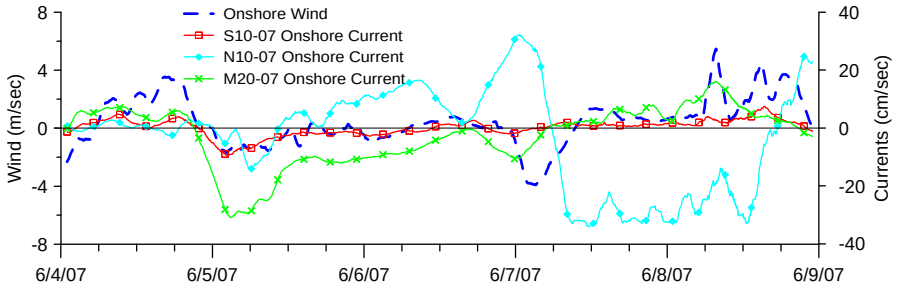

b) Onshore surface current and wind speed

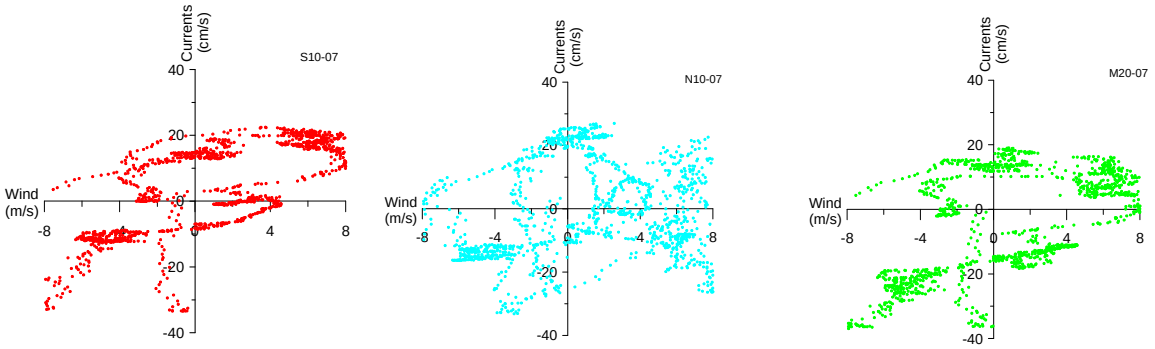

c) Longshore surface current and wind scatter

Figure 3.27 Longshore and onshore surface current and wind speed for June 4 to 8, 2007.

The longshore surface current speeds were less than 45 cm/s. The onshore current speeds were less than 15 cm/s and not correlated with the onshore wind. The longshore currents were shifted back about 3 hour to compensate the wind and currents lag. The shifted currents were somewhat correlated with the wind at S10-07 and M20-07 (r^2 =0.68 and 0.65), and less correlated at N10-07 (r^2=0.38). Similar to Series 1, the high frequency fluctuation in longshore wind were not reflected in longshore currents, but generally a

change in longshore wind direction is followed by a change in current direction. The longshore wind speed and duration are also both important factors in the longshore currents, but when local winds are slow and brief, lake large-scale circulation dominated the local currents.

3.3.3.2 Plume Observations

Plume observations for Series 3 included wind and currents measurement, CTD survey, and SF6 tracer experiments that are described below.

a) Wind and Currents

The wind, current, and river speeds are summarized in Table 3.6 to 3.8 from May 29, to June 10, 2007, when aerial photographs of the plume were available. Current and wind vectors (red and yellow respectively) are again overlaid on the images. These are 6-hour averaged values.

Table 3.8 Summary of wind, river, currents and plume condition for the aerial photographs of May and June 2007.

Date	5/29/07	5/30/07	5/31/07	6/1/07	6/2/07
Time (GMT)	14:16	14:23	14:33	15:53	23:06
Wind *					
Speed (m/s)	2.6	4.0	3.6	2.8	1.8
Direction (deg)	127	165	163	162	201
Surface Currents *					
Speed (cm/s)	11.6	12.9	9.4	11.1	6.6
Direction (deg)	12	2	359	359	343
Surface Longshore Currents Speed (cm/s) *	10.3	12.4	9.1	10.8	6.6
River Velocity (cm/s) **	13.6	13.4	12.6	11.9	11.9
Lake Temp. (°C)	12.8 (Satellite)	13.6 (Satellite)	14.6 (Satellite)	16.3 (Satellite)	18.0 (Satellite)
River Temp. (°C)	21.1 (Intake)	21.1 (Intake)	22.8 (Intake)	22.8 (Intake)	22.8 (Intake)
Photo Current: 5 cm/s Wind: 5 m/s		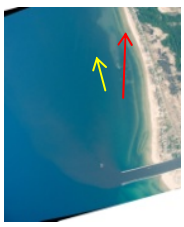			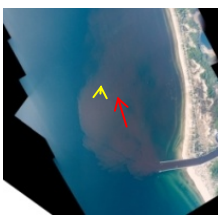

* wind and lake currents speed and direction are all 6-hr averaged at S10-07.
** river velocity is daily-averaged.

Table 3.9 Summary of wind, river, currents and plume condition for the aerial photographs of June 2007.

Date	6/5/07	6/5/07	6/6/07	6/6/07	6/6/07
Time (GMT)	13:42	16:55	12:05	16:15	22:30
Wind *					
Speed (m/s)	4.8	4.8	2.2	3.8	2.0
Direction (deg)	355	349	171	174	172
Surface Currents *					
Speed (cm/s)	11.1	10.0	5.9	3.2	2.0
Direction (deg)	180	177	172	133	139
Surface Longshore Currents Speed (cm/s) *	-10.8	-9.8	-5.9	1.1	1.5
River Velocity (cm/s) **	18.7	18.7	19.9	19.9	19.9
Lake Temp. (°C)	8.2 (CTD)	7.3 (CTD)	5.4 (CTD)	6.9 (CTD)	6.8 (CTD)
River Temp. (°C)	20.8 (CTD)	20.3 (CTD)	19.5 (CTD)	20.0 (CTD)	20.0 (CTD)
Photo Current: 5 cm/s Wind: 5 m/s	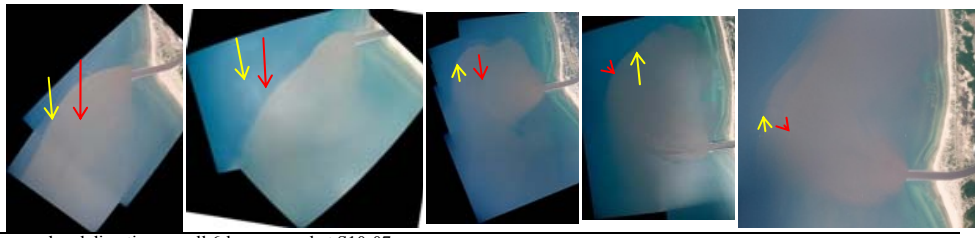				

* wind and lake currents speed and direction are all 6-hr averaged at S10-07.
** river velocity is daily-averaged.

Table 3.10 Summary of wind, river, currents and plume condition for the aerial photographs of June 2007.

Date	6/8/07	6/8/07	6/9/07	6/10/07
Time (GMT)	15:30	23:10	22:58	23:00
Wind *				
Speed (m/s)	6.3	3.9	1.4	1.1
Direction (deg)	185	301	166	170
Surface Currents *				
Speed (cm/s)	21.3	3.5	3.6	11.5
Direction (deg)	353	25	334	356
Surface Longshore Currents Speed (cm/s) *	20.9	2.7	3.6	11.3
River Velocity (cm/s) **	20.4	20.4	19.4	17.2
Lake Temp. (°C)	12.3 (Satellite)	11.4 (Satellite)	15.1 (Satellite)	15.7 (Satellite)
River Temp. (°C)	21.1 (Intake)	21.1 (Intake)	21.1 (Intake)	21.7 (Intake)
Photo Current: 5 cm/s Wind: 5 m/s	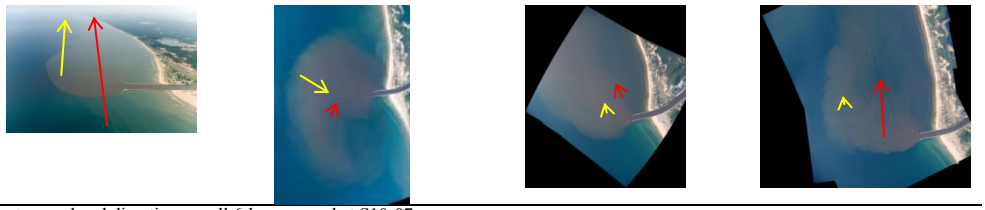			

* wind and lake currents speed and direction are all 6-hr averaged at S10-07.
** river velocity is daily-averaged.

The surface lake temperature varied from 5.4 to 18.0°C. The very low temperature is probably due to upwelling caused by the strong southward winds on June 5 and early June 6. The Ekman transport (Coriolis forces plus the frictional coupling of wind and currents) causes warmer surface waters to move away from the coast and be replaced with colder deeper waters. The river temperature ranged from 19.5 to 22.8°C, so was 9 to 10°C warmer than the lake. The minimum and maximum temperature differences were observed 4.8 and 14.1°C on June 2 and 6, 2007. The effect of temperatures on the plume will be analyzed in Chapter 4.

b) CTD Survey

The CTD survey tracks, surface temperature and conductivity, and selected transects on June 5 and 6, 2007 are shown in Figures 3.28 and 3.29 respectively. The beginning and end points for each transect are noted by letters on the CTD tracks. The towyoed transects show vertical temperature profiles. The conductivity vertical profiles were similar to the temperature, so only temperature contours are shown. The pressure sensor was out of order on June 5, so depth was not recorded. Therefore only the CTD track and horizontal map are shown. The towyoed transects show vertical temperature profiles.

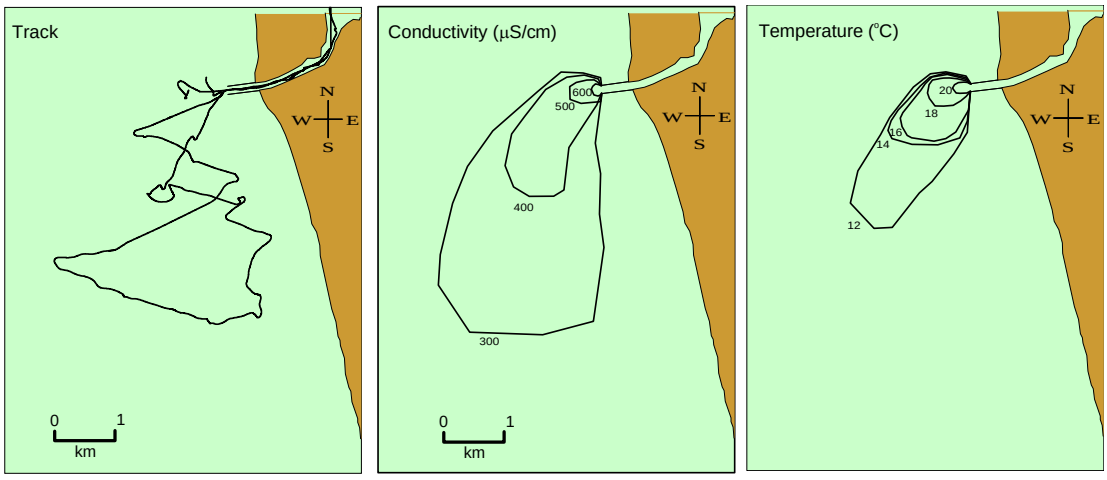

Figure 3.28 CTD survey track, conductivity and temperature on June 5, 2007.

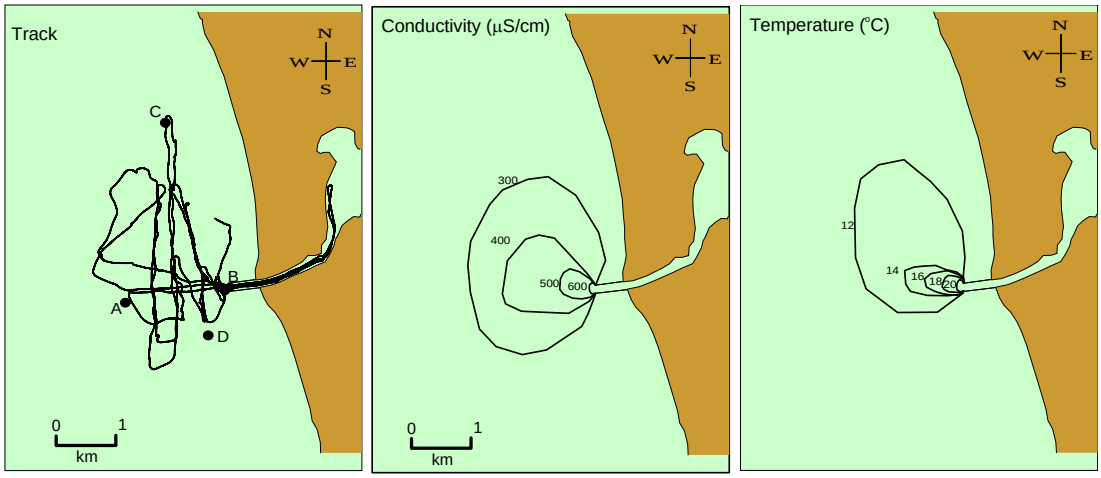

Figure 3.29 CTD survey tracks, conductivity and temperature transects on June 6, 2007.

In addition to the towyo profiling in the lake, vertical CTD casts were made in the river. The cast locations on June 6, 2007 are shown in Figure 3.30. The points were located near the river mouth (A) and upstream (B, C, D, and E). F is the dye release point at the 31 highway bridge. The casts recorded fluorescence, conductivity, and temperature profiles. Since the conductivity and fluorescence sensors were not calibrated, it was difficult to conclude anything from them. However, the temperature profiles assisted us in determining the plume-lake interface and plume thickness that will be discussed in Chapter 4. The profile at A shows the lake water intruding upstream into the river at the mouth, but at other points upstream, fully mixed profiles were observed.

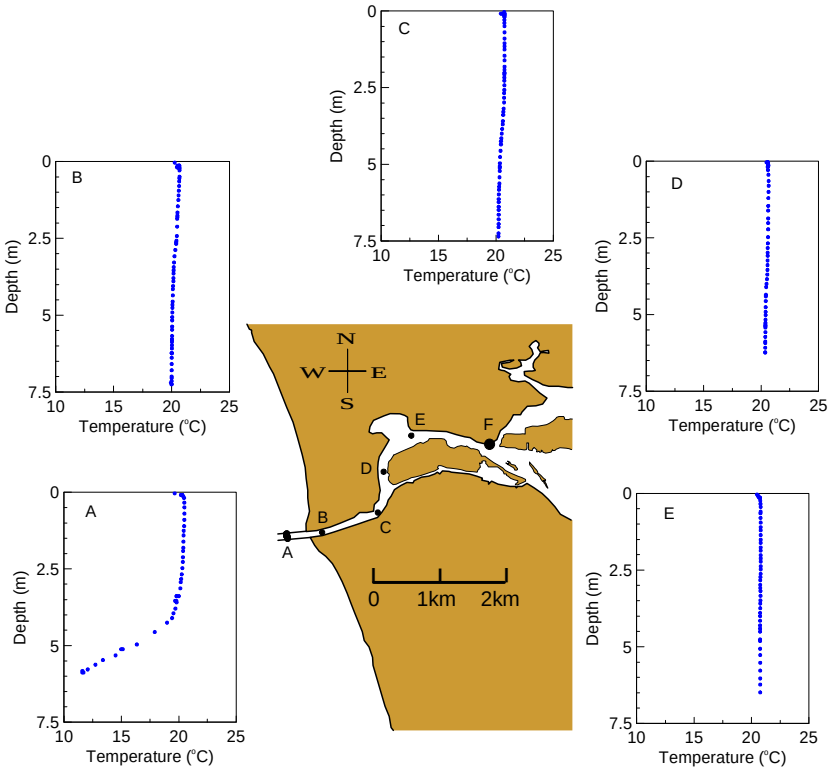

Figure 3.30 CTD temperature profiles on June 6, 2007.

3.3.3.3 Bacterial samples

Surface water samples were taken on June 5 and 6, 2007 in the lake from which E. coli and total coliforms were measured. The results are overlain on aerial photographs and ship tracks in Figures 3.31 and 3.32. On both days, E. coli counts ranged from a maximum of about 40 per 100 ml at the mouth to zero outside of the plume. On June 6, total coliform counts ranged from zero to 7000 per 100 ml, but this range increased on the next day from zero to 12000 counts per 100 ml. The distribution of bacteria was patchy so it was difficult to draw contour plots. Bacteria distribution over the plume and on the beach and its relation to conductivity is discussed in Chapter 4.

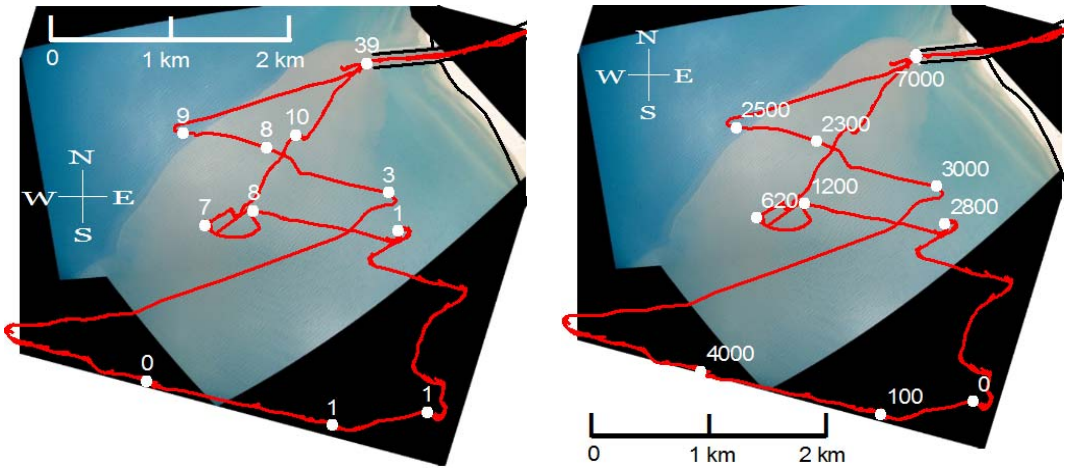

Figure 3.31 Ecoli counts (left) and total coliforms (right) per 100 ml in samples on June 5, 2007.

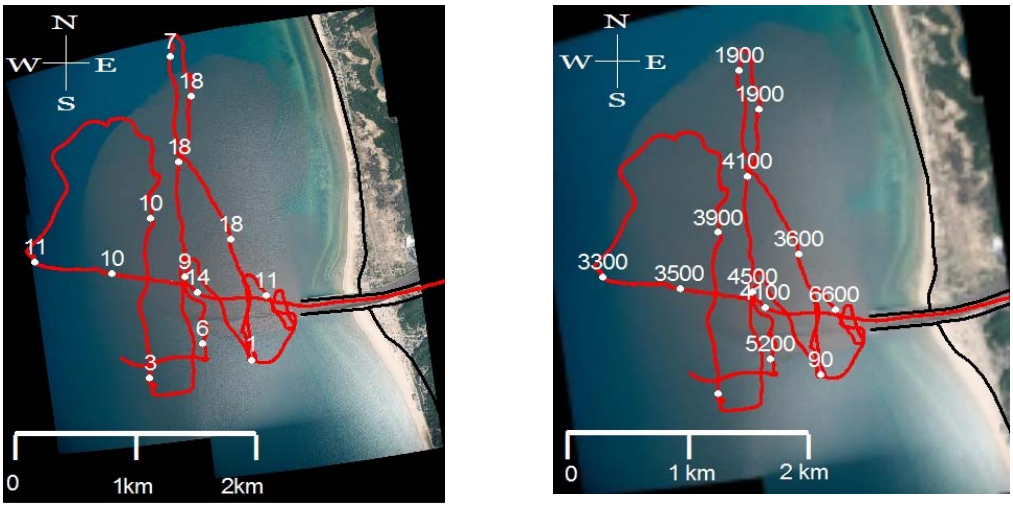

Figure 3.32 Ecoli counts (left) and total coliforms (right) per 100 ml in samples during the survey on June 6, 2007.

3.3.3.4 Discussion

Aerial photos started on May 29 and lasted until June 10. On May 29, 30 and 31, and June 1, and 2, 2007, the currents and wind were to the N or NW. These are not shown on Figures 3.23 to 3.25. The plume was either spreading to the N or attached to the north coast. This was significant, since the main variable is the wind. The lake

currents and temperature difference are fairly constant (Table 3.8) that allows separation of the wind effects. The results of the Series 3 experiments, June 5 and 6, 2007, are discussed below. The referred currents are the surface nearshore currents (at S10-07 and N10-07).

On **June 4**, the wind was blowing slowly (< 3 m/s) from the S, SE and SW most of the time until 16:00, then shifted to blow from the N and NW with a speed that increased to about 10 m/s around 20:30, thereafter was slow again (< 2 m/s). The currents were to the N fairly consistent with a speed of approximately 15 cm/s until 22:00, then reversed to the S and increased to about 40 cm/s at 24:00.

On **June 5**, the wind was mostly from the N, slow until 1:00 when the speed increased to about 10 m/s, the speed decreased slowly to about 5.5 m/s until 10:00, thereafter it blew with approximately the same speed. The currents were mainly to the S, started strong (~40 cm/s), increased to 45 cm/s around 1:00, then slowed to about 12 cm/s until 10:00, thereafter remained approximately about the same speed. The plume at 13:42 and 16:55 extended offshore to the southwest more than 6 km from the mouth. The plume width increased to about 1.5 km at 1 km from the mouth. Minimum dilutions of 2, 5 and 10 occurred at distances of 1.1, 2.5 and 3.7 km from the mouth respectively.

On **June 6**, the wind remained blowing from the N initially with a speed of 5 m/s, it calmed until 4:30 when it reversed and blew from the S, then the speeds increased again to about 4.5 m/s around 13:30, the wind remained blowing from the S but slowed to about 2 m/s until 17:30, blew mostly from SW with small speeds (~ 1.5 m/s) until around 21:30, thereafter it blew from SSE and SE and the speed increased again to about 4 m/s. The currents were initially to the S, with speeds of about 14 cm/s, gradually slowed until around 14:00, when they reversed to the N, thereafter were weak. The plume at 12:05 spread around the mouth due to the slow wind and currents, at 16:15 was to the N and hugged the shore, between 16:15 and 22:30 the onshore wind blew and caused the plume to impact the northern shoreline, and at 22:30 plume again started to slightly move back in front of the mouth because wind was changing direction blowing offshore. The plume thickness at the mouth was 5.3 m and decreased to less than 3.0 m at a distance of only 100 m from the mouth. The plume width increased to about 4 km within 1 km from the

mouth. The minimum dilutions of 2, 5 and 10 occurred at distances of 1.1, 2.0 and 2.3 km from the mouth.

On **June 7**, the winds were strong (average speeds of about 10 m/s) from the S resulting in strong nearshore currents (25.7 cm/s at S10-07 and 33.3 cm/s N10-07) to the N.

On **June 8**, the wind continued strong (~ 12.5 m/s) from the S and SW until around 16:00, causing the currents to flow to the N with an average speed of about 20 cm/s, thereafter the wind changed direction, blowing mostly from NW, and the currents slowed until 24:00. As a result, the plume at 15:30 impacted the north shore, at 23:10 the plume was trapped around the mouth due to the onshore wind and slow currents.

3.3.3.5 Summary

The strong Northerly wind on June 5 (up to 10 m/s) was an important feature of this series. The other strong wind (about 10 m/s) was predominantly Southerly, most of June 7 and June 8 (until 16:00). The winds on June 6 were slower and more variable blowing from the N, S, SW and finally SSE. The maximum wind speeds for this period were less than 20.6 m/s with an average of 12.7 m/s. The currents were characterized by two distinctive and well defined Southerly and Northerly currents were the featured currents of this series. The Southerly currents were the strongest (40 cm/s) on June 5 around 1:00, then calmed until the end of June 6. The currents were mostly to the N on June 4, 7 and 8 varying slightly about an average speed of 20 cm/s. The first principal component (PC1) of the surface currents also confirms the featured longshore currents (generally less than 60 cm/s, to the N nearshore, and to the NNW offshore). The second principal component (PC2) was much weaker (normally less than 15 cm/s and to the E nearshore, and to the ESE offshore).

The longshore wind and currents were somewhat correlated. As discussed for the previous series, persistent strong local winds (>3 m/s), drive the currents and transport the plume in the same direction. Slow and brief local winds (<3 m/s), do not necessarily drive the local currents and the currents are mainly affected by the large scale lake circulation.

The average river velocity from June 5 to 8, doubled from the average in the previous series. Therefore greater initial plume momentum could have moved the plume further offshore with the same longshore current speeds. It is also noteworthy that the shape of the plume is an overlay of different plumes formed over the previous few hours, so the 6-hour averaged wind and currents can help in finding what exactly has caused the present shape of the plume.

The plumes spread offshore to the N on May 29, 30, and 31, and June 1, 2 and 10. The plume moved offshore (southwest) on June 5 at 12:05 due to the southward longshore currents and wind. On June 6 and 8, plumes spread radially around the mouth in the absence of strong wind and currents, and impacted the shore in strong onshore wind and calm currents.

The surface lake temperature ranged from 5.4 to 18.0°C, and the river temperature from 24.2 to 26.5°C. The low lake temperatures are probably due to upwelling caused by the strong southward winds on June 5 and early June 6. The minimum and maximum temperature differences were 4.8 and 14.1°C on June 2 and 6, 2007. The plume thickness was 5.4 m at the mouth on June 6. Minimum dilution of 2 was observed at 1.1 km, 5 at 2 to 2.5 km, and 10 within 2.3 to 3.7 km from the mouth depending on mixing affected by the currents. Ecoli and total coliform maximum counts recorded in the river were 40 and 12000 per 100 ml, and decreased to zero and less than 100 respectively, outside the plume.

3.3.4 Series 4: July 2007

The Series 4 experiments conducted on July 17 and 18, 2007 are described below.

3.3.4.1 Current and Wind Observations

The wind and currents from July 14 to 18, 2007 at moorings S10-07, N10-07 and M20-07 are shown in Figures 3.33 to 3.35. These are feather plots of wind, depth-averaged currents, and currents in selected bins. The bins for S10-07 and N10-07 are at depths of 1.8, 3.8, 4.8, and 6.8 m, and for M20-07 are at depths of 1.8, 2.8, 6.8, 11.8, and 16.8 m. The observed wind is at the S10-06 buoy (see Figure 3.3). A polar wind

histogram and scatter diagrams of the surface and depth-averaged currents are shown in Figure 3.36.

The principal axes of the currents (PC1 and PC2) are indicated on the scatter plots. The currents again have a strongly preferred direction along the first principal axes (to N at S10-07 and N10-07, and NNW at M20-07). The currents along second principal component (to E at S10-07 and N10-07, and ESE at M20-07) are much weaker than the first. The wind and current data at N5-06 and S10-06 are summarized in Table 3.11.

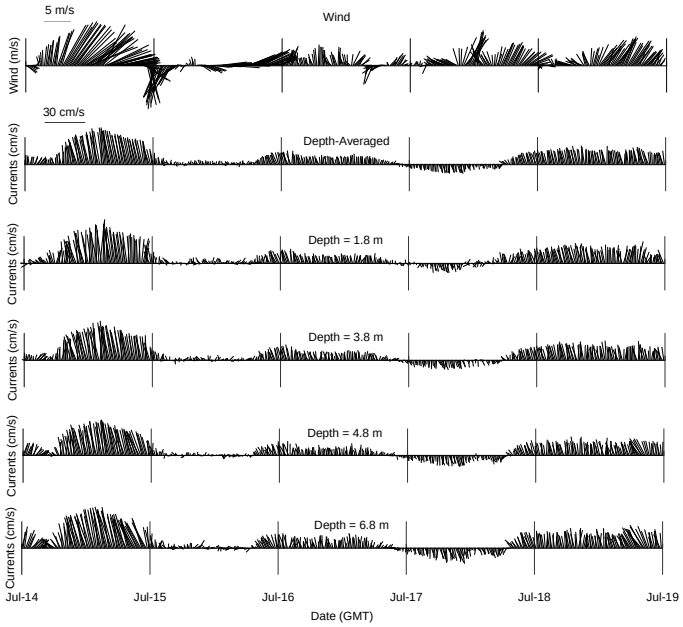

Figure 3.33 Feather plots of the local wind and currents at S10-07 mooring.

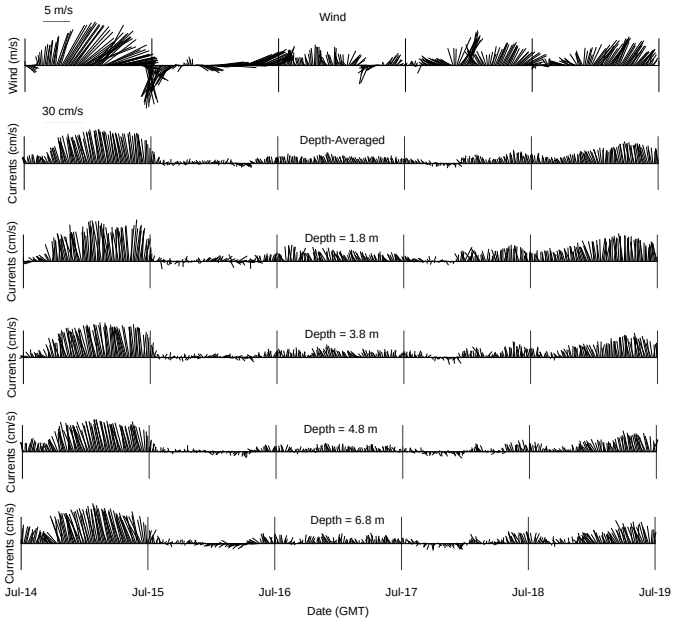

Figure 3.34 Feather plots of the local wind and currents at N10-07 mooring.

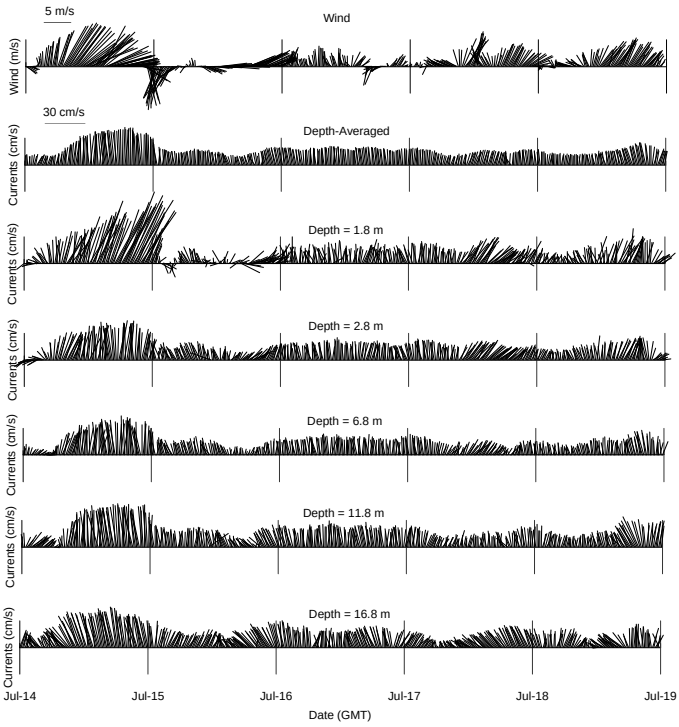

Figure 3.35 Feather plots of the local wind and currents at M20-07 mooring.

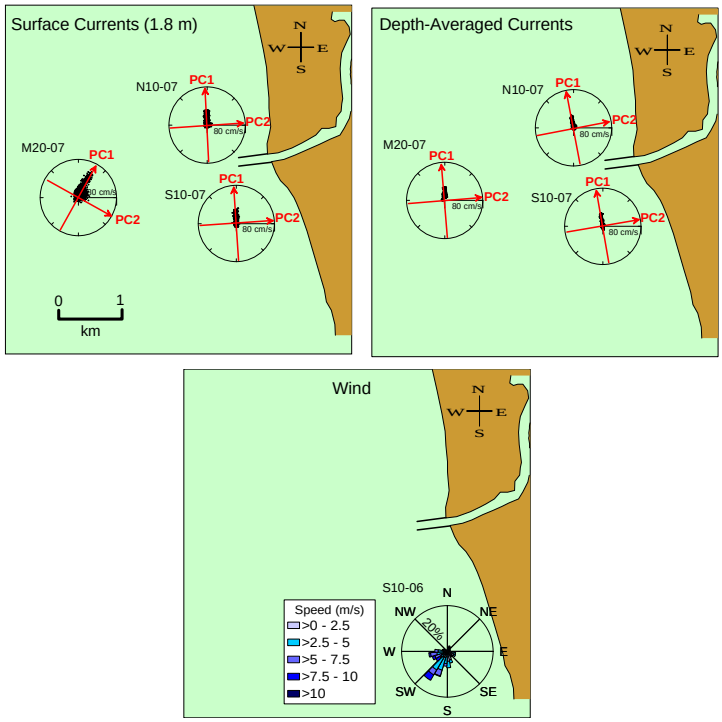

Figure 3.36 Polar wind histogram, surface and depth-averaged currents scatter at S10-07, N10-07 and M20-07 from July 14 to 18, 2007.

Table 3.11 Summary of ADCP and meteorology data for July 14 to 18, 2007.

	S10-07			N10-07		M20-07	
	Surface Currents (1.1 m depth)	**Depth-Averaged Currents**	**Wind**	**Surface Currents (2.0 m depth)**	**Depth-Averaged Currents**	**Surface Currents (2.0 m depth)**	**Depth-Averaged Currents**
PC1 Direction	356°N (~N)	350°N (~N)		357°N (~N)	350°N (~N)	29°N (~NNW)	355°N (~N)
PC2 Direction	86°N (~E)	80°N (~E)		87°N (~E)	80°N (~E)	119°N (~ESE)	85°N (~E)
Current Speed (cm/s)	0.1 –32.8	0.8 – 28.4		0.2 – 32.3	0.9 – 27.2	0.1 – 60.5	4.4 – 28.4
Current Speed Average (cm/s)	8.1	7.8		9.4	7.5	14.9	11.9
Maximum Surface Current Speed (cm/s)	32.8 @ 1.8 m			32.3 @ 1.8 m		60.5 @ 1.8 m	
Maximum Bottom Current Speed (cm/s)	26.4 @ 6.8 m			25.9 @ 6.8 m		27.7 @ 16.8 m	
Wind Speed (m/s)			0 – 9.9				
Wind Speed Average (m/s)			3.6				
Predominant Wind Direction (>15%)			SW				
Next Most Frequent Wind Direction (<10%)			W				

Nearshore surface currents (N10-07 and S10-07) ranged from 0.1 to 32.8 cm/s with an average around 9 cm/s. The offshore currents (M20-07) were stronger with an average of around 15 cm/s. The first principal current component speed was less than 60 cm/s offshore and 40 cm/s nearshore. The weaker onshore component was less than 25 cm/s offshore and 15 cm/s nearshore. The nearshore currents were approximately uniform in speed and direction over depth, so the depth-averaged currents were similar to the surface currents. Offshore currents had a clockwise shift of 15° from depth-averaged currents to surface currents. The depth-averaged currents first principal components were all to N and their speeds were generally less than 40 cm/s. The second component was to the E and normally less than 10 cm/s. PC1 at M20-07 shifted slightly clockwise (about 5° from S10-07) from S10-07 and N10-07. The predominant wind was from the SW (more than 15% of the time). The next most frequent wind blew from the W (less than 10% of the time).

Nine drifters in five sets were released in five phases on July 17 and July 18, 2007. Their trajectories are shown in Figure 3.37. Seven drifters were released at 11:07 (7:07 EDT) on July 17. They moved together with little separation. They were retrieved about an hour later and released again at 12:02. The currents moved them slightly away from each other onshore and offshore. They were retrieved about three and a half hours later. Two other drifters were released at 14:51 and retrieved about three hours later. The currents to the north increased to about 10 cm/s at the end of the experiment. On July 18, six drifters were released, three at 12:33 and three at 13:26, and were retrieved about 9 hours later. They were advected to the north. For the duration of this experiment, the drifters stayed very close to each other except the set released at 12:02, which most of them grounded, so it was not possible to determine the size and growth of the tracer cloud and therefore the eddy diffusion coefficient.

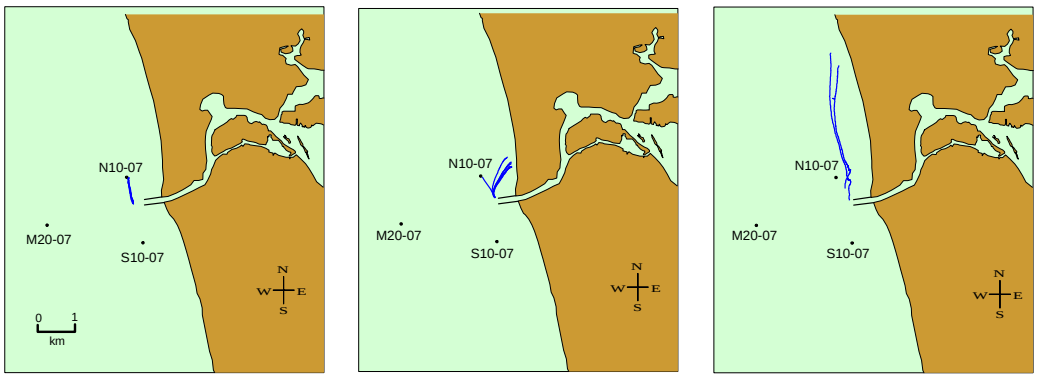

11:7:15 to 12:1:56 | 12:2:26 to 15:27:38 | 14:51:52 to 17:57:38

July 17, 2007

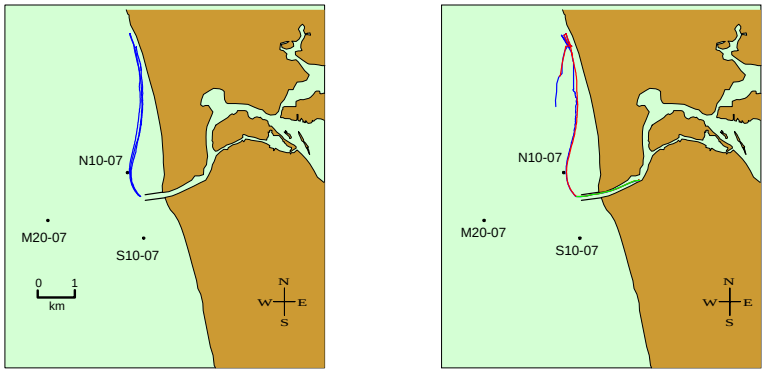

13:26:17 to 22:10:17 | 12:33:22 to 21:36:09

July 18, 2007

Figure 3.37 Drifter release tracks on July 17 (top), and July 18 (bottom).

To investigate possible relationship between wind and currents, the 3-hour averaged longshore and onshore surface current and wind components at S10-07, N10-07 and M20-07 are plotted in Figure 3.38. The currents flowed predominantly alongshore. The onshore current speeds were weak and less than 10 cm/s. Longshore currents were not correlated with the local wind (r^2<0.13).

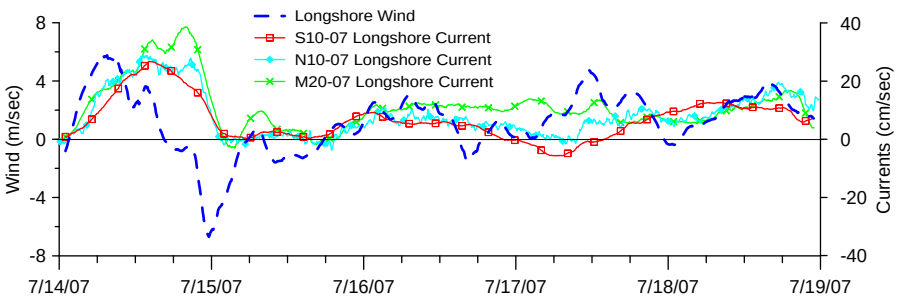

a) Longshore surface current and wind speed

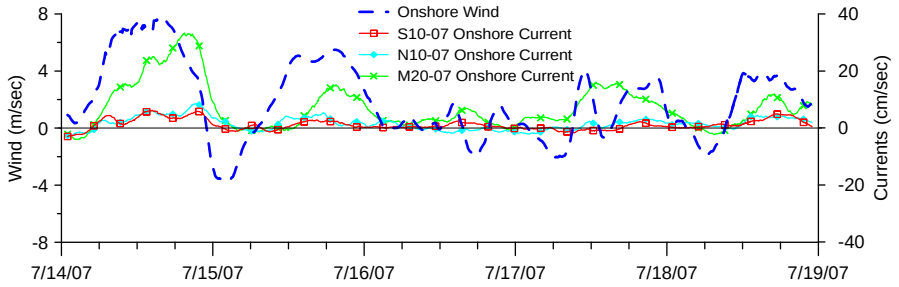

b) Onshore surface current and wind speed

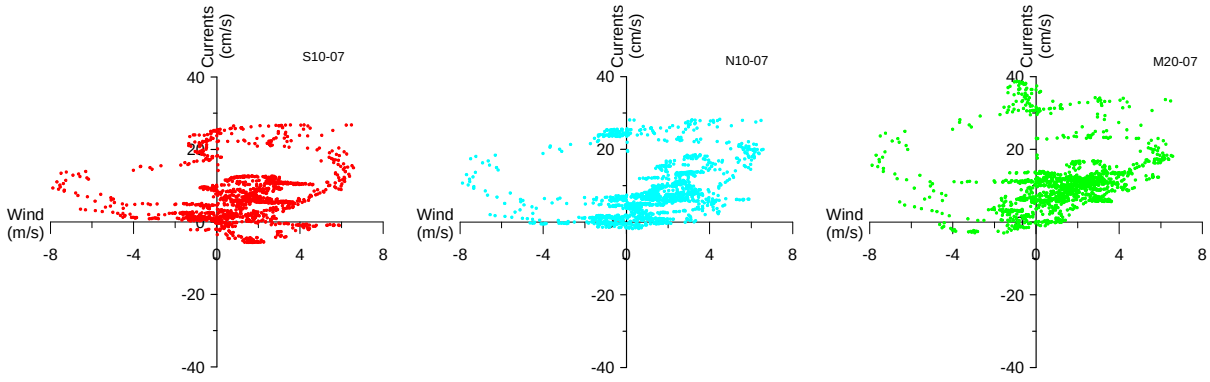

c) Longshore surface current and wind scatter

Figure 3.38 Three-hour averaged longshore and onshore surface current and wind speed for July 14 to 18, 2007.

3.3.4.2 Plume Observations

The plume observations and wind and currents measurement, CTD survey, and SF6 tracer experiments that are described below.

a) Wind and Currents

The wind, river, current and plume conditions on June 30, and July 2, 6, 9, 11, and 13, 2007 and on July 17 and 18, 2007 are summarized in Tables 3.12 and 3.13. Current and wind vectors (red and yellow respectively) are again overlaid on the images. 6-hour averaged surface currents and wind, and daily-averaged river velocity are used.

Table 3.12 Summary of wind, river, currents and plume condition for the aerial photographs of June and July 2007.

Date	6/30/07	7/2/07	7/6/07	7/9/07	7/11/07	7/13/07
Time (GMT)	14:05	23:22	14:06	13:07	23:17	13:00
Wind *						
Speed (m/s)	0.5	2.2	2.1	4.6	4.7	2.3
Direction (deg)	287	12	22	192	282	59
Surface Currents *						
Speed (cm/s)	6.6	5.1	2.7	17.9	17.0	4.1
Direction (deg)	162	132	33	349	173	221
Surface Longshore Currents Speed (cm/s) *	-6.6	-4.3	1.8	17.8	-16.8	-2.7
River Velocity (cm/s) **	8.6	6.7	6.5	5.3	5.2	4.8
Lake Temp. (°C)	14.1 (Satellite)	13.0 (Satellite)	18.9 (Satellite)	17.5 (Satellite)	20.8 (Satellite)	21.4 (Satellite)
River Temp. (°C)	23.9 (Intake)	22.8 (Intake)	23.9 (Intake)	25 (Intake)	25.6 (Intake)	24.4 (Intake)
Photo Current: 5 cm/s Wind: 5 m/s			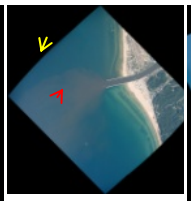			

* wind and lake currents speed and direction are all 6-hr averaged at S10-07.
** river velocity is daily-averaged.

Table 3.13 Summary of wind, river, currents and plume condition for the aerial photographs of July 2007.

Date	7/17/07	7/18/07	7/18/07	7/18/07
Time (GMT)	15:40	00:44	13:15	22:30
Wind *				
Speed (m/s)	4.2	3.2	3.3	3.7
Direction (deg)	189	227	194	214
Surface Currents *				
Speed (cm/s)	2.5	7.9	11.8	9.6
Direction (deg)	231	354	351	9
Surface Longshore Currents Speed (cm/s) *	-1.1	7.8	11.8	8.8
River Velocity (cm/s) **	4.8	4.9	4.9	4.9
Lake Temp. (°C)	21.4 (CTD)	21.4 (CTD)	21.7 (CTD)	22.1 (CTD)
River Temp. (°C)	23.5 (CTD)	24.4 (CTD)	24.6 (CTD)	24.8 (CTD)
Photo Current: 5 cm/s Wind: 5 m/s		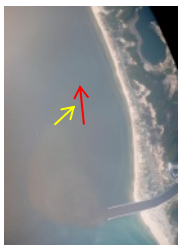		

* wind and lake currents speed and direction are all 6-hr averaged at S10-07.
** river velocity is daily-averaged.

b) CTD Survey

The CTD survey tracks, and surface temperature and conductivity on July 17 and 18, 2007 are shown in Figures 3.39 and 3.40. The V-Fin was set at a constant depth near the surface, so no vertical profiles were obtained. Surface conductivity and temperature contours are shown to indicate the surface extent of the plume. Higher conductivity and temperature closer to the mouth and at the surface are usually observed due to the higher salinity and temperature of the river water.

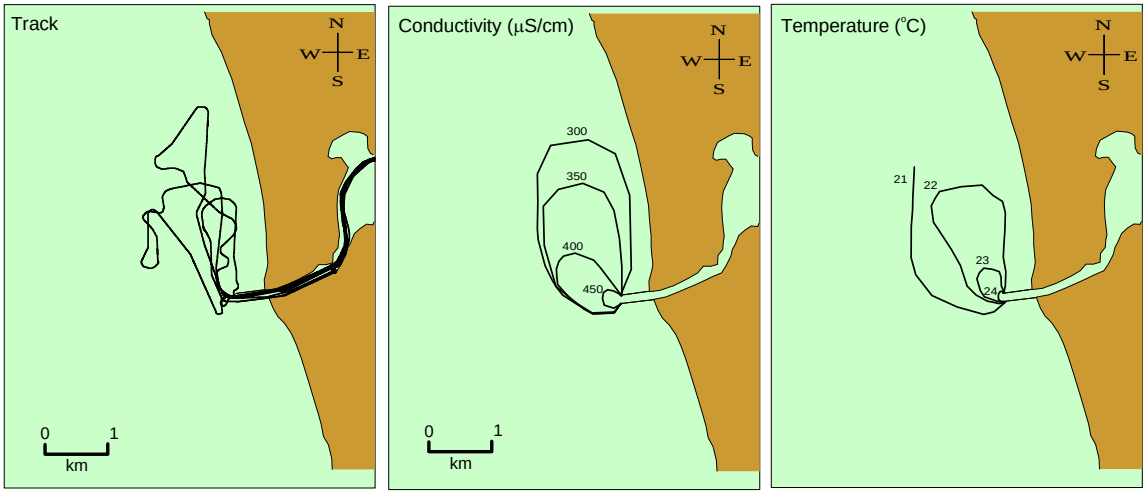

Figure 3.39 CTD survey track and conductivity transects on July 17, 2007.

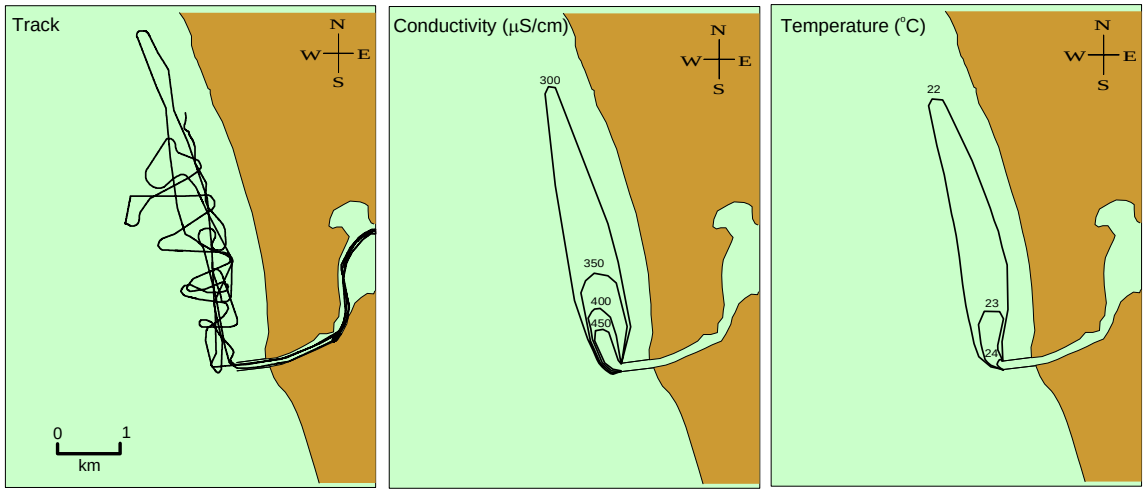

Figure 3.40 CTD survey track and selected conductivity transects on July 18, 2007.

Vertical CTD castings were carried out in the river and the lake along with the towyo CTD profiling. The casting points on July 17 and 18, 2006, are shown in Figure 3.41. The casts recorded conductivity, fluorescence, and temperature profiles. Temperature profiles at two points in the lake around the river mouth (A and B) and at points upstream in the river (B, C, D, and E) are plotted. Rhodamine dye was released at Point F at the US 31 highway bridge. Since the cast conductivity and fluorescence sensors were not calibrated, it was difficult to conclude anything from them. However,

the temperature profiles assisted us in determining the interface between the plume and lake water, and the plume thickness that will be explained in detail in Chapter 4. The profiles at A and upstream points C, D and E, shows the lake water intruding to the river upstream. The intrusion thickness decreased from the river mouth to the upstream. Point B is presumably outside of the plume, since the profile is well-mixed.

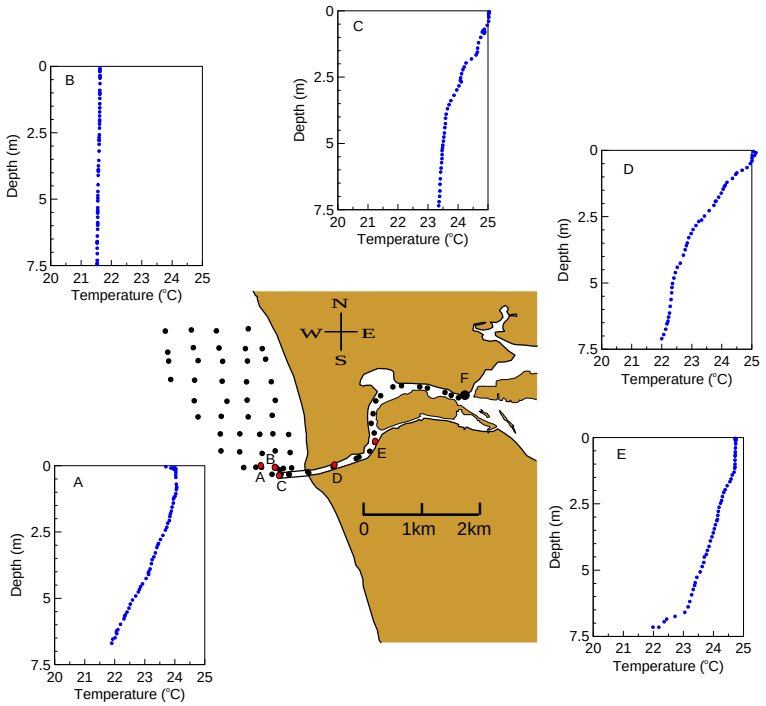

Figure 3.41 CTD casting points and temperature profiles on July 17 and 18, 2007.

3.3.4.3 Discussion

Aerial photography started early, on June 30. On June 30 at 14:05, the currents and wind were both slow (6.6 cm/s and 0.5 m/s) and the onshore wind deflected the plume to the south. On July 2 at 23:22, the currents remained slow, however the offshore wind increased and moved the plume slightly offshore. On July 6 at 14:06, the currents were slow (2.7 cm/s) and the plume extended offshore with the offshore wind. On July 9 at 13:07, the current speeds were strong (18 cm/s) and to the N, and the wind was onshore, resulting in a north shore-attached plume. On July 11 at 23:17, the strong currents (17 cm/s) to the S and the Westerly (onshore) wind created a long narrow plume attached to

the south coast. On July 13 at 13:00, the strong offshore currents and wind (4.1 cm/s and 2.3 m/s, fairly strong for a river velocity of 4.8 cm/s) generated a diffused offshore extending plume. The results of the Series 4 experiments for July 17 and 18, 2007 are discussed below. The referred wind and currents are the nearshore wind and surface currents at S10-07.

On **July 14,** the wind was slow (<3 m/s) until around 3:00, then started blowing from the S, and changed direction slowly until around 10:00 that was blowing from the SW with a high speed of 10 m/s, then the speed decreased to 3 m/s again and slowly changed direction blowing from the W at 21:30, then the speed increased to about 8 m/s and changed direction blowing from the N at 24:00. The corresponding currents were to the N, increased as the wind increased to about 32.5 cm/s around 14:00, and slowed towards the end of the day.

On **July 15**, the wind initially blew from the NNE with a speed of about 7.5 m/s, then slowed until 4:00, remained slow (<2 m/s) until 10:00, then blew from the E mostly with an average speed of about 4.5 m/s until 17:00, then was from the ESE and its speed increased to about 6 around 20:00, then slowed to less than 3 m/s until the end of the day. The currents were fairly weak (<10 cm/s) and to the N.

On **July 16**, the wind was mostly from the S and SW until around 14:00 with a variable speed (average of 3.5 m/s), then blew from the N until 16:00 and the speed increased to about 5 m/s, thereafter slowed and was from the SSW with some random changes in speed. The currents were calm with speeds less than 10 cm/s.

On **July 17**, the wind was slow (< 1 m/s) until 4:00, then was from the ESE with an average of about 4 m/s until 9:00, thereafter was mostly from the S, SSE and SW with a high speed of about 10 m/s around 12:00. The currents were weak until 16:00, then the flowed to the S creating and the speed increased to about 15 cm/s at 24:00. The plume at 15:40 was diffused and impacted the north shore more than 4 km due to the fairly strong onshore wind and weak currents. The plume thickness was 3.2 m at the mouth, and decreased rapidly to less than 0.5 m, within 500 m from the mouth. The plume width increased to about 1.5 km at a distance of 1 km from the mouth. The minimum dilutions of 2, 5 and 10 occurred at 0.8, 2.3, and 4.5 km from the mouth.

On **July 18**, the wind was mostly from SE, S, and SSW with speeds up to about 10 m/s around 16:00. The currents were to the N flowing at a fairly constant speed of about 17.5 cm/s. The plume was deflected the north at 00:44, and was shore-attached at 13:15 and 22:30 due to the onshore wind and fairly strong currents for the river speed of about 5 m/s. Plume width increased to about 800 m just 1 km away from the mouth. The minimum dilutions of 2, 5 and 10 were at distances of 0.5, 2.1 and 2.8 km from the mouth, respectively. The stronger currents caused higher dilutions than the previous day.

3.3.4.4 Summary

For the Series 4 tests, the predominant wind was from the SW on most of July 14, 17 and 18. Directions on the other days were more random. Maximum speeds were 23.6 m/s with an average around 20.2 m/s. The currents were mostly to the N. They were strong on July 14 with high speeds of about 32.5 cm/s around 14:00, and July 18 with fairly constant speeds of 17.5 cm/s, and were weak (<10 cm/s) for the rest of the period. The longshore and onshore currents were not correlated with the wind.

The plumes were attached to the shore during strong longshore currents. When the currents were weak they were affected by onshore-offshore winds. Depending on the direction and magnitude of the onshore-offshore wind component, they either impacted the shore or moved offshore.

For this period, the surface lake temperatures ranged from 21.4 to 22.1°C, and river temperatures from 23.5 to 24.8°C. The minimum and maximum temperature differences were 2.1 and 9.8°C respectively on July 18 and June 30. The plume thickness usually decreased rapidly from the mouth. The plume width increased to 1.5 km just 1 km away from the mouth on July 17, but reached half of that on July 18. Lateral spreading might have been suppressed due to stronger longshore currents on July 18. Minimum dilutions of 2 and 5 occurred within 0.5 to 0.8 and 2.1 to 2.3 km from the mouth. The higher dilution on July 18 than 17, was due to stronger currents and enhanced mixing.

3.4 Discussion

In this chapter, the field observations of the Grand River plume, a major tributary of Lake Michigan, are discussed in order to understand the influence of wind, surface temperature, and water currents on the plume and pathogen transport. Extensive field experiments were carried out over four periods (August and June 2006, and June and July 2007) which included aerial photography over the plume, ADCP deployments, meteorological buoys, drifters, SF6 and Rhodamine WT tracer, 3D CTD profiling over the plume, CTD cast at the river mouth and bacterial sampling. The data assisted prediction of the transport and distribution of contaminants in the lake and highlighted the complex interaction between a buoyant river plume and coastal circulation.

The wind was from the S, SW and SSW for Series 1, 3, and 4. Only in Series 2 was the wind from the N. Generally, wind speeds were less than 24.5 m/s with averages ranging from 12.7 to 22.2 m/s. Currents flowed predominantly alongshore, as also indicated by the drifter measurements. They were fairly uniform in speed and direction over depth. The maximum longshore current (during Series 2) was around 70 cm/s. Alongshore current speeds for the offshore ADCPs were up to 50% faster than speeds nearshore (Series 3 and 4). Onshore current components were weaker and generally less than 20 cm/s.

Longshore currents were somewhat correlated with the local winds for periods 1 and 3. They followed the local wind direction mostly when the local wind was strong (>3 m/s) and blew for at least three hours. In those cases, the plume elongated following the current direction along the shore. Where the longshore local wind was slow (<3 m/s), lake large-scale circulation dominated the local currents. The plume shapes were dependent on the currents, which are influenced by the large scale circulation and the local wind, depending on the wind magnitude and duration

If the longshore currents were strong, the plumes were shore-attached. If the longshore currents were slow several possible scenarios occurred: they extended offshore in strong offshore wind or impacted the shoreline in a strong onshore wind, or spread either radially around the mouth or laterally offshore in slow wind. The plumes were either diffuse or had well-defined boundaries depending on the strength of the onshore-

offshore winds. These observations are the foundation for a proposed classification of surface buoyant plumes in Chapter 4. The strength of the longshore currents and onshore winds are determined and discussed more quantitatively based on the plume-cross-flow length-scale and the Richardson number.

The river was always warmer than the lake so it formed a buoyant layer on the surface. The greatest temperature difference between the lake and river (15.1°C) occurred in Series 3 (June 2007). The lowest (3.2°C) was in Series 2 (August 2006). The thickest observed plume at the mouth was in Series 3 (5.4 m) but it decreased rapidly to less than 0.5 m within a short distance (500 m) from the mouth. The plume also spread laterally and width increased within a short distance (about 1 km). The plume spreading rate was the greatest, in Series 3, on June 6, 2007, when the plume width was 4 km just 1 km from the mouth.

Minimum dilutions of 2, 5 and 10 occurred within 0.4 to 2.5, 1 to 3.5, and 2.3 to 4.5 km respectively from the mouth depending on current speed. Ecoli and total coliform counts were considerable in the river, respectively 40 and 12000 per 100 ml, and decreased to zero outside the river plume. The effect of physical dilution and decay in bacterial survival will be discussed further in Chapter 4.

CHAPTER 4

FIELD DATA ANALYSIS

4.1 Introduction

In Chapter 3, the field data collected over two years of field studies at Grand Haven was presented. In this chapter, an overview of the theory of surface buoyant plumes will be described and the results of the Grand River plume field experiments will be analyzed and discussed. The Grand River plume observations and dynamics are discussed and the previous lateral spreading relationships are complemented. A new hypothesis to determine the plume thickness at the mouth will be devised. The plume is categorized based on the hydrodynamic length scales and nondimensional parameters. An empirical dilution and trajectory formula is developed that expands previous studies on surface buoyant plumes in large aspect ratio channels, and finally the bacterial data are analyzed and the decay rates are discussed.

4.2 Plume Dynamics

For the period of the field experiments, the Grand River always formed a surface buoyant plume in the lake. The shape and geometry of the plume was dependent on the river speed, lake-river temperature difference, and the lake currents and wind. In the following sections, plume geometry (lateral spreading and thickness) will be further discussed, and the plume will be categorized based on these parameters.

4.2.1 Lateral Plume Spreading

A significant feature of surface buoyant plumes from rivers and estuaries is their dynamic lateral spreading. In order to understand the dynamics of mixing in the near and mid-fields (as defined in Chapter 2), it is crucial to recognize the spreading mechanism. In order to show that, the conductivity maps for different dates and times on June 20, and August 9, 2006, and June 5, and July 17, 2007 are compared with the available aerial

photos in Figure 4.1. The photographs have been selected to be representative of all the four periods. The boundaries of the plume are clear from where the water color changes from light brown to blue and corresponds approximately to the 300 µS/cm contour line. Lighter river waters often appear as multiple concentric rings (Garvine, 1984). In our case, rings were not observed, however the plume was laterally spreading as soon as it exited the river mouth.

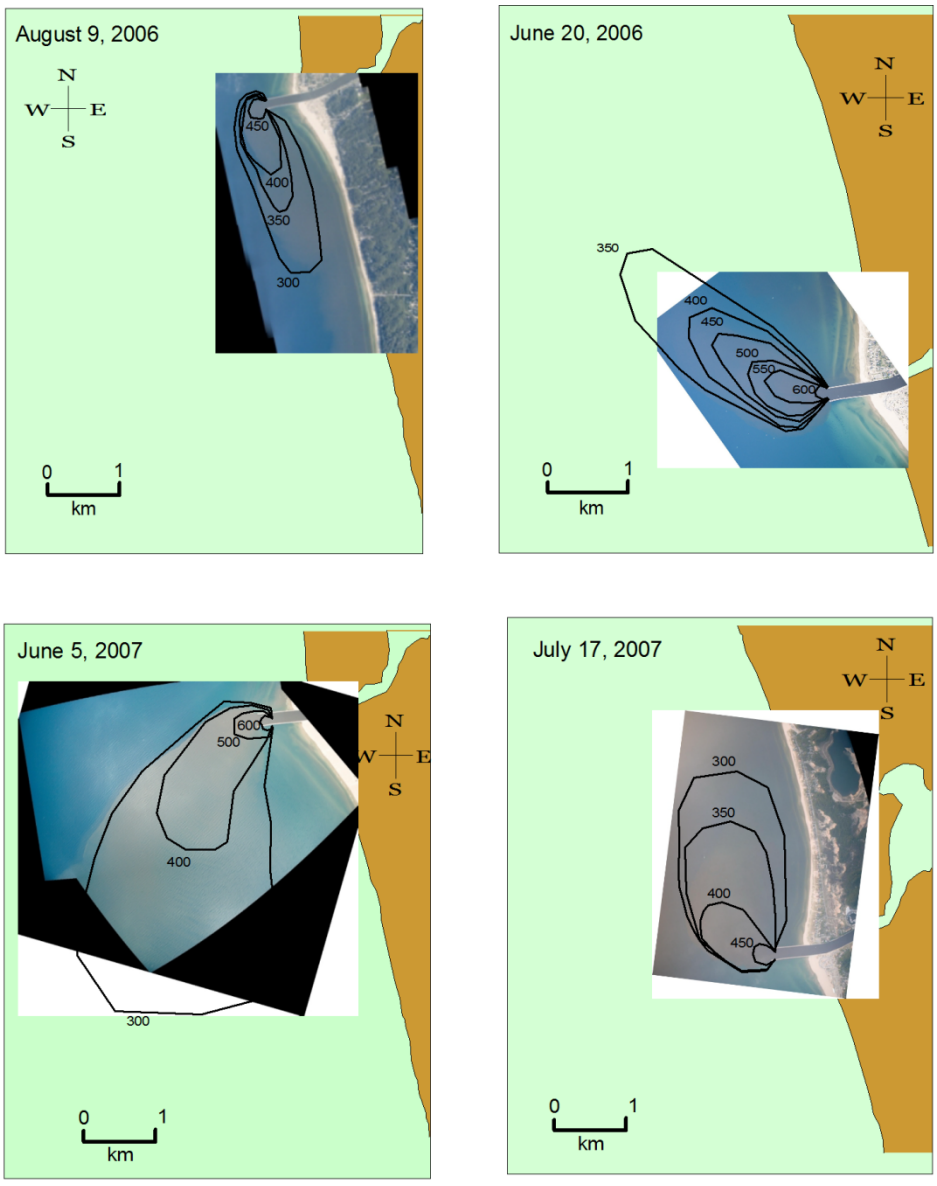

Figure 4.1 Examples of surface conductivity and corresponding aerial photos during the four experiment series.

The four experimental sets within 1 km from the mouth are shown again in Figure 4.2 in order to investigate the plume spreading. The field data shows that the plume spreading rate is the greatest close to the mouth and decreases farther away.

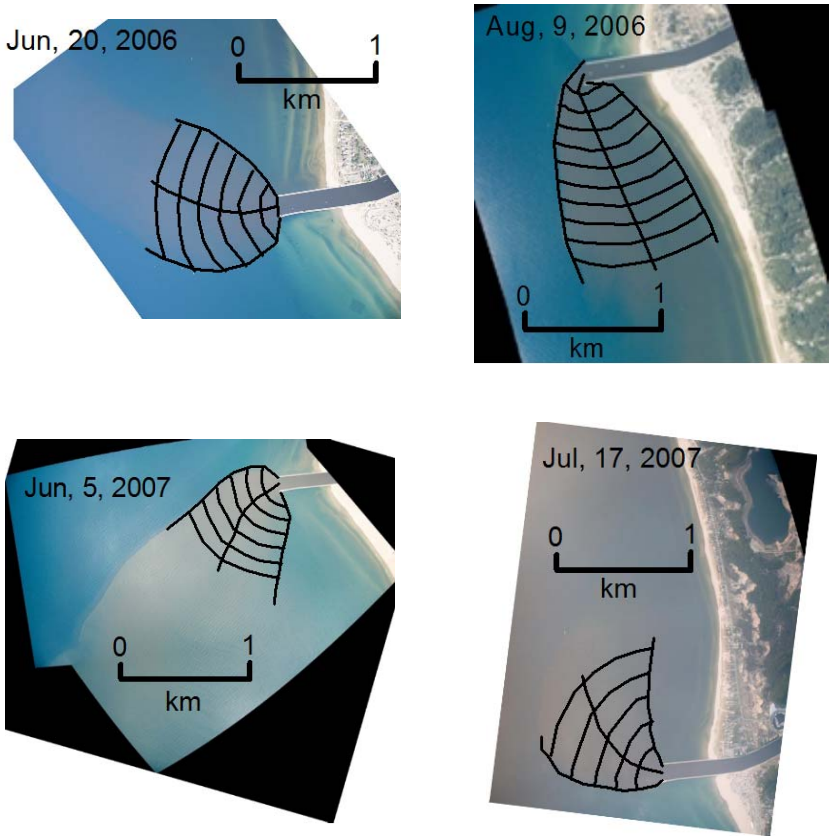

Figure 4.2 Radial spreading of the plume and the overlaid exponential fit within 1 km of the mouth.

As stated in Chapter 2, the relationship by Hetland and MacDonald (2008) is dependent on W_0, that cannot be readily determined. The plume arc lengths or plume widths, W at radial distances of r from the mouth are determined here. Their relationship has been modified to a new power fit on the field data that is dependent on the channel width, b, as below:

$$\frac{W}{b} = \gamma \left(\frac{r}{b} \right)^{1/\beta} \tag{4-1}$$

where β and γ were estimated as 2.0 and 3.0 respectively. These parameters are different from Hetland and MacDonald's for the Merimack river, probably because the Grand River has a smaller aspect ratio (=16) and the formula uses a new multiplier γ. Eqn. 4-1 is compared with the field data in Figure 4.3. The new power function agrees with the data with an r^2>0.95. The new formulae predicts the plume width (or spreading rate) well for distances close to the mouth (< 1 km) with no need to determine W_0, however, it must be tested for farther distances. The empirical constants may change for different rivers (with different geometries and discharges), therefore the formula should be calibrated for other cases.

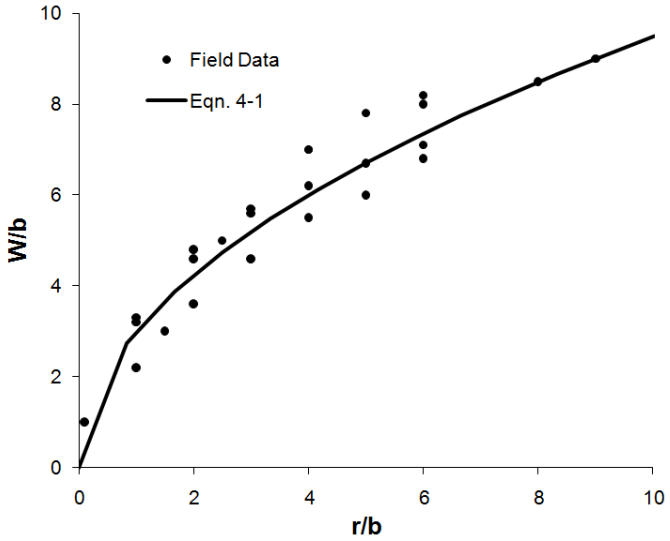

Figure 4.3 Power fit for the Grand River plume radial spreading within 1 km of the mouth.

4.2.2 Plume Thickness

In the Grand River, a three layer profile forms at the mouth due to the river-lake temperature difference: a uniform warmer upper layer in which a gravity current flows, an interface where mixing of the river and lake water occurs and the temperature and conductivity decrease rapidly, and a uniform colder bottom layer consisting of lake water. The plume-lake interface is shown in Figures 4.4 to 4.6.

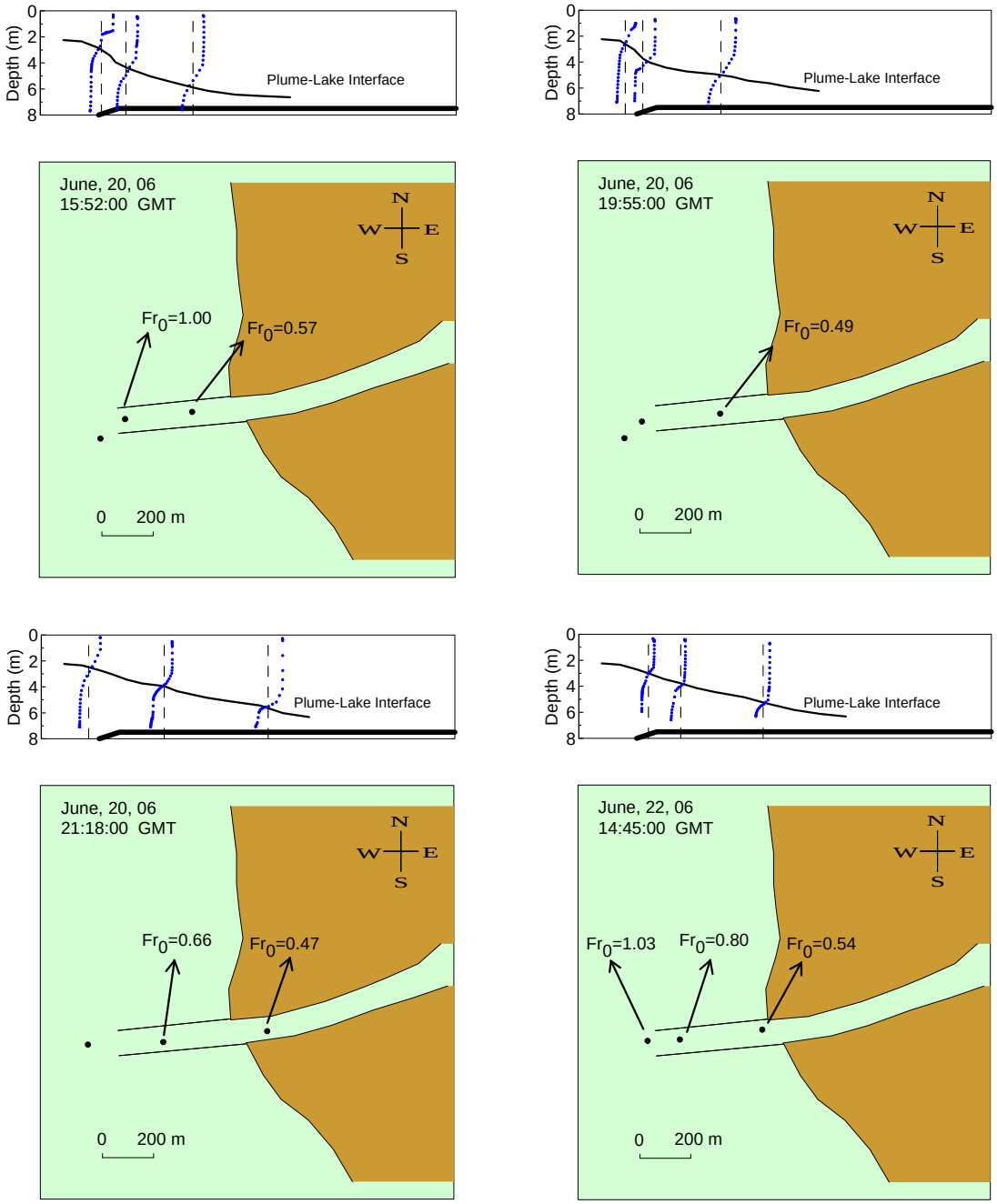

Figure 4.4 Selected temperature profiles along the channel on June 20, 2006; the local densimetric, Fr'_{h0} is based on the plume thickness.

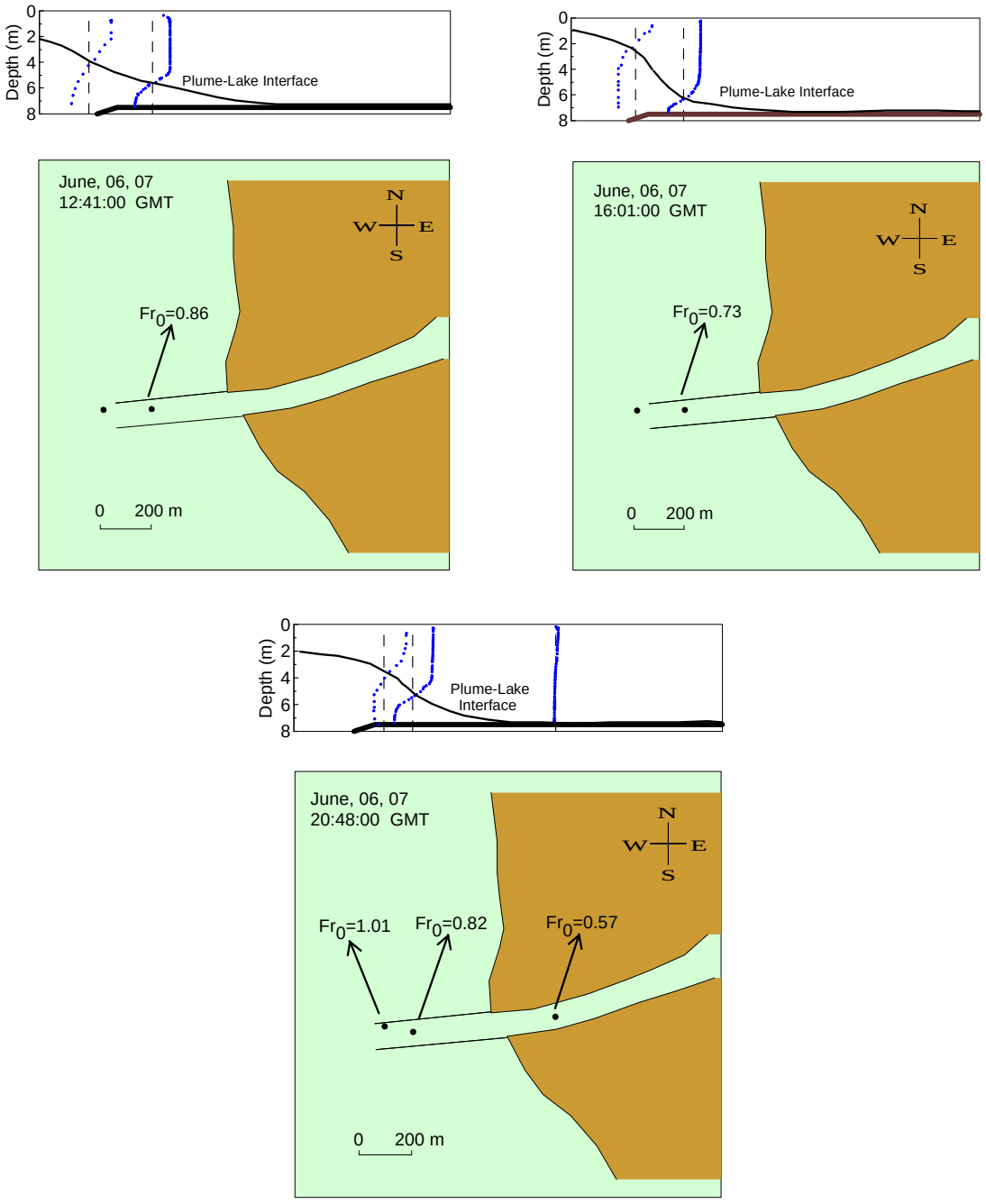

Figure 4.5 Selected temperature profiles along the channel on June 6, 2007; the local densimetric, Fr'_{h0} is based on the plume thickness.

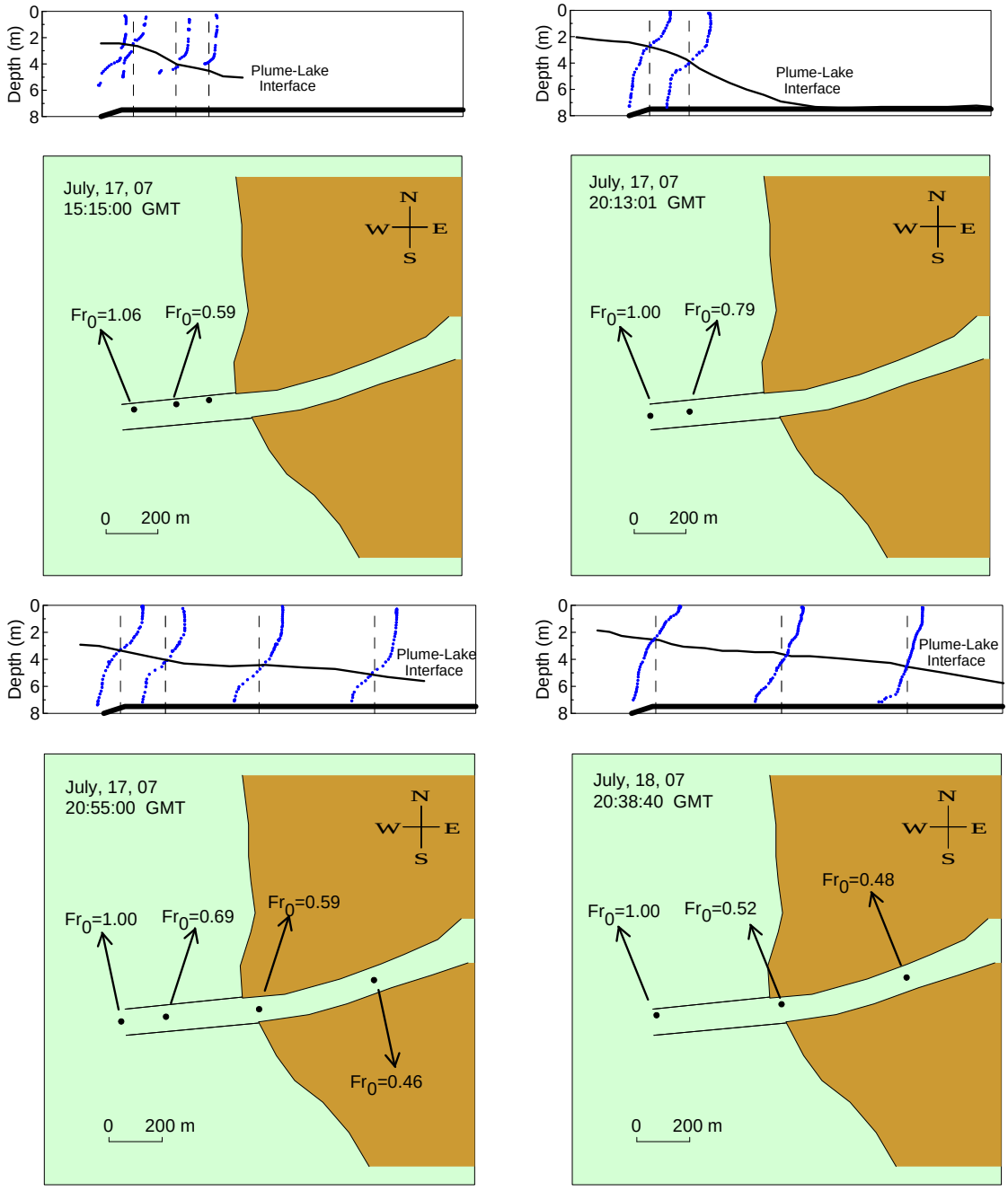

Figure 4.6 Selected temperature profiles along the channel on July 17 and 18, 2007; the local densimetric, Fr'_{h0} is based on the plume thickness.

The densimetric Froude number in the channel is generally calculated based on full river velocity and depth ($Fr'_d = U_0 / \sqrt{g'_0 d}$). If $Fr'_d \geq 1$ the flow is weakly buoyant with large inflow velocity and the plume is well-mixed over the channel depth with no upstream intrusion. However, when $Fr'_d \leq 1$, i.e. a strongly buoyant plume with small inflow velocity, the lake intrudes upstream into the channel and a stratified flow forms at the mouth, where the surface layer thins as it approaches the brink. A Froude number can be calculated based on the surface layer thickness ($Fr'_{h0} = U_{0h_0} / \sqrt{g'_0 h_0}$), where U_{0h_0} is the average flow velocity above the interface. In this case, the Froude number adjusts itself and the flow above the interface becomes critical ($Fr'_{h0} = 1$) approaching the channel outfall (Figures 4.4 to 4.6).

The hypothesis that critical depth occurs at the mouth, is similar to the gradually varied free surface flow at an overfall at the end of a channel with a mild slope (Clayton et al, 2005). The critical depth, h_c (i.e. depth where $Fr'_{h0} = 1$) occurs at a distance of 3 to $4h_c$ upstream of the brink. To find out the distances from the mouth where critical depths occurred, the adjusted Froude numbers (Fr'_{h0}) were determined from the CTD casts and V-Fin CTD profiling data at the river mouth and upstream for various days in June 2006, June and July 2007 are shown in Figures 4.5 to 4.8. They were typically 0.5 about 500 m upstream, and approached unity within about 5d (~ 40 m) from the mouth. The location of the critical depth varied, however, sometimes it occurred right at the mouth.

The critical depth for buoyant discharges in rectangular channels can be calculated in a manner similar to the neutral- or no-buoyancy flows, by assuming the layer thickness as the depth and replacing the gravitational acceleration (g) by the local modified acceleration due to gravity (g'):

$$h_c = (q_0^2 / g')^{1/3} \tag{4-2}$$

where q_0 is the discharge per unit width of the channel. The observed interface depth at the mouth, h_0 from temperature profiling data was closely predicted by the critical depth,

h_c , from Eqn. 4-2 with an r^2= 0.99 and scatter of less than 3% as shown in Figure 4.7. This also verifies the hypothesis discussed above.

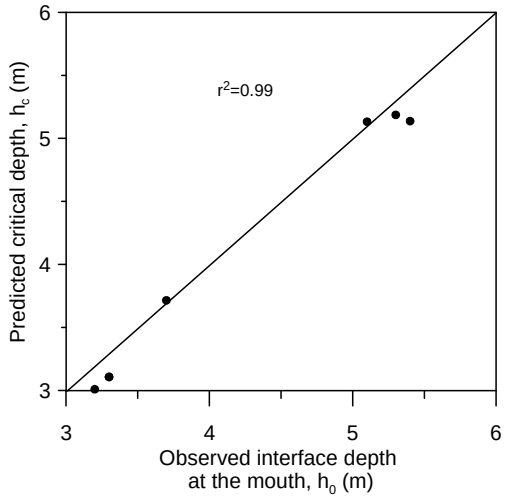

Figure 4.7 Predicted critical depth, h_c versus observed interface depth at the mouth, h_0.

Therefore, the initial plume thickness at the river mouth was considered either the interface depth just upstream of the channel outlet when temperature profiling data was available or was assumed to be equal to the critical depth when data was not available. The observed or computed plume thicknesses at the mouth and the lake-river temperature difference for the four field study periods varied as shown in Table 4.1.

Table 4.1 Lake-river temperature and plume thickness ranges for observation periods.

Series	Dates	Lake-river temperature difference (°C)	Plume thickness at the river mouth (m)
1	June 19-23, 2006	4.0 - 5.6	3.5 - 4.2
2	August 8-11, 2006	2.6 - 7.0	2.9 - 4.3
3	May 29-June 10, 2007	4.8 - 14.1	4.0 - 6.0
4	June 30-July 18, 2007	2.1 - 9.8	2.5 - 2.9

The plume thickness in the lake is controlled by a balance between vertical mixing and spreading (Jay et al, 2009). After the plume leaves the river, the frontal Froude number, $Fr = c/\sqrt{g'h}$ initially increases and then decreases to unity, i.e. the speed and thickness adjust so the frontal Froude number equals 1 (Hetland, 2009), where c is the local internal wave speed as explained in Chapter 2. The thickness of the plume in the

lake along the CTD transects on August 11, 2006, June 22, 2006, and June 6, 2007 are shown in Figure 4.8. The lake-plume interface is marked on the conductivity and temperature profiles.

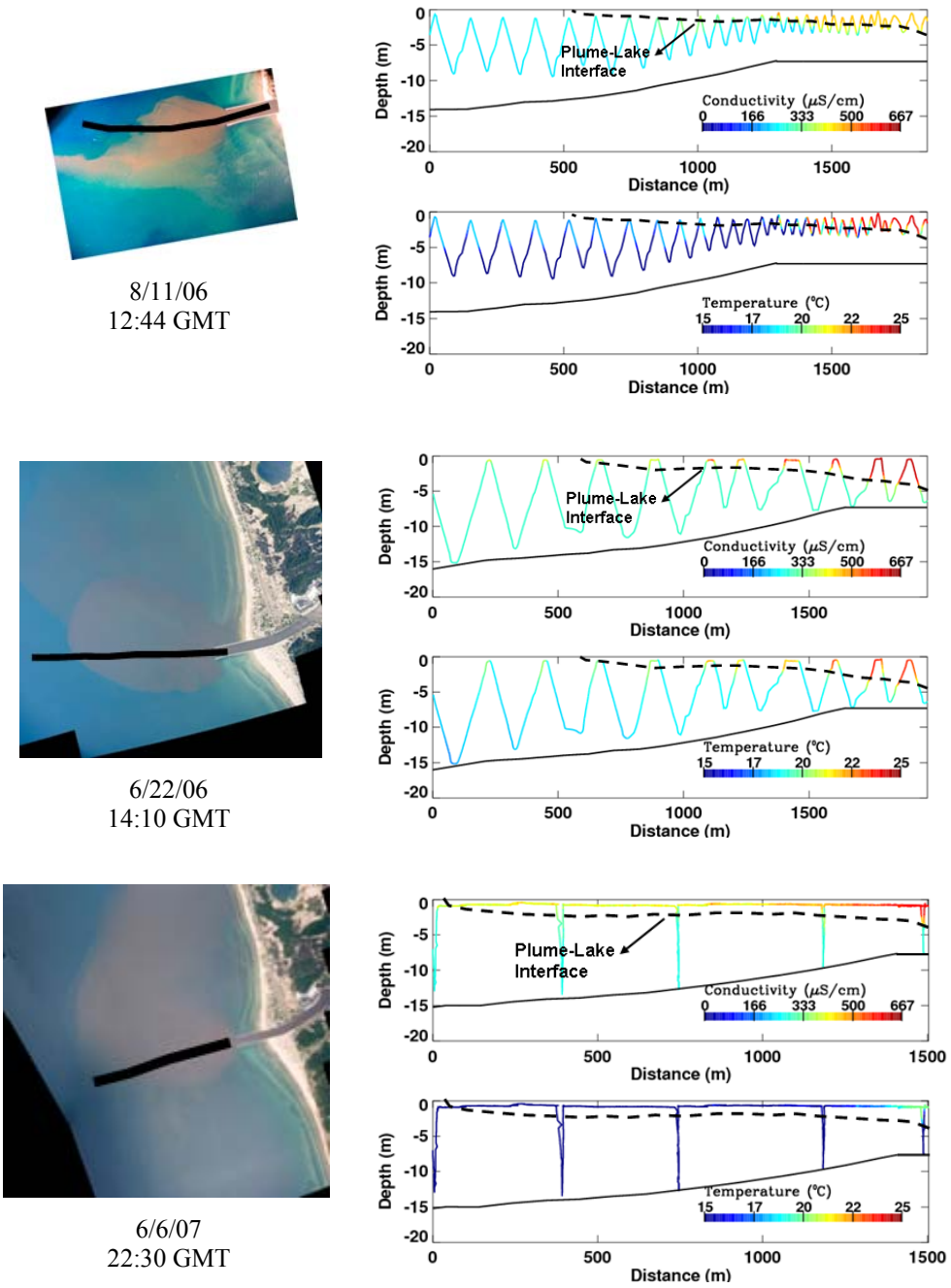

Figure 4.8 Aerial photos, CTD track, and the corresponding temperature and conductivity profiling in the lake: the dotted line designates the plume-lake interface.

Plume thickness variation in the lake along the trajectory centerline was also determined from sample vertical conductivity and temperature profiles along the plume centerline. The plume thickness (h) decreased rapidly, to less than 30% of the initial plume thickness (h_0), only within ξ=200 m from the mouth, where ξ is the distance along the plume centerline trajectory. Thereafter, it slowly decreased between ξ=200 m to 1 km (Figure 4.9). A power function was fit to the field data with an $r^2 = 0.88$ as below:

$$\frac{h}{h_0} = 0.3\left(\frac{\xi}{b}\right)^{-1/4} \tag{4-3}$$

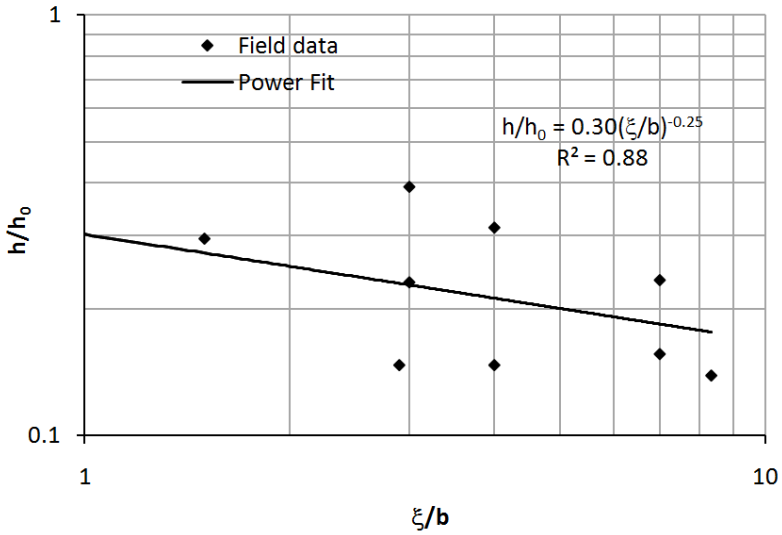

Figure 4.9 Best-fit curve of the plume thickness along the plume centerline.

4.3 Plume Classification

The Grand River plume conditions and flow characteristics for June and August 2006, and June and July 2007, when the aerial images were available, are summarized in Tables 4.2 to 4.9. In all the calculations, the channel depth, d, and the width, b_0 were assumed to be 7.5 and 120 m respectively. The inflow velocity, U_0, and the Froude number, Fr_d, were based on the full depth river velocity. The surface lake temperature (T_L) was obtained either from the satellite coastwatch surface temperature reading or from the CTD measurements. The river temperature (T_R) was obtained either from the

power plant intake located about 1 km upstream of the river mouth or from the CTD data in the river.

Table 4.2 Summary of river conditions, non-dimensional parameters, and plume classification for the aerial photographs on June 19, 20, 22, and 23, 2006.

Date	6/19/06	6/20/06	6/20/06	6/22/06	6/22/06	6/23/06
Time (GMT)	21:32	15:17	21:03	14:02	21:10	21:42
Lake Temp. (°C)	18.0 (Satellite)	18.0 (CTD)	18.0 (CTD)	18.6 (CTD)	18.6 (CTD)	18.2 (Satellite)
River Temp. (°C)	22.2 (Satellite)	23.6 (CTD)	23.6 (CTD)	23.3 (CTD)	23.3 (CTD)	22.2 (Satellite)
$Fr'_d = U_0/\sqrt{g'd}$	0.31	0.27	0.27	0.35	0.35	0.41
Critical Depth (h_c)	3.5	3.3*	3.3*	3.7*	3.7	4.1
L_b/d	15	1498	9421	552	103	63
Ri	1.2×10^{-2}	4×10^{-3}	1.1×10^{-2}	3.1×10^{-2}	5×10^{-3}	3×10^{-2}
Flow Classification	Shore Attached	Diffuse Offshore Spreading	Side Deflecting	Side Deflecting	Shore Impacting	Shore Attached
Photo Current: 5 cm/s Wind: 5 m/s	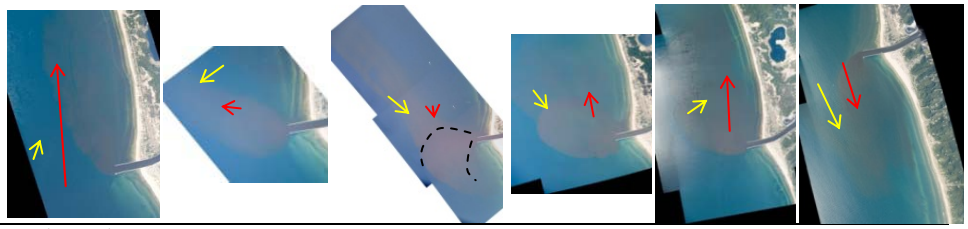					

* observed plume thickness at the mouth

Table 4.3 Summary of river conditions, non-dimensional parameters, and plume classification for the aerial photographs on August 8, 9 and 10, 2006.

Date	8/8/06	8/8/06	8/9/06	8/9/06	8/10/06
Time (GMT)	13:50	22:30	13:22	21:06	13:16
Lake Temp. (°C)	23.9 (CTD)	23.9 (CTD)	22.7 (CTD)	22.7 (CTD)	23.2 (CTD)
River Temp. (°C)	26.5 (CTD)	26.5 (CTD)	26.1 (CTD)	26.1 (CTD)	26.2 (CTD)
$Fr'_d = U_0/\sqrt{g'd}$	0.42	0.42	0.34	0.34	0.33
Critical Depth (h_c)	4.2	4.2	3.7	3.7	3.6
L_b/d	28	2	25	9	291
Ri	2×10^{-3}	1.0	6×10^{-3}	4×10^{-3}	7×10^{-3}
Flow Classification	Shore Attached	Shore Attached	Shore Attached	Shore Attached	Offshore Spreading
Photo Current: 5 cm/s Wind: 5 m/s					

Table 4.4 Summary of river conditions, non-dimensional parameters, and plume classification for the aerial photographs on August 10 and 11, 2006.

Date	8/10/06	8/10/06	8/11/06	8/11/06
Time (GMT)	17:16	23:14	12:42	15:40
Lake Temp. (°C)	23.3 (CTD)	23.3 (CTD)	18.0 (CTD)	18.0 (CTD)
River Temp. (°C)	26.2 (CTD)	26.2 (CTD)	25.0 (CTD)	25.0 (CTD)
$Fr'_d = U_0/\sqrt{g'd}$	0.33	0.33	0.23	0.23
Critical Depth (h_c)	3.6	3.6	2.8	2.8
L_b/d	797	233	516	328
Ri	1.9×10^{-3}	1.6×10^{-3}	9×10^{-4}	1×10^{-3}
Flow Classification	Diffuse Offshore Spreading	Diffuse Offshore Spreading	Diffuse Offshore Spreading	Diffuse Offshore Spreading
Photo Current: 5 cm/s Wind: 5 m/s				

Table 4.5 Summary of river conditions, non-dimensional parameters, and plume classification for the aerial photographs of May and June 2007.

Date	5/29/07	5/30/07	5/31/07	6/1/07	6/2/07
Time (GMT)	14:16	14:23	14:33	15:53	23:06
Lake Temp. (°C)	12.8 (Satellite)	13.6 (Satellite)	14.6 (Satellite)	16.3 (Satellite)	18.0 (Satellite)
River Temp. (°C)	21.1 (Intake)	21.1 (Intake)	22.8 (Intake)	22.8 (Intake)	22.8 (Intake)
$Fr'_d = U_0/\sqrt{g'd}$	0.42	0.43	0.37	0.39	0.44
Critical Depth (h_c)	4.2	4.3	3.9	4.0	4.3
L_b/d	210	161	654	279	892
Ri	2.3×10^{-2}	2.9	3.9	2.4	4×10^{-2}
Flow Classification	Offshore Spreading	Offshore Spreading	Offshore Spreading	Offshore Spreading	Side Deflecting
Photo Current: 5 cm/s Wind: 5 m/s	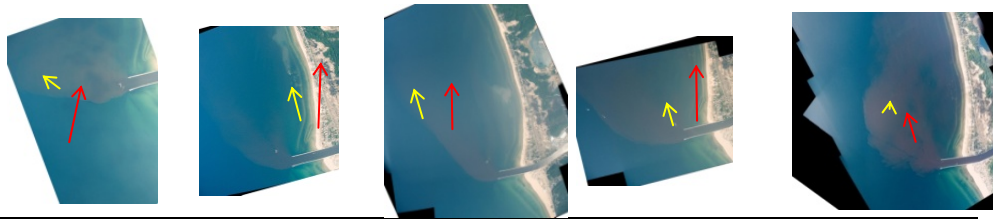				

Table 4.6 Summary of river conditions, non-dimensional parameters, and plume classification for the aerial photographs of June 2007.

Date	6/5/07	6/5/07	6/6/07	6/6/07	6/6/07
Time (GMT)	13:42	16:55	12:05	16:15	22:30
Lake Temp. (°C)	8.2 (CTD)	7.3 (CTD)	5.4 (CTD)	6.9 (CTD)	6.8 (CTD)
River Temp. (°C)	20.8 (CTD)	20.3 (CTD)	19.5 (CTD)	20.0 (CTD)	20.0 (CTD)
$Fr'_d = U_0/\sqrt{g'd}$	0.52	0.53	0.58	0.57	0.57
Critical Depth (h_c)	4.8	4.9	5.3*	5.4*	5.1*
L_b/d	719	701	652	81092	63654
Ri	7.4×10^{-2}	3.3×10^{-1}	6.3	3×10^{-1}	3.8×10^{-1}
Flow Classification	Offshore Spreading	Offshore Spreading	Radial Spreading	Side Deflecting	Side Deflecting
Photo Current: 5 cm/s Wind: 5 m/s		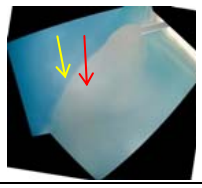		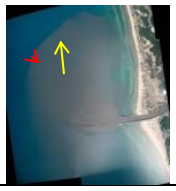	

* observed plume thickness at the mouth

Table 4.7 Summary of river conditions, non-dimensional parameters, and plume classification for the aerial photographs of June 2007.

Date	6/8/07	6/8/07	6/9/07	6/10/07
Time (GMT)	15:30	23:10	22:58	23:00
Lake Temp. (°C)	12.3 (Satellite)	11.4 (Satellite)	15.1 (Satellite)	15.7 (Satellite)
River Temp. (°C)	21.1 (Intake)	21.1 (Intake)	21.1 (Intake)	21.7 (Intake)
$Fr'_d = U_0/\sqrt{g'd}$	0.62	0.60	0.68	0.59
Critical Depth (h_c)	5.6	5.5	6.0	5.5
L_b/d	49	5475	24425	143
Ri	8×10^{-3}	1.2×10^{-2}	4.3	2.6
Flow Classification	Shore Attached	Side Deflecting	Side Deflecting	Shore Impacting
Photo Current: 5 cm/s Wind: 5 m/s			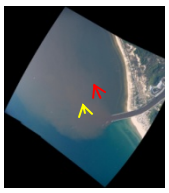	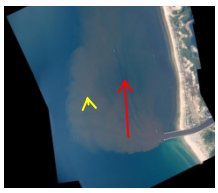

Table 4.8 Summary of river conditions, non-dimensional parameters, and plume classification for the aerial photographs of June and July 2007.

Date	6/30/07	7/2/07	7/6/07	7/9/07	7/11/07	7/13/07
Time (GMT)	14:05	23:22	14:06	13:07	23:17	13:00
Lake Temp. (°C)	14.1 (Satellite)	13.0 (Satellite)	18.9 (Satellite)	17.5 (Satellite)	20.8 (Satellite)	21.4 (Satellite)
River Temp. (°C)	23.9 (Intake)	22.8 (Intake)	23.9 (Intake)	25 (Intake)	25.6 (Intake)	24.4 (Intake)
$Fr'_d = U_0/\sqrt{g'd}$	0.23	0.19	0.23	0.15	0.18	0.21
Critical Depth (h_c)	2.9	2.5	2.9	2.2	2.5	2.7
L_b/d	183	5×10^{6}	1327	48	65	9653
Ri	3×10^{-1}	4×10^{-2}	2×10^{-2}	8×10^{-3}	2×10^{-3}	3×10^{-3}
Flow Classification	Side Deflecting	Offshore Spreading	Offshore Spreading	Shore Attached	Shore Attached	Diffuse Offshore Spreading
Photo Current: 5 cm/s Wind: 5 m/s	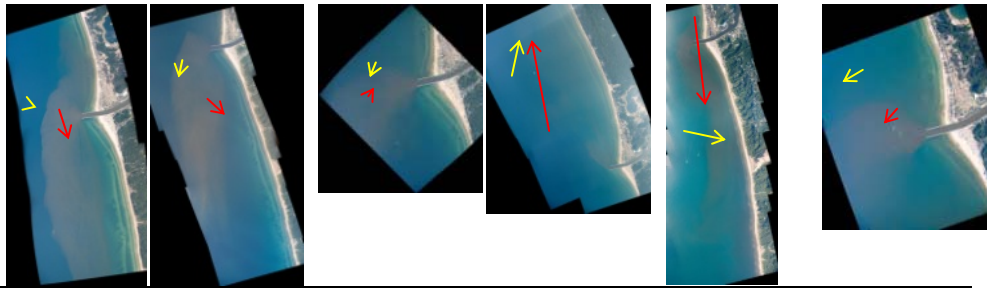					

Table 4.9 Summary of river conditions, non-dimensional parameters, and plume classification for the aerial photographs of June and July 2007.

Date	7/17/07	7/18/07	7/18/07	7/18/07
Time (GMT)	15:40	00:44	13:15	22:30
Lake Temp. (°C)	21.4 (CTD)	21.4 (CTD)	21.7 (CTD)	22.1 (CTD)
River Temp. (°C)	23.5 (CTD)	24.4 (CTD)	24.6 (CTD)	24.8 (CTD)
$Fr'_d = U_0/\sqrt{g'd}$	0.25	0.21	0.22	0.22
Critical Depth (h_c)	3.2*	3.2	3.2	3.2
L_b/d	1576	70	42	65
Ri	5×10^{-3}	2×10^{-3}	7×10^{-3}	2×10^{-3}
Flow Classification	Diffuse Shore Impacting	Diffuse Shore Impacting	Shore Attached	Shore Attached
Photo Current: 5 cm/s Wind: 5 m/s				

* observed plume thickness at the mouth

The jet or plume criterion based on the Jones et al. (2007) classification is $L_M/\left(L_Q A^{1/4}\right)$ or $Fr'_d/A^{1/4}$, where L_Q and L_M are determined from Eqns. 2-2 and 2-3, and A is the aspect ratio of the channel. This ratio is always less than 1.5 for our data, suggesting that the Grand River generates a plume-like flow, not a jet (i.e. negligible effect of momentum over buoyancy). Their shore-hugging or upstream intruding criterion ($L_b A^{1/2}/L_Q$) is also mostly greater than one, i.e. an upstream intruding plume case. Both of their plume categories include only nearshore cases and do not encompass all the shapes and dynamic of the plumes reported in Chapter 3, e.g. offshore plumes. In addition their classification is limited to the channels with aspect ratios less than 5, and wind effects are not included.

Based on Tables 4.2 to 4.9, a new classification is proposed that expands the plume-like class of CORMIX3 by adding more possible plume shapes for unattached or offshore extending categories and including wind effects. It considers crossflow (or depth-averaged longshore currents) as the main driver in plume longshore transport versus buoyancy, to determine whether the plume is shore attached or unattached. It uses a ratio of plume-crossflow length scale, L_b from Eqn. 2-5, over the channel depth, d which is L_b/d. If the plume is unattached, this classification accounts for wind-induced surface stresses in the plume's onshore-offshore movement versus buoyancy, and uses the Richardson number, Ri, similarly defined in Fischer et al. (1979) for characterizing wind-induced mixing in lakes. However, the only difference is wind shear velocity has been substituted here by W_y, the onshore wind component, and the average depth by the plume initial thickness, h_0. It is defined as:

$$Ri = g'h_0/W_y^2 \tag{4-1}$$

The non-dimensional parameters (L_b/d and Ri), for the different Grand River plume shapes are given in Tables 4.2 to 4.9. Based on the range of these observations, a flowchart is presented in Figure 4.10 that classifies surface buoyant plumes into six different classes. The plume is divided into two major attached and unattached categories. Shore Attached plumes occur when the longshore currents are strong ($L_b/d < 65$).

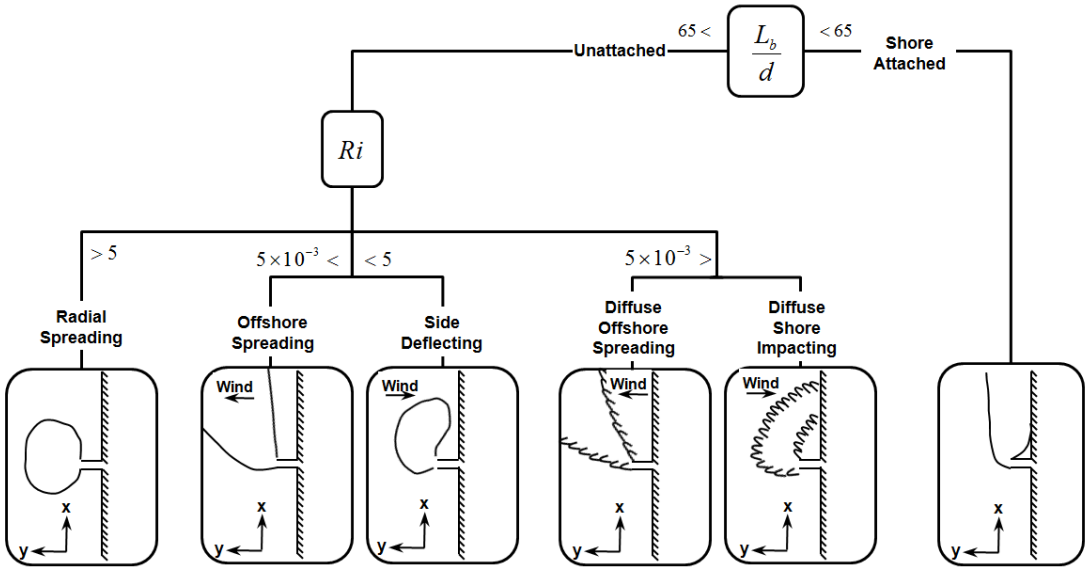

Figure 4.10 Proposed surface buoyant plumes classification.

Unattached plumes occur in weak longshore currents ($L_b/d > 65$) where the effect of onshore wind becomes important. The Ri is the ratio of stability due to stratification over the stress caused by wind. When $Ri > 5$, wind effect is negligible, the plume is mainly driven by buoyancy and spreads radially. If $5\times10^{-3} < Ri < 5$, plume mixing is enhanced by the wind and spreads offshore or deflects to the side depending on the offshore or onshore wind. When $Ri < 5\times10^{-3}$, mixing is dominated by strong winds and the plume becomes diffuse, spreading offshore or impacting the shore. Note that the criterion constants (65 for attached, 5 and 5×10-3 for unattached) are determined from the Grand River observations and might vary for a channel with a different channel aspect ratio or offshore extension length.

4.4 Plume Trajectory and Dilution

The river outflow forms a surface buoyant jet, of which there have been many studies reported in the engineering and oceanographic literature. Due to the 3D flow characteristics, and dependence of the flow on different weather conditions, field data collection is costly and difficult, and most studies have primarily focused on channel

outlets with small aspect ratios (b/d< 3). Only a few studies have investigated wider channels ($3 < b/d$). The Grand River channel has $b/d = 16$. In this chapter, a new model for surface buoyant plumes in large aspect ratio channels is developed and evaluated with the comprehensive field studies. Following Rajaratnam (1988), the jet trajectory can be simplified to the following power law expression:

$$y/\alpha d = C_1 \left(x/\alpha d \right)^{n_1} \tag{4-4}$$

where C_1 is 4.3, and n_1 is 0.5 for shore attached plumes. Eq. 4-5 was evaluated for various attached and unattached cases. The empirical constants (C_1 and n_1) depend on the onshore wind magnitude for unattached cases based on the plume categorization in Figure 4.10. The average values of 6.3 and 0.5 are recommended for C_1 and n_1 in unattached plumes. The proposed model predictions for an attached jet trajectory case on July 18, 2007 and unattached case on June 5, 2007 are compared with Rajaratnam (1988), and AGM (1996) models (Eqns. 2-9 and 2-13) and the field data as shown in Figures 4.11 and 4.12.

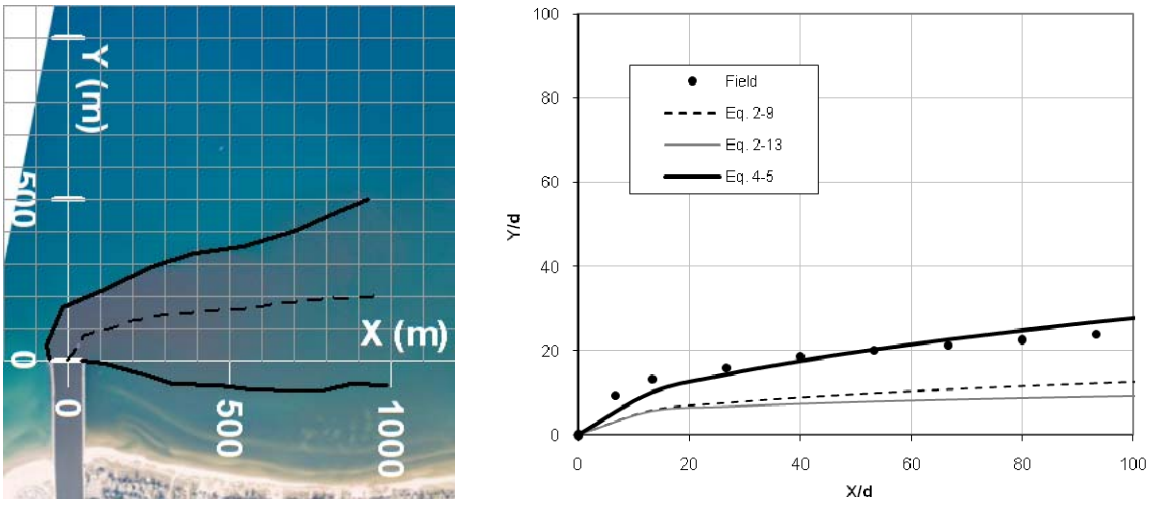

Figure 4.11 A shore attached jet trajectory overlaid on the aerial photo on July 18, 2007 13:15 GMT (left); and comparison of predicted and observed jet trajectory (right).

The Rajaratnam and AGM models underestimate the extent of the plume intrusion possibly because they were both developed for circular jets in crossflow, whereas we

have a rectangular outfall with large aspect ratio. The proposed model agrees fairly well with the field data. It predicts plume trajectory with an uncertainty of about 10 percent.

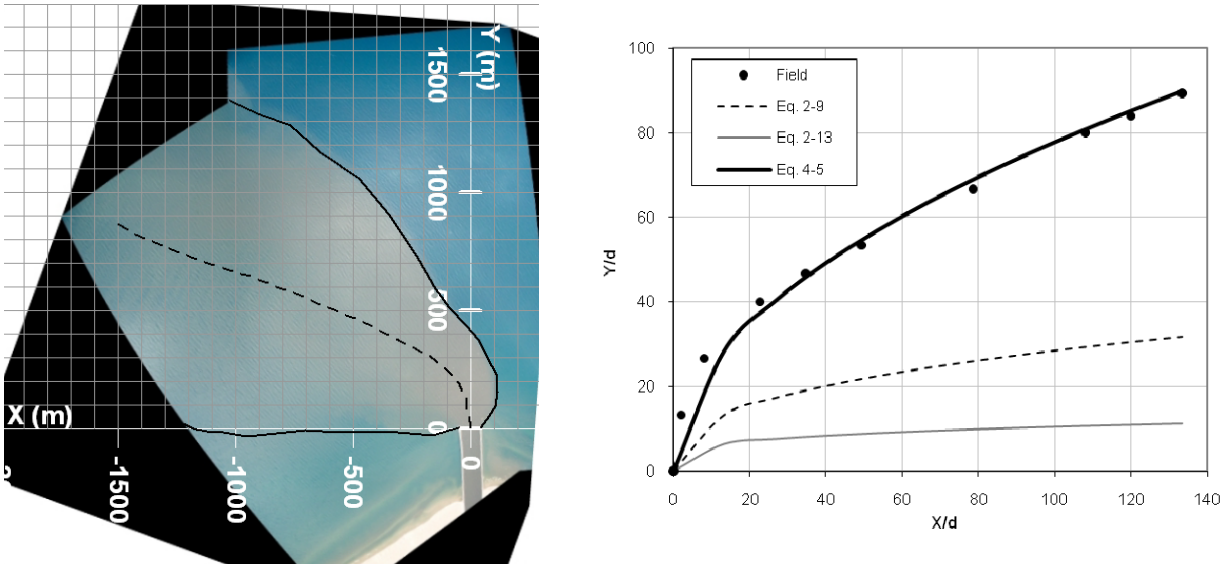

Figure 4.12 An unattached jet trajectory overlaid on the aerial photo on June 5, 2007 16:55 GMT (left); and comparison of predicted and observed jet trajectory (right).

The minimum dilution can also be described by an equation similar to McCorquodale (2007):

$$S_{\min} = (\xi / b)^{n_2} \alpha^{0.06} \left[1 + (1 + Fr_0')^{-1}\right]^{1.5} (d/b)^{0.2} \geq 1.0 \qquad (4\text{-}5)$$

for the ranges of $\xi / b < 8$, $\alpha < 12$, 40<Q_0 (m^3/s)<180, and 0.15< Fr_d' < 0.70. n_2 was determined by fitting the best power curve on the cases studied from the Grand River plume. It is 1.0 for a fully attached plume, and approaches 0.5 as the plume spreads offshore depending on the onshore wind for unattached plumes. It was assumed that Fr_0' = 1 at the source, based on the hypothesis that critical depth occurs at the river mouth for a strongly buoyant plume (Fr_d' < 1). The Grand River channel was also considered to have an aspect ratio of $d/b = 1:16$, and an extension of about 250 m to the lake. The minimum dilution models, Eqn. 2-11 (McCorquodale, 2007), Eqn. 2-10 (Carnelos 2000), Eqn. 2-12 (AGM model; Abdel-Gawad, 1985); and Eqn. 4-14 (this study) are compared with two sample attached and unattached field observed cases in Figure 4.13. The field

dilutions were calculated from Eq. 3-1. Note that Eqns. 2-11 and 2-10 are not valid for $\xi / b < 3$ and Eqn. 2-12 for $\xi < \xi_0$, and cannot predict dilution in those ranges.

In the attached case, Eqn. 2-12 predicts minimum dilutions of 7 for $\xi / b = 8$, the closest to the field data and Eqn. 4-6, however Eqns. 2-10 and 2-11 underestimated dilutions. Eqn. 2-12 is based on the experiments including channels with offshore extensions, which may be why it predicts higher dilutions than the other models (Eqns. 2-11 and 2-10) for the attached plumes. Eqns. 2-11 and 2-10 were developed from data for outfalls placed on the shoreline (without offshore extension), which reduces entrainment and consequently decreases the dilution. Eqn. 2-11 also assumes $Fr_0' < 1$ and does not account for the adjustment of the Froude number to unity at the outlet for strongly buoyant plumes. That can result in underestimation of minimum dilution in the attached plumes.

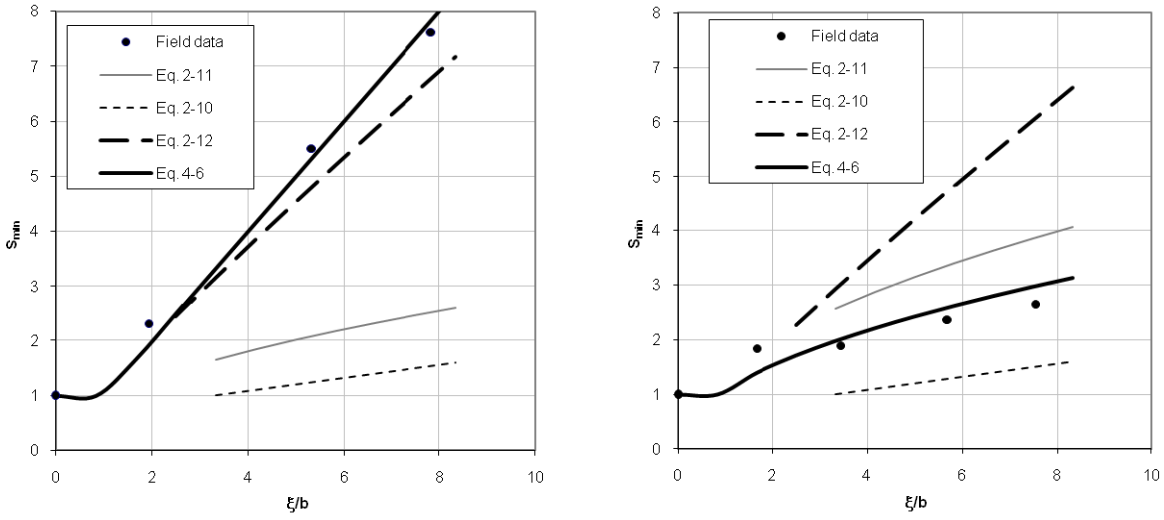

Figure 4.13 Comparison of predicted and observed minimum dilutions of an attached plume on July 18, 2007 13:15 GMT (left), and an unattached plume on June 5, 2007 16:55 GMT (right).

In the unattached case, Eqn. 2-12 overestimates the dilution possibly due to the small aspect ratio of the outfall (<3) on which the experiments were conducted and therefore greater lateral mixing rates. The minimum dilution predictions of Eqn. 2-11 are the closest to the field data in the unattached cases. Eqn. 2-10 underestimates in both

attached and unattached cases, possibly because it is a simplified relationship that does not consider Fr_0'.

4.5 Bacteria measurements

As discussed in Section 3.3.3.3, surface fecal indicator bacteria (E. coli and total coliform) samples were collected on June 5 and 6, 2007 along with the CTD profiling. Sewer overflows that occur after heavy rain events can be a significant source of bacterial pollution (McLellan, 2007). Therefore the total daily rainfall data is analyzed for the summer season (June to August) of 2006 and 2007.

4.5.1 Rainfall and discharge

Rainfall data were obtained from the National Weather Service stations at Grand Rapids Kent County International Airport (42°52′N, 85°31′W) and Muskegon County Airport (43°10′N, 86°14′W). The Grand Rapids station is located inside the Grand River drainage basin almost 70 km upstream of the river. Muskegon County Airport station is about 6 km from the river mouth but is located outside the basin. Since there was no rainfall record closer to Grand Haven, both stations were used to evaluate the rainfall effect in river discharge.

River flows were obtained from the United States Geological Survey (http://waterdata.usgs.gov/nwis) daily stream records. The gage is located on the Grand River right bank 500 ft upstream from the bridge on Fulton Street in Grand Rapids (at 42°57′52″, 85°40′35″ more than 90 km upstream of the Grand Haven pier). As stated in Chapter 3, the daily average discharge was recorded at Grand Rapids (http://waterdata.usgs.gov/nwis) and corrected for the effect of the downstream watershed up to the river outlet multiplying by a catchment area correction factor of 1.156 (GLERL). The results are shown on Figure 4.14.

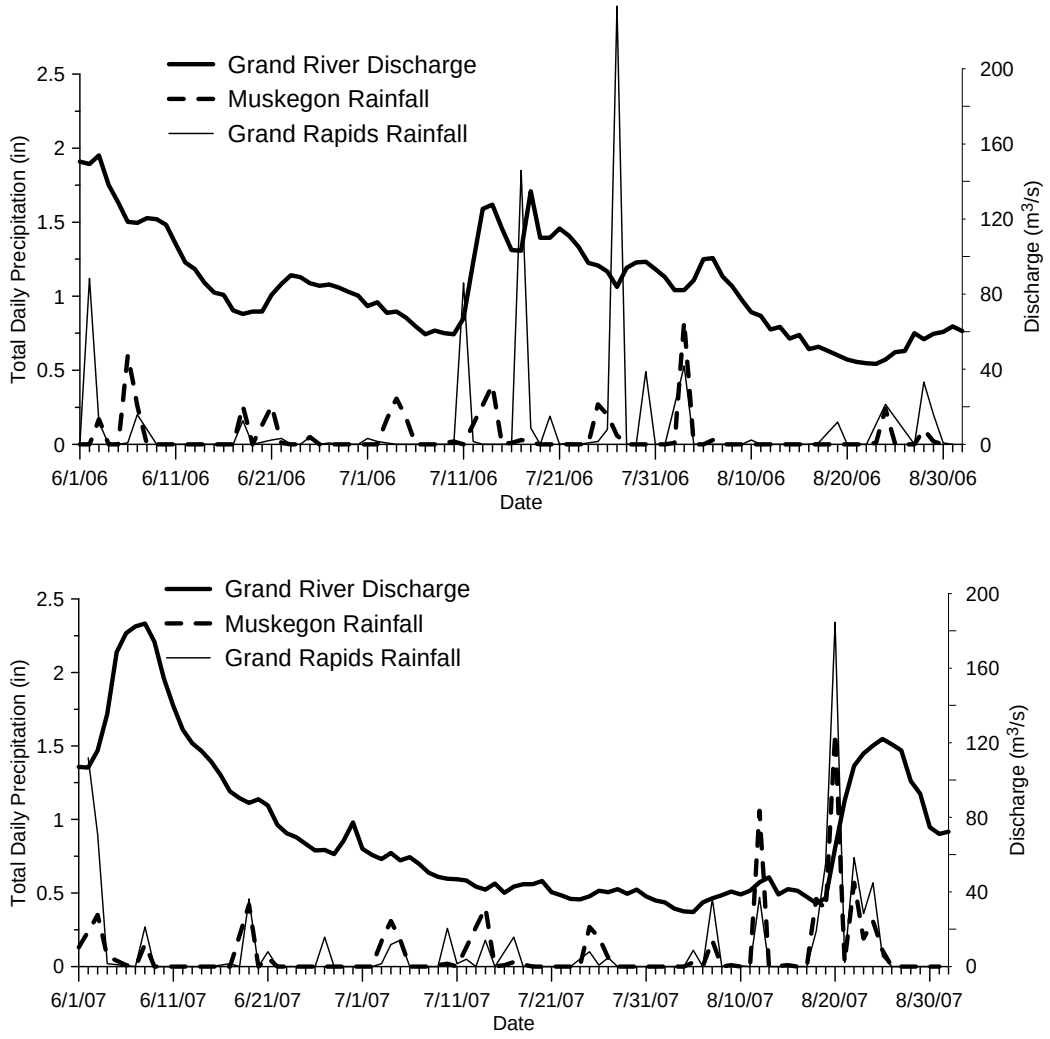

Figure 4.14 Rainfall record and the hydrograph of the Grand River during June, July and August of 2006 (bottom), and 2007 (top).

In both years 2006 and 2007, the river discharge peaks are generally observed soon after a rainfall event. At the beginning of June 2006, the discharge rate was fairly high (154 m^3/s) following a rainfall event of 1.9 inches. After that, until July 11, no significant rainfall occurred, and the next series of rainfall events started with a season record high precipitation of 2.96 inches on July 27. The river flow rate ranged from 43 m^3/s to 154 m^3/s with an average of 85 m^3/s from June to August 2006.

The period of June-August 2007 started with a heavy rainfall of 1.42 inches that caused a fairly high river discharge of 184 m^3/s on June 9. Following that, there were some smaller rain events until August 20, where the season greatest rain (2.34 inch) took

place. The river flow rate ranged from 29 m^3/s to 184 m^3/s with an average of 72 m^3/s over this period.

4.5.2 Beach bacteria

Beach bacterial data were obtained from the Michigan Department of Water Quality beach monitoring data base (http://www.deq.state.mi.us/beach/). The Ottawa County Health Department collects weekly samples every summer season at regular times (three individual daily samples and average). Data were obtained from seven beaches (Figure 4.15).

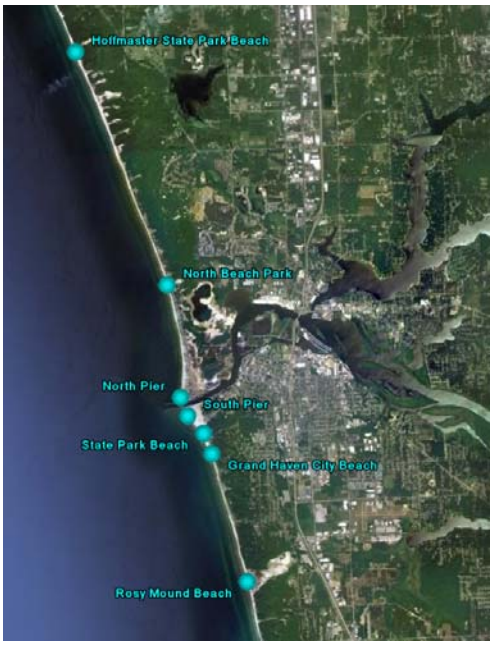

Figure 4.15 Beach bacterial sampling locations near Grand Haven.

They include Grand Haven City Beach (43° 2' 51.97", -86° 14' 35.77"), Grand Haven State Park (43° 3' 7.20", -86° 14' 43.44"), Hoffmaster Public Beach (43° 7' 52.72", -86° 16' 42.38"), North Beach (43° 4' 58.08", -86° 15' 16.20"), Rosy Mound Recreation Area (43° 1' 16.46", -86° 14' 3.41"), North Pier (43° 3' 34",-86° 15' 6"), and South Pier (43° 3' 20", -86° 14' 59"). During our field experiments beach samples were collected at North Beach and Grand Haven Pier on June 5 and 6, 2007 in addition to the Ottawa County data.

The meteorological conditions along with the field measurements will assist us in identifying the major sources of plume bacteria. The bacterial counts and total daily precipitation are plotted in Figure 4.16. The rainfall peaks sometimes correspond with the bacterial spikes in 2006 (such as June 21, July 11, July 18, and August 24), and in 2007 (June 20, June 28, and July 19), but the greatest precipitation does not necessarily result in the highest beach bacteria level.

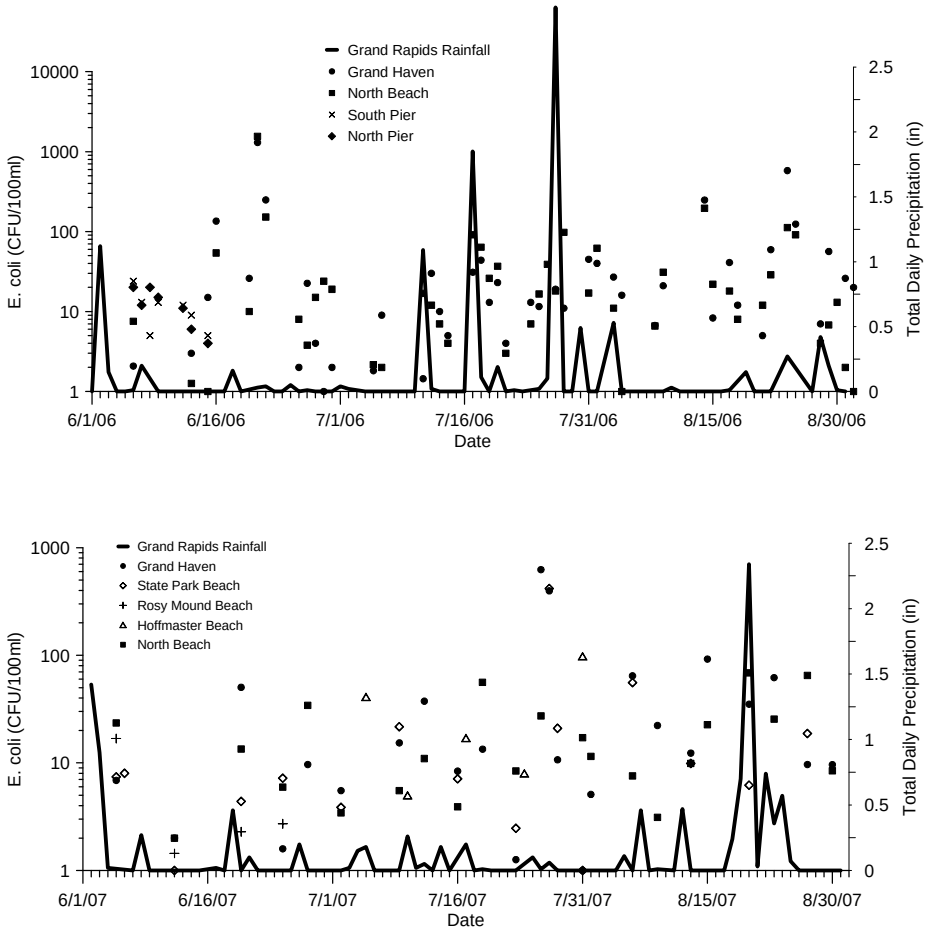

Figure 4.16 Beach bacterial samples and total daily precipitation at selected beach sites during May-August 2006 (top) and 2007 (bottom).

Beach bacteria can be influenced by factors other than river discharge, such as beach sand. It is believed that beach sand can provide a suitable environment for survival and reactivation of bacteria (Yamahara et al, 2007). Therefore, establishing a link between beach bacteria and the offshore plume that is primarily affected by river

contamination is difficult. In the present study we focus on the plume, as the river can be a source of beach bacteria. In the next sections, the spatial variation of bacteria in the plume is analyzed and compared with surface conductivity, and the effect of radiation is investigated to better understand the relative effects of physical dilution and die off.

4.5.3 Plume bacterial observations

The plume bacterial surveys were conducted on June 5 (15:38-19:31 EDT) and 6 (15:45-20:00 EDT), 2007. The boat tracks, surface bacterial counts (shown previously in Figures 3.31 and 3.32), and surface conductivity measurements (for depths less than 1.5 m) on both days are shown in Figure 4.17. Sampling extended from about 1 km into the channel out into the lake in the plume where it was visible or an elevated conductivity level was detected. E. coli levels varied from 0 (outside the plume) to 40 CFU/100ml (in the river) on the 5th, and to 47 CFU/100ml on the 6th. Total coliforms varied from 0 outside the plume to 12,000 CFU/100ml in the river on the 5th, and to 20,000 CFU/100ml the 6th. Surface conductivities ranged from 285 to 625 μS/cm on June 5, and from 281 to 593 μS/cm on June 6. The relationship between bacterial concentration and conductivity is discussed further in Section 4.5.3.1.

Bacterial reductions can be caused by both physical dilution (mixing), and decay (mortality). In order to understand and evaluate both roles, their effects must be assessed individually. We can estimate physical dilution and bacteria travel time from the conductivity and current data, and the die-off rate from the bacterial concentration. We can also determine the relative levels of importance of physical dilution and die-off in bacterial reduction. This is discussed in Section 4.5.3.2. Bacterial decay is strongly affected by solar radiation or cloud cover that is covered in Section 4.5.3.3.

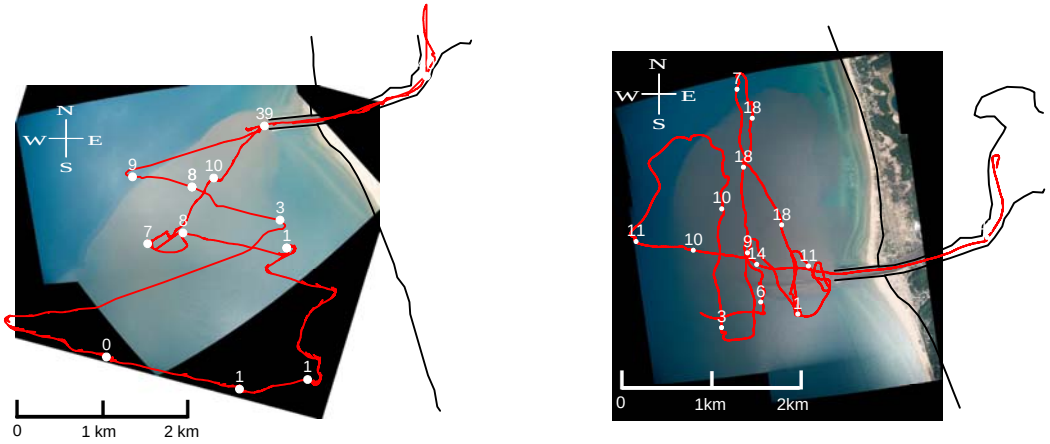

a) E. coli counts/100 ml in surface samples on June 5 (right), and 6 (left), 2007.

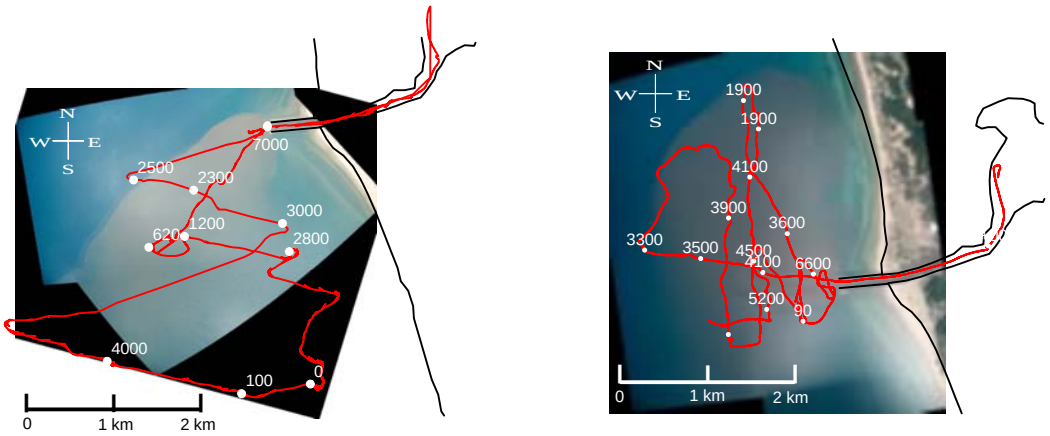

b) Total coliform counts/100 ml on June 5 (right), and 6 (left), 2007.

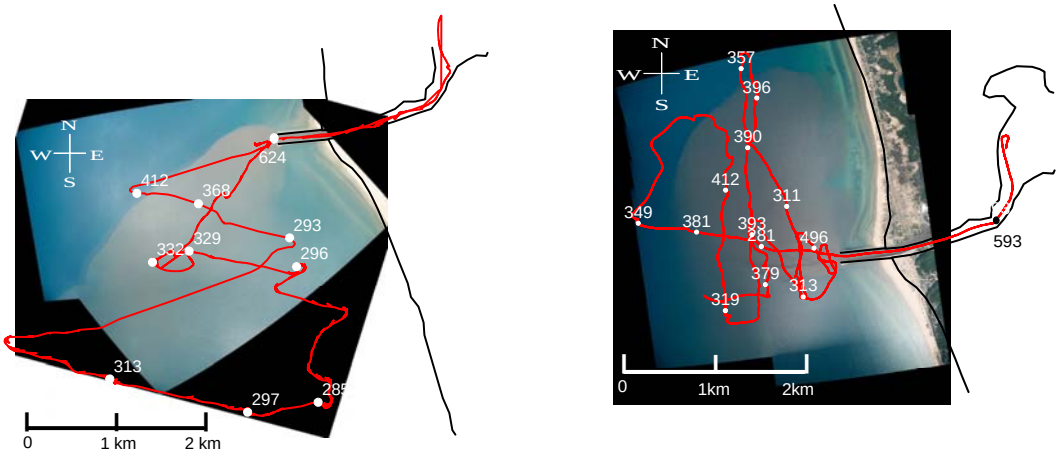

c) Surface conductivity in µS/cm on June 5 (right), and 6 (left), 2007.

Figure 4.17 E. coli and total coliform counts, and surface conductivity on June 5 and 6, 2007.

4.5.3.1 Conductivity and bacteria

E. coli and total coliform are plotted versus conductivity for both days in Figure 4.18.

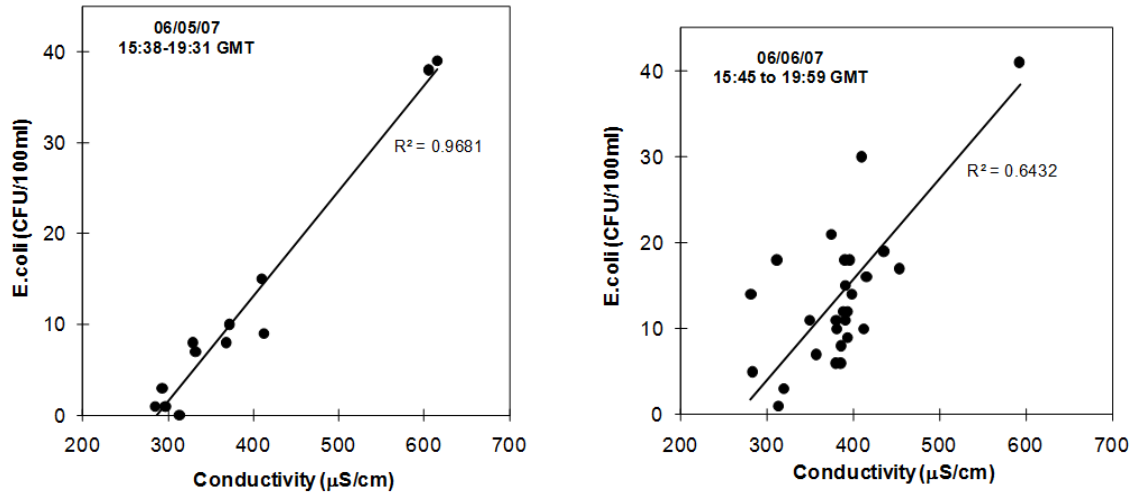

a) E. coli

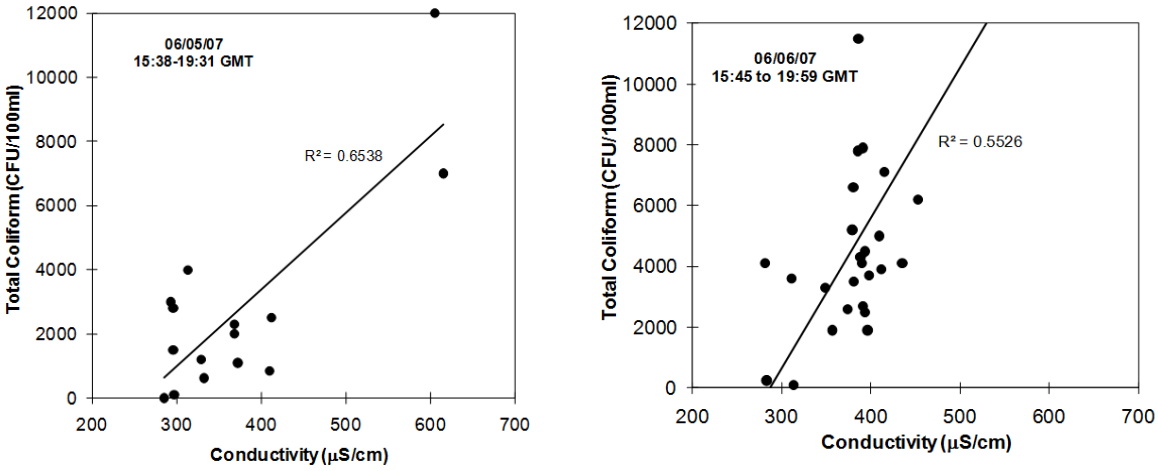

b) Total coliform

Figure 4.18 Bacteria versus conductivity and best fit line on June 5, and 6, 2007.

A linear relationship with a high correlation ($r^2 = 0.97$), between the conductivity and E. coli is observed on June 5. The correlation decreases on June 6 ($r^2 = 0.64$) and the data are more scattered. Higher E. coli levels on June 6 were recorded on the first two hours of sampling (16:00 to 18:00 EDT). During these hours the cloud cover was 25%, so the

solar radiation was reduced probably causing the increase in E. coli. More discussion on cloud cover is given in the next section. Total coliform show lower correlation with conductivity on both days. This suggests different die-off mechanisms for total coliform from the E. coli.

4.5.3.2 Solar radiation and cloud cover

Solar radiation and cloud cover records were obtained at the NOAA Muskegon Field Station. The average photosynthetically active radiation is expressed in micro Einsteins per area per time unit ($\mu E/m^2/s$) which is a photon flux unit. It is a measure of light most often used by physiologists. 1μE=1μmol of photons at a specific wavelength (6.022×10^{17} photons) (Rosato, 2007). The active radiation is compared to the cloud cover data from Muskegon County Airport Station in Figure 4.19.

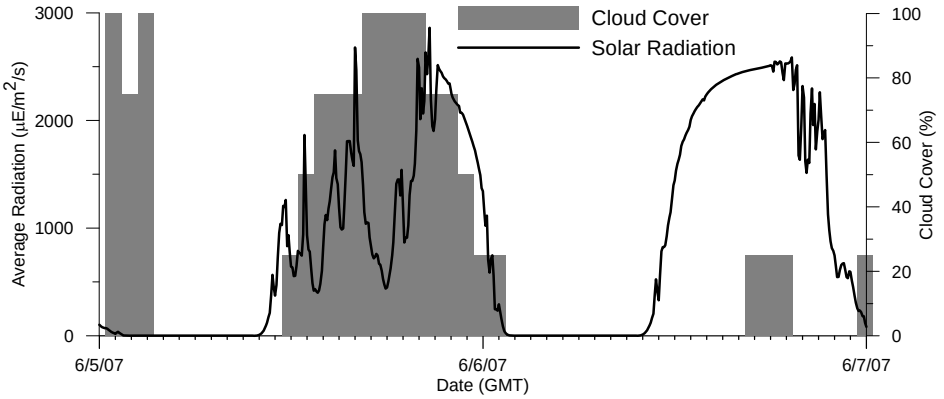

Figure 4.19 Solar radiation ($\mu E/m^2/s$) and cloud cover (%) on June 5 and 6, 2007 at NOAA Muskegon Field Station, and County Airport Meteorological Station.

The cloud cover shows that during the experiment hours from 15:35 to 19:30 GMT on June 5, 2007, the sky had 100% cloud cover causing a drop to less than 500 $\mu E/m^2/s$ in the sunlight radiation. On June 6, 2007, from 15:45 to 19:59 GMT the sky was partially covered (25% cloud cover) which did not significantly decrease the solar radiation. The cloud cover, wind, current, temperature, wave, discharge condition for the sampling period on June 5 and 6, 2007 are summarized in Table 4.10.

Table 4.10 Cloud cover, wind, current, temperature, wave, discharge condition for the sampling period on June 5 and 6, 2007.

Date	Cloud cover (%)	Wind		Currents		River temp. (°C)	Lake temp. (°C)	Wave ht (m)	River disch. (m^3/s)	Solar rad. ($\mu E/m^2/s$)
		Sp. (m/s)	Dir.(°)	Sp. (cm/s)	Dir. (°)					
6/5/07	100	5.6	NNW	13.4	S	20.3	7.3	0.36	167	1205
6/6/07	25	2.3	SSE	3.9	NNE	20.0	6.9	0.19	179	2436

On June 5, the average wind was 5.6 m/s from the NNW that resulted in currents of 13.4 cm/s to the South. The plume followed the current and moved southward. The river temperature was 20.3°C and the lake temperature was 7.3°C. The 13°C temperature difference created a strongly buoyant plume. Wave height was 0.36 m and river discharge was 167 m^3/s. The next day, insolation increased, the wind slowed to 2.3 m/s and changed direction to SSE. It resulted in slower NNE currents with a speed around 3.9 cm/s. The lake and river temperature did not change significantly. The wave height decreased to 0.19 m.

The above meteorological and discharge conditions along with the field measurements will assist us in identifying the effective mechanisms for bacteria survival and behavior. In the next section the spatial bacteria and conductivity measurements, their relations and the solar radiation effect are described.

4.5.3.3 Dilution versus decay

Physical dilution can be calculated from conductivity and can be compared with the reduction in E. coli counts. Physical dilutions were calculated using Eqn. 3-1. Effective dilution is estimated from E. coli counts using the same equation. The maximum E. coli counts in the river, C_0, was 40 and 47 CFU/100ml for June 5 and 6, and the minimum or background concentration in the lake, C_b, was zero for both days. Travel time was estimated from the current data from the Table 4.10. Normalized concentrations of E. coli and conductivity (or inverse of dilution) and exponential fits are plotted versus travel time in Figure 4.20. The former includes decay and the latter shows physical dilution only.

On June 5, E. coli and conductivity track each other. The physical dilution curve is very close to the E. coli dilution line. They diverge on the 6th, however, implying that bacteria is mainly reduced by dilution on June 5 and decay is negligible, due to the 100% cloud cover and the lower solar radiation. On June 6, sunlight decay of bacteria increased due to higher solar radiation (about twice that on June 5), and less cloud cover (25%).

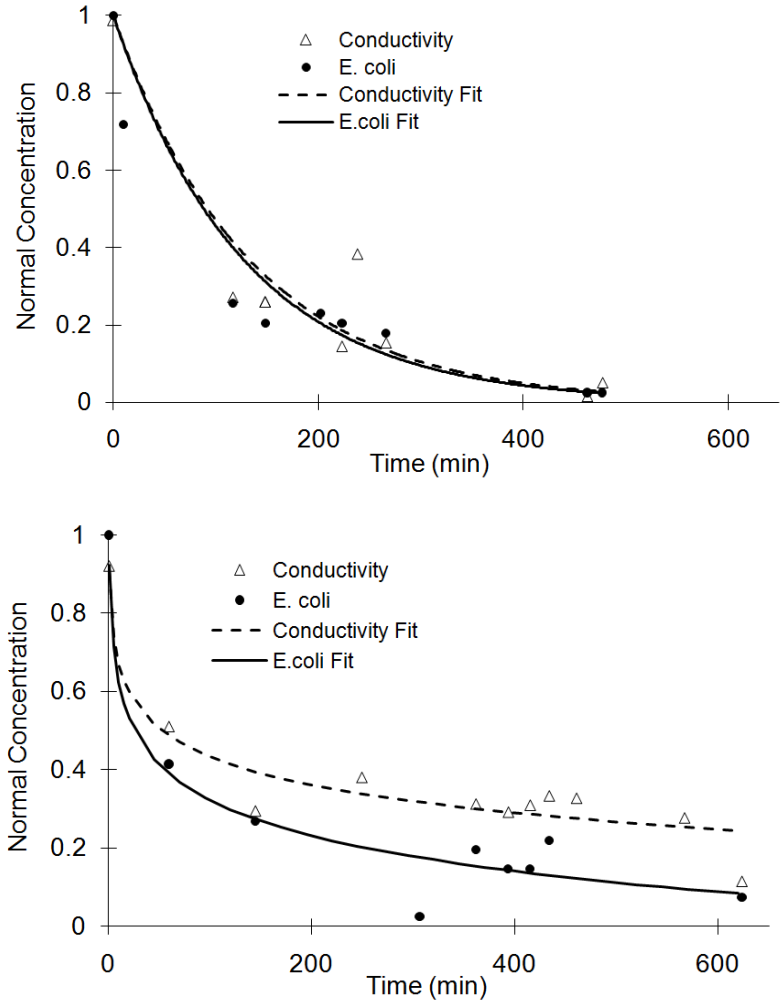

Figure 4.20 Normal E. coli and conductivity concentrations versus travel time on June 5 (top), and 6 (bottom), 2007.

Using Eqn. 2-26 and C=0.026 and C_0=0.028 at t=480 min (8 hr) on June 5, and C=0.11 and C_0=0.26 at t=600 min (10 hr) on June 6, yields k =0.2 day^{-1} on June 5, and 2.2 day^{-1} on June 6. Previous estimates of k for E. coli in Lake Michigan, Chicago beaches have been in the range of 0.41 to 0.75 day^{-1} for different sunny and cloudy days

(Whitman et. al, 2004). In a more recent study, Liu et al. (2006) found E. coli decay rate ranging between 0.5-2.0 day^{-1} for some southern Lake Michigan Beach sites which is close to our range (0.2-2.2).

The decay rates can also be expressed as T_{90} (according to Eqn. 2-27), yielding a T_{90} = 252 hr (10.5 days) and 25 hr (1.1 days) on June 5 and 6 respectively. T_{90} is about 10 times longer on June 5, since the bacteria decay was very slow. Clearly, solar radiation and cloud presence can significantly affect the bacterial mortality rates.

4.6 Discussion

Temperature profiles along the channel showed that the Grand River forms a surface buoyant plume in the summer acting as a gravity current that transitions from subcritical flow upstream to critical flow near the river mouth. This is similar to gradually varied flows in open channels, where the flow transitions from a mild to a steep slope and critical flow (Fr_0=1) occurs at a distance of 3-4h_c from the outlet. In our case, the Froude number based on channel depth was typically 0.5 at around 500 m upstream from the river mouth and approached unity, where critical depth occurred, near the mouth. The location of the critical depth varied from 5d upstream to the mouth. The critical depth was close to the average plume thickness at the mouth. Plume thickness varied from 2.5 to 6.0 m. The lake-river temperature difference ranged from 2.1 to 14.1°C. An empirical power function based on a best fit of the data, was developed to predict the plume thickness along the centerline.

Hetland and MacDonald's (2008) lateral spreading model for buoyant river plumes and their relationship to the internal gravity wave and plume width was reviewed. Based on their study, the Grand River plume with an aspect ratio of 16 was convergent; i.e. the speed of moving away from the mouth was slower than their lateral spreading. Their relationship was modified to a new formulae that predicts the plume width (or spreading rate) well in distances close to the mouth (< 1 km) with no need to determine the initial width. The new relationship should be tested for farther distances and calibrated for other cases, since its empirical constants may change for different rivers with different

geometries and discharges. The devised spreading rate formula will be used in the near field in Chapter 6 to estimate the plume width.

A new classification for surface buoyant plumes was presented that complements the Jones et al. scheme for plume-like flow. It is based on a ratio that includes the plume-crossflow length scale, L_b, which incorporates the effect of buoyancy versus longshore currents and predicts whether the plume is attached ($L_b/d < 65$) or unattached ($L_b/d > 65$). Unattached plumes are classified into 5 categories (radial spreading, offshore spreading, side deflecting, diffuse offshore spreading, and diffuse shore impacting) based on a Richardson number that includes the effect of buoyancy and the onshore-offshore wind speed. The plume radially spreads in slow winds (Ri>5), spreads offshore or deflects to the side in medium winds (5>Ri>5×10^{-3}), and become diffuse, either spreading offshore or impacting the shore in strong winds (Ri<5×10^{-3}).

A power law expression for the jet trajectory with different coefficients for attached and unattached plumes was developed following Rajaratnam (1988). The Rajaratnam and AGM models both underestimated the plume intrusion since they were both developed for circular jets in crossflow, whereas the Grand River has a rectangular outfall with a large aspect ratio. The proposed model agreed fairly well with the field data. The trajectory formula is developed for discharge ranges of 40<Q(m^3/s)<180, $\alpha < 12$ and densimetric Froude numbers less than unity. It should be tested for other discharge ranges and densimetric Froude numbers greater than unity where there is no exchange flow or lake intrusion into the river.

The minimum dilution along the plume trajectory was described by an equation similar to McCorquodale (2007) valid for the same range of parameters in trajectory formula and within distances of $\xi / b < 8$ from the mouth. It includes the inflow to ambient current ratio, densimetric Froude number, and the aspect ratio. It was assumed that Fr_0' = 1 at the source. The AGM model overestimated dilution for unattached plumes, the Carnelos model underestimated for both attached and unattached cases, and the McCorquodale model underestimated in attached cases and overestimated in unattached cases. In the attached cases, extension of the channel into the lake and strong longshore currents possibly contributed to higher dilutions.

During the study periods of June to August in 2006 and 2007, river discharge peaks were generally observed soon after a rainfall event. The highest discharge rate did not necessarily result in the highest beach bacteria level, however, it is known that beach bacteria can be influenced by factors other than river discharge such as beach sand and wave-induced resuspension (Yamahara et al, 2007). Nevertheless, plume bacteria offshore is primarily affected by the river contamination and can impact beaches directly.

Bacteria were measured in the river and plume on June 5 and 6, 2007. E. coli counts in the river plume were highly correlated with surface conductivity on June 5, where the physical dilution and effective dilution (including decay) tracked each other closely with negligible difference due to significant (100%) cloud presence. Solar radiation can significantly affect the rate of bacterial mortality. The correlation decreased on the next day due to increased solar radiation, where the physical and effective dilution curves diverged due to higher decay rates. The total coliform die-off rate on June 5, unlike E. coli, could not be solely attributed to solar radiation.

The E. coli decay rate in the Grand River plume range was close to the results of previous studies in southern Lake Michigan. Assuming a first order decay, T_{90} was about 10 days on June 5 (due to the full cloud cover) and about 1 day on June 6. This shows that bacterial decay rates in river plumes can vary substantially from day to day and more research is needed to improve our knowledge of the factors that determine bacterial decay.

4.7 Summary

The Grand River plume field data was analyzed for the effects of geometry, inflow speed, buoyancy, and wind conditions. An empirical formula for plume thickness along the trajectory was developed. A simplified spreading rate formula was also proposed that improves previous studies in the near field. The result was confirmed by the field data. An empirical model was proposed for the trajectory and minimum dilution of the plume based on the observations and previous studies. The model can be applied to buoyant surface discharges for large aspect ratio channels.

A new classification scheme for surface buoyant plumes was devised. It depends on the plume-crossflow length scale and the Richardson number that incorporates wind effects. A hypothesis for the flow conditions at the outlet was proposed and verified by the field data. It assumes the densimetric critical Froude number to be equal to unity and can be used to estimate the plume thickness at the mouth.

Plume bacterial data were analyzed. Surface conductivity and E. coli were highly correlated during periods of no sunlight, but less correlated on a sunny day. T_{90} was calculated for the E. coli bacteria in the plume and compared with previous estimates. The models of plume dynamics and inactivation rates will be used to better define the tracer source and the mass decay and improve the transport model in Chapter 6.

CHAPTER 5

3D HYDRODYNAMIC MODELING

5.1 Introduction

In the past few decades hydrodynamic models have been developed that have many applications to coastal and estuarine circulation. They are being increasingly used to predict the fate and transport of coastal discharges, as field measurements are expensive and restricted to few locations and short time periods and physical models cannot meet all scale conditions. Hydrodynamic mathematical models have many applications in different conditions and can resolve unsteady flows in three dimensions, over long time scales, for a range of ambient flow and discharge conditions. Moreover, the proper combination of hydrodynamic models with field studies provide validated spatial data for periods when boundary conditions are missing. This is not feasible in laboratory and field tests.

The choice between two and three dimensional models depends on a number of factors. 2D (usually depth-averaged) models may be adequate for fairly shallow unstratified waters, where wind and tidal currents keep the water column well-mixed, i.e. homogeneous in salinity and temperature. In deeper water bodies with density stratification, however, especially with wind-shear, 3D models are needed. Due to this fact, 3D ocean circulation models are being increasingly used to predict pollutant dispersion in coastal areas. They can be used to study nearshore current patterns and predict bacteriological pollution when combined with mass transport models (Wu, 1994; Carnelos, 2003). Hydrodynamic models have also been successfully used to predict submerged outfall plumes (Blumberg et al., 1996; Zhang, 1995). Integrated 3D hydrodynamic and water quality models have been applied to study marine outfalls over flood and ebb tides in coastal seas (Liu et al., 2007).

Some commonly used ocean circulation models were listed in Table 2.1. For the present study, POMGL was used for the hydrodynamic simulations since it was already

running as part of the NOAA Great Lakes Coastal Forecasting System (GLCFS) that will be described below.

5.2 Model (POMGL) Description

POMGL, a modified version of the Princeton Ocean Model (POM) (Blumberg and Mellor, 1987), a widely used 3D hydrodynamic model, is used in the present study. It was adapted for the Great Lakes hydrodynamic simulations at the National Oceanic and Atmospheric Administration Great Lakes Environmental Research Laboratory (Schwab and Bedford, 1994; Beletsky and Schwab, 2001). POMGL and POM are quite similar, with the differences mainly in the boundary conditions definition.

POM is a nonlinear, fully three-dimensional, primitive equation, finite difference model that solves the heat, mass, and momentum conservation equations of fluid dynamics. It assumes incompressibility and is hydrostatic and Boussinesq, so that density variations are neglected except where they are multiplied by gravity in the buoyancy force terms. The basic equations are based on continuity, momentum, and thermodynamics including temperature and salinity and are described in Appendix B. The governing equations are solved numerically using the finite difference method on an Arakawa C type staggered grid. In this model, a Leap Frog time-stepping scheme with the mode-splitting technique is used because it permits the calculation of the free surface equation with little sacrifice in computational time.

POM uses two modes: external and internal. The external mode solves the depth-averaged transport equations that contain propagation of fast moving shallow water waves on a short time step. The internal mode solves the 3D transport equations that contain propagation of slow moving internal gravity waves on a long time step. The internal-mode calculation, separated into an implicit time step for a vertical diffusion and an explicit time step for both advection and horizontal diffusion, gives updated information for velocities and turbulence quantities. A tri-diagonal solver with implicit treatment is used for vertical viscosity and diffusivity.

The external mode provides water surface elevation horizontal gradients for insertion into the internal mode equations which are solved over a longer time period.

Once the vertical structure has been determined the equations are updated and the next external mode solution begins. The external-mode calculation discretized by midpoint leap-frog approximation provides updated information for surface elevations and depth averaged velocities.

5.3 Model Limitations

Some restrictions of POM are its applicability only to structured grids, under- and over-shooting with central differencing scheme in advection and horizontal diffusion, and small time step requirement resulting in relatively long run-times (Carnelos, 2003). The time step is limited by the Courant-Friedrichs-Lewy (CFL) stability condition. The stability conditions on external and internal mode time steps (noted by Δt_E and Δt_I) are as follows:

$$\Delta t_E \le \frac{1}{C_t}\left|\frac{1}{\delta_x^2}+\frac{1}{\delta_y^2}\right|^{-1/2} \tag{5-1}$$

$$\Delta t_I \le \frac{1}{C_T}\left|\frac{1}{\delta_x^2}+\frac{1}{\delta_y^2}\right|^{-1/2} \tag{5-2}$$

where for external mode: $C_t = 2\sqrt{gH} + \bar{U}_{\max}$, where $\bar{U}_{\max}$ is the maximum average velocity expected (taken as 100 m/s in POM), H is the bottom depth, and for the internal mode: $C_T = 2C + U_{\max}$, where C is the maximum internal gravity wave speed commonly of order of 2 m/s, $U_{\max}$ is the maximum advective speed, and δ_x and δ_y are the grid spacing in x and y directions. The internal mode time step is far less limiting since most of the fast-moving external effects are removed when a suitable external mode time step is selected. Additional limits are imposed by horizontal diffusion of momentum

$$\Delta t_I \le \frac{1}{4A_H}\left|\frac{1}{\Delta_x^2}+\frac{1}{\Delta_y^2}\right|^{-1} \tag{5-3}$$

and earth's rotation:

$$\Delta t_I \le \frac{1}{f} = \frac{1}{2\Omega \sin \Phi} \tag{5-4}$$

where A_H is the horizontal diffusivity, Δ is the discretization size, f is the Coriolis parameter, Ω is the angular velocity of the earth, and Φ is the latitude. However, the horizontal diffusion and rotation limitations are not as restrictive as the stability conditions imposed by external and internal mode time steps (Blumberg and Mellor, 1987).

5.4 Nesting Technique

Due to these computational restrictions, it is usually not practical to model a large area with enough resolution for the area of interest. Therefore, a common approach is to model a large area (e.g. the whole lake) with a coarse grid and to embed a finer-scale model within it. The fine-grid model derives its boundary conditions from the larger model and is said to be nested within it. The nested model uses more refined bathymetry than the coarse whole lake model, therefore it is expected to improve nearshore predictions. Its grid size is also small enough to resolve scales of interest.

POMGL was used as the fine-grid model to predict the transport of pollutants from the Grand River to the adjacent beaches in Lake Michigan (Nekouee et al. 2008, 2009). Circulation and thermal structure in the whole lake is modeled on a yearly basis in three dimensions on a coarse grid with 2 km resolution (Schwab and Bedford 1994; Beletsky and Schwab 2001). The nested model had a domain of 6×24 km and a 100 m horizontal grid size was implemented around the river mouth as shown in Figure 5.1. The size of the nested domain was chosen large enough so that the reflections from open boundaries would not influence the plume and its impact on local beaches. The nested horizontal grid size was chosen as an optimum length (approximately the channel width) in order to both satisfy the CFL criteria and also represent the fine scale circulation of the plume. Both models (whole-lake and nested) employ a terrain-following vertical coordinate system (sigma-coordinate) with 20 vertical levels (sigma levels, which represent a proportion of a vertical column) with finer spacing near the surface and the bottom. The vertical sigma

levels are fractions of local depth as follows: σ=0.00, -0.05, -0.11, -0.16, -0.21, -0.26, -0.32, -0.37, -0.42, -0.47, -0.53, -0.58, -0.63, -0.68, -0.74, -0.79, -0.84, -0.89, -0.95, -1.00.

The nested model was run for the four field study series: June 19 to 24, 2006; August 7 to 11, 2006; June 4 to 8, 2007; July 14 to 18, 2007 with an external time step of 1 sec, and internal time step of 20 sec.

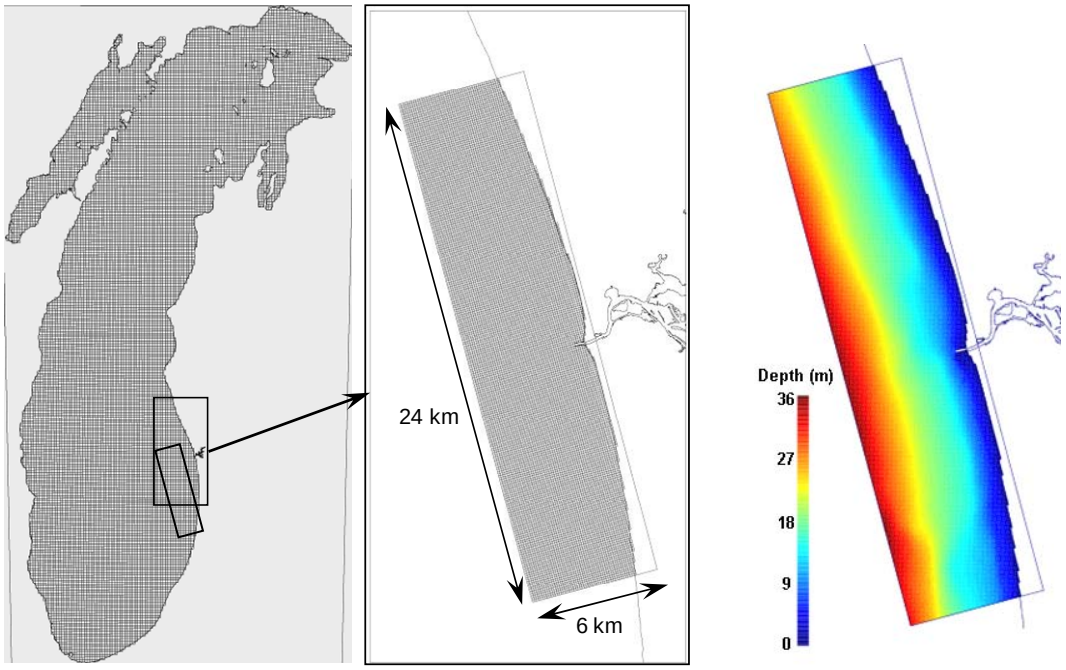

Figure 5.1 Whole-lake simulation with a 2 km grid (left) and the nested simulation with a 100 m grid (right).

5.5 Model Setup, Initial and Boundary Conditions

POM uses time-dependent wind stress and heat flux forcing at the surface, zero heat flux at the bottom, free-slip lateral boundary conditions, and quadratic bottom friction. The free surface boundary conditions are:

$$\rho_0 K_M \left(\frac{\partial U}{\partial z}, \frac{\partial V}{\partial z} \right) = \left(\tau_{0x}, \tau_{0y} \right) \tag{5-5}$$

$$\rho_0 K_H \left(\frac{\partial \theta}{\partial z}, \frac{\partial S}{\partial z} \right) = \left(\dot{H}, \dot{S} \right) \tag{5-6}$$

$$q^2 = B_1^{2/3} u_{\tau s}^2, \qquad q^2 \ell = 0 \tag{5-7}$$

$$W = U\frac{\partial \eta}{\partial x} + V\frac{\partial \eta}{\partial y} + \frac{\partial \eta}{\partial t} \tag{5-8}$$

where U , V , W are the velocity vectors in *x*, *y*, and *z* directions, θ, and S are the potential temperature and salinity, $\dot{H}$ and $\dot{S}$ are the heat and salinity flux respectively, η is the water surface elevation, K_H is the heat/salt vertical eddy diffusivity, K_M is the momentum vertical eddy diffusivity, $\vec{\tau}_0 = \rho_0 C_D \left|\vec{V}_0\right| \vec{V}_0$ is the surface wind stress with $u_{\tau s}$ the magnitude of the surface friction velocity vector, q^2 is the kinetic energy term, and ℓ is the turbulence macroscale (Blumberg and Mellor, 1987). The bottom boundary conditions are:

$$\rho_0 K_M \left(\frac{\partial U}{\partial z}, \frac{\partial V}{\partial z}\right) = \left(\tau_{bx}, \tau_{by}\right) \tag{5-9}$$

$$q^2 = B_1^{2/3} u_{\tau b}^2, \qquad q^2 \ell = 0 \tag{5-10}$$

$$W_b = -U_b \frac{\partial H}{\partial x} + V_b \frac{\partial H}{\partial y} \tag{5-11}$$

where *H* is the bottom topography, B_1 is an empirical constant, $u_{\tau s}$ the magnitude of the bottom friction velocity vector, and $\vec{\tau}_b = \rho_0 C_D \left|\vec{V}_b\right| \vec{V}_b$ is the bottom friction stress with the drag coefficient given as $C_D = \left[\frac{1}{k}\ln\left[(H + z_b)/z_0\right]\right]^{-2}$. V_b is the velocity near the bottom, and *k* is the *von Karman* constant. The drag coefficient in the bottom friction formulation is spatially variable. In POM, it is calculated by assuming a logarithmic bottom boundary layer using constant bottom roughness (z_0) of 1 cm.

In POMGL, this constant has been modified to an asymptotic function ($z_0 = 0.001 + 0.02/(1+H)$) that approaches 0.021 in shallower waters and decreases to 0.001 in deeper waters. z_b is also defined as the $Max(2z_0, \Delta H)$, where ΔH is the depth difference between bottom and the grid point. Horizontal diffusion is calculated with a

Smagorinsky eddy diffusivity parameterization (with a multiplier of 0.1) to give a greater mixing coefficient near strong horizontal gradients. Vertical diffusion is computed as a function of Richardson number. Diffusion coefficients will be further explained in Chapter 6.

Specifying boundary conditions for open coastal waters is a major problem. Detailed information is needed on the variations of currents and water level, stratification, and other parameters and their temporal variations around these boundaries. POM has several possible options for open boundary conditions in the external and internal modes as summarized in Table 5.1.

Table 5.1 Possible external and internal mode boundary conditions in POM

External mode boundary conditions		Internal mode boundary conditions	
Inflow	$\bar{U} = \bar{U}_{bc}$	Inflow	$U = U_{bc}$
Elevation	$\eta = \eta_{bc}$	Radiation	$\frac{\partial U}{\partial t} \pm c_i \frac{\partial U}{\partial x} = 0$
Radiation (1)	$H\bar{U} \pm c_e \eta = BC$	Upstream advection	$\frac{\partial T}{\partial t} \pm U \frac{\partial T}{\partial x} = 0$
Radiation (2)	$\frac{\partial \bar{U}}{\partial t} \pm c_e \frac{\partial \bar{U}}{\partial x} = 0$	Cyclic	$U_{east} = U_{west}$, $T_{east} = T_{west}$
Radiation (3)	$\frac{\partial \eta}{\partial t} \pm c_e \frac{\partial \eta}{\partial x} = 0$		
Cyclic	$\bar{U}_{east} = \bar{U}_{west}$, $\eta_{east} = \eta_{west}$		

where c_e is the local shallow water wave speed ($\sqrt{gH}$), and c_i is the baroclinic phase speed proportional to $\sqrt{H}$, where H is the water depth.

The open boundary conditions in POMGL (summarized in Table 5.2) are adapted for the Great Lakes conditions, where tidal forcing is negligible so the cyclic boundary condition is not prescribed. Since the variation of salinity over the lake is negligible, the mean salinity is also set to a constant value of 0.2 ppt.

Table 5.2 External and internal mode boundary conditions in POMGL

External mode boundary conditions		Internal mode boundary conditions	
Inflow and Outflow	$\bar{U} = \bar{U}_{bc}$, $\bar{V} = \bar{V}_{bc}$	Inflow	$U = U_{bc}$, $V = V_{bc}$, $T = T_{bc}$
		Outflow	$\frac{\partial U}{\partial t} \pm c_i \frac{\partial U}{\partial x} = 0$
		Upstream advection for S or T *	$\frac{\partial T}{\partial t} \pm U \frac{\partial T}{\partial x} = 0$

* (plus tangential smoothing)

The external lateral boundary conditions of the nested model (Northern, Western and Southern boundaries) were set equal to the depth-averaged velocities ($\bar{U}_{bc}$ and $\bar{V}_{bc}$) predicted by the whole lake model. For the internal mode boundary conditions, in the case of inflow (e.g. at open boundaries or from a river), 3D currents and temperatures (U_{bc}, V_{bc}, and T_{bc}), and in the case of outflow, the radiation condition were assigned (as explained in Table 5.2). 3D currents and temperatures were extracted from the coarse grid model runs and used along the nested model open boundaries.

5.6 Forcing Functions Accuracy

Blumberg and Georgas (2008) showed that bathymetry resolution is more important than wind in accurate results in the NY-NJ Harbor Estuary because tides are the dominant forces. The Great Lakes have negligible tides and other forcing functions (wind, surface heat fluxes) are more important. In Lake Michigan, wind is the major forcing function in driving the currents and must be specified accurately. Surface heat fluxes, including radiation transmitted to the water surface, also affect circulation. Therefore comprehensive meteorological data (wind, temperature, dew point, and cloud cover) were obtained from GLERL to be used as forcing functions for the nested model.

They use hourly meteorological data from the National Weather Service (NWS) which are measured from land stations, buoys, U.S. Coast Guard marine observational stations and ships in Lake Michigan, and interpolate it over the whole-lake grid (2 km). We use their interpolation codes to extract the forcing functions on the nested grid (100 m). In order to check how well the interpolation technique (Beletsky, 2001) represents

local winds, the buoy wind data at S10-06 was compared with the interpolated wind (Figure 5.2). The comparison shows good agreement, therefore the interpolated NWS data was used for the nested model forcing functions.

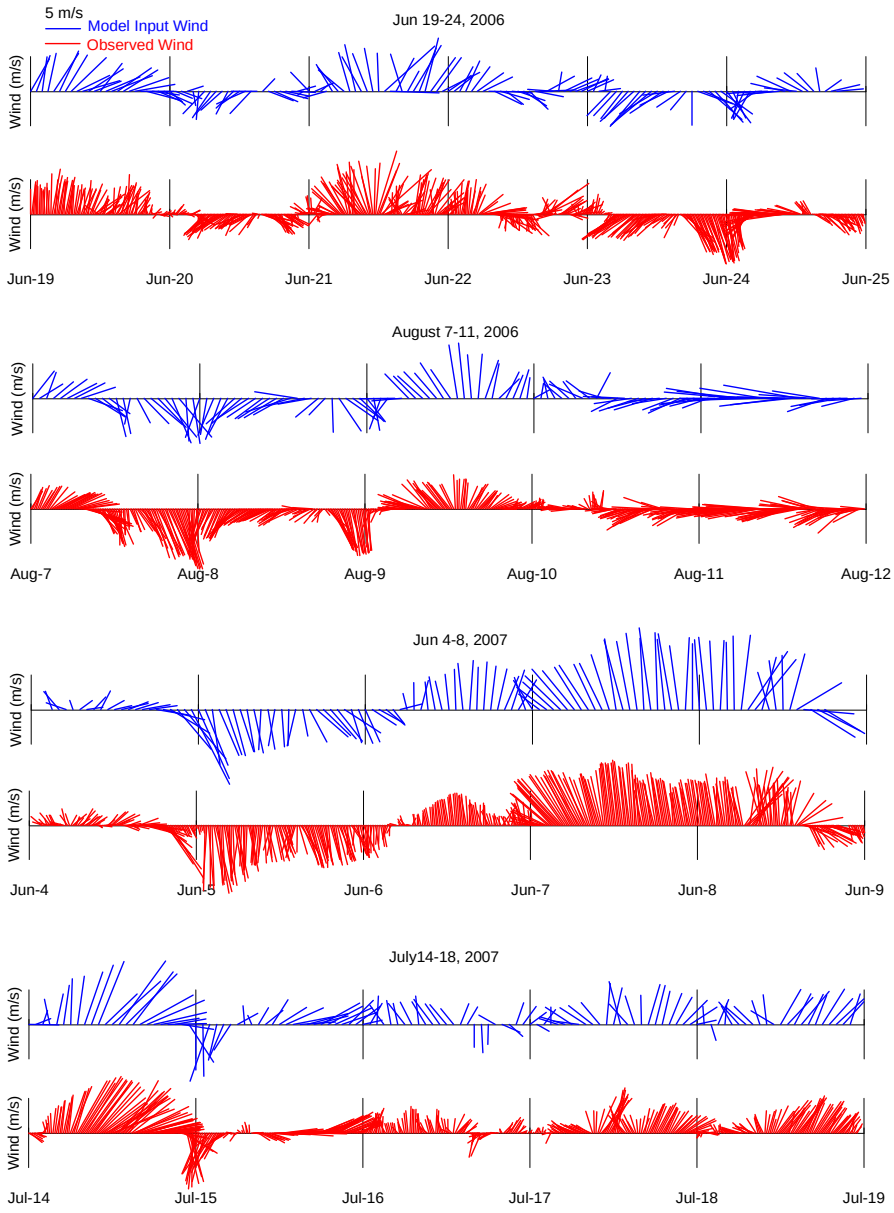

Figure 5.2 Interpolated versus observed winds at S10-06 and S10-07 for the four simulation periods.

5.7 Model Evaluation

POM has been extensively tested and evaluated. In the present study, the accuracy and efficiency of nested POMGL is investigated by comparing the model output with the Grand Haven data. The results are described below.

5.7.1 Current Predictions

Whole lake simulations were conducted by GLERL for the above periods. The lake wide snapshots on the left in Figures 5.3 and 5.4, show examples of surface and depth-averaged current simulations on August 9, 2006 at 0100 GMT. The lake wide simulation results were used as boundary conditions (3D velocity and temperature profiles) for the nested simulations. The nested model currents are shown in snapshots on the right sides of Figures 5.3 and 5.4. Small-scale current features, such as vortices and gyres resulting from flow separation around the piers are evident in the nested simulations. Modeling this detail is essential to modeling bacterial transport to local beaches.

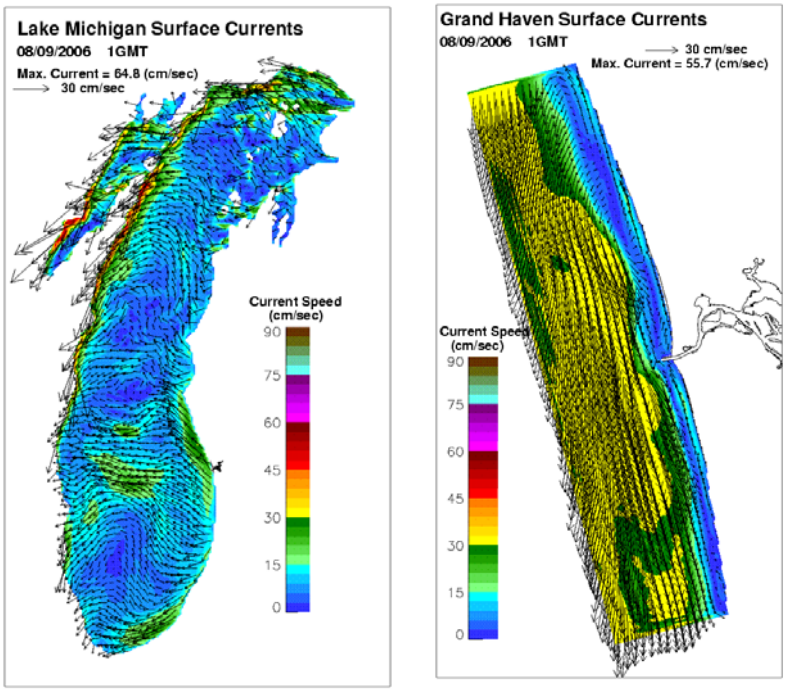

Figure 5.3 Whole lake and nested grid surface currents predictions for August 7-11, 2006.

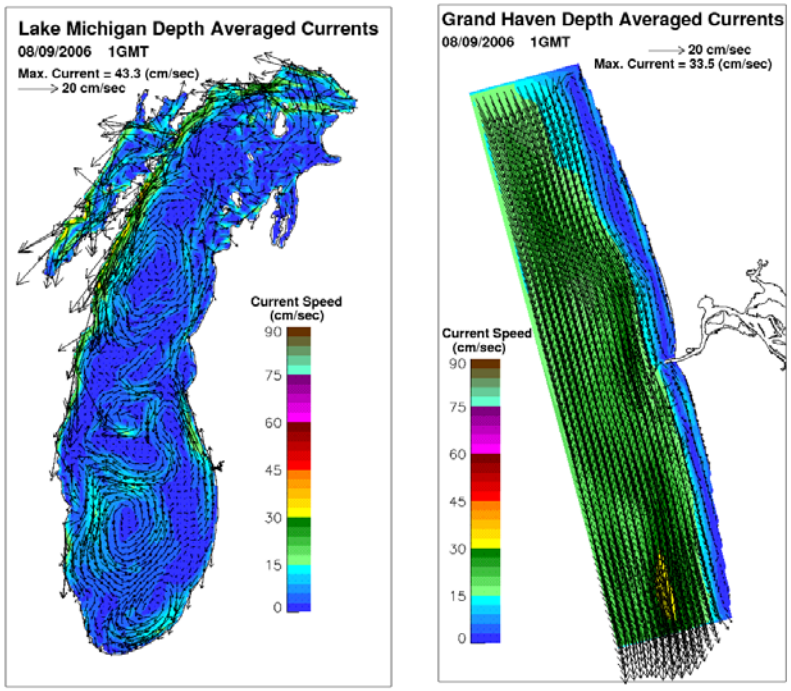

Figure 5.4 Whole lake and nested grid depth-averaged currents predictions for August 7-11, 2006.

Time series of the observed wind, observed and nested model predicted depth-averaged currents, and currents at different depths for different simulation periods and ADCP locations are shown in Figures 5.5 to 5.13. Predicted and observed current vectors are compared at S10-06 and N5-06 for June 19 to 24, 2006; S10-06 for August 7 to 11, 2006; S10-07, N10-07, and M20-07 for June 4 to 8, 2007, and July 14 to 18, 2007.

a) June 19 to 24, 2006 predictions at S10-06

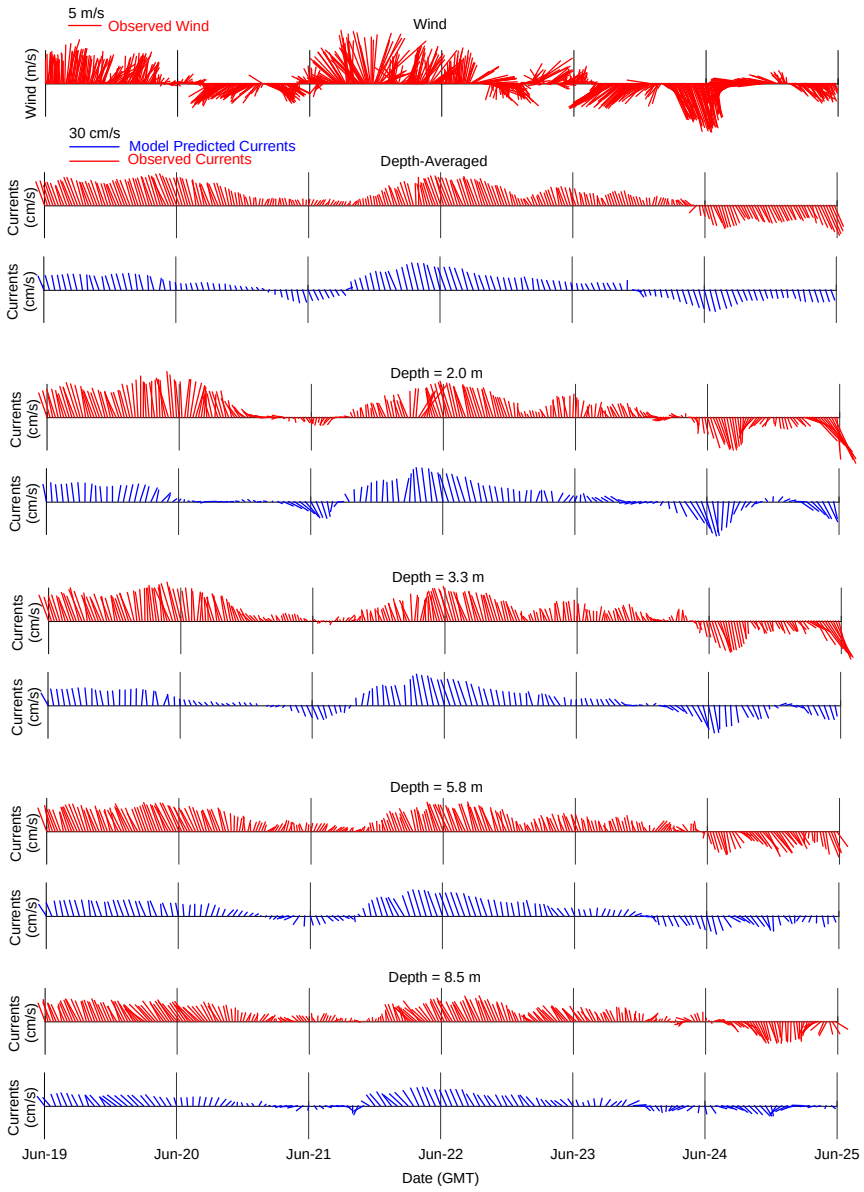

Figure 5.5 Time series of observed wind (red), observed currents (red) versus predicted currents (blue) for June 19 to 24, 2006 simulation at S10-06.

b) June 19 to 24, 2006 predictions at N5-06

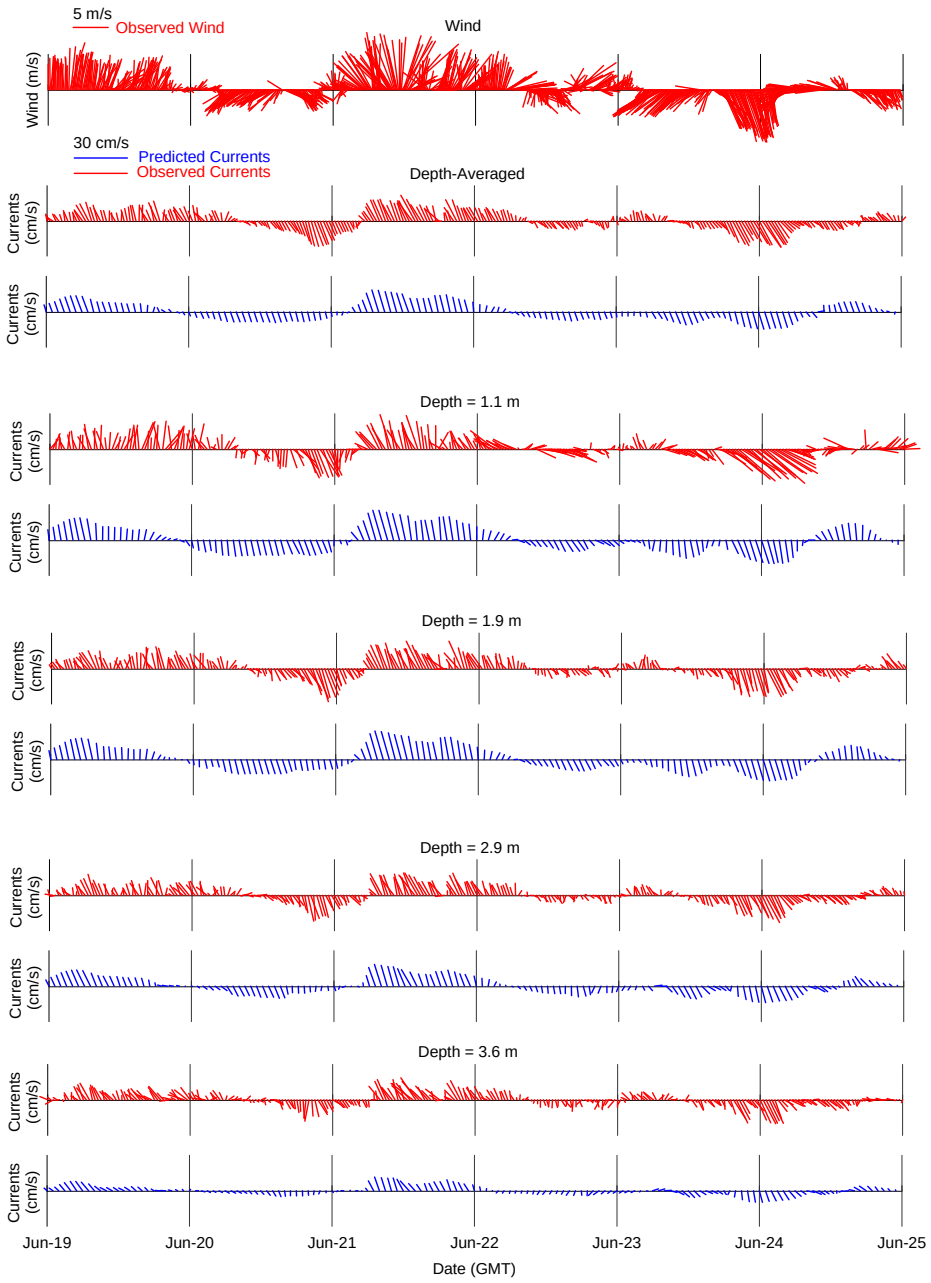

Figure 5.6 Time series of observed wind (red), observed currents (red) versus predicted currents (blue) for June 19 to 24, 2006 simulation at N5-06.

c) August 7 to 11, 2006 predictions at S10-06

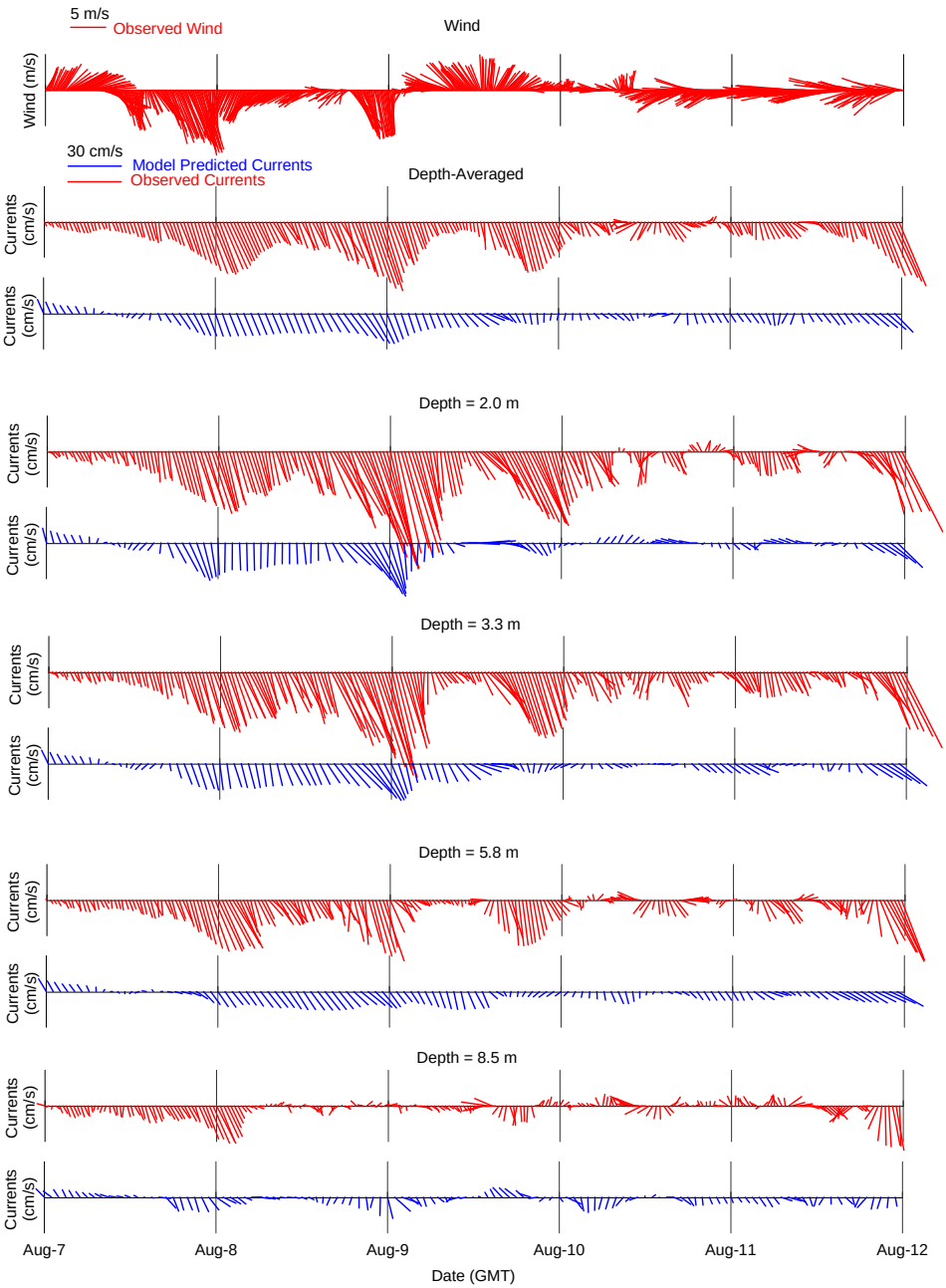

Figure 5.7 Time series of observed wind (red), observed currents (red) versus predicted currents (blue) for August 7 to 11, 2006 simulation at S10-06.

d) June 4 to 8, 2007 predictions at S10-07

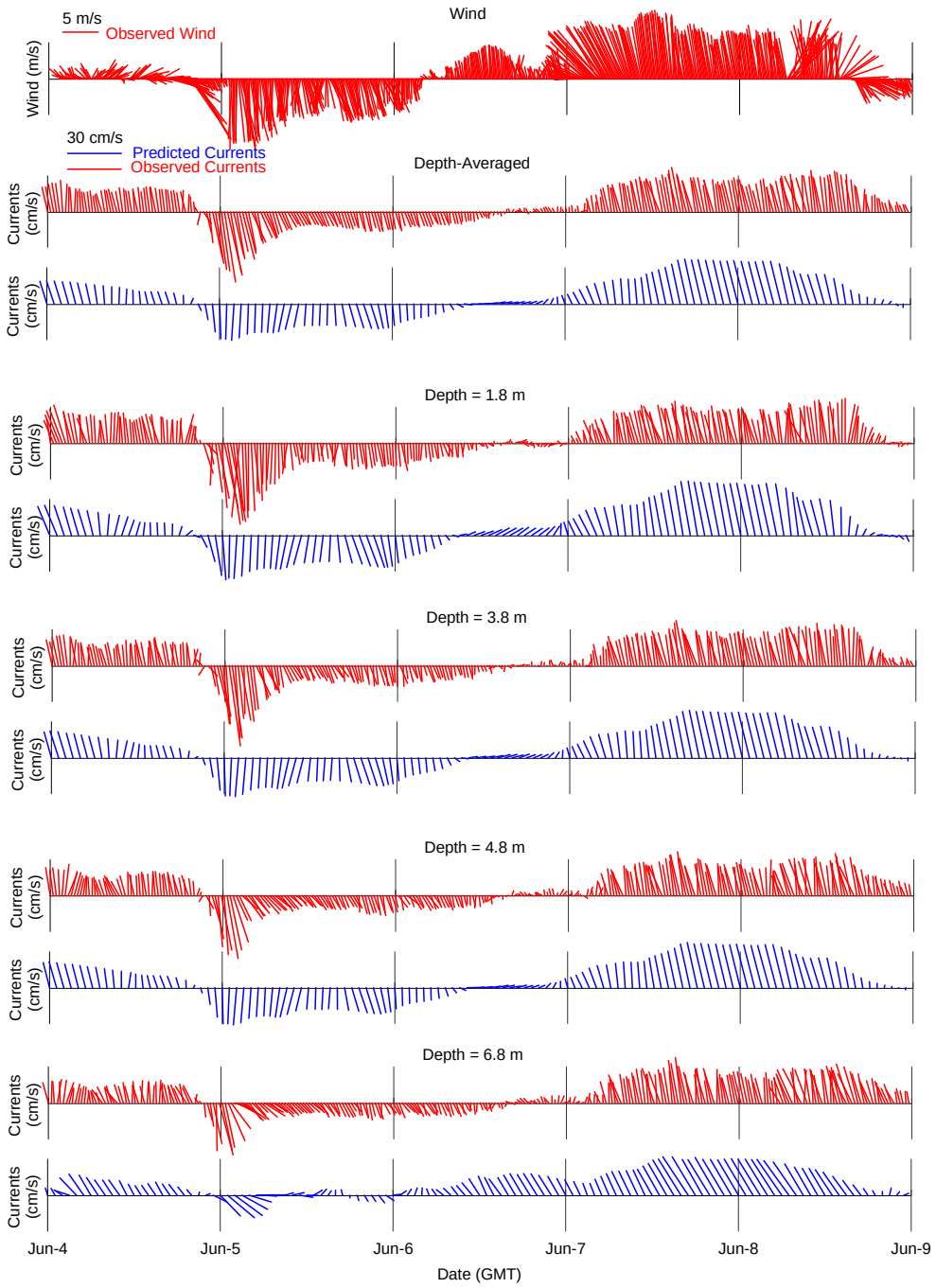

Figure 5.8 Time series of observed wind (red), observed currents (red) versus predicted currents (blue) for June 4 to 8, 2007 simulation at S10-07.

e) June 4 to 8, 2007 predictions at N10-07

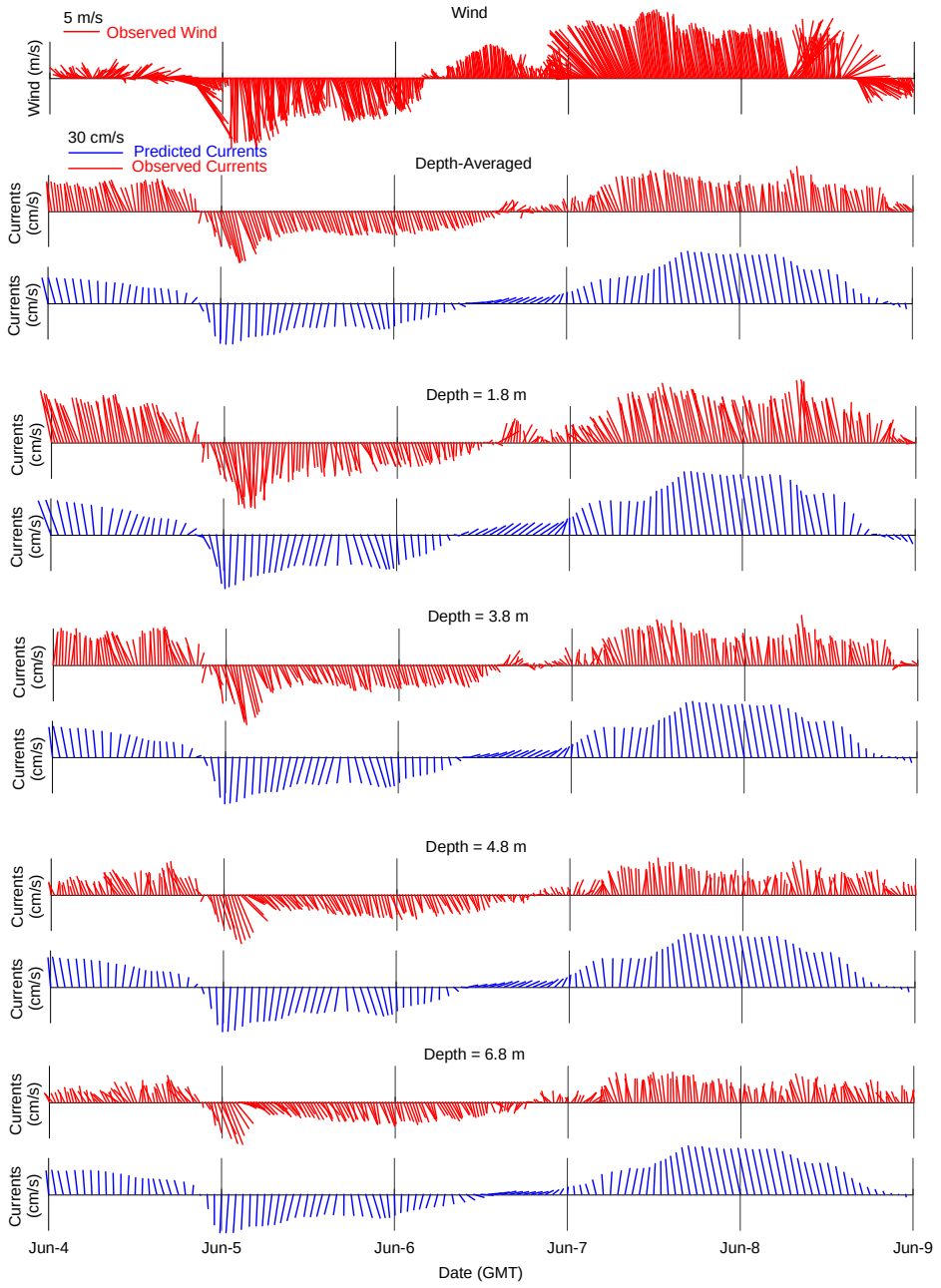

Figure 5.9 Time series of observed wind (red), observed currents (red) versus predicted currents (blue) for June 4 to 8, 2007 simulation at N10-07.

f) *June 4 to 8, 2007 predictions at M20-07*

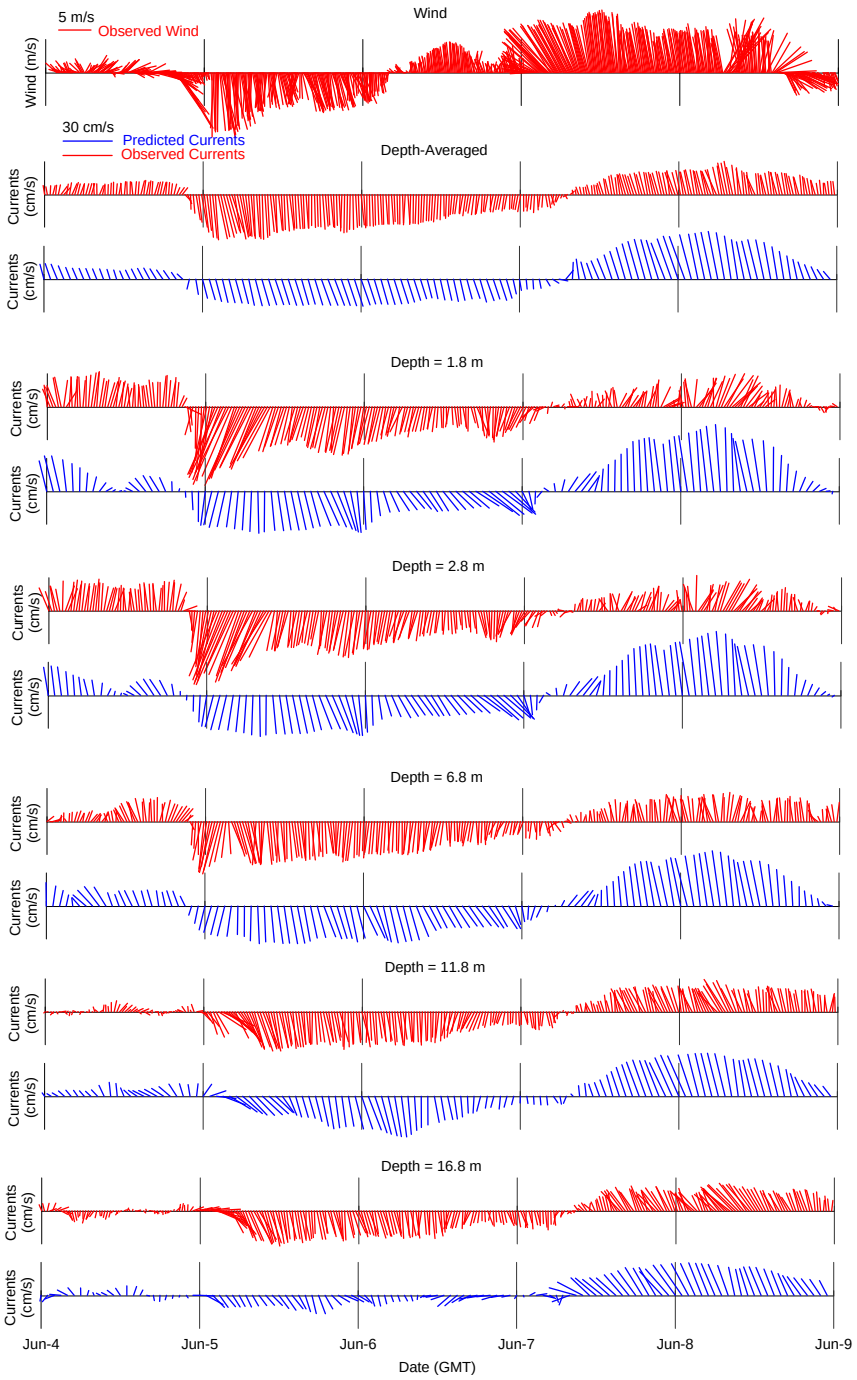

Figure 5.10 Time series of observed wind (red), observed currents (red) versus predicted currents (blue) for June 4 to 8, 2007 simulation at M20-07.

g) July 14 to 18, 2007 predictions at S10-07

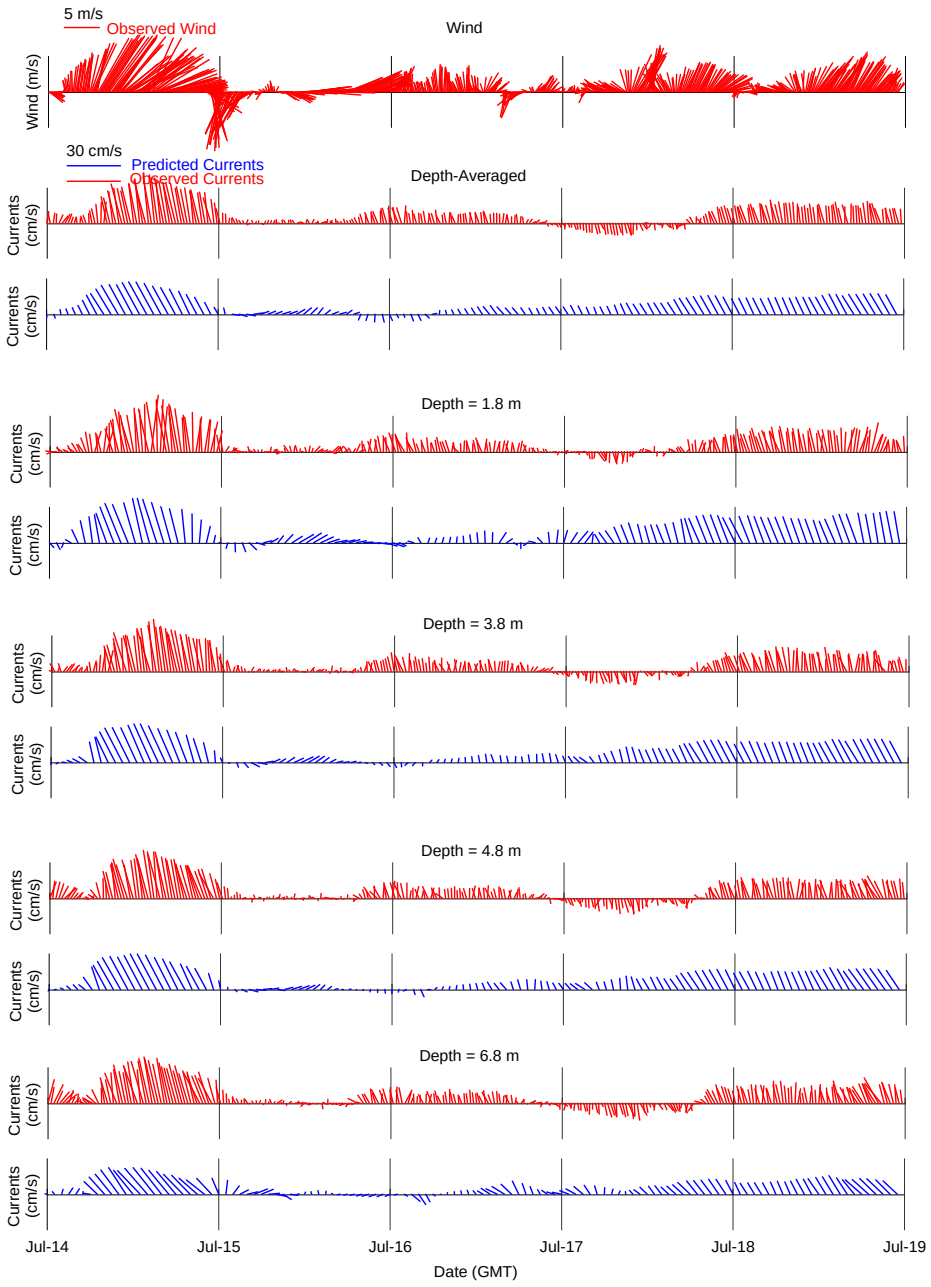

Figure 5.11 Time series of observed wind (red), observed currents (red) versus predicted currents (blue) for July 14 to 18, 2007 simulation at S10-07.

h) June 14 to 18, 2007 predictions at N10-07

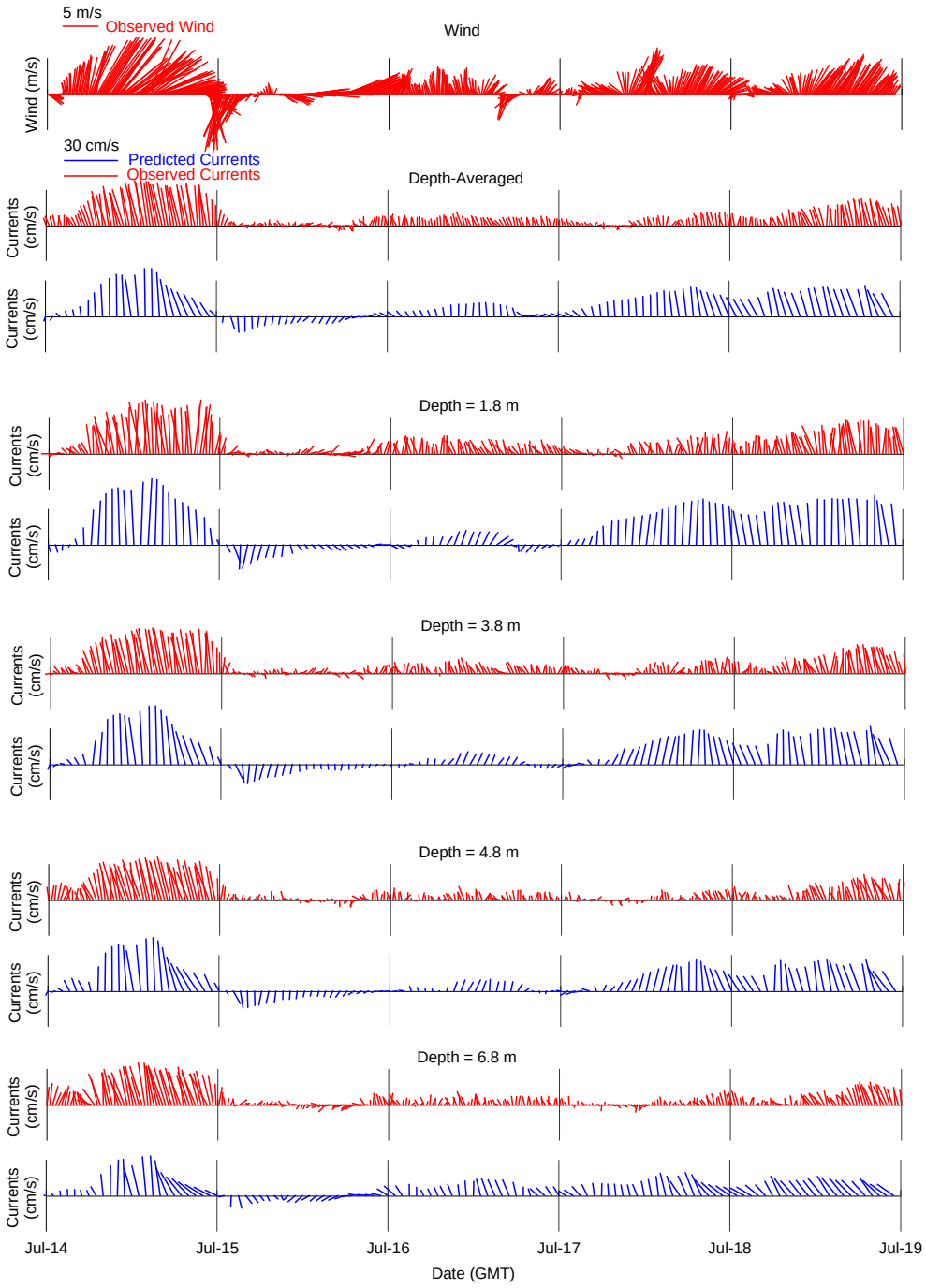

Figure 5.12 Time series of observed wind (red), observed currents (red) versus predicted currents (blue) for July 14 to 18, 2007 simulation at N10-07.

i) *June 14 to 18, 2007 predictions at M20-07*

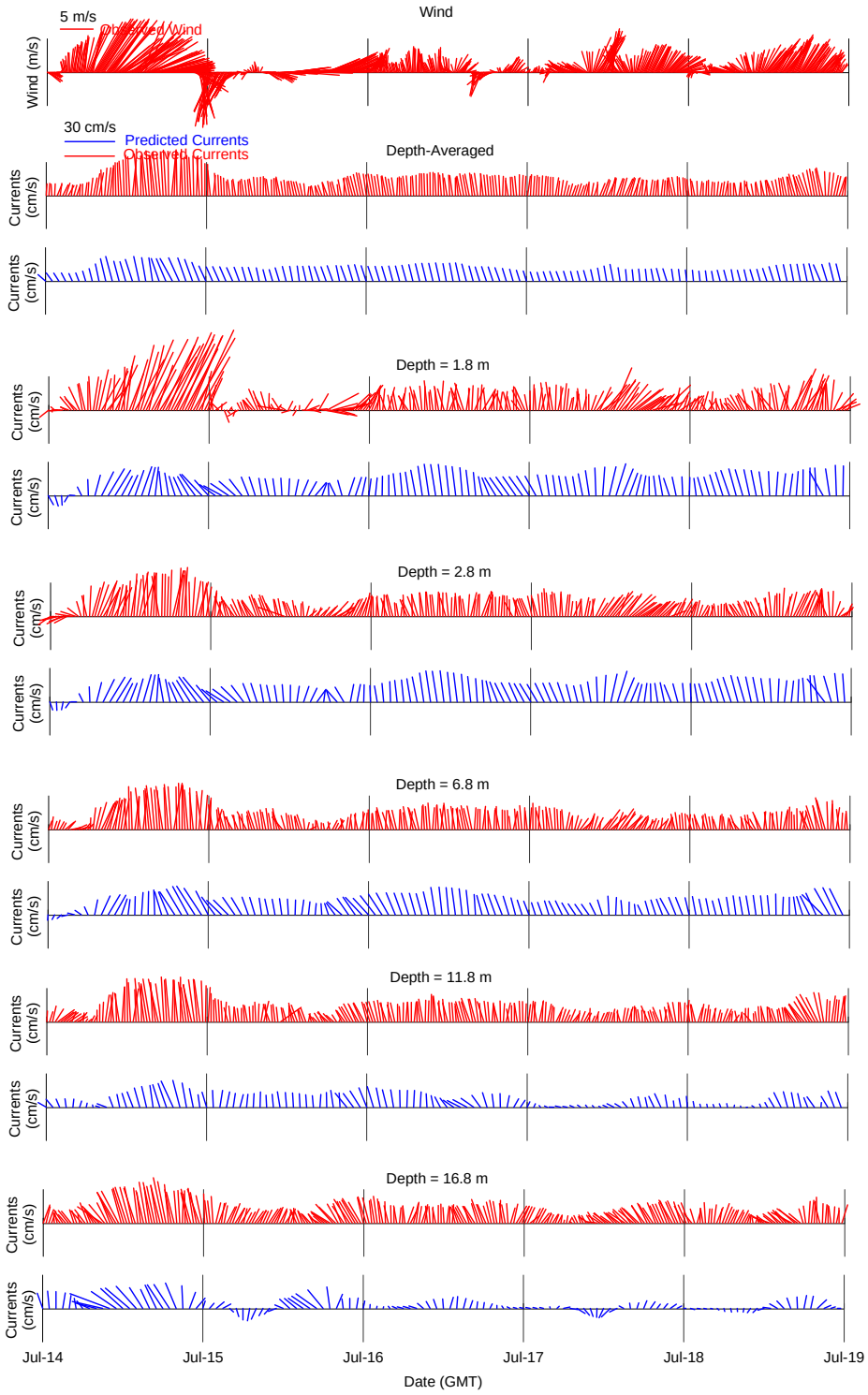

Figure 5.13 Time series of observed wind (red), observed currents (red) versus predicted currents (blue) for July 14 to 18, 2007 simulation at M20-07.

Model accuracy was assessed using NRMSE (Normalized Root Mean Square Difference). NRMSE which compares the relative difference between two scalar quantities (longshore and onshore current speed) from the model and observation. It is defined as follows:

$$NRMSE = \frac{RMSE}{Range\ of\ obs.} = \frac{1}{v_{o\max} - v_{o\min}} \sqrt{\frac{\sum_{i=1}^{M\Delta t} (v_p - v_o)^2}{M}} \tag{5-12}$$

where v_o and v_p are the observed and predicted velocities, $v_{o\max}$ and $v_{o\min}$ are the maximum and minimum observed velocities, and M is the number of time steps. In order to show a more quantitative comparison of the difference between velocity vector quantities, a statistical criterion similar to NRMSE was used that shows the bias of prediction from observation in vector format. The RMSE of two vector series ($\vec{v}_p, \vec{v}_o$) can be defined as follows:

$$\left\| \vec{v}_p, \vec{v}_o \right\| = \left(\frac{1}{M} \sum_{t=0}^{M\Delta t} \left| \vec{v}_p - \vec{v}_o \right|^2 \right)^{1/2} \tag{5-13}$$

The normalized form, also called the Fourier norm (Beletsky and Schwab, 2001), can be written as:

$$Fn = \left\| \vec{v}_p, \vec{v}_o \right\| / \left\| \vec{v}_o, 0 \right\| = \frac{\left(\sum_{t=0}^{M\Delta t} \left| \vec{v}_p - \vec{v}_o \right|^2 \right)^{1/2}}{\left(\sum_{t=0}^{M\Delta t} \left| \vec{v}_o \right|^2 \right)^{1/2}} \tag{5-14}$$

This statistical parameter represents the fractional difference between these two quantities. *Fn*=0 is perfect correlation and as it increases, the error rises. For zero current prediction ($\vec{v}_p = 0$), *Fn* equals unity. The comparisons for the four simulation periods at the ADCP locations using *Fn* and NRMSE are summarized in Table 5.3.

The best and worst predictions were found for the June 4-8, 2007 and August 7-11, 2006 simulations, where *Fn* and NRMSE were lowest and highest respectively. The

model underestimated the current speeds but showed better accuracy in predicting depth-averaged currents than surface currents. The nearshore currents (10 m depth) were better predicted and offshore current directions (20 m depth) were not very well predicted in 2007. The current magnitudes were overestimated in August, 2006 at S10-06, and June, 2007 at S10-07. The maximum calculated error (NRMSE) was about 20% for longshore currents in August 2006.

Table 5.3 Summary of Statistical Analyses for Simulation Periods.

	June 19-24, 2006		August 7-11, 2006	June 4-8, 2007			July 14-18, 2007		
	S10-06	N5-06	S10-06	S10-07	N10-07	M20-07	S10-07	N10-07	M20-07
Longshore Current Speed NRMSE									
Surface (%)	13	15	21	8	14	17	12	13	17
Depth-averaged (%)	10	12	20	5	6	14	10	10	13
Onshore Current Speed NRMSE									
Surface (%)	17	23	17	14	15	17	15	17	16
Depth-averaged (%)	13	19	15	10	12	14	12	13	19
Currents Fourier Norm									
Surface	0.60	0.67	0.68	0.46	0.58	0.65	0.53	0.57	0.65
Depth-averaged	0.51	0.56	0.60	0.41	0.39	0.60	0.49	0.51	0.60

5.7.2 Temperature Predictions

The temperature boundary condition at the river mouth was derived from the CTD data and temperature recorded at the power plant just upstream. A sample snapshot of the predicted temperature on June 20, 2006 at 0100 GMT is shown in Figure 5.14. The warmer plume is shown by red and orange contours.

Predicted vertical temperature profiles are compared with the CTD profiles at 4 points along a CTD transect (Figure 5.15). There is about 5°C temperature difference between the lake and the river. The model shows a weaker stratification at point 1 where there should be a surface well-mixed layer. The model also underestimates surface temperatures possibly due to the slow adjustment of the surface temperature field to the boundary conditions, errors of initialization, or vertical resolution (Beletsky, 2006).

The plume and buoyant spreading are not well simulated by the hydrodynamic model. This is why a near field model is needed, as shown in Chapter 6.

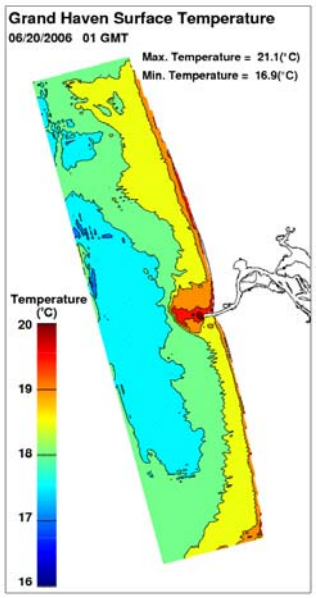

Figure 5.14 Predicted surface temperature on June 20, 2006 at 0100 GMT.

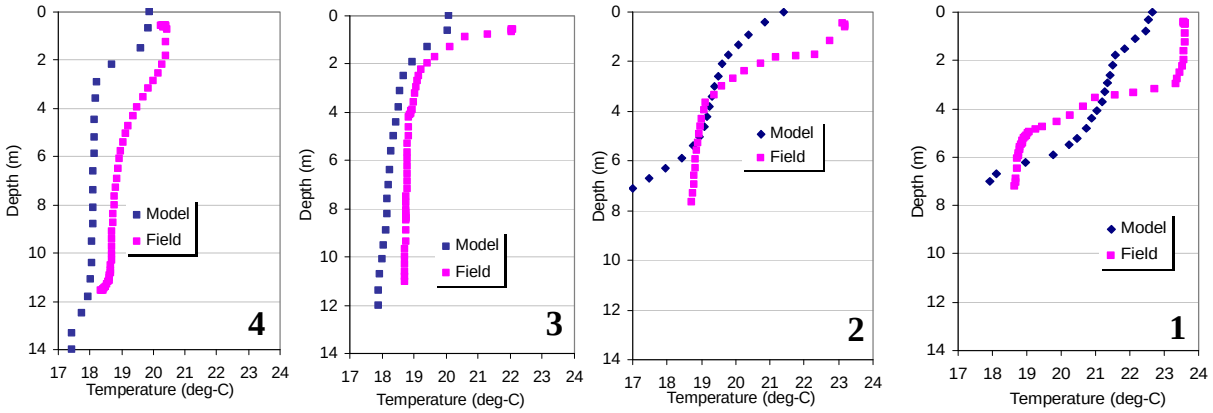

Figure 5.15 Model temperature versus field data on August 22, 2006.

5.8 Model Sensitivity and Calibration

To evaluate and improve the model accuracy, the errors in defining the forcing functions and initial and boundary conditions must be determined and minimized. Model physics restrictions and discretization errors can also create inaccuracies. Since the effect of the bottom roughness is not physically determined and is represented by an asymptotic function, a generic formula, $z_0 = a + b/(c+h)$, was used, where *a* and *c* have units of m and *b* is in m^2.

The model sensitivity was determined by varying the parameters *a*, *b*, and *c*. The model was run for several *a* (0.0005, 0.001, and 0.002 m), *b* (0.01, 0.02, and 0.03 m^2), and *c* (1 and 2 m) values. These parameter variations did not significantly affect the current predictions. Details are given in Appendix C. Therefore, *a*=0.001m, *b*=0.02 m^2, and *c*=1m were assumed for all simulations that yield the bottom roughness to approach 0.021m in shallower waters and decrease to 0.001m in deeper waters.

Horizontal diffusion is another parameter for which sensitivity of the model was assessed. It is calculated from a Smagorinsky eddy parameterization (with a multiplier named HORCON) to give a greater mixing coefficient near strong horizontal gradients. The model was run for HORCON=0.01, 0.05, 0.10, and 0.15 and compared to the observations (Appendix C). The change in current predictions was insignificant so HORCON was set to the recommended value of 0.1 for all runs.

5.9 Discussion

The POMGL nested hydrodynamic predictions were studied and compared with the observations. The best and worst current predictions were found for the June 4-8, 2007 and August 7-11, 2006 simulations respectively, where *Fn* and NRMSE were the lowest and the highest values. The model underestimated current speeds and directions but showed better accuracy in predicting depth-averaged currents than surface currents. The maximum calculated error (NRMSE) was about 20% for longshore currents.

The problem of too shallow mixed top layer and weak stratification in the plume has been observed in previous lake-wide studies (Beletsky et al, 2001, and 2006, and Martin, 1985). It can be caused by model physics limitations in representing non-

hydrostatic effects in small scales near buoyant river plumes. Addition of non-hydrostatic terms increases the computational costs significantly, however, improvement of the turbulence Mellor-Yamada model has been shown to improve predictions (Ezer 2000), but more work is needed to improve the momentum and thermodynamic equations.

Nested POMGL plume temperature predictions show enhanced vertical diffusion in the near field, however, near the river mouth, vertical diffusion in the mixed top layer is small and lateral spreading due to the temperature difference and buoyancy is the dominant process. In Chapter 6, we use a particle tracking model to overcome this issue by adding artificial diffusion in the far field and incorporating a near field model that represents buoyant spreading in the near field.

5.10 Summary

3D hydrodynamic simulation around Grand Haven was carried out using POMGL. A nested technique was used with refined bathymetry and forcing functions. The model current predictions were compared to available observations at various nearshore and offshore current meters. Current predictions were in good agreement with the observed data. The plume dynamics were poorly represented near the river mouth. Plume exchange flow due to vertical thermal stratification causes buoyant lateral spreading that is probably attributed to more complex and non-hydrostatic effects. In the next chapter, we incorporate a near field model to account for these phenomena and improve the accuracy of predictions.

CHAPTER 6

PARTICLE TRACKING

6.1 Introduction

Particle tracking models have been widely used to model coastal bigeochemical processes in the past decades. Unlike Eulerian models that solve the mass transport equations on a fixed grid, particle tracking models have a moving grid system (Lagrangian) that represents the diffusive substance as particles. They retain exact mass conservation. Eulerian models create numerical diffusion near high concentration gradients, and cannot resolve concentrations on scales smaller than the grid size. This deficiency is overcome in particle tracking models. The discharge is represented by a number of particles that are advected (transported) by the local current with a simple random walk formulation to represent turbulent diffusion. The particles can be assigned properties, such as mass and age, which makes the method particularly well suited to bacterial predictions. Spatial variability of diffusion such as enhanced mixing in the surf zone can be accommodated in particle tracking models that makes the magnitude of diffusion coefficients easier to estimate. The sources are easily represented and a near field model can be readily adapted.

6.2 Model (PARTIC3D) Description

The particle tracking model used here, PARTIC3D, takes advantage of the TRACE subroutine originally written by Jarle Berntsen (1991, Institute of Marine Research, Bergen-Nordnes, Norway) that computes the advection of the particles from the velocities in three directions from POMGL:

$$\begin{Bmatrix} dx_i/dt \\ dy_i/dt \\ dz_i/dt \end{Bmatrix} = \begin{Bmatrix} u_i(x,y,z,t) \\ v_i(x,y,z,t) \\ w_i(x,y,z,t) \end{Bmatrix} \tag{6-1}$$

where *x*, *y*, *z*, and *t* are the three-dimensional position of the particles and time, and *u*, *v*, *w* are the velocities in the three directions. The code has been modified and adapted for Great Lakes applications (Schwab, 1994). It was successfully tested with satellite-tracked drifters and larval transport in Lake Michigan (Beletski et al, 2006 and 2007). A second order scheme for horizontal components has been implemented (Bennett and Clites, 1987). The model represents the domain as an array of square grid cells (same as the nested model grid). Horizontal advective (deterministic) velocities are used from the nested POMGL hydrodynamic predictions and interpolated from the grid centers to grid square corners on the Arkawa-C grid. A Taylor series expansion of these velocities with first-order time differences results in:

$$\frac{x^{n+1}-x^n}{\Delta t} = u(x^n, y^n) + \frac{1}{2}\frac{\partial u}{\partial x}(x^{n+1}-x^n) + \frac{1}{2}\frac{\partial u}{\partial y}(y^{n+1}-y^n) \tag{6-2}$$

$$\frac{y^{n+1}-y^n}{\Delta t} = v(x^n, y^n) + \frac{1}{2}\frac{\partial v}{\partial x}(x^{n+1}-x^n) + \frac{1}{2}\frac{\partial v}{\partial y}(y^{n+1}-y^n) \tag{6-3}$$

where *n* and *n*+1 are the current and next time steps. $u(x^n, y^n)$ and $v(x^n, y^n)$ are the horizontal velocities at the current particle position (x^n, y^n) inside the grid. They are computed by a bilinear interpolation from the grid corners. The velocity derivatives are computed using a bilinear assumption from the grid sides. The new position of the particle (x^{n+1}, y^{n+1}) is determined by solving the set of linear Eqns. 6-2 and 6-3. The time step Δt, is selected to restrict particle travel to a maximum of 1/8 the distance between horizontal grid points.

The *z*-coordinates are transformed to the sigma coordinate system before the tracers are transported. After particle propagation the coordinates are transformed back to the physical coordinate system. The sigma coordinate is computed using a bilinear interpolation to the particle location:

$$\sigma(x^n, y^n) = z^n / d(x^n, y^n) \tag{6-4}$$

Where d is the water depth, and σ and z are the vertical coordinates. Vertical velocities are computed by interpolating vertical velocities at the sigma levels. The vertical particle location is calculated as:

$$z^{n+1} = z^n + w\Delta t \tag{6-5}$$

The particle tracking model assumes that free surface displacement is not important for trajectory calculations. The particles are assumed dead if they reach the free surface, lake bottom or horizontal open boundaries. This way, particles do not pile up at stagnation points at grid corners, along the shoreline, or at the boundaries. This is an advantage of this method over traditional first-order horizontal particle tracking methods.

Diffusion due to turbulence has a significant role in plume mixing and must be included in the model. As explained in Chapter 2, the horizontal and vertical velocities are assumed to include a random (stochastic) component. The velocity components are divided into two different terms due to advection and diffusion:

$$\begin{Bmatrix} u_i \\ v_i \\ w_i \end{Bmatrix} = \begin{Bmatrix} u_i^{adv}(x,y,z,t) \\ v_i^{adv}(x,y,z,t) \\ w_i^{adv}(x,y,z,t) \end{Bmatrix} + \begin{Bmatrix} u_i^{ran} \\ v_i^{ran} \\ w_i^{ran} \end{Bmatrix} \tag{6-6}$$

These velocities represent small-scale turbulent mixing that are formulated as follows:

$$\begin{Bmatrix} u_i^{ran} \\ v_i^{ran} \\ w_i^{ran} \end{Bmatrix} = \frac{1}{\sqrt{\Delta t}} \begin{Bmatrix} \varepsilon_i \sqrt{2K_h} \\ \varepsilon_i' \sqrt{2K_h} \\ \varepsilon_i'' \sqrt{2K_v} \end{Bmatrix} \tag{6-7}$$

where K_h is the horizontal diffusion coefficient, K_v is the vertical diffusion coefficient, and ε , ε', and ε'' are three sets of independent random numbers in the range of [$-\sqrt{3}, \sqrt{3}$] range (Chin and Roberts, 1985). In some similar studies two other terms (e.g. in x direction $\frac{dK_h}{dx}\Delta t, \frac{K_h}{h}\frac{dh}{dx}\Delta t$) have been added to the stochastic displacement components. These are artificial velocities due to the horizontal gradient of diffusion coefficient and uneven bathymetry (Dimou, 1989, and Suh, 2004). In the present study,

the diffusion gradient term was considered insignificant and bathymetry does not change abruptly so those two terms were neglected.

The particles' random displacement at each time step is added to the right side of Eqs. 6-2 and 6-3 to determine the total particle displacement at each time step:

$$x(t+1) = x(t) + u(t)\Delta t + \varepsilon_i \sqrt{2K_h \Delta t} \tag{6-8}$$

$$y(t+1) = y(t) + v(t)\Delta t + \varepsilon_i' \sqrt{2K_h \Delta t} \tag{6-9}$$

$$z(t+1) = z(t) + w(t)\Delta t + \varepsilon_i'' \sqrt{2K_v \Delta t} \tag{6-10}$$

In order to evaluate the tracer concentration, such as bacteria level, the number of particles is computed in each cell. Mass is assigned to each particle and the concentration is computed based on the total number of particles released. A first-order decay process is assumed to occur with a variable decay rate based on irradiation, and temperature.

$$C = C_0 \cdot e^{(-k \cdot \Delta t)} \tag{6-11}$$

where C_o is the initial concentration, C is the corrected concentration after time Δt, k is the overall decay rate constant, and Δt is the model time step. The overall decay rate was assumed similar to Eqn. 2-28, the formula in Thupaki et al. (2010). Because the second term (base mortality) is at least an order of magnitude smaller than the first term (the loss of bacteria due to sunlight insolation), it was simplified to:

$$k = \left(k_I I_0(t) e^{(-k_e z)}\right) 1.07^{T-20} \tag{6-12}$$

where k_I, the insolation inactivation rate, was assumed 0.0026 $W^{-1}m^2d^{-1}$ (3×10^{-8} $W^{-1}m^2s^{-1}$ as in Thupaki et al, 2010) for the total range of sunlight bandwidth (300-3000 nm). $I_0(t)$, the sunlight intensity in Wm^{-2} at the surface was used as time series from the NOAA Real-Time Meteorological Observation Network (RECON) observation at Muskegon Field Station, Lake Michigan. k_e, the light extinction coefficient was assumed 0.48 m^{-1} as an average for photosynthetically active radiation (PAR) and Near Infrared (NIR) (CAEDYM Manual, Hipsey et al, 2007), since UV radiation has only a minor effect on E. coli in the water column (Whitman, 2004) in turbid plumes, z was the depth

of particles in m, and T was the water temperature, that was assumed to be the average of the lake and plume water temperatures.

6.3 Model Limitations

PARTIC3D has some shortcomings that are common to every particle tracking model. It is not well suited to prediction of water quality parameters such as nutrients that involve chemical reactions between constituents. The numbers of particles may be restricted by memory and computation time. In order to simulate a real and continuous flow a substantial number of particles should be released. Therefore the conversion of particles to mass and obtaining a physical dilution is computationally intensive. Also when particles hit the closed or open boundaries they are set as "dead" particles, because there is no further information about them. So the mass within the boundaries will not be conserved. The model uses a first order advection scheme that has some truncation error.

6.4 Model Setup, Initial and Boundary Conditions

In PARTIC3D the user must supply a description of the bathymetry, the 3D velocities, 3D horizontal and vertical diffusivities, control parameters (time step between currents, time step between tracer particle positions, time step between the insolation record, and duration of run), tracer particle initial positions, and the solar insolation intensities time series. Horizontal diffusivity in lakes has been measured between 0.01-10 m^2/s (Csanady, 1964 and 2006; Peeters, 1994; Stevens et al, 2004; Stocker and Imberger, 2003). Initial runs were conducted with constant horizontal diffusions of 0.01, 0.1, 1.0 and 10.0 m^2/s over the whole domain. But these average values are not representative of spatial variability of the diffusivities. Diffusivities increase near high velocity gradients (e.g. near the river mouth), and diminish in low velocity gradients. Therefore, K_h was used from the POMGL simulations output (similar to Korotenko et al, 2004). The POMGL Smagorinsky formula for horizontal diffusion is dependent on horizontal velocity gradients as below:

$$K_h = C\Delta x\Delta y\frac{1}{2}\left[(\partial u/\partial x)^2 + (\partial v/\partial x + \partial u/\partial y)^2/2 + (\partial v/\partial y)^2\right]^{1/2} \qquad (6\text{-}13)$$

Horizontal advective velocities (u_i^{adv} and v_i^{adv}) ranged between 0.1-50 cm/s and the random velocities (u_i^{ran} and v_i^{ran}) computed from POMGL horizontal diffusivities ranged between 0.001-2 cm/s.

Vertical diffusivities in lakes have been measured between 0.5×10^{-3} to 1×10^{-3} m^2/s for the epilimnion and thermocline, and 1×10^{-3}-5×10^{-3} m^2/s for the hypolimnion. Rao et al. (2004), used a simple vertical diffusion in Lake Ontario:

$$K_v = \frac{K_0}{(1+5Ri)^2} + K_0 \tag{6-14}$$

where K_0 is an adjustable parameter (set to $10^{-2} m^2 s^{-1}$), $K_b = 10^{-6} m^2 s^{-1}$ is the background eddy viscosity, and Ri is the Richardson number defined as:

$$Ri = \frac{N^2}{Shear^2} = \frac{-\frac{g}{\rho_0}\frac{\partial \rho}{\partial z}}{\left(\frac{\partial u}{\partial z}\right)^2 + \left(\frac{\partial v}{\partial z}\right)^2} \tag{6-15}$$

where N is the Brunt-Vaisala frequency, ρ_0 is the reference density, $\frac{\partial \rho}{\partial z}$, $\frac{\partial u}{\partial z}$, and $\frac{\partial v}{\partial z}$ are density and horizontal velocity gradients in z direction. POMGL predicts vertical diffusivities from:

$$K_v = f(Ri) \tag{6-16}$$

$$Ri = l\frac{\frac{g}{\rho_0}\left[\frac{\partial \rho}{\partial z} - \frac{1}{c_s^2}\frac{\partial p}{\partial z}\right]}{q^2} \tag{6-17}$$

where l is the turbulence length scale, q is the turbulent kinetic energy, p is the hydrostatic pressure, and c_s is the speed of sound. POMGL underestimates the strong stratification profile due to the plume in the near field close to the river mouth as described in Chapter 5. This stratification suppresses vertical mixing and turbulent diffusion. The sharp edge of the plume close to the mouth seen in the aerial photos also indicates that buoyant spreading is dominant and so vertical diffusion is small.

The vertical diffusion is more rapid in the far field where the vertical density gradient is smaller and ambient turbulent diffusion dominates. It is negligible at the plume-lake interface however, where the sharp jump in temperature exists, and occurs across time scales much longer than the vertical turbulent diffusion decay time scales in the far field (Csanady, 1964; Pearson et al. 1983). The random vertical velocities (w_i^{ran}) computed from POMGL vertical diffusivities around the mouth were also typically between 0.05-0.1 cm/s in the higher end of deterministic vertical velocities, w_i^{adv} (0.001-0.1 cm/s), which shows that POMGL predicts incorrect vertical mixing in the near field. Therefore vertical diffusivities were set to zero up to a radius of 1200 m (~10 times the channel width) from the mouth, and at farther distances the vertical diffusivities predicted by POMGL were used.

The release of particles is set within the model initial conditions. Every particle is assigned a time such that whenever that time is passed, the particle is released. 10 particles were released every minute uniformly at the river mouth at depths of 0.5 and 1.5 m in the initial simulations (without the near field model), that resulted in 1200 particles per hour or a total of 144000 particles for the 5-day runs (August 2006, and June and July 2007) and 172800 particles for the 6-day run (June 2006). The code was run under Windows on a Pentium 4 with a 3.4GHz CPU and 1 GB of RAM which limited the total number of particles to 180000.

6.5 Model Evaluation

The PARTIC3D simulations were initially compared with a 2D gradient-diffusion model. The original 2D code was written by Schwab (2005) and is currently running in the Great Lakes Coastal Forecasting System (GLCFS). Snapshots from both models simulation on August 8, 2006 are shown in Figure 6.1. As seen the 3D particle tracking model represents the behavior and shape of the plume better and shows patchiness that is more realistic than the smooth gradients predicted by the 2D gradient-diffusion model.

PARTIC3D was run for all the four hydrodynamic simulation periods discussed in Chapter 5 (June 19-24, 2006; August 7-11, 2006; June 4-8, 2006; and July 14-18, 2007). The PARTIC3D simulation results were also compared with the available aerial photos.

In Figure 6.2, particle distributions and tracer concentrations from the simulation on June 6, 2007 show quite good correspondence with the shape of the plume in the composite aerial photo.

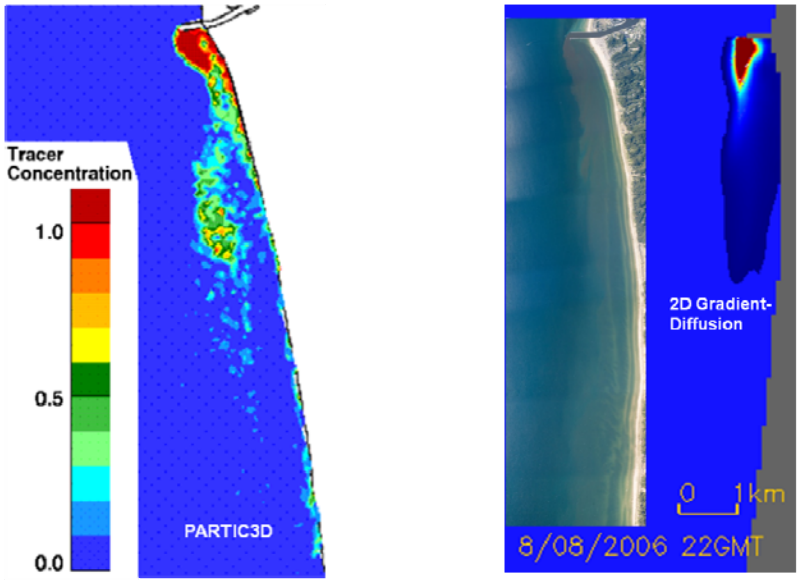

Figure 6.1 Tracer concentration snapshots of a 2D advection/diffusion and PARTIC3D model, and aerial photography on August 8, 2006.

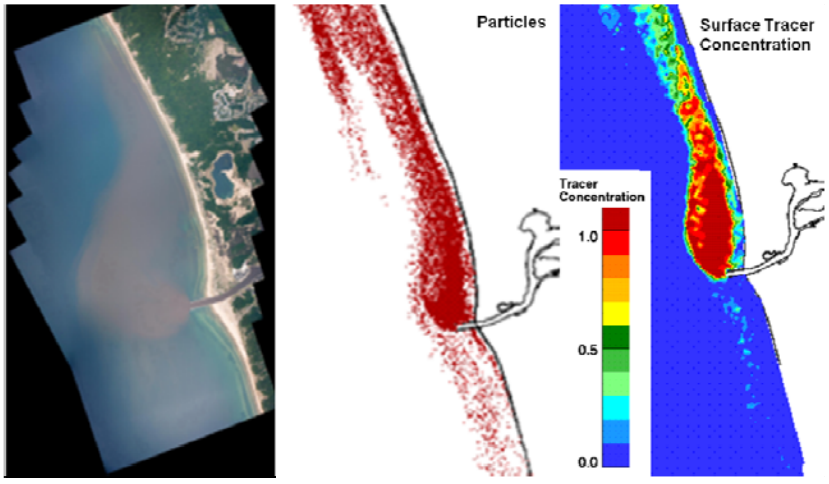

Figure 6.2 Composite aerial photo (left), and PARTIC3D simulation snapshots: particles (middle) and tracer concentration (right) on June 6, 2007.

In order to further test the accuracy of PARTIC3D, predicted tracer dilutions were compared with observed dilution from the conductivity measurements. Model dilutions

were computed from Eqn. 3-1, setting $C_b = 0$ and C_0 equal to the average concentration from nine cells at the mouth. The results for CTD transects on June 22, 2006, June 6, 2007, and July 17, 2007 are shown in Figures 6.3 to 6.5.

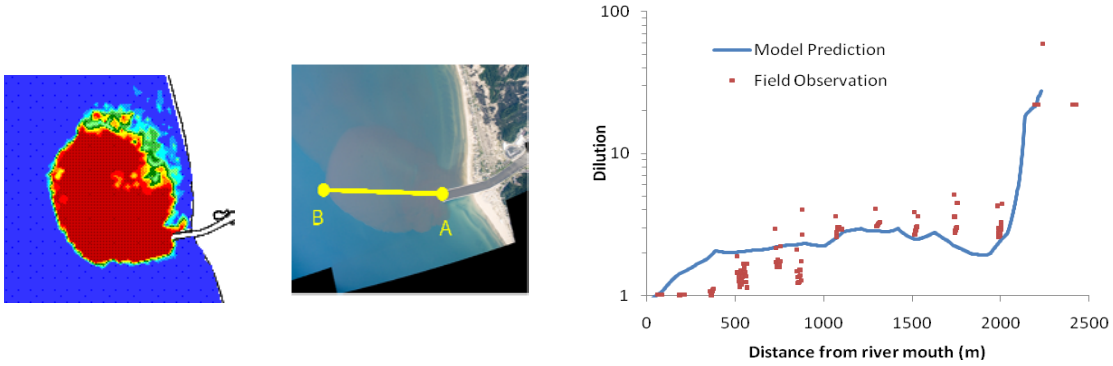

Figure 6.3 Comparison of PARTIC3D predicted and observed dilution on June 22, 2006.

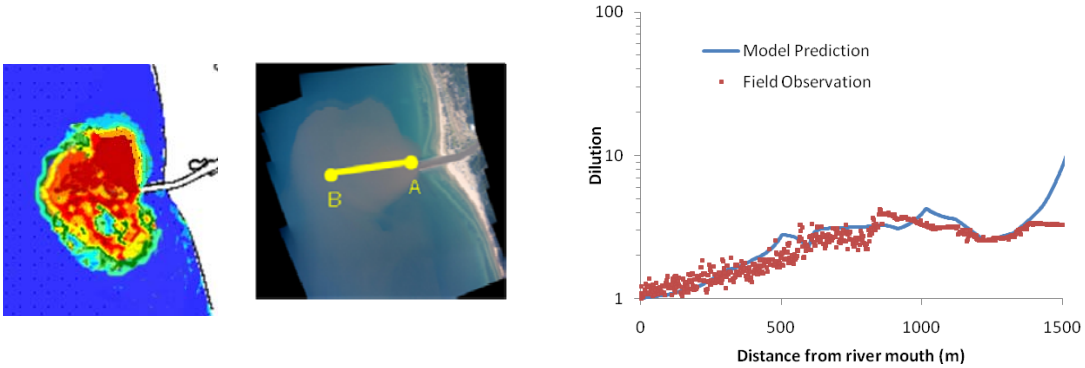

Figure 6.4 Comparison of PARTIC3D predicted and observed dilution on June 6, 2007.

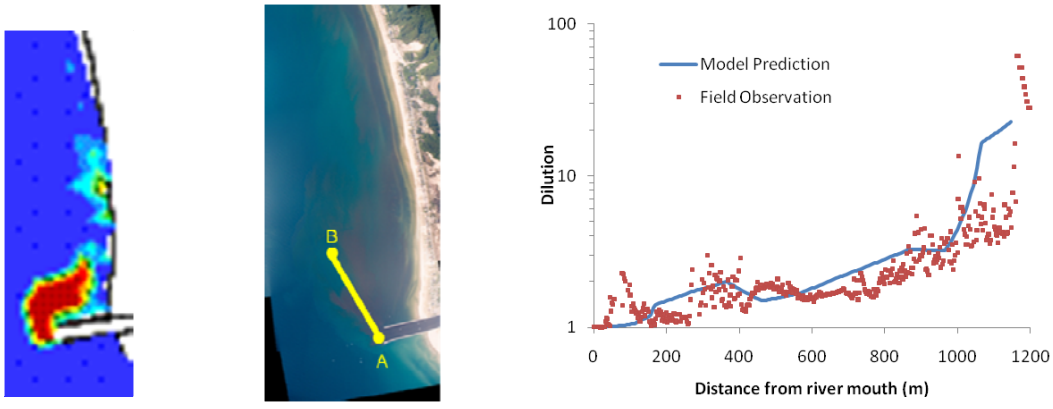

Figure 6.5 Comparison of PARTIC3D predicted and observed dilution on July 18, 2007.

The model shows promising agreement with the observations. However, the model dependency on the hydrodynamic simulation necessitates an accurate current field prediction. In cases where the predicted currents were different due to imprecise boundary conditions and forcing functions, PARTIC3D predictions differed from observations. The behavior of the plume in the near field is also affected by buoyant spreading that must be incorporated. We try to overcome this deficiency by improving the model with a near field empirical model in the next section.

6.6 Coupling the Near Field and Far Field Models

The PARTIC3D model as a far field model uses currents from the hydrodynamic simulations. Entrainment due to the initial momentum of the plume is not represented in the hydrodynamic model due to the difference in length and time scales where near field processes occur. As a result, an empirical near field model was coupled with the far field model to incorporate lateral spreading in the near field.

A separate near field model can be incorporated within the model initial conditions by defining the location and number of particles to be released. These particle specifications are determined based on the empirical relationships in Chapter 4. The minimum dilution and centerline trajectory were computed along the plume centerline at every 100 m transect up to ξ=1200 m using Eqns. 4-5 and 4-6. The mean dilution was assumed to be 1.4 times the minimum dilution (Fischer et al, 1979). At every cross section, the mean concentration was computed and particles were distributed uniformly across the width of that transect.

The plume width and thickness were determined from Eqns. 4-1 and 4-3 respectively. Based on the cross section dimensions (width and depth), particles were distributed in the vertical using an exponential function. Vertical diffusion coefficients were set to zero within the near field. The extent of the near field was estimated to extend approximately 10b (b= channel width) from the mouth based on the aerial photo observations that the plume sharp edge became diffuse and buoyant spreading diminished beyond 10b. The same number of particles (1200 per hour) were released in the near field and the model was run on the same system as explained in Section 6.4. As the particles

entered the far field, vertical diffusion computed from the hydrodynamic simulations was used. A schematic of the particle release and model coupling is shown in Figure 6.6.

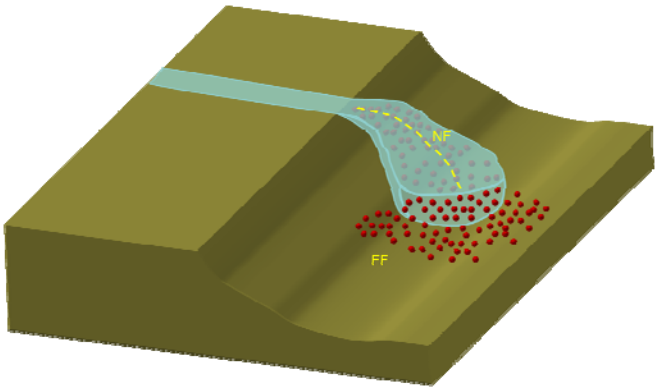

Figure 6.6 Schematic of the near and far field models coupling.

The coupled model dilution predictions were compared with the measured dilution contours (2:1, 5:1, and 10:1), and the single far field model on June 6, 2007 as shown in Figure 6.7. Its prediction matches the dilution contours better within the near field, showing the empirical near field trajectory used by the coupled model improves prediction.

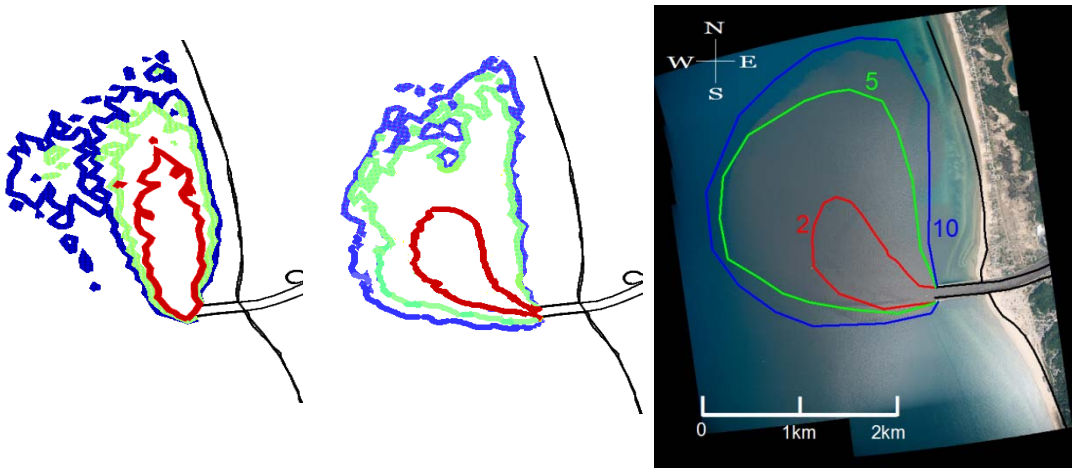

a) Single FF model prediction **b) Coupled NF-FF model prediction** **c) E. coli dilution**

Figure 6.7 Comparison of E. coli dilution contours (red 2:1, green 5:1, and blue 10:1) with the single FF and coupled NF-FF model predictions on June 6, 2007.

The E. coli dilutions on plume centerline trajectory have been compared with predictions from the single FF and coupled NF-FF model as shown in Figure 6.8. The single FF model underestimates the dilution, but the coupled model shows more accurate predictions.

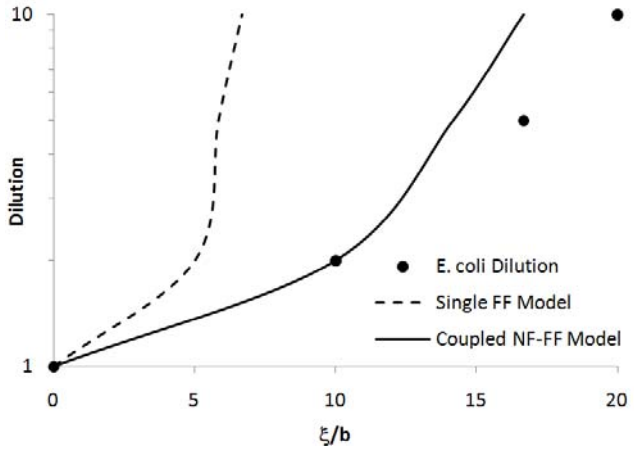

Figure 6.8 E. coli dilution observation, and single FF and coupled NF-FF model predictions on plume centerline trajectory on June 6, 2007.

6.7 Discussion

In this chapter we attempted to overcome the deficiencies of gradient diffusion models in nearshore bacterial predictions by using a random walk particle tracking model (PARTIC3D). In addition, the 3D model represents the fate and transport of bacteria better than the conventional 2D models (e.g. the present Great Lakes coastal forecasting model) in a surface river discharge, since the flow characteristics in the surface layer can be considerably different from the depth-averaged transport.

The model showed good agreement with observed dilutions which are typically less than 10:1 within 10*b* from the mouth. Model adjustment for horizontal diffusion improved the model. The POMGL horizontal diffusion is based on Smagorinsky's formula and horizontal velocity gradients that provide a more accurate estimation than constant diffusion. Vertical mixing and diffusion in the model were switched off in the near field to better represent reduction in vertical mixing due to stratification.

Solar insolation plays a significant role in bacterial decay and its variation during the day can affect the predicted dilutions. Therefore a comprehensive model from previous bacterial transport studies in Lake Michigan was used that uses solar radiation field time series and other empirical constants. The constants however should be tested to calibrate for the model.

The coupled technique advances surface buoyant discharge predictions. Good agreement was observed between the model prediction and field dilutions, but the model must be tested and evaluated for other sites. The coupled model has the same limitation as the near field model for discharge that was explained in Chapter 4. Further improvement to the near field model makes the coupled model more robust for wider ranges of input. The transition from the near field to the far field also needs to be further investigated to make it more accurate and smoother.

6.8 Summary

A 3D particle tracking model was used to predict the surface buoyant discharge at Grand Haven. The model assigns mass and time to the particles that represent bacteria concentration. It was improved by adding artificial velocity terms to include the effects of turbulent diffusion in the far field. Model sensitivity for different diffusion coefficients was assessed. The model showed good agreement for the observed cases. A coupling technique was developed to accommodate an empirical near field model within the far field particle tracking that is using the results of hydrodynamic simulations. The coupled model improved dilution prediction in the near field at sub-grid scales that far field models cannot resolve. These advancements can contribute to more accurate nearshore transport predictions for the Great Lakes Coastal Forecasting System and lead to improved beach bacteria prediction and management.

CHAPTER 7

SUMMARY AND CONCLUSIONS

7.1 Summary

The objective of this research was to improve understanding of the fate and transport of bacteria carried by rivers into lakes by means of field experiment and numerical simulation. The ultimate outcome of this study is to develop a more accurate numerical technique that can be applied to the NOAA Great Lakes Coastal Forecasting System (GLCFS) for nearshore contaminant transport and beach water quality predictions. This is essential to informed decisions about beach closures in order to avoid unnecessary beach closures with their accompanying economic losses and possible loss of public confidence, and the design of infrastructure such as river outfalls, CSO schemes and water intakes to obviate exposure of the public to potential pathogens.

Extensive field work on the dynamics of the Grand River plume was carried out in summers of 2006 and 2007 that included simultaneous aerial photography, measurements of lake physical properties, the addition of artificial tracers to track the plume, and bacterial sampling. The river formed a surface plume that thinned rapidly within a distance of a few hundred meters from the mouth while spreading laterally. The plume behavior and shape were changing within every few hours, and previous studies (e.g. Jones et al. scheme) did not encompass all its shapes and dynamics.

Beaches can become directly impacted by offshore plume bacteria. The Grand River plume data indicated bacterial reductions due to dilution were generally small (less than 10:1) up to 4.5 km from the river mouth. E. coli concentrations were highly correlated with conductivity (as a measure of water salinity) on one day (June 5, 2007), indicating that bacterial decay was negligible (T_{90} ~ 10.5 days). On the next day (June 6, 2007), the field data implied a higher decay rate (T_{90} ~ 1.1 days) due to increased solar radiation. This indicates that bacterial decay rates in river plumes can vary substantially from day to day, and further research is needed to evaluate the dominant factors. Decay

rates ranged from 0.2 to 2.2 day^{-1} and were within the range of previous studies in Lake Michigan. Total coliform survived longer than E. coli suggesting different die-off mechanisms.

Some existing common mathematical models, developed for the nearshore bacterial transport prediction, were also reviewed. Gradient-diffusion models have significant drawbacks for bacterial modeling. They are subject to numerical diffusion, especially at the plume boundaries, and cannot model the sharp gradients that we observed in the Grand River plume. Numerical diffusion is particularly a problem with bacteria where the numbers are large and can lead to predictions of transport to beaches where none in fact occurs. In addition, they always predict concentrations that vary smoothly in space, and have no mechanism to predict the patchy fields of bacteria that is almost always found in nature.

Random walk particle tracking models have considerable advantages over gradient diffusion models in simulating bacterial behavior nearshore. Multiple bacterial sources, especially those with differing characteristics, for example buoyant velocities or decay or growth rates, are easier to incorporate. A particle tracking model was used that gave us the capability to track a decaying tracer and better quantify mixing due to turbulent diffusion. This resulted in an improved representation of bacteria diffusion, decay and transport.

7.2 Contributions

A new empirical relationship for lateral spreading was presented that completes previous studies in distances within 1 km from the river mouth, and determines the plume width based on the channel width instead of a variable initial width that depends on the local internal wave celerity.

A near field empirical model of trajectory and minimum dilution for large aspect ratio surface discharge channels was also developed that is better suited to conditions typical of the Great Lakes than previous models. Few authors have addressed the issue of near field dynamics or even acknowledged it, especially in river plumes with large aspect ratio that are common for rivers discharging to the Great Lakes. The near field model and

empirical relationships describing plume geometry simulate the plume dynamics and mixing close to the source better, such as dynamic surface spreading and reduced vertical mixing.

A new classification scheme based on the relative magnitude of the plume-crossflow length scale and a Richardson number based on wind speed was devised, that included longshore current components and onshore-offshore wind effects. The combination of the length scale and Richardson number could predict whether the plume was shore attached or unattached, and how the onshore wind can spread the unattached plume offshore, deflect it back to shore, or diffuse it. Our observed results showed more flow classes than included in previous studies (e.g. CORMIX).

A nested hydrodynamic modeling scheme was employed. The nearshore refined hydrodynamic simulation associated with the 3D transport predictions also represented the surface river discharges better than present 2D models. The measured and modeled currents agreed fairly well. 2D models (often depth-averaged) are a poor approximation to the thin surface spreading layer that actually occurs in the Great Lakes where the processes are clearly 3D.

Due to computational limitations, it is not presently feasible to capture the wide range of spatial and temporal hydrodynamic processes in one mathematical model. A coupled empirical near field model with the far field particle tracking model was developed that improved prediction of the behavior of the Grand River discharge nearshore compared to the existing models. The coupling technique application was novel for buoyant surface discharges and revealed the deficiencies of the usual engineering approach of using single models.

The method can also have implications for forecasting and real-time assessment of pathogen indicators in recreational beach waters. This goal was accomplished by refining POMGL large scale hydrodynamic simulations, applying a 3D far field particle tracking model coupled with an empirical near field model that was tested with Grand Haven extensive field studies.

7.3 Recommendations for Future Research

The empirical near field model should be tested for other sites and other ranges of input parameters, e.g. Froude number, inflow, and ambient current speed. The coupled model should be improved to enable a smooth transition from the near field to the far field. It is recommended to test using other Lagrangian near field models based on entrainment (e.g. Jay et al, 2010) with the far field particle tracking model since linking two Lagrangian mathematical models can possibly make a robust final model. PARTIC3D is suggested to be evaluated and calibrated with the observations for the other sites and estuary systems before operational setting.

The possibility of wave-induced resuspension of bacteria is a concern that is not addressed in the model. Wind-generated surface waves in the Great Lakes have significant effects in transport of sediments. Bed shear stresses due to wave-induced currents can be orders of magnitude higher than stresses resulting from currents alone. Therefore addition of the wave resuspension effects can make the model more realistic and representative of beach bacterial reactivation and longer survival rates.

The results of this research can also have broad industrial application and implications for environment protection, and assist in minimizing economic operation and construction costs of water and wastewater related infrastructure. The model can be applied to locate the best water intake locations that minimizes the entrainment of bacteria (and sediment), therefore protecting drinking water supplies. It can also improve and optimize the design and operation of CSO regulating systems, domestic sewer outfalls, and water intakes. Incorporating the model in wastewater treatment plants operation will be of great help to optimize the addition of chlorine or other costly treatments.

Finally, using the particle tracking method to model diffusion in the Great Lakes is advantageous to studies of biological processes as well. Its ability to couple physical and biological processes such as a food web model is a unique feature, and can easily be incorporated into the field experiments on thermal stratification and oxygen depletion.

APPENDIX A: AERIAL PHOTOS

A.1. June 2006

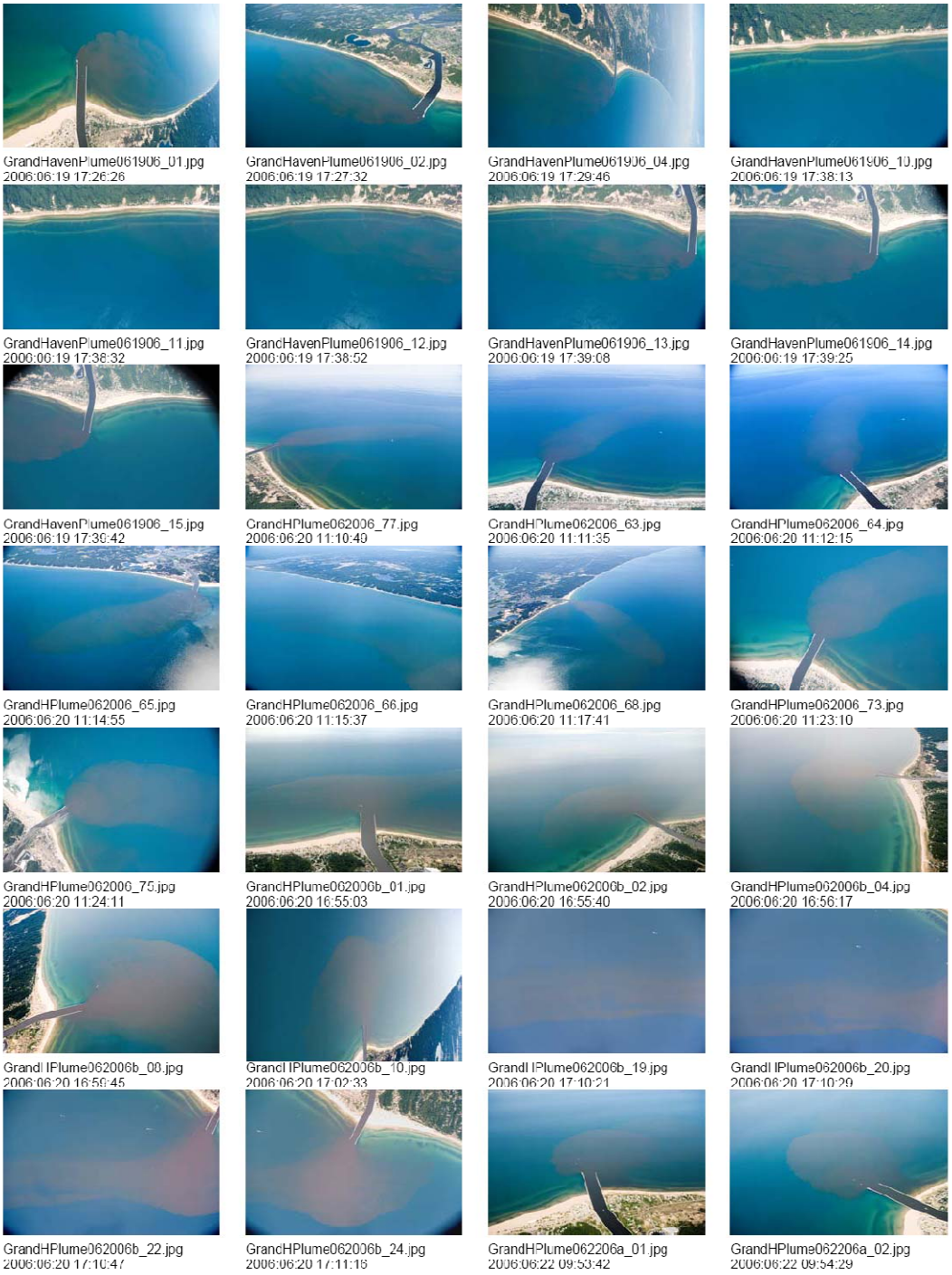

Figure A.1. Aerial pictures of the Grand Haven Plume from June 19, 2006 17:26:26 EDT to June 22, 2006 9:54:29 EDT.

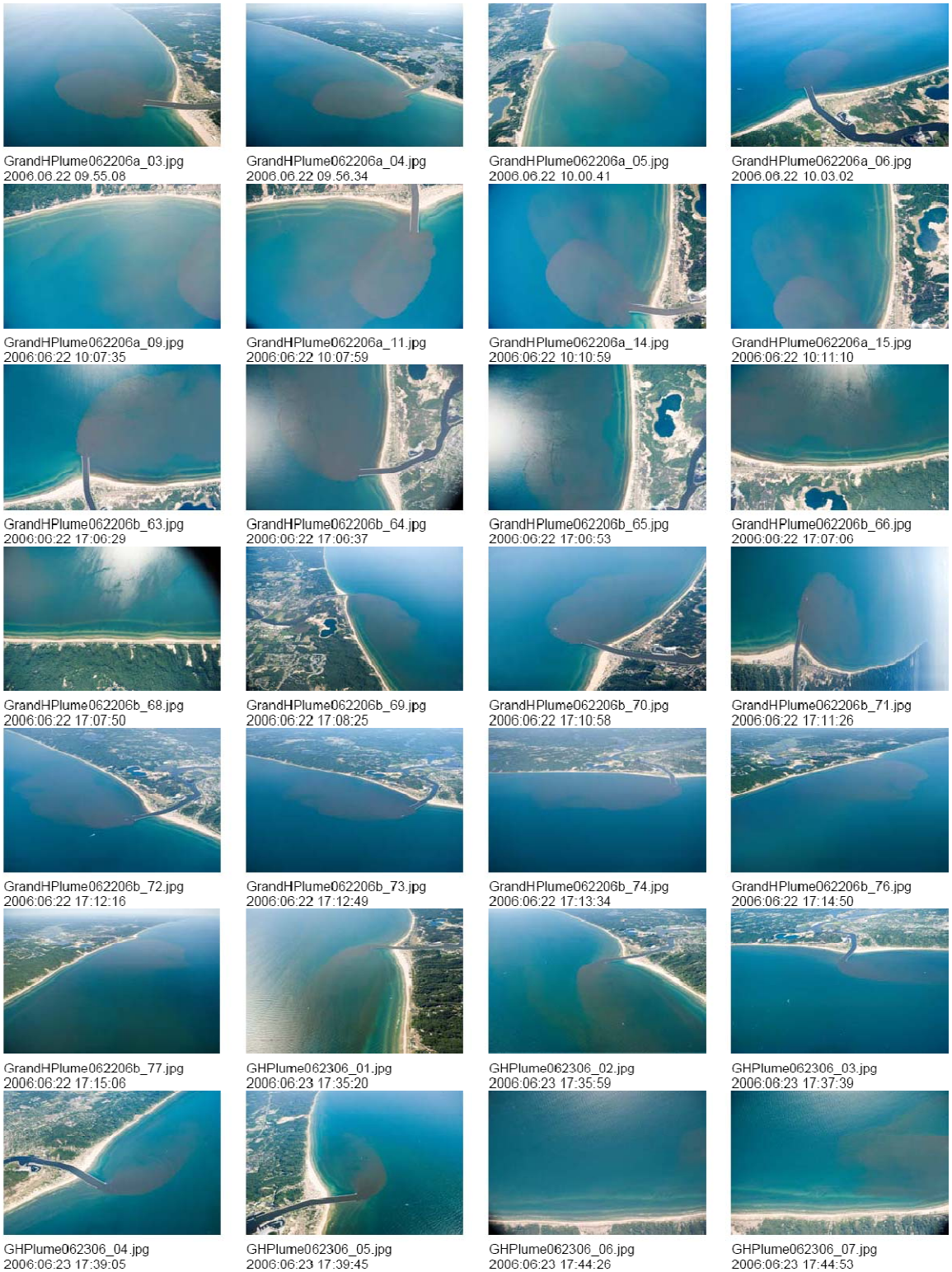

Figure A.2. Aerial pictures of the Grand Haven Plume from June 22, 2006 9:55:08 EDT to June 23, 2006 17:44:53 EDT.

Figure A.3. Aerial pictures of the Grand Haven Plume from June 22, 2006 from 9:55:08 EDT to June 23, 2006 17:44:53 EDT.

A.2. August 2006

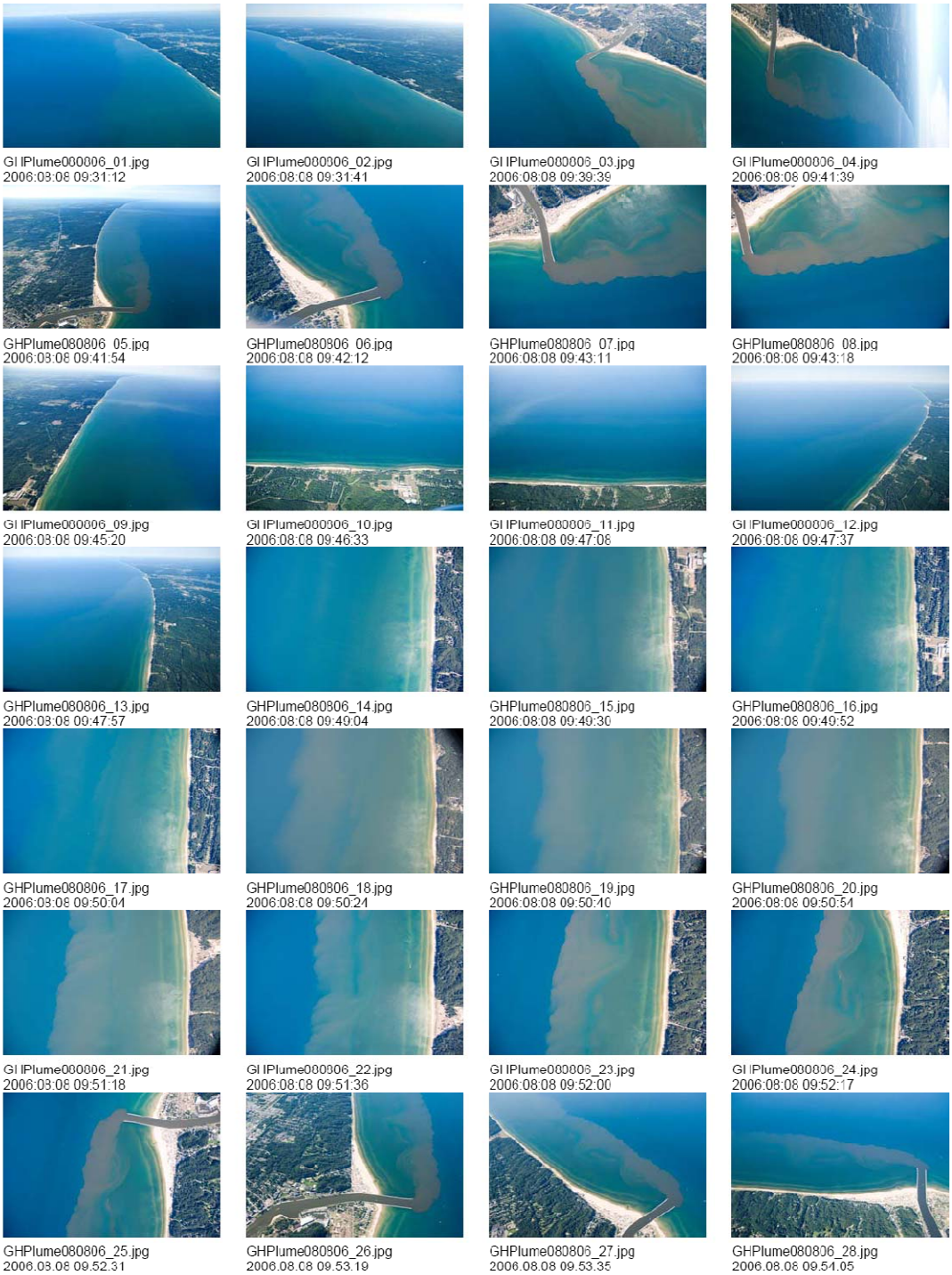

Figure A.4. Aerial pictures of the Grand Haven Plume on August 8, 2006 from 09:13:12 to 09:54:05 EDT.

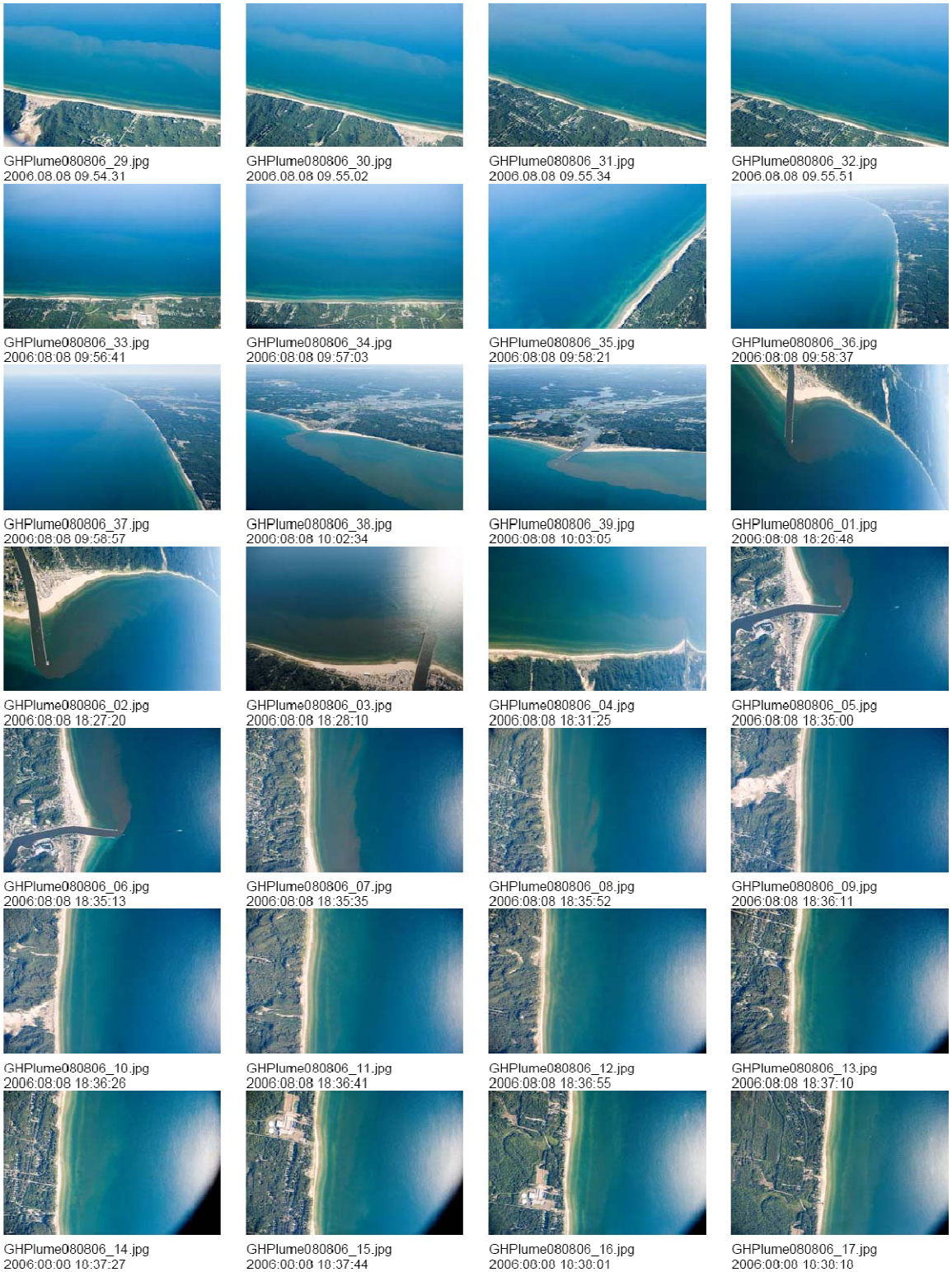

Figure A.5. Aerial pictures of the Grand Haven Plume on August 8, 2006 from 09:54:31 to 18:38:18 EDT.

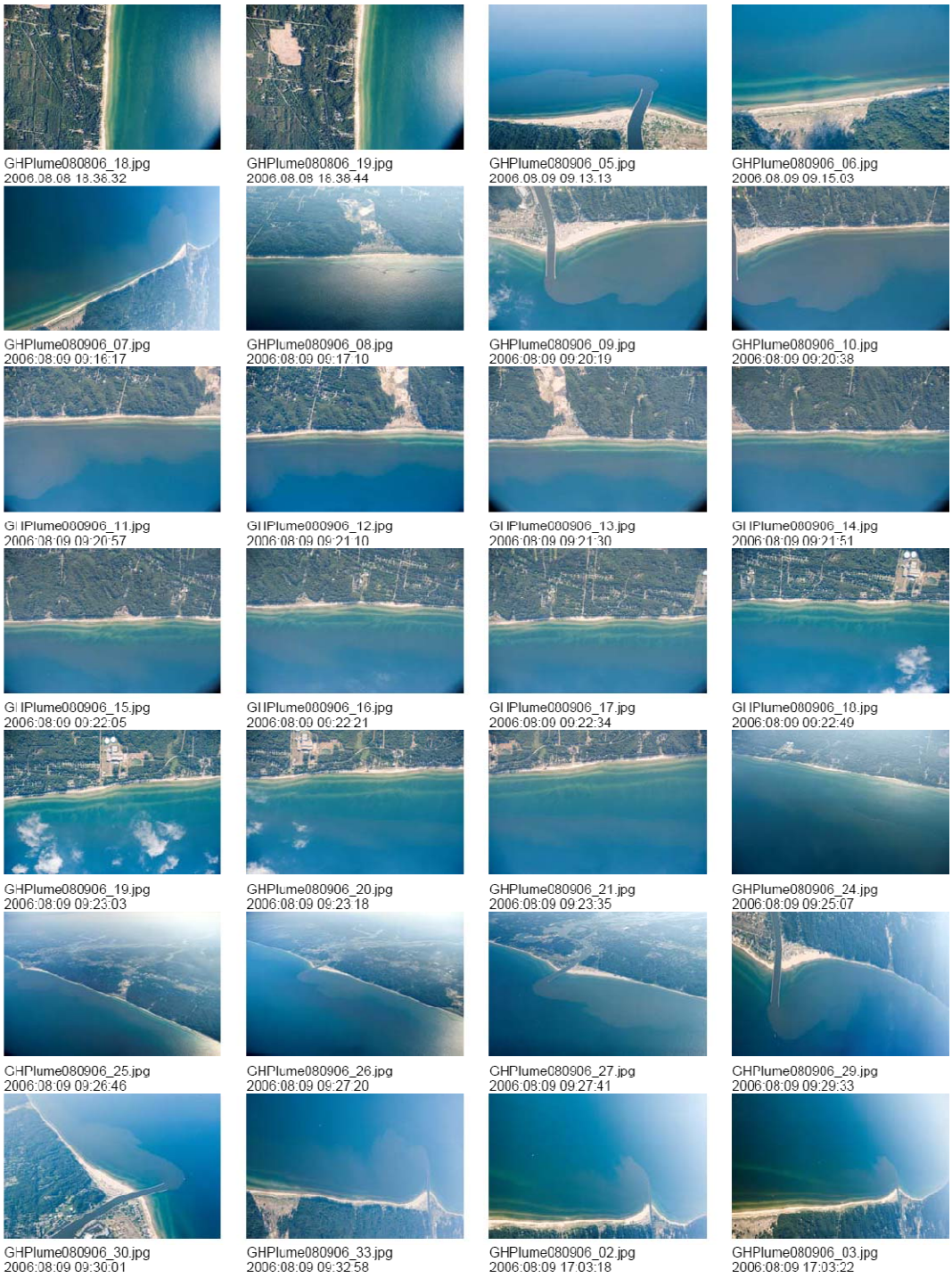

Figure A.6. Aerial pictures of the Grand Haven Plume on August 9, 2006 from 18:38:22 to 17:03:22 EDT.

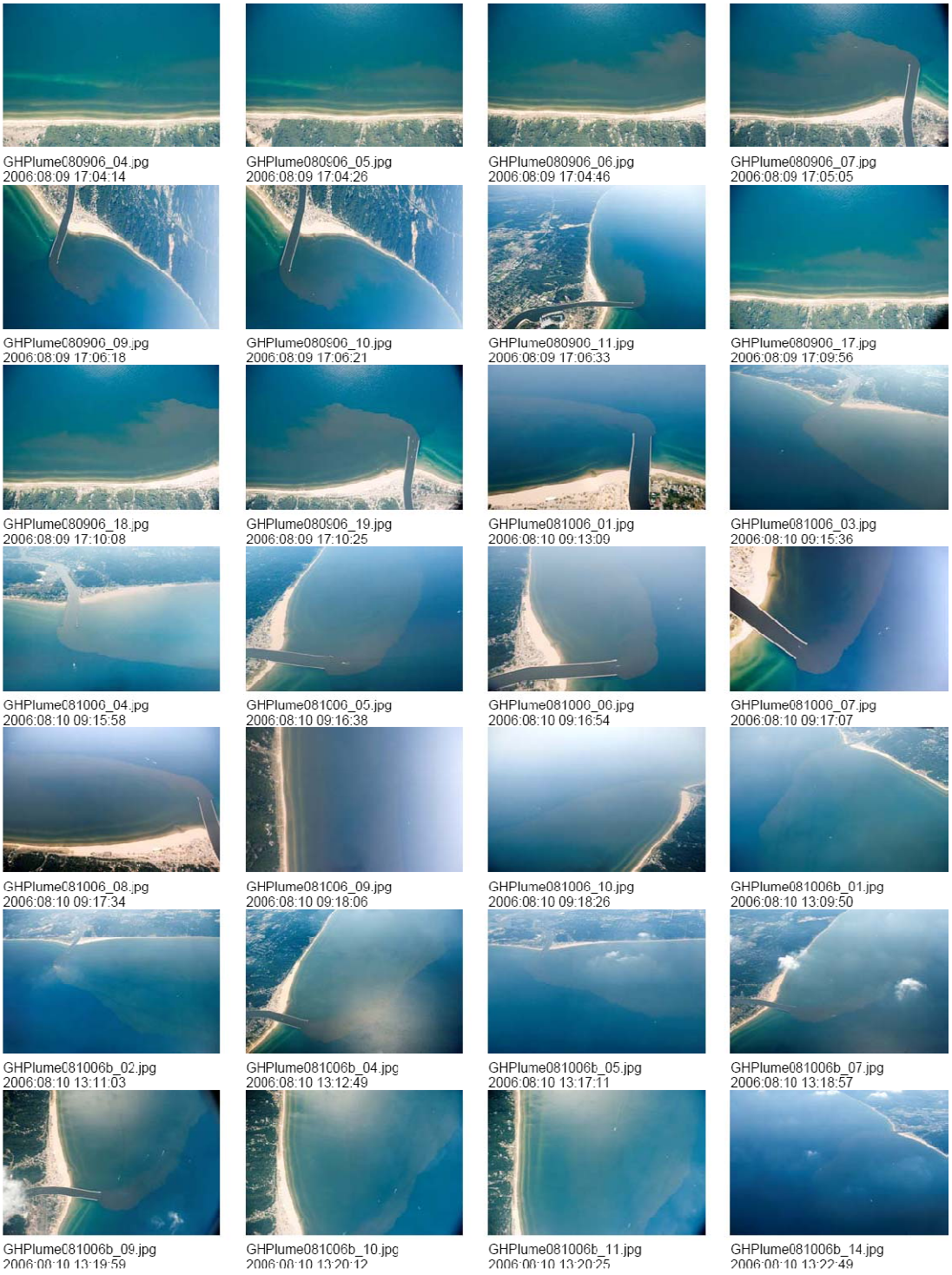

Figure A.7. Aerial pictures of the Grand Haven Plume on August 9, 2006 from 17:4:14 to 13:22:49 EDT.

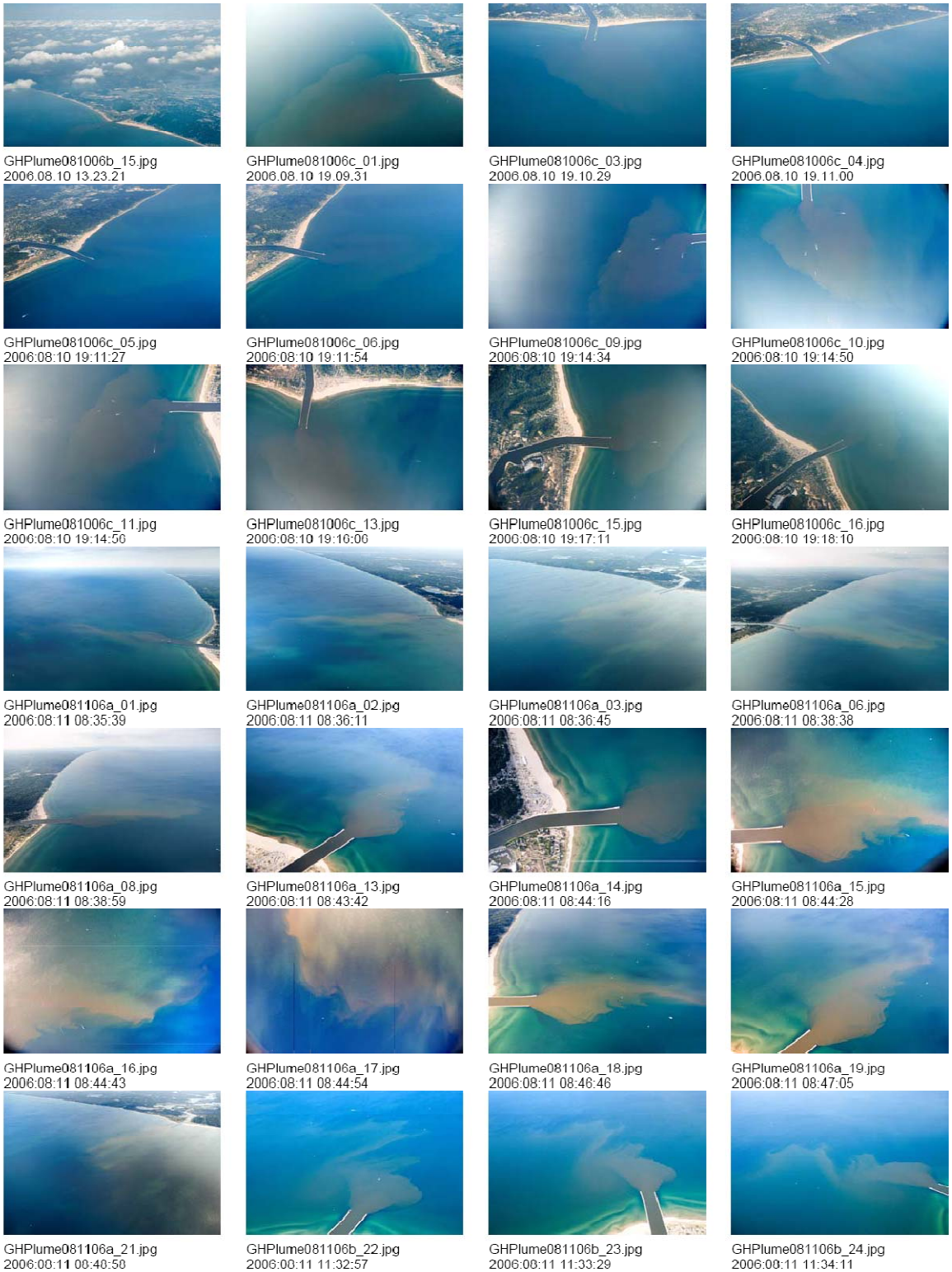

Figure A.8. Aerial pictures of the Grand Haven Plume on August 10, 2006 from 13:23:21 to 11:34:11 EDT.

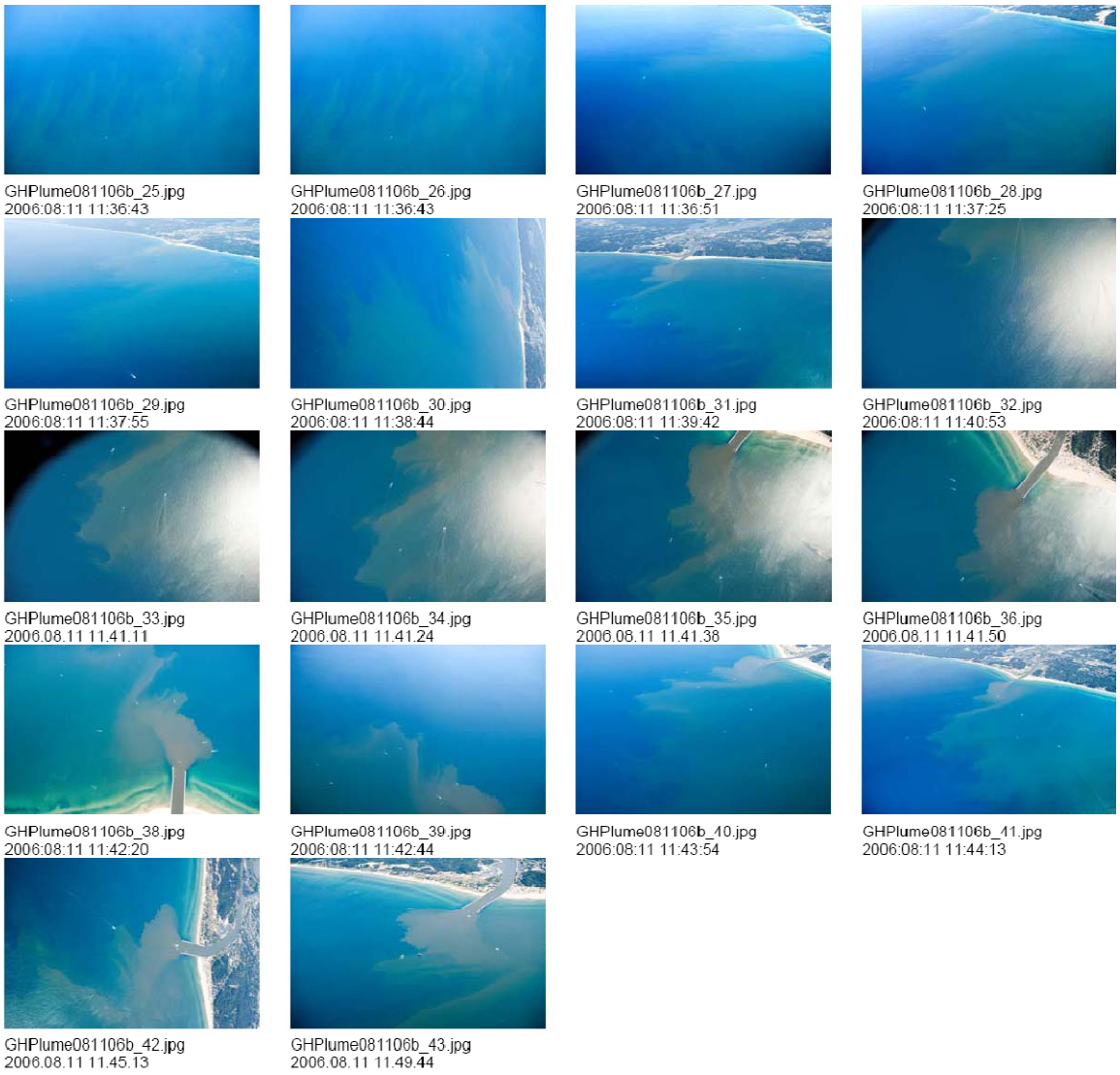

Figure A.9. Aerial pictures of the Grand Haven Plume on August 11, 2006 from 11:36:43 to 11:49:44 EDT.

A.3. May 2007

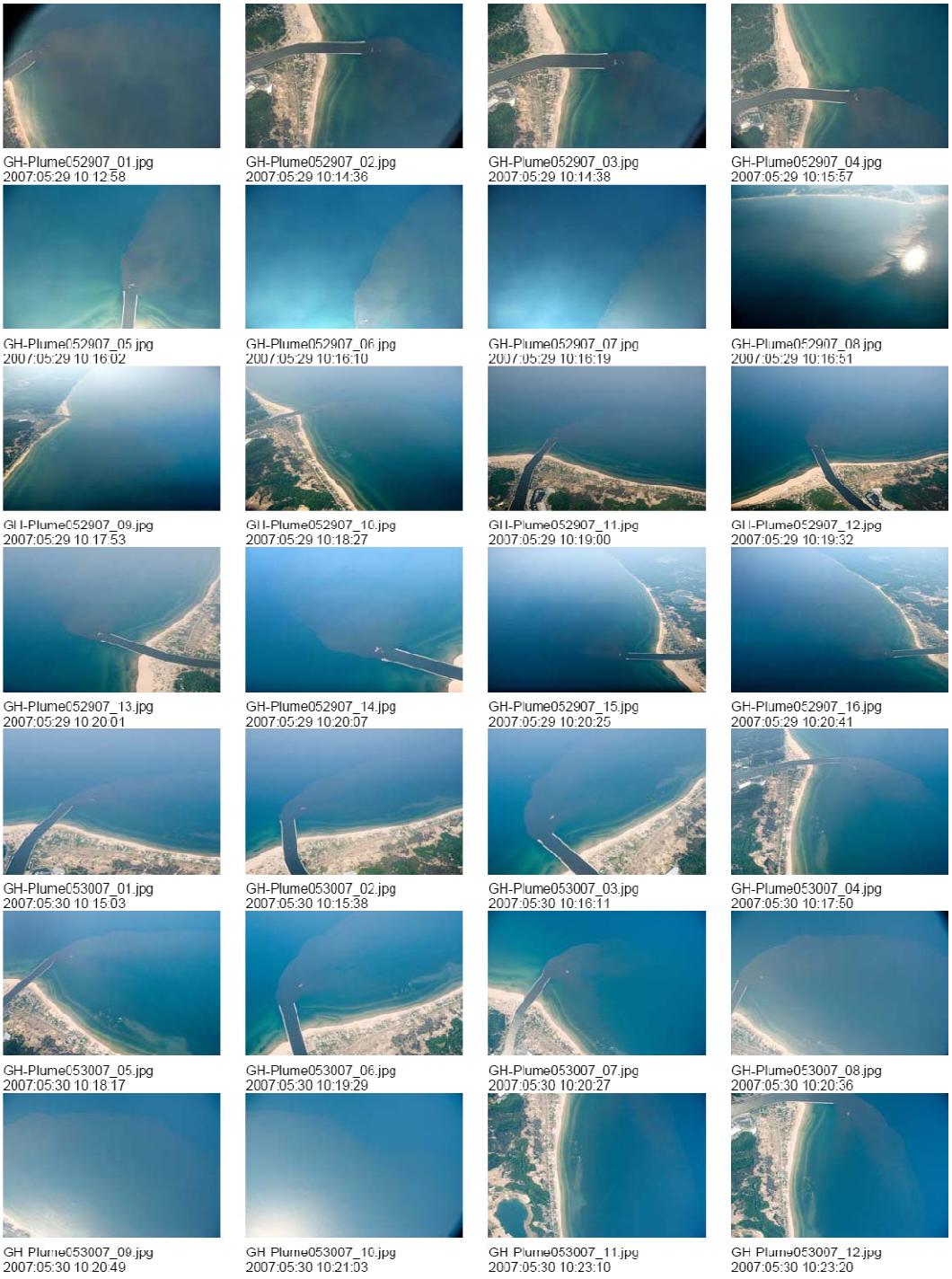

Figure A.10. Aerial pictures of the Grand Haven Plume from May 29, 2007 10:12:58 EDT to May 30, 2007 10:23:20 EDT.

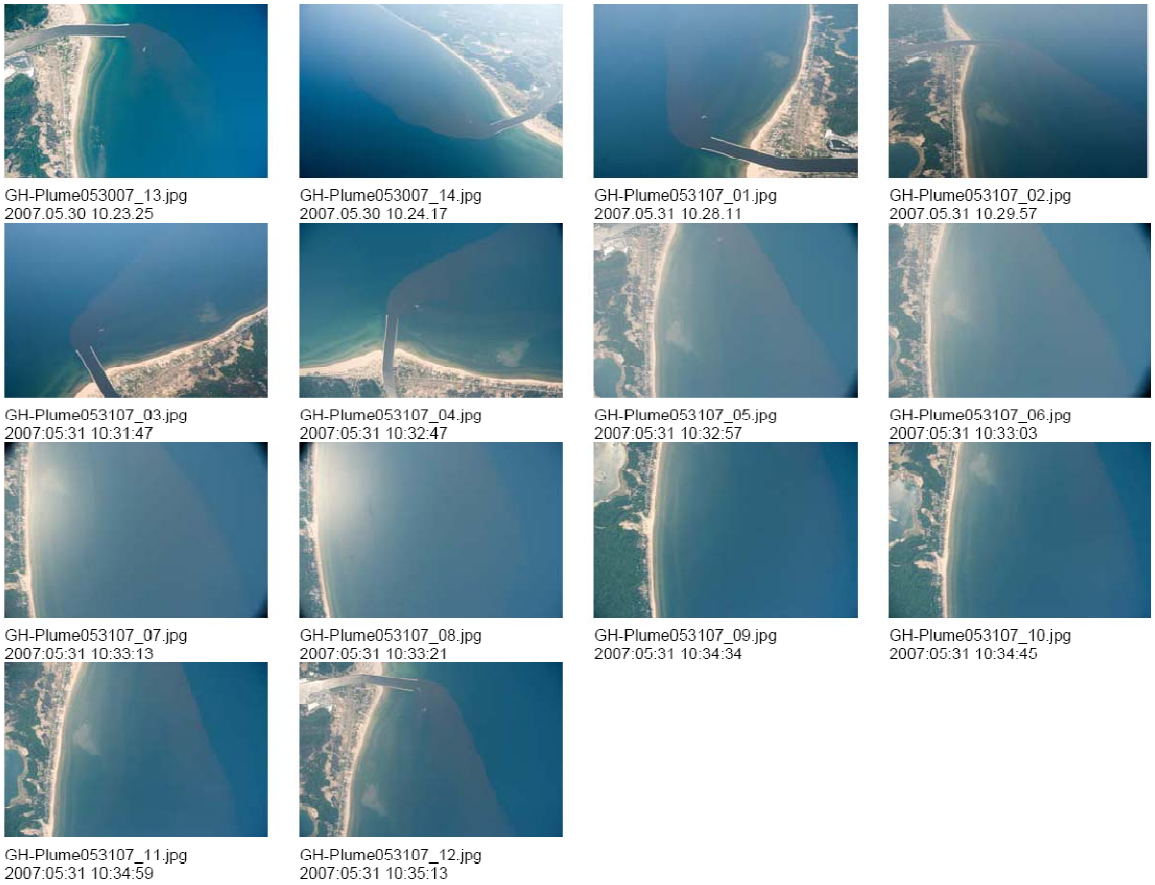

Figure A.11. Aerial pictures of the Grand Haven Plume during May 30, 2007 10:23:25 EDT to May 31, 2007 10:35:13 EDT.

A.4. June 2007

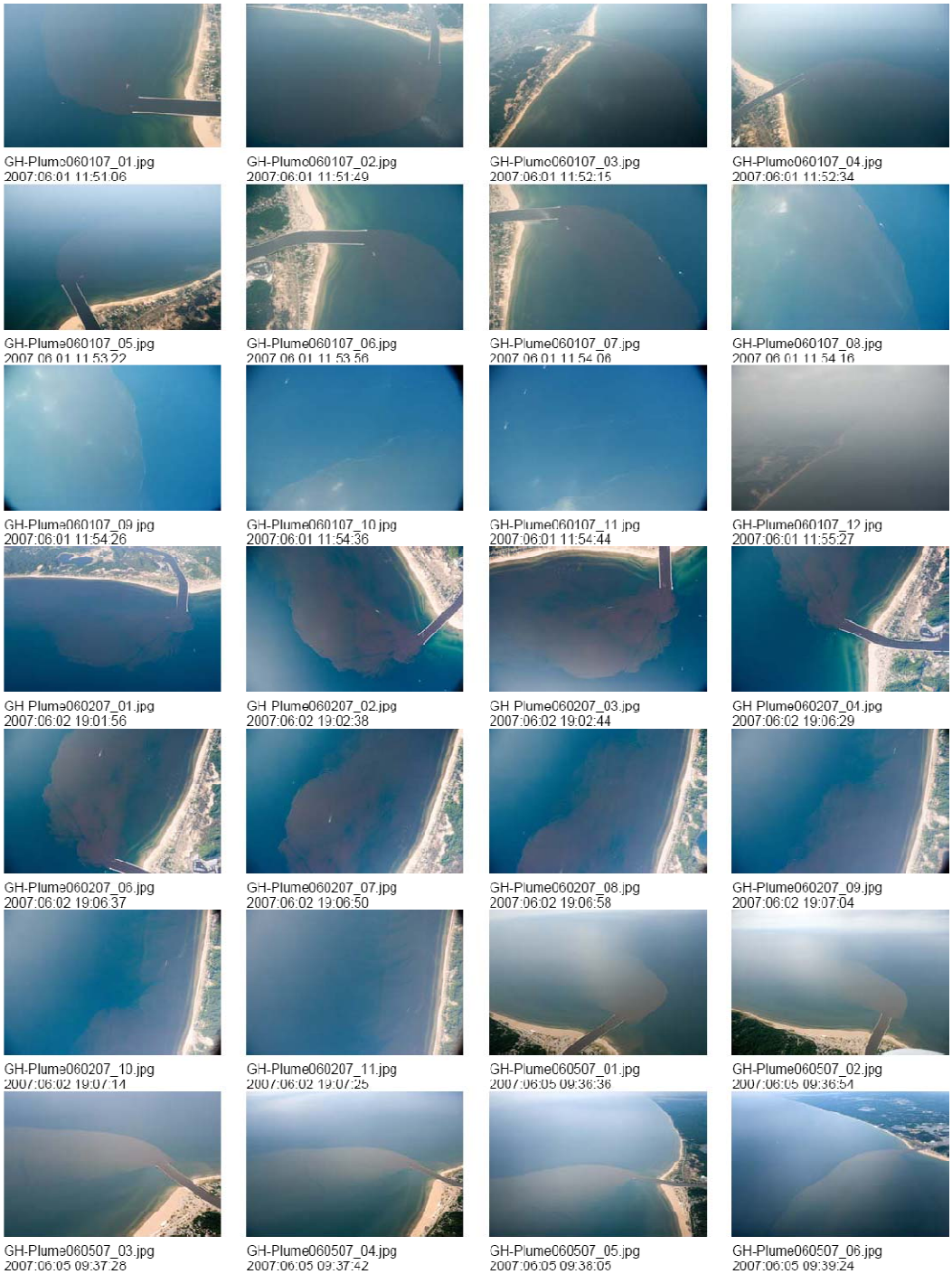

Figure A.12. Aerial pictures of the Grand Haven Plume from June 1, 2007 11:51:06 EDT to June 5, 2007 09:39:24 EDT.

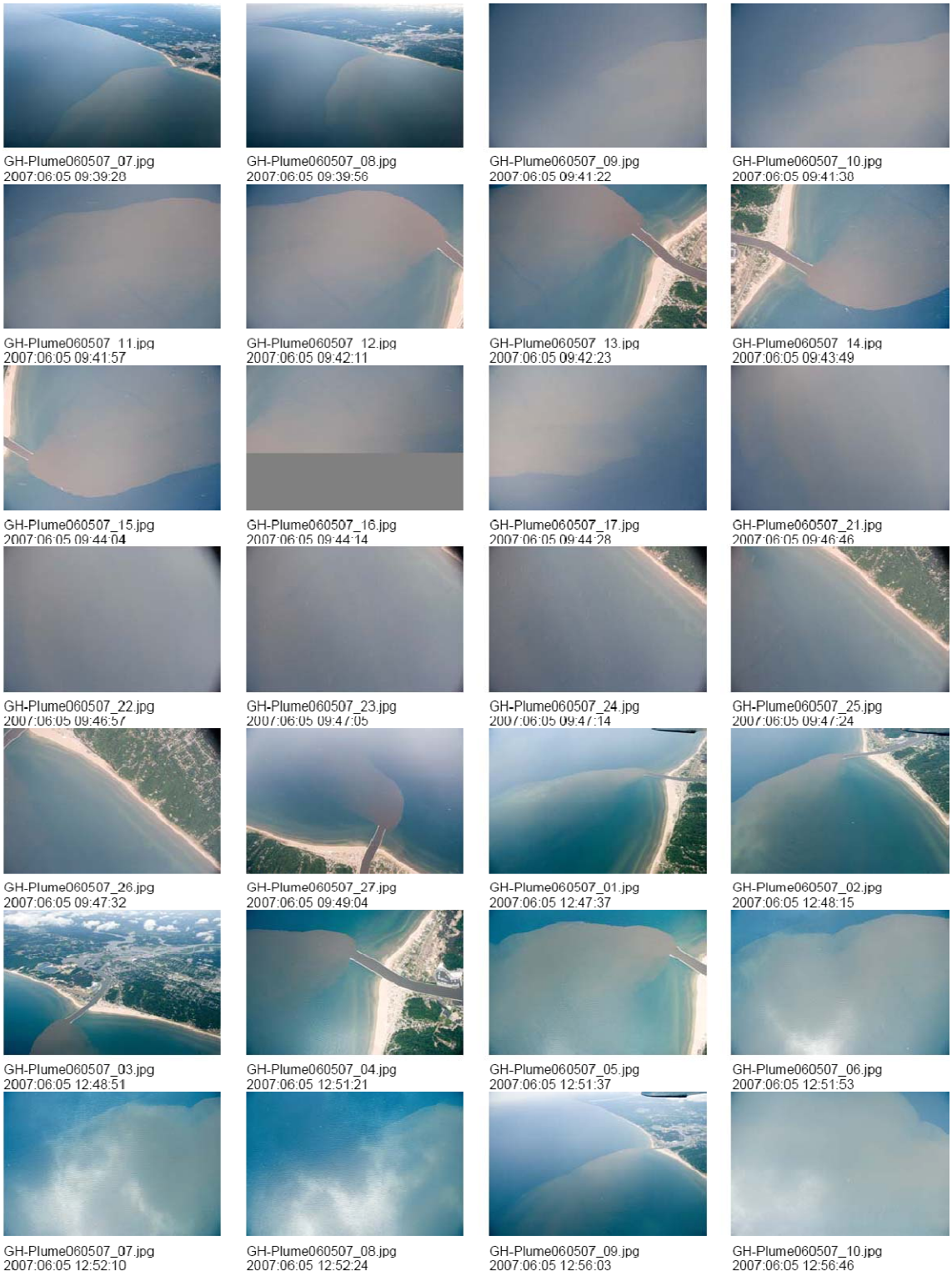

Figure A.13. Aerial pictures of the Grand Haven Plume on June 5, 2007, from 09:39:28 to 12:56:46 EDT.

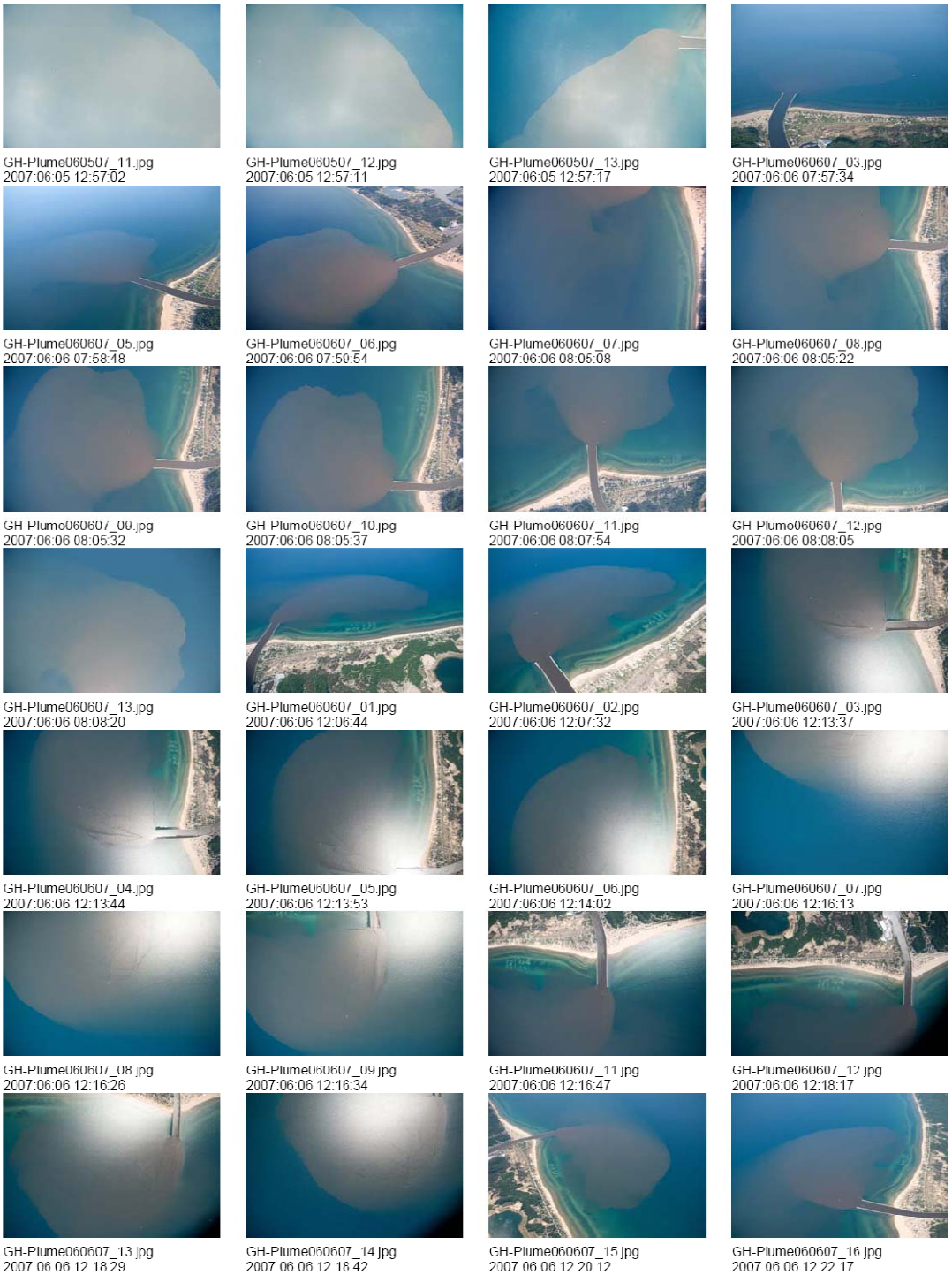

Figure A.14. Aerial pictures of the Grand Haven Plume from June 5, 2007 12:57:02 to June 6, 2007 12:22:17 EDT.

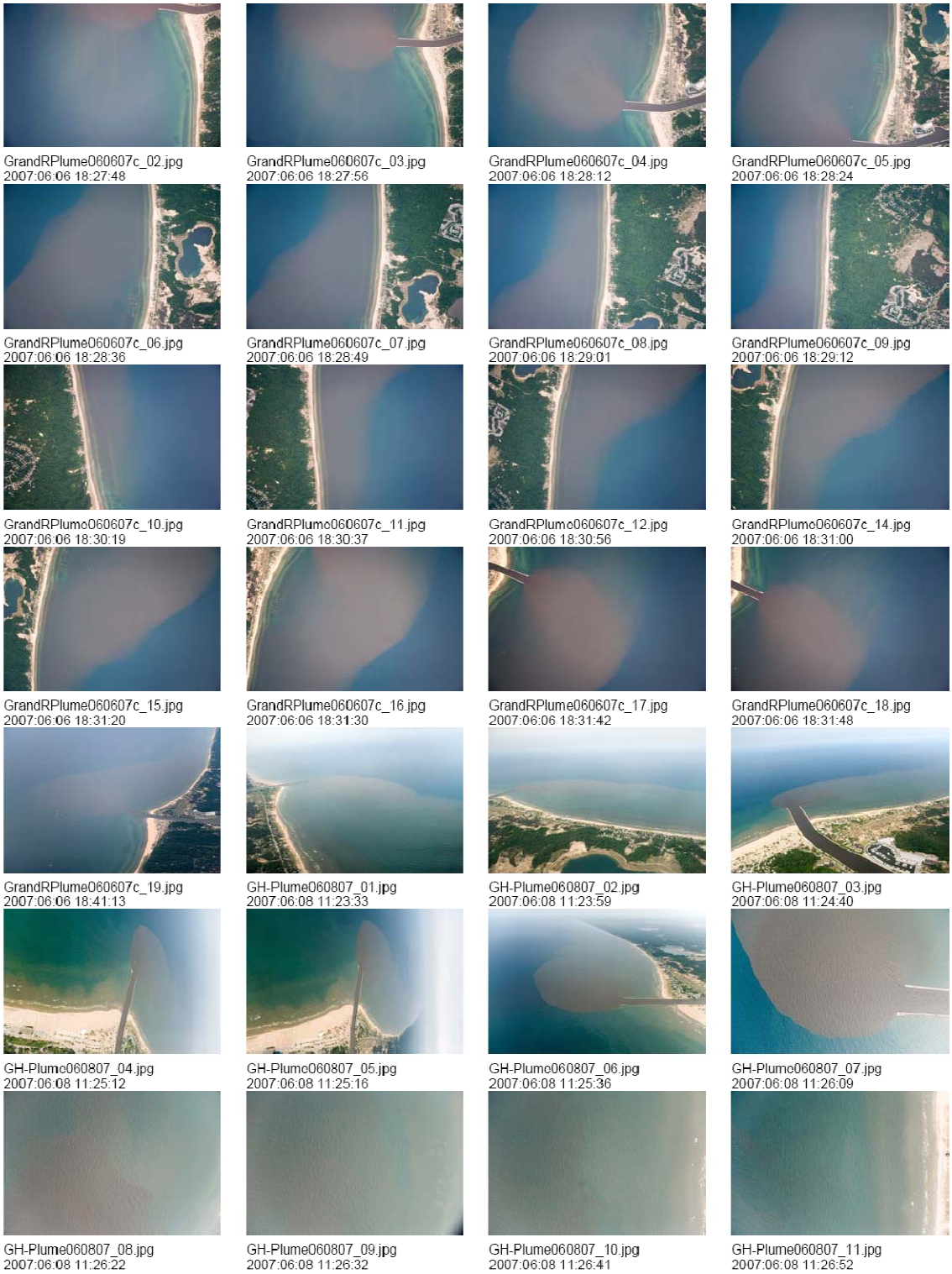

Figure A.15. Aerial pictures of the Grand Haven Plume from June 6, 2007, 18:27:48 to June 8, 2007, 11:26:52 EDT.

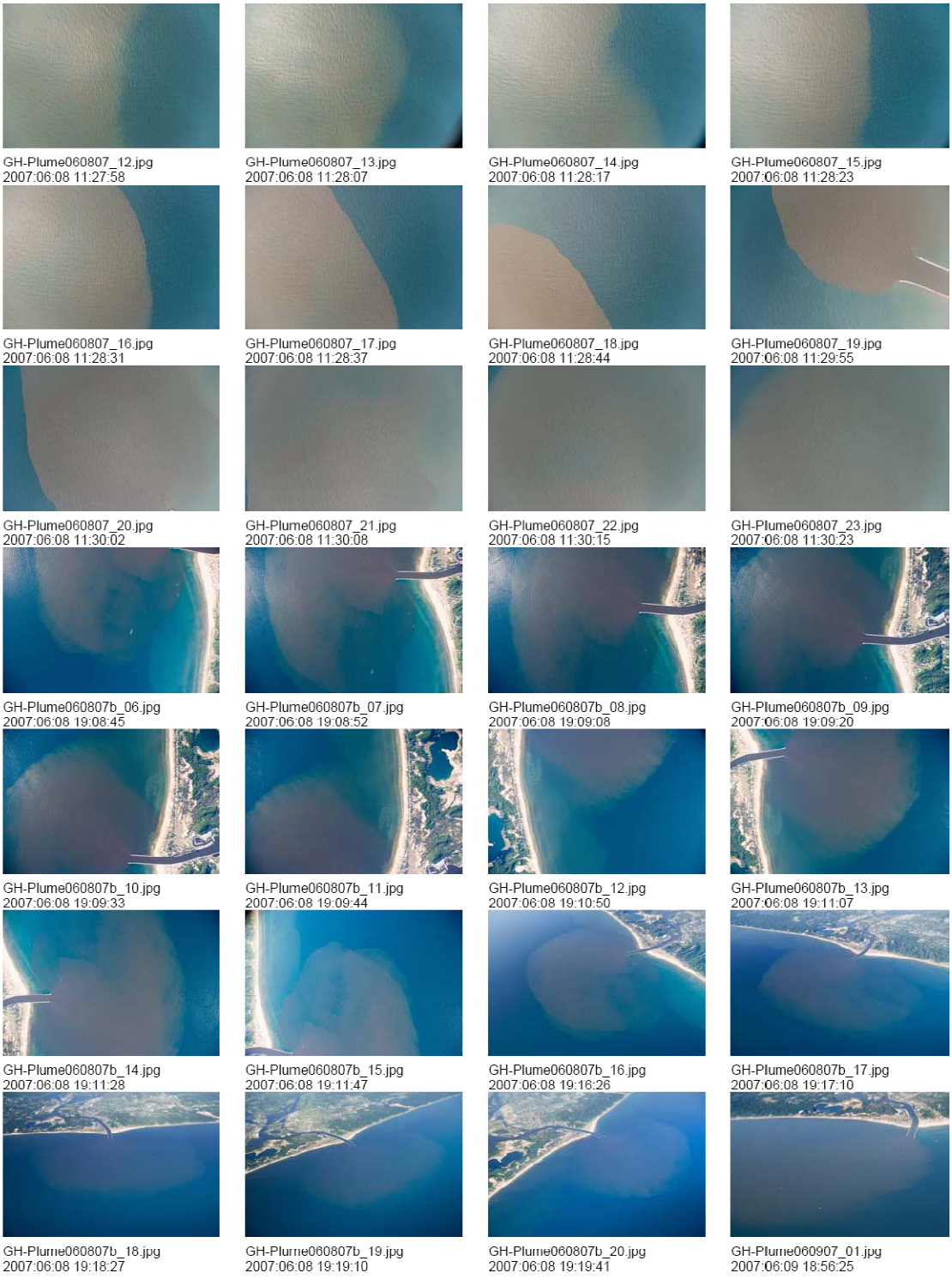

Figure A.16. Aerial pictures of the Grand Haven Plume from June 8, 2007, 11:27:58 to June 9, 2007, 18:56:25 EDT.

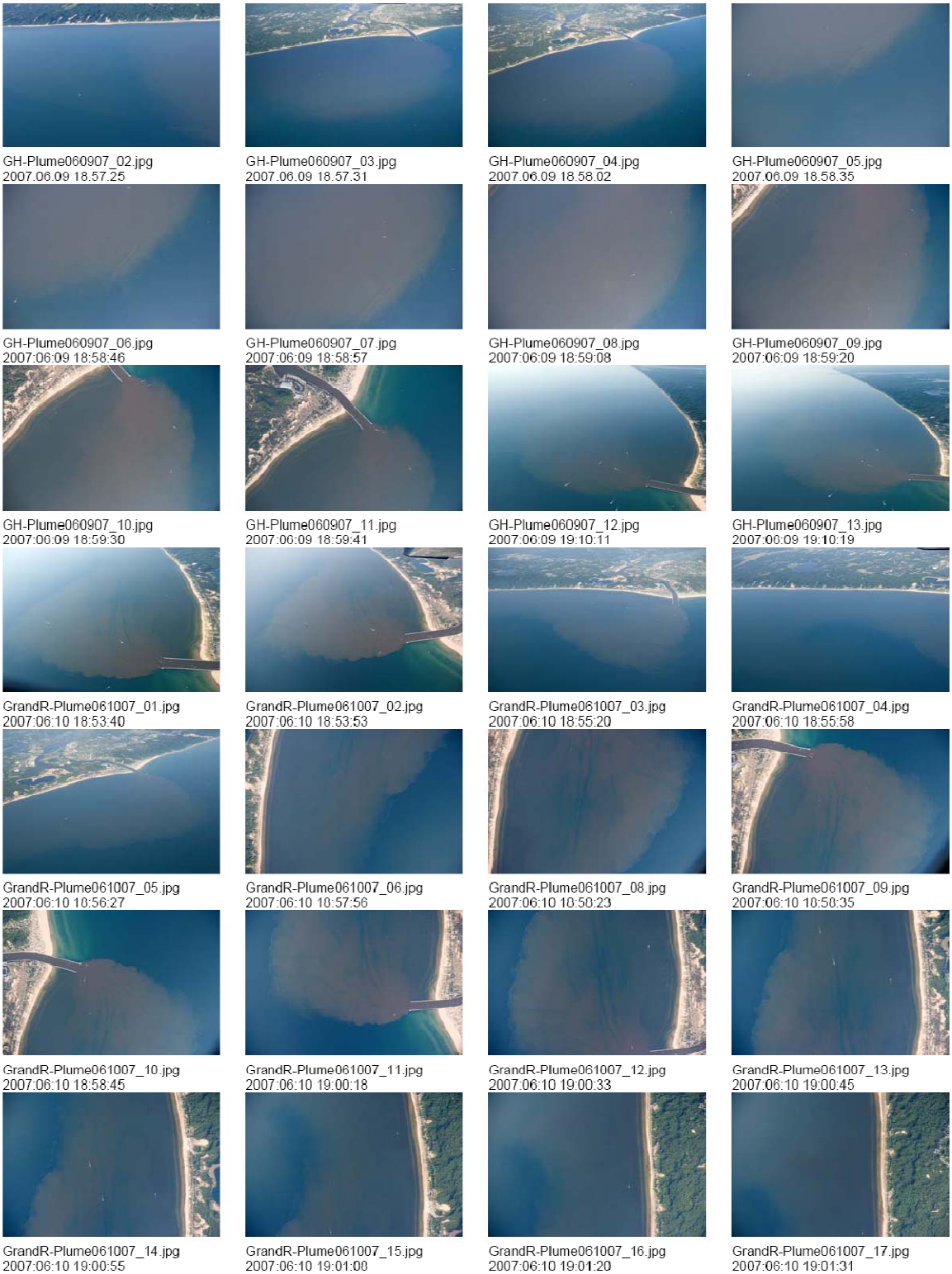

Figure A.17. Aerial pictures of the Grand Haven Plume on June 9, 2007, from 18:57:25 to June 10, 2007, 19:01:31 EDT.

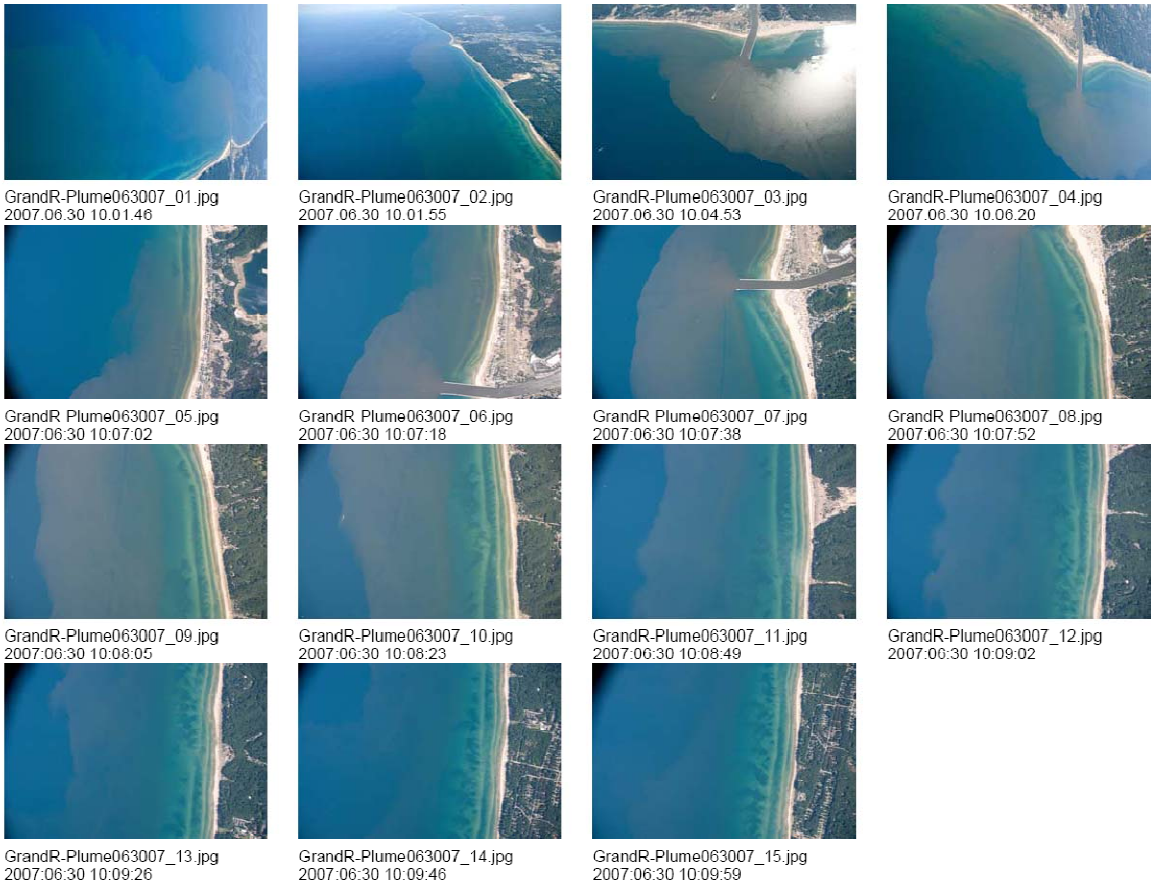

Figure A.18. Aerial pictures of the Grand Haven Plume on June 30, 2007, from 10:01:46 to 10:09:59 EDT.

A.5. July 2007

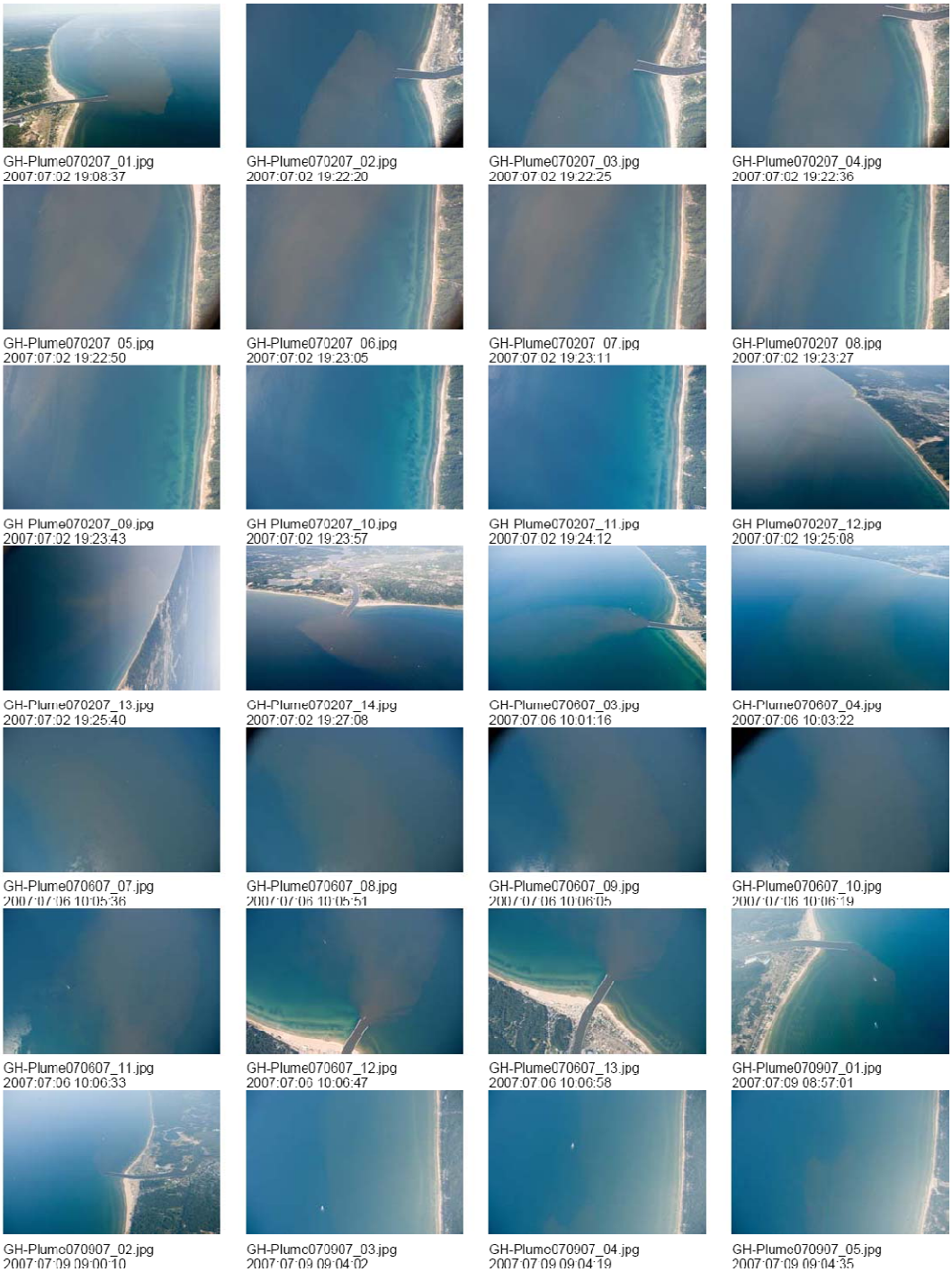

Figure A.19. Aerial pictures of the Grand Haven Plume from July 2, 2007, 19:08:37 to July 9, 2007, 09:04:35 EDT.

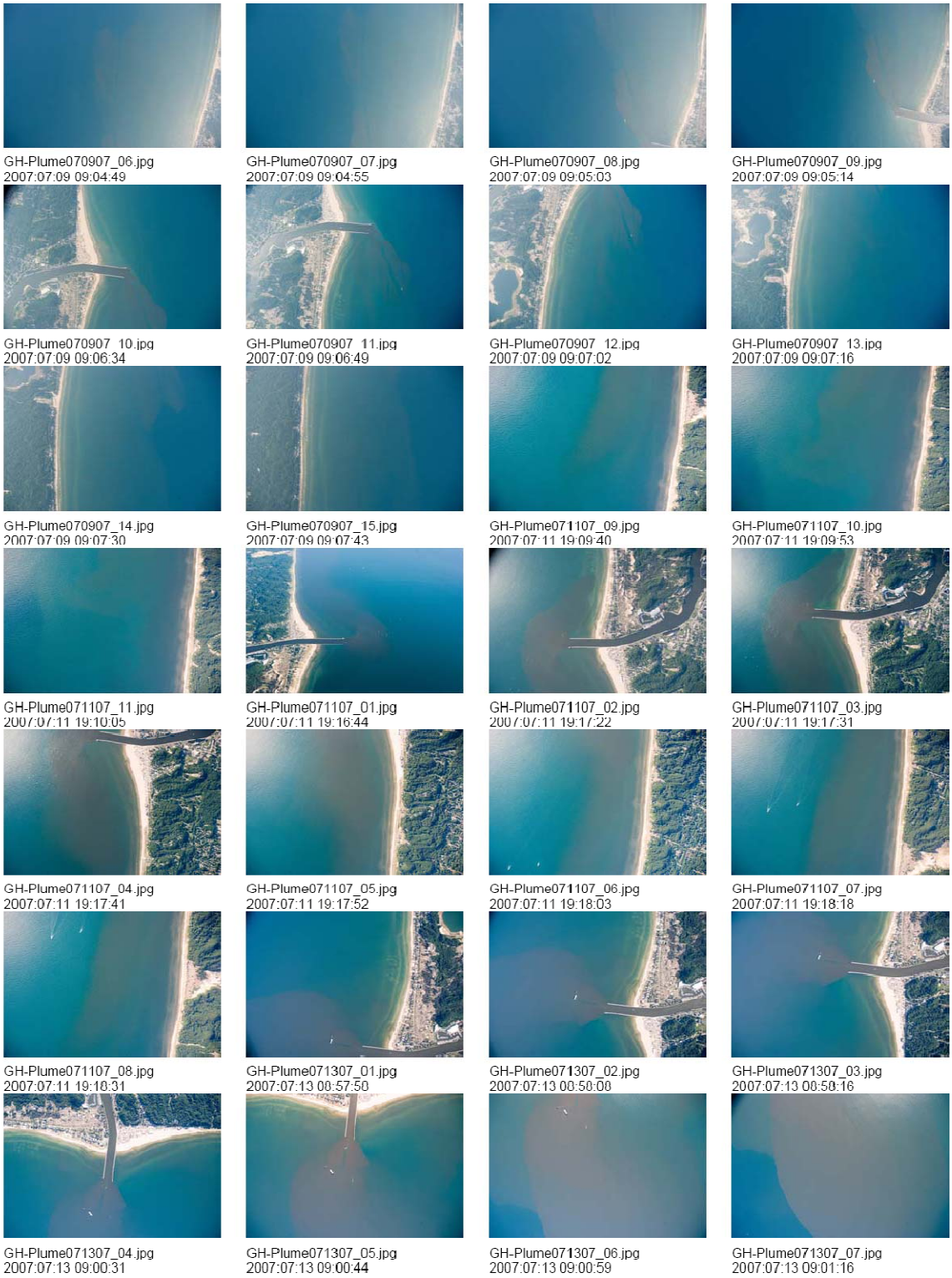

Figure A.20. Aerial pictures of the Grand Haven Plume from July 9, 2007, 09:04:49 to July 13, 2007, 09:01:16 EDT.

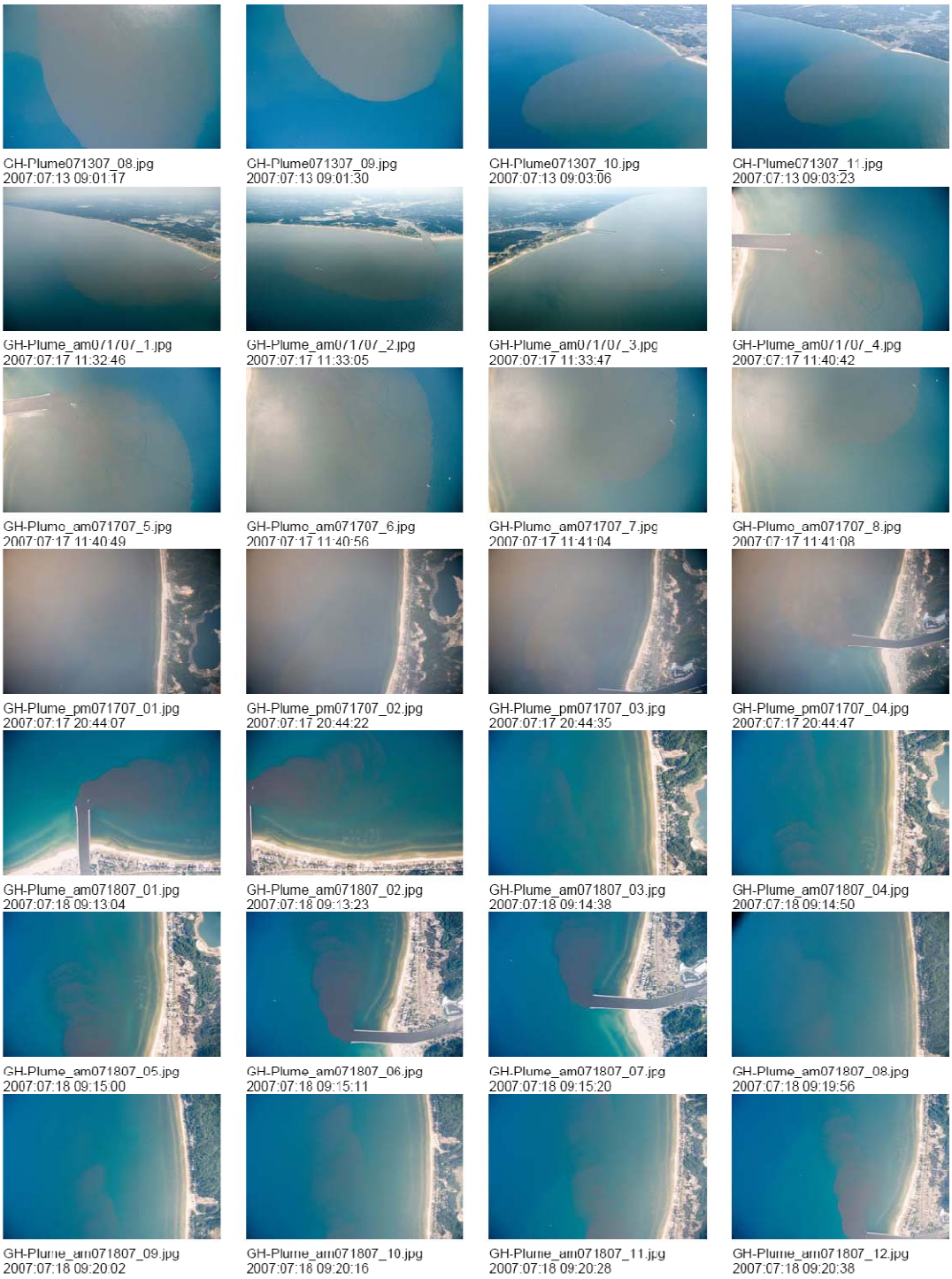

Figure A.21. Aerial pictures of the Grand Haven Plume from July 13, 2007 09:01:17 to July 18, 2007 09:20:38 EDT.

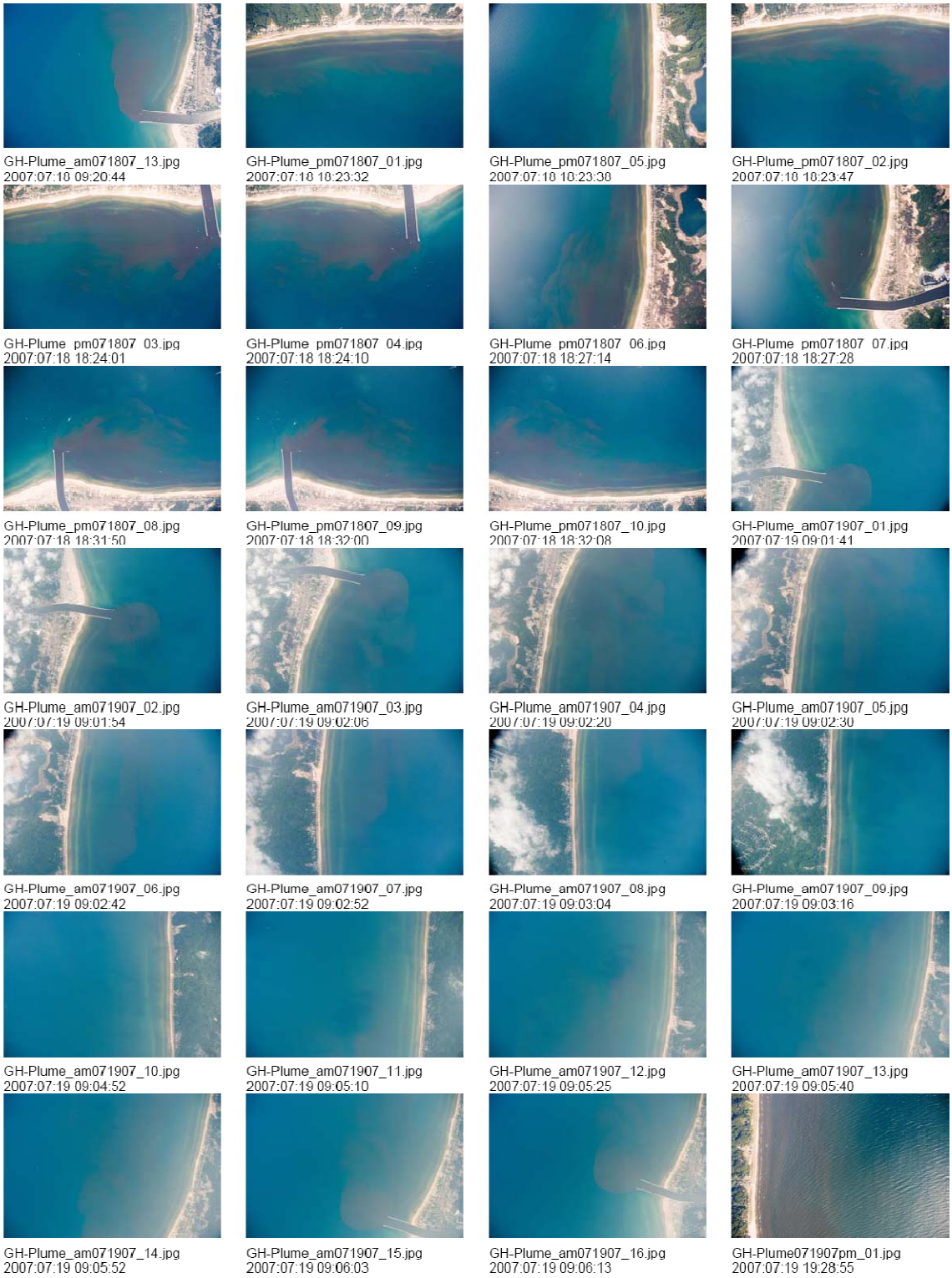

Figure A.22. Aerial pictures of the Grand Haven Plume from July 18, 2007, 09:20:44 to July 19, 2007 19:28:55 EDT.

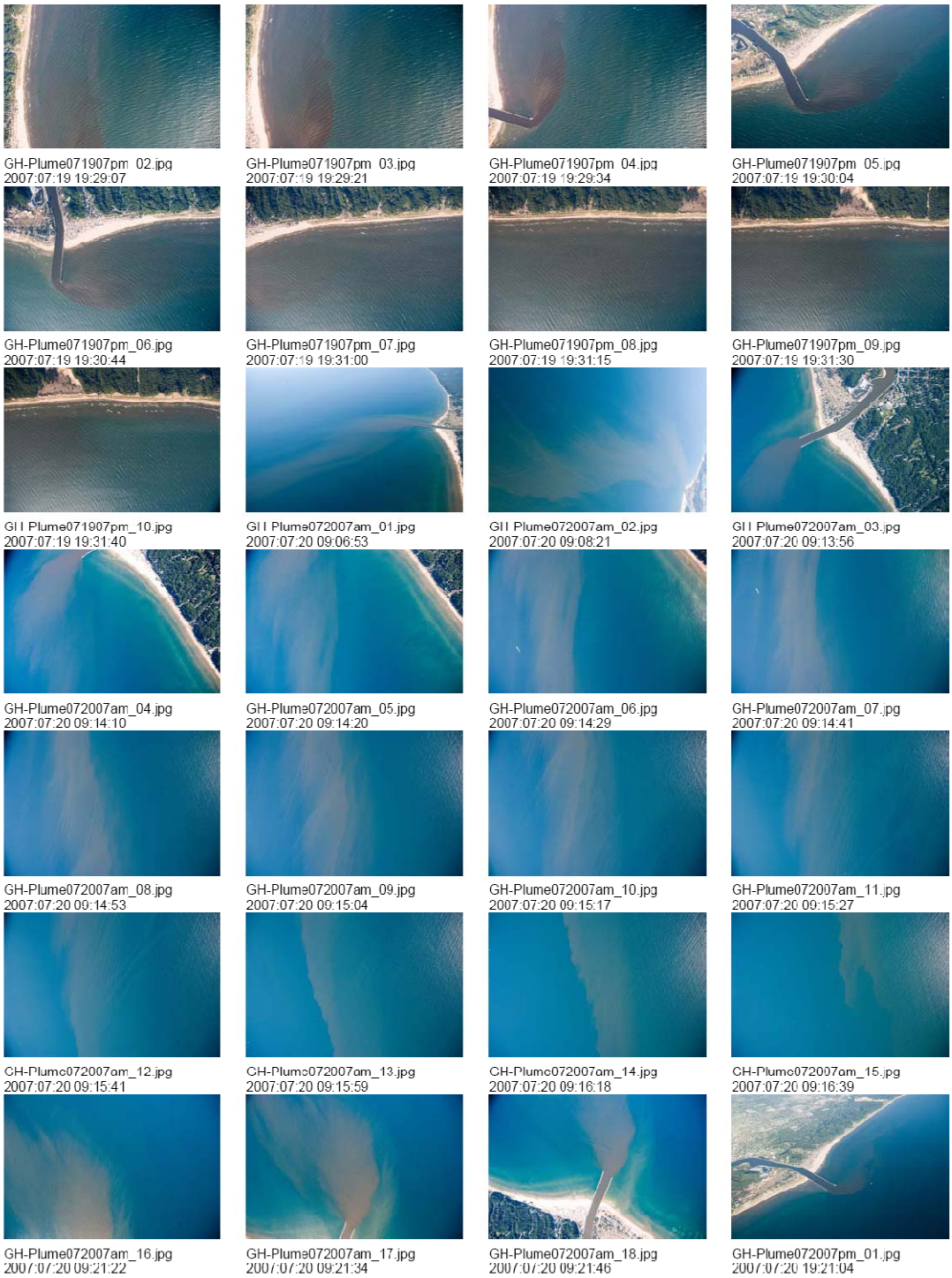

Figure A.23. Aerial pictures of the Grand Haven Plume from July 19, 2007, 19:29:07 to July 20, 2007 19:21:04 EDT.

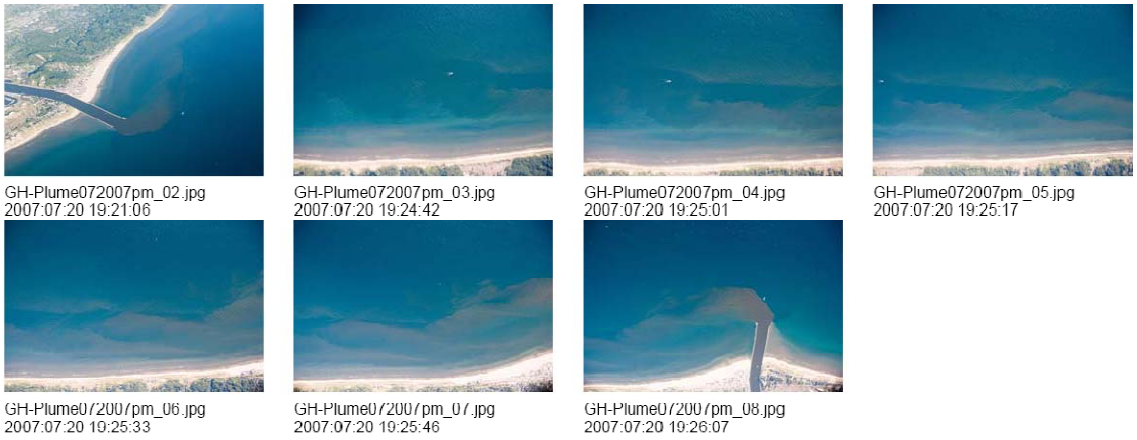

Figure A.24. Aerial pictures of the Grand Haven Plume on July 20, 2007, from 19:21:06 to 19:26:07 EDT.

APPENDIX B: POM GOVERNING EQUATIONS

The incompressibility, hydrostatic, and Buossinesq assumptions made in POM are as follows:

$$\frac{D\rho}{Dt} = 0 \tag{B-1}$$

$$P(x, y, z) = P_{atm} + g\rho_{\circ}\eta + g\int_{z}^{0} \rho(x, y, z', t)dz' \tag{B-2}$$

$$\frac{\partial P}{\partial x} = \frac{\partial P_{atm}}{\partial x} + \rho_{\circ} g \frac{\partial \eta}{\partial x} + \int_{z}^{0} \frac{g}{\rho_{\circ}} \frac{\partial P}{\partial x} dz \tag{B-3}$$

$$\frac{1}{\rho}\frac{\partial P}{\partial x} = g\frac{\partial \eta}{\partial x} + \int \frac{g}{\rho_{\circ}} \frac{\partial P}{\partial x} dz \tag{B-4}$$

Basic equations of continuity, momentum, and thermodynamics including temperature and salinity in Cartesian coordinates are described are as follows:

$$\nabla \cdot \bar{V} + \frac{\partial W}{\partial z} = 0 \tag{B-5}$$

$$\frac{\partial U}{\partial t} + \bar{V} \cdot \nabla U + W\frac{\partial U}{\partial z} - fV = -\frac{1}{\rho_0}\frac{\partial P}{\partial x} + \frac{\partial}{\partial z}\left(K_M \frac{\partial U}{\partial z}\right) + F_X \tag{B-6}$$

$$\frac{\partial V}{\partial t} + \bar{V} \cdot \nabla V + W\frac{\partial V}{\partial z} - fU = -\frac{1}{\rho_0}\frac{\partial P}{\partial y} + \frac{\partial}{\partial z}\left(K_M \frac{\partial V}{\partial z}\right) + F_Y \tag{B-7}$$

$$\frac{\partial \theta}{\partial t} + \bar{V} \cdot \nabla \theta + W\frac{\partial \theta}{\partial z} = \frac{\partial}{\partial z}\left(K_H \frac{\partial \theta}{\partial z}\right) + F_\theta \tag{B-8}$$

$$\frac{\partial S}{\partial t} + \bar{V} \cdot \nabla S + W\frac{\partial S}{\partial z} = \frac{\partial}{\partial z}\left(K_H \frac{\partial S}{\partial z}\right) + F_S \tag{B-9}$$

The equation of state (Mellor, 1991) calculates the density as a function of temperature, salinity, and pressure:

$$\rho = \rho(\theta, S, p) \tag{B-10}$$

where θ, and S are respectively the potential temperature and salinity, U , V , W are the velocity vectors in *x*, *y*, and *z* directions, *p* is the pressure, f is the Coriolis term, K_H is the heat/salt vertical eddy diffusivity and K_M is the momentum vertical eddy diffusivity.

F_x , F_y , and $F_{\theta,S}$ are the horizontal viscosity terms. The horizontal viscosity and diffusion terms are:

$$F_x = \frac{\partial}{\partial x}\left[2A_M \frac{\partial U}{\partial x}\right] + \frac{\partial}{\partial y}\left[A_M\left(\frac{\partial U}{\partial y} + \frac{\partial V}{\partial x}\right)\right] \tag{B-11}$$

$$F_y = \frac{\partial}{\partial y}\left[2A_M \frac{\partial V}{\partial y}\right] + \frac{\partial}{\partial x}\left[A_M\left(\frac{\partial U}{\partial y} + \frac{\partial V}{\partial x}\right)\right] \tag{B-12}$$

$$F_{\theta,S} = \frac{\partial}{\partial x}\left[2A_M \frac{\partial(\theta,S)}{\partial x}\right] + \frac{\partial}{\partial y}\left[A_H \frac{\partial(\theta,S)}{\partial x}\right] \tag{B-13}$$

$$A_M = C\Delta x\Delta y \frac{1}{2}\left|\nabla V + \left(\nabla V\right)^T\right| \tag{B-14}$$

where A_M (the same as K_h in PARTIC3D), and A_H are horizontal eddy diffusivities that damp small-scale computational noise. Horizontal momentum diffusion is assumed to be equal to horizontal thermal diffusion where the primary mixing process is eddy diffusion. The Smagorinsky diffusivity, A_M, is small for computations with high resolution and small velocity gradient.

The model includes the Mellor and Yamada (1982) level 2.5 turbulence closure parameterization.

$$\frac{\partial q^2}{\partial x} + \vec{V}\cdot\nabla q^2 + W\frac{\partial q^2}{\partial z} =$$

$$\frac{\partial}{\partial z}\left(K_q \frac{\partial q^2}{\partial z}\right) + 2K_M\left(\left(\frac{\partial U}{\partial z}\right)^2 + \left(\frac{\partial V}{\partial z}\right)^2\right) + \frac{2g}{\rho_\circ}K_H\frac{\partial \rho}{\partial x} - \frac{2q^3}{B_1 l} + F_q \tag{B-15}$$

and

$$\frac{\partial\left(q^2\ell\right)}{\partial t} + \vec{V}\cdot\nabla\left(q^2\ell\right) + W\frac{\partial\left(q^2\ell\right)}{\partial z} =$$

$$\frac{\partial}{\partial z}\left(K_q \frac{\partial\left(q^2\ell\right)}{\partial z}\right) + \ell E_1 K_M\left(\left(\frac{\partial U}{\partial z}\right)^2 + \left(\frac{\partial V}{\partial z}\right)^2\right) + \frac{\ell E_1 g}{\rho_\circ}K_H\frac{\partial \rho}{\partial z} - \frac{q^3}{B_1}\tilde{W} + F_\ell \tag{B-16}$$

where

$$K_M \equiv \ell q S_M, \qquad K_H \equiv \ell q S_H, \qquad K_q \equiv \ell q S_q \tag{B-17}$$

and K_M, K_H (the same as K_v in PARTIC3D), and K_q are the turbulence mixing coefficients, and S_M, S_H, and S_q are the analytical stability functions, ℓ is the turbulence macroscale, q is the turbulence kinetic energy, F_q and F_l are horizontal turbulence mixing terms, and, B_1 and E_1 are empirical constants (refer to Blumberg and Mellor, 1987 for further detail).

The above basic equations are given in a horizontal Cartesian z-coordinate system. In terms of grids, horizontal orthogonal-curvilinear coordinates and Cartesian are easily implemented. In POM Sigma vertical coordinates (important for varying topography) are also included (Figure B.1).

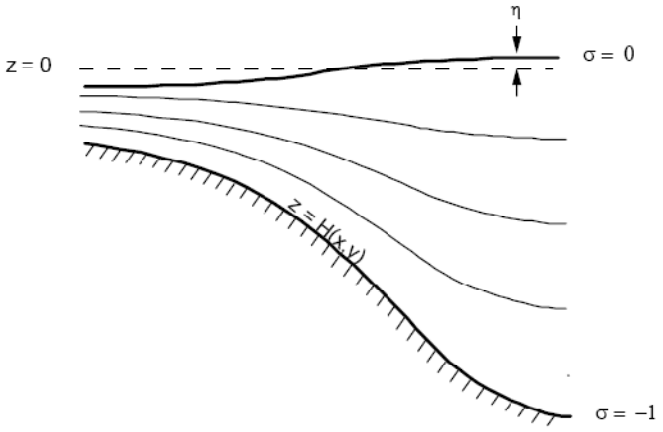

Figure B.1. Sigma Coordinates.

The transformed equations after applying sigma level coordinates are below.

$$x^* = x, \quad y^* = y, \quad \sigma = \frac{z-\eta}{H+\eta}, \quad t^* = t \tag{B-18}$$

$$\frac{\partial DU}{\partial x} + \frac{\partial DV}{\partial y} + \frac{\partial \omega}{\partial \sigma} + \frac{\partial \eta}{\partial t} = 0 \tag{B-19}$$

$$\begin{aligned} &\frac{\partial UD}{\partial t} + \frac{\partial U^2 D}{\partial x} + \frac{\partial UVD}{\partial y} + \frac{\partial U\omega}{\partial \sigma} - fVD + gD\frac{\partial \eta}{\partial x} + \\ &\frac{gD^2}{\rho_\circ}\int_\sigma^0 \left[\frac{\partial \rho'}{\partial x} - \frac{\sigma'}{D}\frac{\partial D}{\partial x}\frac{\partial \rho'}{\partial \sigma'}\right] d\sigma' = \frac{\partial}{\partial \sigma}\left[\frac{K_M}{D}\frac{\partial U}{\partial \sigma}\right] + F_x \end{aligned} \tag{B-20}$$

$$\frac{\partial VD}{\partial t}+\frac{\partial UVD}{\partial x}+\frac{\partial V^2D}{\partial y}+\frac{\partial V\omega}{\partial \sigma}+ fUD+gD\frac{\partial \eta}{\partial y}+ \frac{gD^2}{\rho_\circ}\int_\sigma^0\left[\frac{\partial \rho'}{\partial y}-\frac{\sigma'}{D}\frac{\partial D}{\partial y}\frac{\partial \rho'}{\partial \sigma'}\right]d\sigma'=\frac{\partial}{\partial \sigma}\left[\frac{K_M}{D}\frac{\partial V}{\partial \sigma}\right]+F_y \tag{B-21}$$

$$\frac{\partial TD}{\partial t}+\frac{\partial TUD}{\partial x}+\frac{\partial TVD}{\partial y}+\frac{\partial T\omega}{\partial \sigma}=\frac{\partial}{\partial \sigma}\left[\frac{K_H}{D}\frac{\partial T}{\partial \sigma}\right]+F_T-\frac{\partial R}{\partial z} \tag{B-22}$$

$$\frac{\partial SD}{\partial t}+\frac{\partial SUD}{\partial x}+\frac{\partial SVD}{\partial y}+\frac{\partial S\omega}{\partial \sigma}=\frac{\partial}{\partial \sigma}\left[\frac{K_H}{D}\frac{\partial S}{\partial \sigma}\right]+F_S \tag{B-23}$$

$$\frac{\partial q^2D}{\partial t}+\frac{\partial Uq^2D}{\partial x}+\frac{\partial Vq^2D}{\partial y}+\frac{\partial \omega q^2}{\partial \sigma}=\frac{\partial}{\partial \sigma}\left(\frac{K_q}{D}\frac{\partial q^2}{\partial \sigma}\right)+ \frac{2K_M}{D}\left(\left(\frac{\partial U}{\partial \sigma}\right)^2+\left(\frac{\partial V}{\partial \sigma}\right)^2\right)+\frac{2g}{\rho_0}K_H\frac{\partial \tilde{\rho}}{\partial \sigma}-\frac{2Dq^3}{B_1\ell}+F_q \tag{B-24}$$

$$\frac{\partial q^2\ell D}{\partial t}+\frac{\partial Uq^2\ell D}{\partial x}+\frac{\partial Vq^2\ell D}{\partial y}+\frac{\partial \omega q^2\ell}{\partial \sigma}=\frac{\partial}{\partial \sigma}\left(\frac{K_q}{D}\frac{\partial q^2\ell}{\partial \sigma}\right) \tag{B-25}$$

$$W=\omega+U\left(\sigma\frac{\partial D}{\partial x}+\frac{\partial \eta}{\partial x}\right)+V\left(\sigma\frac{\partial D}{\partial y}+\frac{\partial \eta}{\partial y}\right)+\sigma\frac{\partial D}{\partial t}+\frac{\partial \eta}{\partial t} \tag{B-26}$$

$$F_x=\frac{\partial}{\partial x}\left[H\tau_{xx}\right]+\frac{\partial}{\partial y}\left[H\tau_{yy}\right] \tag{B-27}$$

$$A_M=C\Delta x\Delta y\frac{1}{2}\left[\left(\partial u/\partial x\right)^2+\left(\partial v/\partial x+\partial u/\partial y\right)^2/2+\left(\partial v/\partial y\right)^2\right]^{1/2} \tag{B-28}$$

APPENDIX C: POMGL SENSITIVITY ANALYSIS

Bottom roughness was defined as an asymptotic function, $z_0 = a + b/(c+h)$. Below are the model sensitivity in response to variation of the parameters *a*, *b*, and *c*.

C.1. Effect of parameter a in roughness height on POMGL predictions

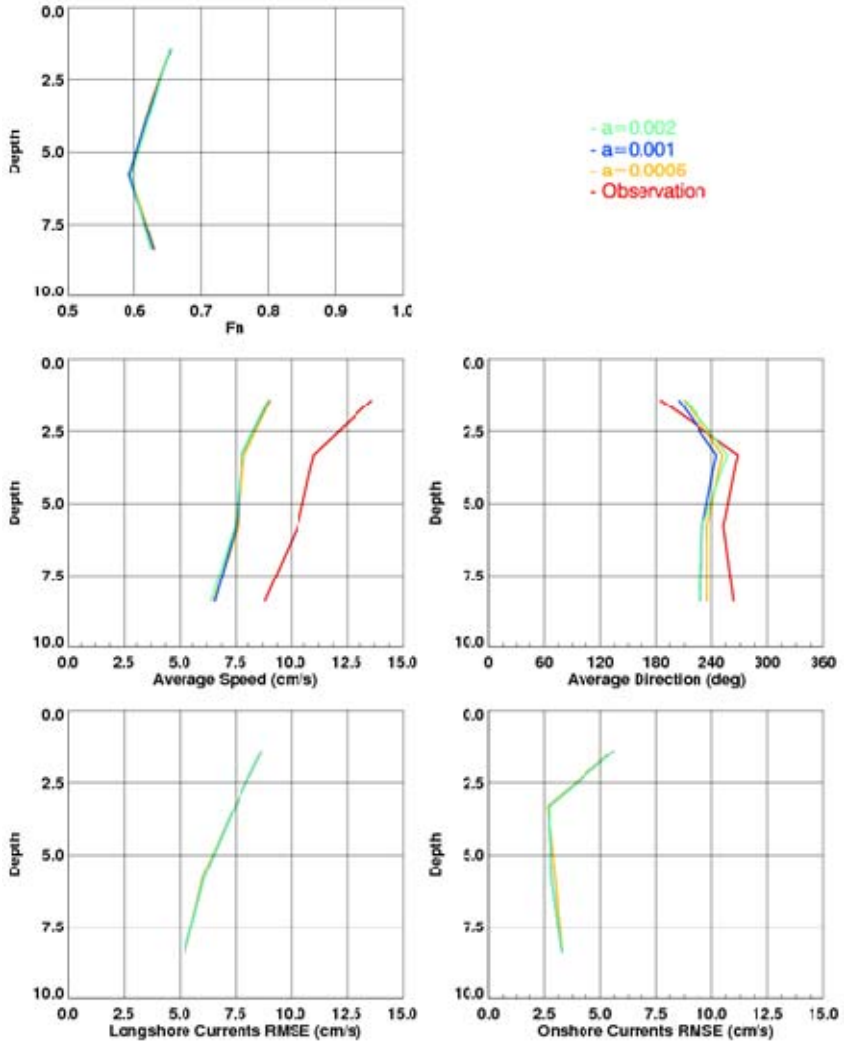

Figure C.1 Effect of parameter a on Fourier Norm, average speed and direction, and longshore and onshore currents RMSE during June 19-24, 2006; observation is in red.

C.2. Effect of parameter b in roughness height on POMGL predictions

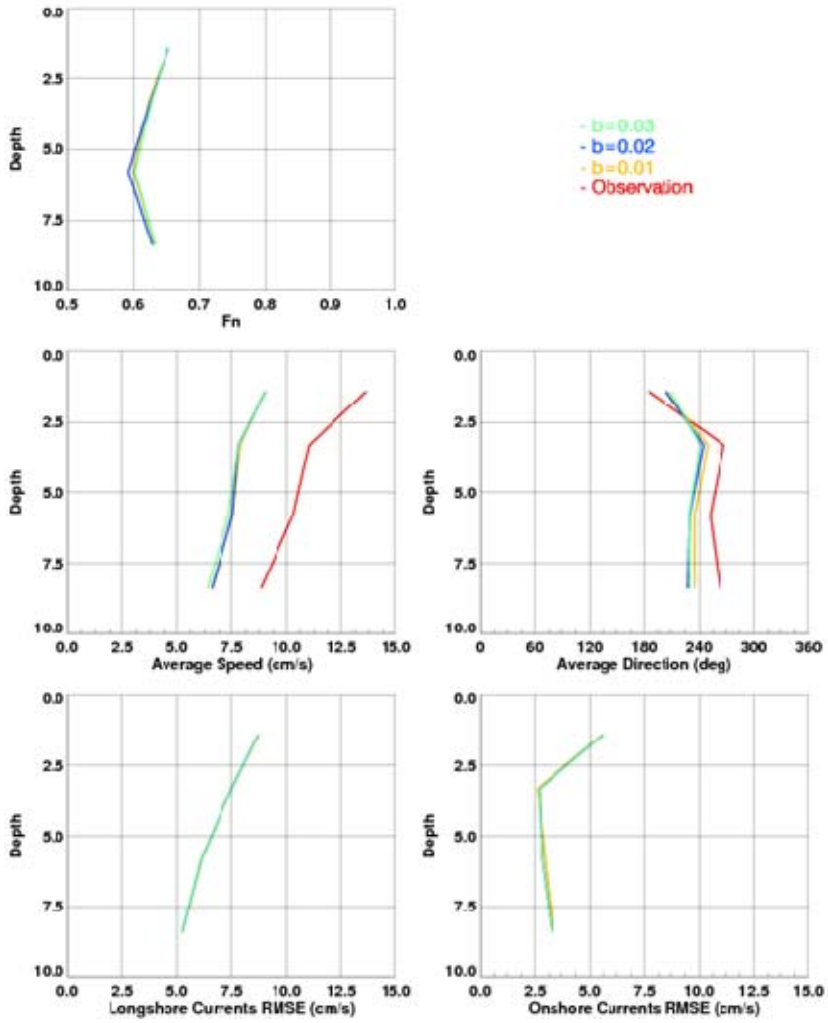

Figure C.2 Effect of parameter b on Fourier Norm, average speed and direction, and longshore and onshore currents RMSE during June 19-24, 2006; observation is in red.

C.3. Effect of parameter c in roughness height on POMGL predictions

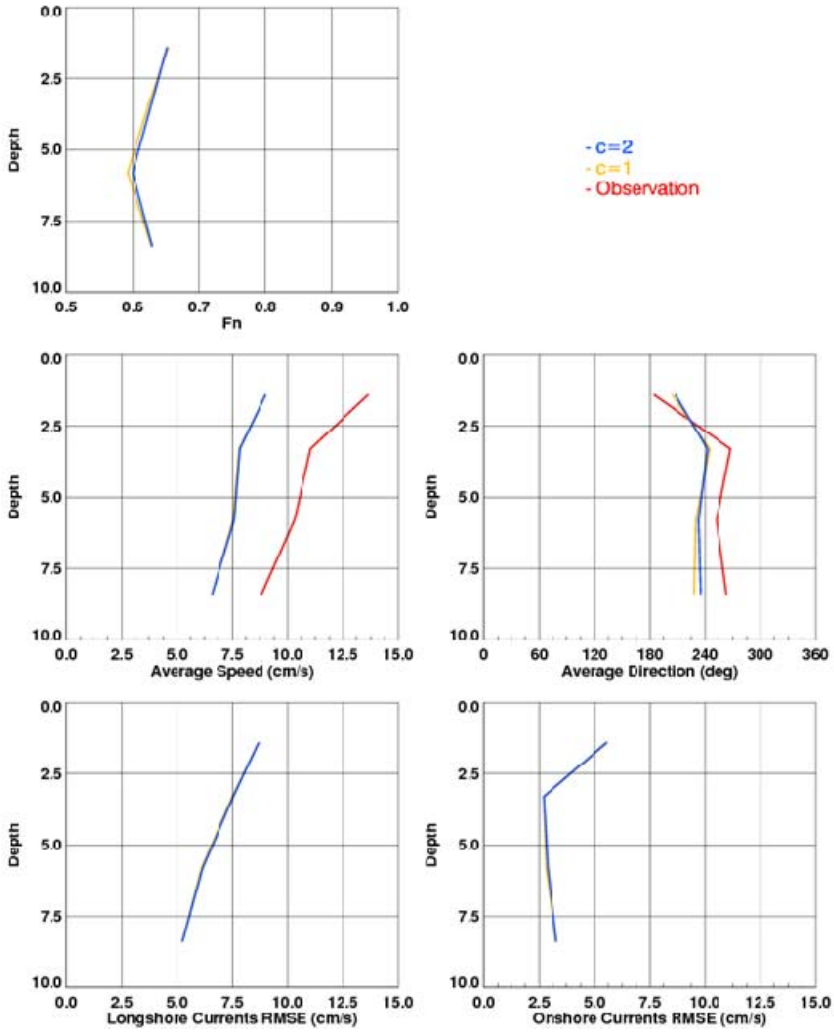

Figure C.3 Effect of parameter c on Fourier Norm, average speed and direction, and longshore and onshore currents RMSE during June 19-24, 2006; observation is in red.

Sensitivity of the model to horizontal diffusion is tested by changing the HORCON parameter in Smagorinsky eddy term. The results are shown below.

C.4. Effect of parameter HORCON (horizontal diffusion) on POMGL predictions

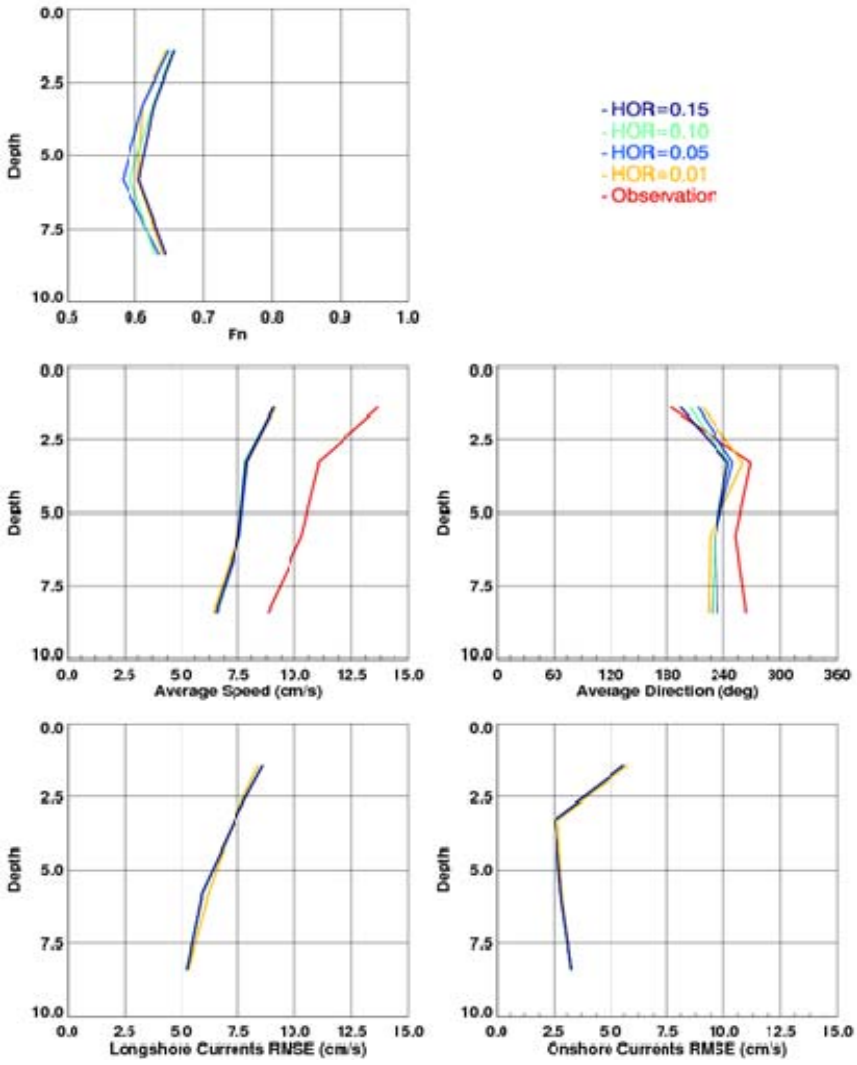

Figure C.4 Effect of parameter HORCON on Fourier Norm, average speed and direction, and longshore and onshore currents RMSE during June 19-24, 2006; observation is in red.

REFERENCES

Abdel-Gawad, S.T. 1985. Mixing and decay of pollutants from shore-based outfalls discharging into cross-flowing streams. *Ph.D. thesis, Department of Civil Engineering, University of Windsor, Windsor, Ont*.

Abdel-Gawad, S.T., and McCorquodale, J.A. 1985. Initial mixing of cross-flowing jets in trapezoidal channels. *In Proceedings of the 21st Congress of the International Association for Hydraulic Research, Melbourne, Australia*, 19–23 August 1985. Institution of Engineers, Barton, Australia. pp. 140–145.

Abdel Gawad, S.T., McCorquodale, J.A., and Gerges, H. 1996. Near-field mixing at an outfall. *Canadian Journal of Civil Engineering*, 23(1): 63–75.

Abdelwahed, M. S. T., and Chu, V. H. (1981). "Surface jets and surface plumes in cross-flows." Technical Rep. No. 81-1, *Fluid Mechanics Laboratory, McGill Univ., Montreal*.

Beletsky, D., Mason, D. M., Schwab, D. J., Rutherford, E. S., Janssen, J., Clapp, D. F., and Dettmers, J. M. (2007). "Biophysical model of larval yellow perch advection and settlement in Lake Michigan." *Journal of Great Lakes Research*, 33(4), 842-866.

Beletsky, D., and Schwab, D. J. (2001). "Modeling circulation and thermal structure in Lake Michigan: Annual cycle and interannual variability." *J. Geophys. Res.*, 106(9), 19,745–19,771.

Beletsky, D., Schwab, D. J., and McCormick, M. (2006). "Modeling the 1998–2003 Summer Circulation and Thermal Structure in Lake Michigan." *J. Geophys. Res.*, 111, 1-18.

Bennett, J. R., and Clites, A. H. (1987). "Accuracy of Trajectory Calculation in a Finite-Difference Circulation Model." *J. Comput. Phys.*, 68(2), 272-282.

Bleninger T., Jirka G. H. (2004). "Near- and Far-Field Model Coupling Methodology for Wastewater Discharges." *14th Congress of Asia and Pacific Division, International Association of Hydraulic Engineering and Research*, 12, 15 - 18.

Blumberg, A. F., and Georgas, N. (2008). "Quantifying Uncertainty in Estuarine and Coastal Ocean Circulation Modeling." *Journal of Hydraulic Engineering*, 134(4), 403-415.

Blumberg, A. F., Ji, Z.-G., and Ziegler, C. K. (1996). "Modeling Outfall Plume Behavior Using Far Field Circulation Model." *Journal of Hydraulic Engineering*, 122(11), 610-616.

Blumberg, A. F., and Mellor, G. L. (1987). "A Discription of a Three-Dimensional Coastal Ocean Circulation Model." *Three dimensional coastal ocean models*, Vol. 4, N. Heaps, ed., American Geophysicists Union, Washington, D.C., 1–16.

Carnelos, S. L. (2003). "Urban Stormwater Runoff Discharges to Lake Pontchartrain: 3-D Hydrodynamic Model for Plume Behavior and Fate and Transport of Pathogens in the Effluent." *Thesis (University of New Orleans)*, 474.

Carvalho, J. L. B., Feitosa, R. C., Rosman, P. C. C., and Roberts, P. J. W. (2006). "A Bacterial Decay Model for Coastal Outfall Plumes." *(SI 39 (Proceedings of the 8th International Coastal Symposium, Itajaí, SC, Brazil))*, 1524 - 1528.

Carter, H. H., and Regier, R. (1974). "The three-dimensional heated surface jet in a crossflow." *Technical Rep. No. 88, Chesapeake Bay Institute, Johns Hopkins Univ., Baltimore*.

Chambers, R. L., and Eadie, B. J. (1980). "Nearshore Chemistry in the Vicinity of the Grand River, Michigan." NOAA Technical Memorandum ERL GLERL-28, Great Lakes Environmental Research Laboratory, Ann Arbor, Michigan.

Chen, F., MacDonald, D. G., and Hetland, R. D. (2009). "Lateral spreading of a near-field river plume: Observations and numerical simulations." *J. Geophys. Res.*, 114.

Chick, H., (1910). "The process of disinfection by chemicals agents and hot water." *J. Hygiene Cambridge*, 10, 237–286.

Chin, D. A., and Roberts, P. J. W. (1985). "Model of dispersion in coastal waters." *Journal of Hydraulic Engineering*, 111 (1), 12-28.

Csanady, G. T.. (1964) Turbulent diffusion in a stratified fluid. *Atmos. Sci.* 21, 439-447.

Csanady, G. T. (2006). "Turbulent diffusion in Lake Huron." *Journal of Fluid Mechanics Digital Archive*, 17(03), 360-384.

Csanady, G. T., Sullivan, P. J., Berretta, M., Bergs, A., and Hale, A. M. (1964). "Hydrodynamic Studies on Lake Huron at Baie Du Dore." *Report No. PR 19, Water Resources Institute, University of Waterloo and Great Lakes Institute, University of Toronto*.

Cowell, S. E., Hurley, J. P., Schafer, M. M. and P. E. Hurley. (1995). "Mercury partitioning and transport in Lake Michigan Tributaries". Presented at 38th Conference. International Association of Great Lakes Research.

Davis, L. R. (1999). "Fundamentals of Environmental Discharge Modeling." *Boca Raton : CRC Press*.

Dimou, K. (1992). "3-D Hybrid Eulerian-Lagrangian / Particle Tracking Model for Simulating Mass Transport in Coastal Water Bodies," *Thesis, MIT Thesis, Massachusetts Institute of Technology*.

Dinelli, G., and Parrini, F. (1975). "An experimental evaluation of heat transfer to the environment by cooling water discharges from the Vado Ligure power plant using an infrared technique." *Proc., 16th Congress of Int. Assoc. for Hydraulic Research*, Sao Paulo, Brazil, 3, 246–254.

Ezer, T., and Mellor, G. L. (2000). "Sensitivity studies with the North Atlantic sigma coordinate Princeton Ocean Model." *Dyn. Atmos. & Oceans*, 2000(32), 185-208.

Fischer, H.B., List, E.J., Koh, R.C.Y., Imberger, J., and Brooks, N.H. 1979. "Mixing in inland and coastal waters". *Academic Press, New York*.

Fong, D.A., Geyer, W.R., (2001). "Response of a river plume during an upwelling favorable wind event". *J. Geophys. Res.* 106 (C1), 1067–1084.

Frick, W. E., Ge, Z., and Zepp, R. G. (2008). "Nowcasting and Forecasting Concentrations of Biological Contaminants at Beaches: A Feasibility and Case Study." *Env. Sc. Tech.*, 42(13), 4218-4824.

Garvine, R.W., (1999). "enetration of buoyant coastal discharge onto the continental shelf: a numerical study". *J. Phys. Oceanogr.* 29, 1892–1909.

Garvine, R. W. (1989) "Radial Spreading of Buoyant, Surface Plumes in Coastal Waters." *J. Geophys. Res*., 89, 1989-1996.

Great Lakes Commission, (2000). "Assessment of the Lake Michigan Monitoring Inventory: A Report on the Lake Michigan Tributary Monitoring Project", August, 2000.

Hall, D. W. and T. E. Behrendt. (1995). "Polychlorinated byphenyls and pesticides in Lake Michigan tributaries, 1993-95". Presented at 38th Conference. International Association of Great Lakes Research. MDEQ, (2006). "Michigan Beach Monitoring Year 2004 Annual Report", Michigan Department of Water Quality, Staff Report #MI/DEQ/WB-06/030. March 2006.

Hetland, R.D., (2005). "Relating river plume structure to vertical mixing". *J. Phys. Oceanogr.* 35 (9), 1667–1688.

Hetland, R. D. (2009). "The effects of mixing and spreading on density in near-field river plumes." *Dynamics of Atmospheres and Oceans*, In Press, Corrected Proof.

Hetland, R. D., and MacDonald, D. G. (2008). "Spreading in the near-field Merrimack River plume." *Ocean Modeling*, 21(1-2), 12-21.

Hipsey, M. R., Antenucci, J. P., and Brookes, J. D. (2008). "A generic, process-based model of microbial pollution in aquatic systems." *Water Resources Research*, 44(7), 26.

Holtschlag, D. J., Shively, D., Whitman, R. L., Haack, S. K., and Fogarty, L. R. (2008). "Environmental Factors and Flow Paths Related to Escherichia Coli Concentrations at Two Beaches on Lake St. Clair, Michigan, 2002–2005." Scientific Investigations Report 2008–5028, U.S Department of the Interior, U.S Geological Survey, Reston, VA, 38 pp.

HydroQual, Inc. (2005). "ECOMSED: three-dimensional hydrodynamic and sediment transport model". *HydroQual, Inc.*, Mahwah, N.J. Available online from www.hydroqual.com/ehst_ ecomsed.html

Jay, D. A., Zaron, E. D., and Pan, J. (2010). "Initial expansion of the Columbia River tidal plume: Theory and remote sensing observations." *J. Geophys. Res.*, 115.

Jirka, G. H. (2007). "Buoyant Surface Discharges into Water Bodies. I: Jet Integral Model." *Journal of Hydraulic Engineering*, 133(9), 1021-1036.

Jirka, G. H., Adams, E. E., and Stolzenbach, K. D. (1981). "Buoyant Surface Jets." *Journal of the Hydraulics Division-ASCE*, 107(11), 1467-1487.

Jones, G. R., Nash, J. D., and Jirka, G. H. (1996). "Cormix3: An Expert System for Mixing Zone Analysis and Prediction of Buoyant Surface Discharges." Technical *Report, DeFrees Hydraulics Laboratory, Cornell University*.

Jones, G. R., Nash, J. D., Doneker, R. L., and Jirka, G. H. (2007). "Buoyant surface discharges into water bodies. I: Flow classification and prediction methodology." *Journal of Hydraulic Engineering*, 133 (9), 1010-1020.

Kim, Y. D., Seo, I. W., Kang, S. W., and Oh, B. C. (2002). "Jet Integral Particle Tracking Hybrid Model for Single Buoyant Jets." *Journal of Hydraulic Engineering*, 128(8), 753.

Kim, Y. D., Seo, I. W., Kang, S. W., and Oh, B. C. (2001). "Modeling the Mixing of Wastewater Effluent Discharged from Ocean Outfalls using a Hybrid Model." *Coastal Engineering Journal*, 43(4), 259.

Koester, G. E. (1974). "Experimental study of submerged single-port thermal discharges." *MS thesis, Dept. of Civil Engineering, M.I.T., Cambridge, Mass*.

Koh, R. C. Y., and Brooks, N. H. (1975). "Fluid Mechanics of Waste Water Disposal in the Ocean." *Annual Review of fluid Mechanics*, 7, 187-211.

Kuhlman, J. M., and Prahl, J. M. (1974). "Laboratory modeling of surface thermal plumes." *Rep. No. FTAS/TR-74-102, School of Engineering, Case Western Reserve Univ., Cleveland*.

Korotenko, K. A., Mamedov, R. M., Kontar, A. E., and Korotenko, L. A. (2004). "Particle tracking method in the approach for prediction of oil slick transport in the sea: modelling oil pollution resulting from river input." *Journal of Marine Systems*, 48(1-4), 159-170.

Liu, L., Phanikumar, M. S., Molloy, S. L., Whitman, R. L., Shively, D. A., Nevers, M. B., Schwab, D. J., and Rose, J. B. (2006). "Modeling the transport and inactivation of e. Coli and enterococci in the near-shore region of lake michigan." *Environmental Science & Technology*.

Liu, W. C., Kuo, J. T., Young, C. C., and Wu, M. C. (2007). "Evaluation of marine outfall with three-dimensional hydrodynamic and water quality modeling." *Environmental Modeling & Assessment*, 12(3), 201-211.

Martin, P. J., (1985). "Simulation of the mixed layer at OWS November and Papa with several models." *J. Geophys. Res.*, (90), 903-916.

McCormick M., Schwab D., Beletsky D., Roberts P.J.W, Winkelman A., Foley A., Gungor E., and Nekouee N. "Dispersion of the Grand River Plume into the Coastal Waters of Lake Michigan". *IAGLR Conference, University Park, Pennsylvania* (2007).

McCorquodale, J. A. (2007). "Storm-Water Jets and Plumes in Rivers and Estuaries." *Canadian Journal of Civil Engineering*, NRC Research Press, 691-702.

McCorquodale, J.A., Georgiou, I., Carnelos, S., and Englande, A.J. (2004). "Modeling coliforms in storm water plumes". *Journal of Environmental Engineering and Science*, 3: 419–431.

McCorquodale, J.A., Hannoura, A.A., and Carnelos, S. (2000). Urban storm and waste water outfall modeling. *Final project report to US Environmental Protection Agency, New Orleans, La. Urban Waste Management Research Center, College of Engineering, The University of New Orleans, New Orleans, La.*

McLellan, S. L., Hollis, E. J., Depas, M. M., Van Dyke, M., Harris, J., and Scopel, C. O. (2007). "Distribution and Fate of Escherichia Coli in Lake Michigan Following Contamination with Urban Stormwater and Combined Sewer Overflows." *J. Great Lakes Res.*, 33(3), 566-580.

Mellor, G. L. (1991). "An equation of state for numerical-models of oceans and estuaries." *Journal of Atmospheric and Oceanic Technology*, 8 (4), 609-611.

Mellor, G. L., and Yamada, T. (1982). "Development of a turbulence closure-model for geophysical fluid problems." *Reviews of Geophysics*, 20 (4), 851-875.

Motz, L. H., and Benedict, B. A. (1970). "Heated surface jet discharged into a flowing ambient stream." *Rep. No. 4, Dept. of Environmental, and Water Resources Engineering, Vanderbilt Univ., Nashville, Tenn*.

Nekouee, N., Roberts P.J.W., "3D Numerical Prediction of the Grand River Plume". *IAGLR Conference, Toledo, Ohio (2009).*

Nekouee, N., Roberts P.J.W., Schwab D., "Far Field Prediction of the Grand River Plume". *The 12th International Workshop on Physical Processes in Natural Waters*, Lake Tahoe, USA (2008).

Nevers, M. B., and Whitman, R. L. (2008). "Coastal Strategies to Predict Escherichia coli Concentrations for Beaches along a 35 km Stretch of Southern Lake Michigan." *Environmental Science & Technology*, 42(12), 4454-4460.

O'Donnell, J., (1990). "The formation and fate of a river plume: a numerical model". *J. Phys. Oceanogr*. 20 (4), 551–569.

Peeters, F. 1994. Horizontale Mischung in Seen (Horizontal mixing in lakes). *Ph.D. thesis, Eidgenossische Technische Hochschule, Zurich*.

Pearson, H. J., Puttock, J. S., Hunt J. C. R., (1983) "A statistical model of fluid element motions and vertical diffusion in a homogeneous stratified flow". *J. Fluid Mech*., vol. 129, pp. 219-249.

Rao, Y. R., Skafel, M. G., and Charlton, M. N. (2004). "Circulation and turbulent exchange characteristics during the thermal bar in Lake Ontario." *Limnology and Oceanography*, 49(6), 2190-2200.

Roberts, P. J. W. (1979). "Line Plume and Ocean Outfall Dispersion." *Journal of the Hydraulic Division, ASCE*, 105(4), 313-331.

Roberts, P. J. W. (1999). "Modeling Mamala Bay Outfall Plumes. I: Near Field." *Journal of Hydraulic Engineering*, 125(6), 564-573.

Roberts, P. J. W. (1999). "Modeling Mamala Bay Outfall Plumes. II: Far Field." *Journal of Hydraulic Engineering*, 125(6), 574-583.

Robertson, D. M. (1997). "Regionalized loads of suspended sediment and phosphorus to Lakes Michigan and Superior-High flow and long-term average". *Journal of Great Lakes Research*. 23:416-439.

Rosato, E. (2007). "Circadian Rhythms, Methods and Protocols" *Human Press Inc., New Jersey*.

Rose, J. B., and Phanikumar, M. S., (2007). " Water Pollution Studies for the Lower Grand River, Michigan" Presentation, Ottawa County Water Quality Forum.

Ruberg, S. A., Guasp, E., Hawley, N., Muzzi, R. W., Brandt, S. B., Vanderploeg, H. A., Lane, J. C., Miller, T. C., and Constant, S. A. (2008). "Societal benefits of the Real-time Coastal Observation Network (RECON): Implications for municipal drinking water quality." Marine Technology Society Journal, 42(3), 103-109.

Runchel, A. K. (1983) . "An Evaluation of Effluent Dispersion and Fate and Transport Models for OCS Platforms", Volume 1, Proceedings of the Workshop, Prepared for the Minerals Management Service, U.S. Department of Interior, Contract No. 14-12-0001-29122, Santa Barbara, California.

Schwab, D. J., and Bedford, K. W. (1994). "Initial Implimentation of the Great Lakes Forecasting System: A Real-Time System for Predicting Lake Circulation and Thermal Structure." *Water Pollut. Res. J. Can.*, 29, 203-220.

Shaffer, M. M., Overdier, J. T., Baldino, R. A., Hurley, J. P. and P. E. Hughes. (1995). "Levels, partitioning, and fluxes of six trace elements in Lake Michigan tributaries". *38th Conference of the International Association of Great Lakes Research*.

Shen, C., Phanikumar, M. S., Fong, T. T., Aslam, I., McElmurry, S. P., Molloy, S. L., and Rose, J. B. (2008). "Evaluating Bacteriophage P22 as a Tracer in a Complex Surface Water System: The Grand River, Michigan." *Environ. Sci. Technol.*, 42(7), 2426-2431.

Shirazi, M ., L . Davis, (1974) . "Workbook of Thermal plume Predictions", Volume 2, Surface Discharge, National Environmental Research Center, Office of Research and Development, U.S. Environmental Protection Agency, Corvallis, Oregon.

Stacey, M. T., Cowen, E. A., Powell, T. M., Dobbins, E., Monismith, S. G., and Koseff, J. R. (2000). "Plume Dispersion in a Stratified, near-Coastal Flow: Measurements and Modeling." *Continental Shelf Research*, 20(6), 637-663.

Stevens, C. L., Lawrence, G. A., and Hamblin, P. F. (2004). "Horizontal Dispersion in the Surface Layer of a Long Narrow Lake." *J. Environ. Eng. Sci.*, 3(5), 413-417.

Stocker, R., and Imberger, J. (2003). "Horizontal Transport and Dispersion in the Surface Layer of a Medium-Sized Lake." *Limnol. Oceanogr.*, 48(3), 971-982.

Suh, S.-W. (2006). "A Hybrid Approach to Particle Tracking and Eulerian-Lagrangian Models in the Simulation of Coastal Dispersion." *Environmental Modelling & Software*, 21(2), 234-242.

Tsanis, I. K., and Wu, J. (2000). "Application and Verification of a Three-Dimensional Hydrodynamic Model to Hamilton Harbour, Canada." *Global Nest: the Int. J.*, 2(1), 77-89.

Thupaki, P., Phanikumar, M. S., Beletsky, D., Schwab, D. J., Nevers, M. B., and Whitman, R. L. (2010). "Budget Analysis of Escherichia coli at a Southern Lake Michigan Beach." Environmental Science & Technology, 44, 1010-1016.

USEPA, (1986). "Ambient Water Quality Criteria for Bacteria-1986", EPA 440/5-84/002.

USEPA, (1999). "Preliminary Investigation of the Extent of Sediment Contamination in the Lower Grand River", October, 1999, EPA-905-R-99-010.

USEPA, (2001). "Protocol for Developing Pathogen TMDLs", January 2001, EPA 84/R-00-002.

USEPA, (2002). "National Beach Guidance and Required Performance Criteria for Grants", EPA 823-B-02-004.

USEPA, (2004). "Impacts and Control of CSOs and SSOs", Office of science and Technology, USEPA, Washington, D.C.

Varlamov, S. M., Yoon, J.-H., Hirose, N., Kawamura, H., and Shiohara, K. (2000). "Simulation of the oil spill processes in the Sea of Japan with regional ocean circulation model." *Journal of Marine Science and Technology*, 4(3), 94-107.

White, M., Feigheryt, L., Bowers, D., O'Riain, G., and Bowyert, P. (2005). "Using Digital Cameras for River Plume and Water Quality Measurements." International Journal of Remote Sensing, Taylor & Francis Ltd, 4405-4419.

Whitman, R. L., Nevers, M. B., Korinek, G. C., and Byappanahalli, M. N. (2004). "Solar and Temporal Effects on Escherichia Coli Concentration at a Lake Michigan Swimming Beach." *Appl. Environ. Microbiol.*, 70(7), 4276-4285.

Wu, J. (1994). "An Integrated Hydrodynamic and Pollutant Transport Model for the Nearshore Areas of the Great Lakes and Their Tributaries," *Ph.D. Thesis, McMaster University, Canada*.

Yamahara, K. M., Layton, B. A., Santoro, A. E., and Boehm, A. B. (2007). "Beach sands along the California coast are diffuse sources of fecal bacteria to coastal waters." *Environmental Science & Technology*, 41(13), 4515-4521.

Yankovsky, A. E., and Chapman, D. C. (1997). "A Simple Theory for the Fate of Buoyant Coastal Discharges." *Journal of Physical Oceanography*, 27(7), 1386-1401.

Ye, J., and McCorquodale, J.A. 1997. Three-dimensional numerical modelling of mass transport in curved channels. *Canadian Journal of Civil Engineering*, 24(3): 471–479.

Zhang, X. Y. (1995). "Ocean Outfall Modelling-Interfacing near and Far Field Models with Particle Tracking Method." *Thesis, MIT*.

Zhang, X. Y., and Adams, E. E. (1999). "Prediction of near Field Plume Characteristics Using Far Field Circulation Model." *Journal of Hydraulic Engineering*, 125(3), 233-241.

The Alliance of the Great Lakes Annual Report, 2001: http://www.greatlakes.org (October, 2008)

http://astro.neutral.org/articles/tea/tea.html (November, 2009)